POLISH ACADEMY OF SCIENCES – WROCŁAW BRANCH

WROCŁAW UNIVERSITY OF TECHNOLOGY

ISSN 1644-9665
INDEX 375667

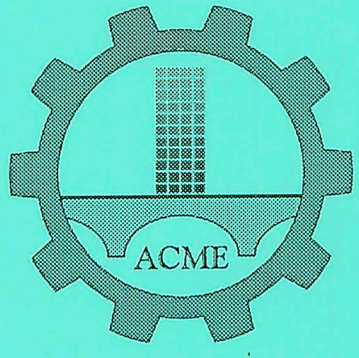

ARCHIVES OF CIVIL AND MECHANICAL ENGINEERING

Quarterly
Vol. VII, No. 3

WROCŁAW 2007

ADVISORY COMMITTEE

EDITORIAL BOARD

[1] The Faculty of Civil Engineering, Wrocław University of Technology
Wybrzeże Wyspiańskiego 27, 50-370 Wrocław, Poland
Tel. +48 71 320 41 35, Fax. +48 71 320 41 05, E-mail: jan.kmita@pwr.wroc.pl

[2] The Faculty of Mechanical Engineering, Wrocław University of Technology
ul. Łukasiewicza 5, 50-371 Wrocław, Poland
Tel. +48 71 320 21 73, Fax. +48 71 320 34 22, E-mail: jerzy.gronostajski@itma.pwr.wroc.pl

POLISH ACADEMY OF SCIENCES – WROCŁAW BRANCH
WROCŁAW UNIVERSITY OF TECHNOLOGY

ARCHIVES OF CIVIL AND MECHANICAL ENGINEERING

Quarterly
Vol. VII, No. 3

WROCŁAW 2007

EDITOR IN CHIEF

JERZY GRONOSTAJSKI

EDITORIAL LAYOUT AND PROOF-READING

MARCIN R. ODELSKI

TYPESETTING

SEBASTIAN ŁAWRUSEWICZ

SECRETARY

TERESA RYGLOWSKA

Publisher: Committee of Civil and Mechanical Engineering
of Polish Academy of Sciences – Wrocław Branch,
Faculty of Civil Engineering and Faculty of Mechanical Engineering
of Wrocław University of Technology

OFICYNA WYDAWNICZA POLITECHNIKI WROCŁAWSKIEJ
Wybrzeże Wyspiańskiego 27, 50-370 Wrocław
http://www.oficyna.pwr.wroc.pl
e-mail: oficwyd@pwr.wroc.pl

ISSN 1644-9665

Drukarnia Oficyny Wydawniczej Politechniki Wrocławskiej. Zam. nr 674/2007.

Contents

Spis treści

ARCHIVES OF CIVIL AND MECHANICAL ENGINEERING

Vol. VII 2007 No. 3

Application of a Stereo PIV System for Investigations of Flow Fields in Towing Tank and Cavitation Tunnel

P. ANSCHAU, K.P. MACH
Potsdam Model Basin, Marquardter Chaussee 100, 14469 Potsdam
anschau@sva-potsdam.de, mach@sva-potsdam.de

A newly installed submersible stereo PIV system, designed for the use in the towing tank and operating perpendicular to the main flow direction, is described. This Stereo Particle Image Velocimetry system allows the contactfree, 3-dimensional determination of velocity fields in the towing tank and cavitation tunnel. Flow conditions can be analyzed with a resolution of a few thousand points simultaneously, with a frame rate of up to 15 pictures per second, providing a good insight into flow characteristics without disturbing the flow. The paper will describe two applications of the system that have already been carried out (propeller in open water condition and in the cavitation tunnel) and will discuss merits and disadvantages of the new system. The potentials for validation of CFD calculations will be shortly discussed. Future plans for further applications of the system will be introduced.

Keywords: *particle image velocimetry, stereoscopic PIV, fluid mechanics, ship hydrodynamics*

1. Introduction

A thorough knowledge of flow conditions is an important prerequisite for competitive ship and propeller design. Measurements of velocity fields behind a model ship with and without working propeller are usually done with a conventional five-hole pressure probe. It is easy and quickly to use but gives only time averaged results with comparably poor spatial resolution; moreover it disturbs the flow field and cannot give the necessary insight into flow separation phenomena. Additionally, inflow directions of only up to 25° can be measured. A more advanced technique is the “Laser Doppler Velocimetry” (LDV), which has been successfully applied at the Potsdam Model Basin for many years [1]. While the resolution in time and space can be very high when using LDV (which can be useful for the investigation of unsteady periodic flow phenomena), determination of velocity fields in a larger area and/or with high spatial resolution becomes very time-consuming. The investigation of a greater variety of conditions (different operating points, rudder and drift angles, in various combinations) is virtually not practicable respectively affordable in this way. Conventional two-dimensional PIV measurements are not satisfying for the mentioned purposes because perspective errors cannot be corrected from the measured velocity field and the third velocity component is not obtainable at all.

To overcome these limitations a new Stereo Particle Image Velocimetry (SPIV) system from TSI was installed at Potsdam Model Basin which allows the contactfree,

3-dimensional determination of velocity fields in both the towing tank and the cavitation tunnel. The system allows the exploration of flow conditions with a resolution of several thousand points simultaneously. The size of the physical area being watched depends on the kind of optics being used. The double frame rate is up to 15 pictures per second, which is not sufficient for high frequency transient phenomena, but provides a good insight into flow characteristics without disturbing the flow. This way time averaged flow fields can be measured with a considerable spatial resolution. Thanks to its modular design, the system can be set up in several ways, thus allowing for symmetric as well as asymmetric configuration of cameras and lightsheet (see Figure 1).

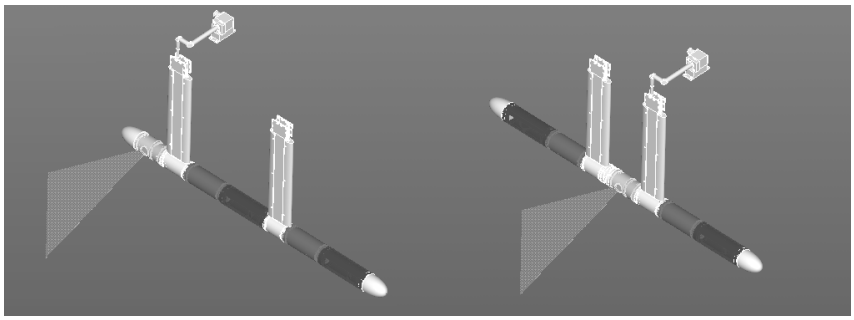

Fig. 1. Two out of several possible arrangements of the modular SPIV system [2].
Left: Cameras on same side of lightsheet. *Right*: Symmetric, cameras on both sides

In this paper we will describe two experimental setups for which SPIV measurements were conducted: a) open water tests in the towing tank and b) the cavitation tunnel. Roughly similar experiments in a circulating water channel have been reported already in [3], but were conducted in a very different flow regime. In our experiments all four "quadrants" (positive/negative direction of inflow and rotation) of operating conditions of the propeller were investigated. We will present selected results and additionally will compare these to CFD calculations. Finally, we will take a short look at future applications of the system.

2. Experimental set-up

With PIV technique the velocity field is measured by capturing two consecutive pictures of the same illuminated area in the fluid. Illumination is done with a light sheet generated by a laser beam which is spread by a cylindrical lens. The fluid needs to be seeded with small particles that reflect the laser light. The displacement of the particle images between the two pictures is measured using cross correlation methods, and with the known Δt the velocity field can be calculated. If two cameras are used (i.e. stereo PIV is applied), even the out of plane displacement of the particles can be calculated.

2.1. Open water test

A schematic sketch of the SPIV system setup for use in the towing tank is shown in Figure 2; an overview of experimental conditions is given in Table. The system consists of a submersible tube (120 mm diameter, 2300 mm length) fixed at two streamlined struts which allow an operating depth of up to 0.7 m (see Figure 3). The tube contains the two cameras, the corresponding tilted mirrors, the converging and cylindrical lenses for laser beam focusing and spreading and the mirror for the laser beam emission at the front end of the tube. The distance between the adjustable tilt mirrors was set to ~750 mm, which is a compromise between achieving the desired field of view, a possibly large angle between the two cameras respectively mirror center axes and a preferably small skewness of the front camera's (CCD 1) viewing area.

Table. Main experimental conditions in open water and cavitation tunnel propeller test

		Open water test	Cavitation tunnel	Unit
Propeller	advance coefficient	0.3	varying	–
Laser	laser type	Nd:YAG	Nd:YAG	–
	max. power	190	190	mJ/puls
	max. pulse repetition rate	15	15	Hz
Recording	focal width (cam1/cam2)	55/105	28/28	mm
	viewing angle between cams.	15	20	degree
	resolution	1200×1600	1200×1600	px^2
	max. double frame capt. rate	15	15	frames/s
	converging lens focal length	1000	500/1000	mm
	cylindrical lens focal length	50	25	mm
	viewing area at light sheet	160×250	~210×330	mm^2
Analysis	interrogation window size	32×32	32×32	px^2
	equivalent physical area	4.8×4.8	6×6	mm^2
Plane of observation	position of light sheet	0.2/0.4/0.6 D_P behind	centerline	–
	plane of light sheet	*YZ*	*XZ*	–

The laser beam is directed from atop via a mirror tube that goes through the front strut down to the lenses, where it is first focused and then expanded to a sheet of light.

The light sheet is aligned perpendicular to the main flow direction; it is generated by a dual-laser system with two frequency-doubled (532 nm), pulsed Nd:YAG lasers with a maximum energy of 190 mJ/pulse. The beams from the two lasers are combined into a collinear beam. On the one hand, with the dual-laser system the timing of the two consecutive laser pulses can be adjusted almost arbitrarily. Another advantage is the similarity of the laser intensity of the two pulses. On the other hand the alignment of the two laser beams poses a certain difficulty. Spreading of the laser beam is done with a cylindrical lens, the focal length of which can be varied between 10 mm to 50 mm. The thickness of the light sheet is about 1 mm in the measurement area but varies between 0.5 mm and 2 mm, depending on the distance from the waist of the beam. Following [4], the thinner the light sheet is, the better the spatial resolution gets even in z and y direction, but the resulting signal-to-noise ratio decreases. Δt was ad-

justed after some preliminary tests to give the highest number of measured vectors and varied between 150 and 350 μs, depending on the investigated quadrant and the distance between light sheet and propeller plane. Also Δt must be selected in a way that particles will not pass the subject plane before the second capture is taken.

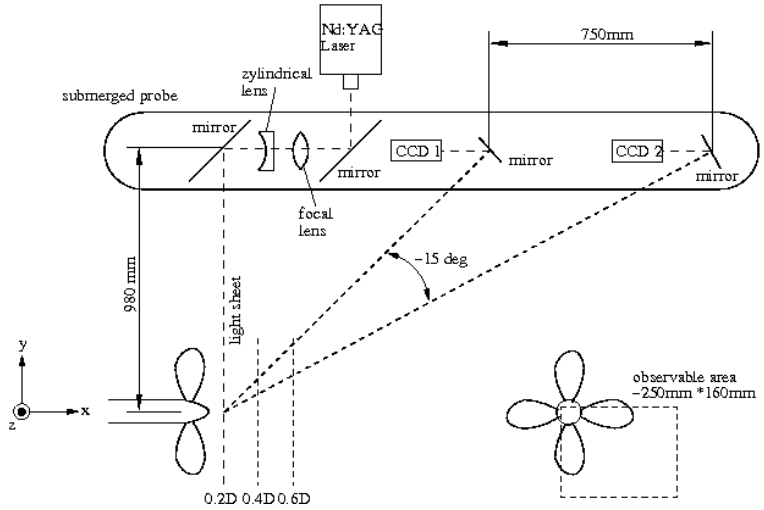

Fig. 2. Schematic sketch of experimental setup in open water test (not in scale)

The two cameras being used have a resolution of 12bit/pixel and a 1200×1600 pixel^2 CCD chip. The lenses are of Nikkor type. The focal length can be varied stepwise between 28 mm and 105 mm and was set to 55 mm (CCD 1) respectively 105 mm (CCD 2).

Seeding particles of about 90 μm were used to give the necessary number of at least 10 particle images per interrogation window (the small piece of the picture being analyzed with cross correlation).

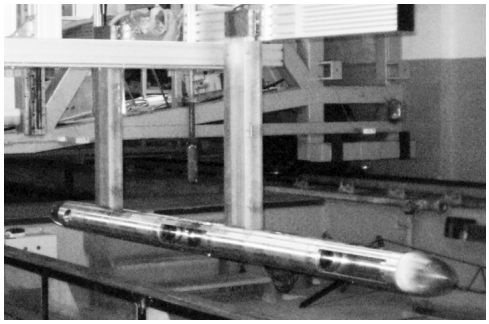

Fig. 3. SPIV probe mounted under towing carriage

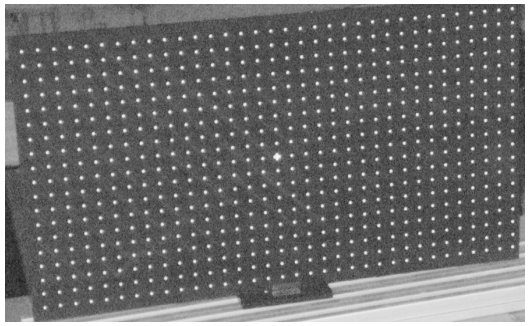

Fig. 4. Calibration target, 19x34 dots, 20 mm spacing

The Calibration of the system is accomplished with a four plane calibration target (see Figure 4) with a 20 mm spaced lattice of white dots aligned with diagonal bands of alternating levels (1 mm difference) on either side. The retrieved mapping functions allow the reconstruction of the 3D vector field from the two particle displacement fields of the two cameras.

2.2. Cavitation tunnel

The laser and the cameras from the submersible SPIV probe were used to carry out 3D measurements in the cavitation tunnel with the same propeller as before. Figure 5 schematically shows the arrangement of cameras and light sheet; the main difference to the previous experiment is the light sheet alignment with the propeller axis. The mirror tube of the previous experiment was not used, as the laser sheet enters through a window from below the cavitation tunnel. In this experiment, all four quadrants were investigated in front of and behind the propeller plane, providing a more detailed insight also into the propeller inflow. The distance between cameras and light sheet was about 600 mm, the focal length of the cameras was 28 mm. No additional seeding was used in order to avoid contamination of the water; the natural load of micro bubbles in the tunnel water turned out to be sufficient anyway. To avoid cavitation (laser reflections on cavitation bubbles can cause damage to the CCD chip), pressure was increased by 0.8 atmospheres. The calibration had to be accomplished in pressurised condition as the observation windows camber a few millimeters, which causes significant distortion in the reconstruction of the velocity fields.

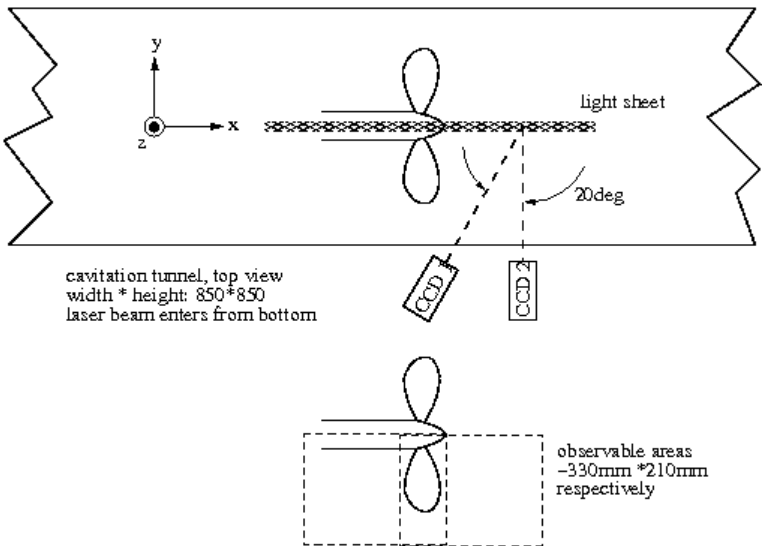

Fig. 5. Schematic sketch of experimental setup in cavitation tunnel (not in scale)

Essential for both experiments is the blackened hub and propeller: Not only will strong reflections destroy pixels in the CCD camera, but – even more important – they will mess up the measurement, as particles completely outside the actual lightsheet can be illuminated. At best, cross correlation will only create lots of spurious vectors, but in the worst case the analysis will produce velocity fields hardly identifiable as being wrong.

3. Image processing

Data acquisition and analysis is done with the provided software (INSIGHT 3G). The 2D analysis of the left and right particle image displacements is carried out with a multiple pass algorithm with interrogation window deformation, taking into account the resulting vector field of the previous pass. This is especially suitable for flows with high velocity gradients where the particle image displacement may vary across the window. The window size was 32×32 px^2. After each pass a mean filter was applied to remove spurious vectors. Finally, another mean filter was utilized to fill holes in the vector field with interpolated data from neighboring vectors. Figure 6 shows an example of raw 2D vectors after the very first processing step (left). Several spurious vectors can be detected, especially along the radius of the tip vortex location. As this is the area of high shear flow, several holes are present in the picture. Figure 6 (right) shows the smoothed and filled vector field after completed processing; the tip vortex and the characteristic acceleration of the tangential velocities caused by the trailing edge vortices can be clearly identified.

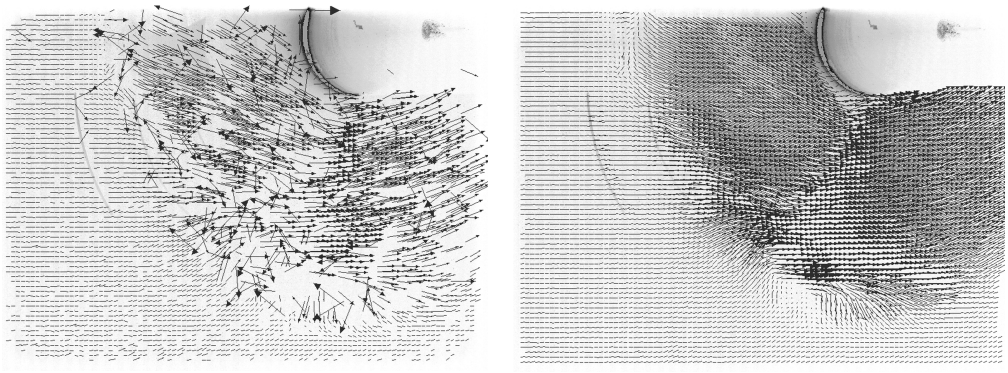

Fig. 6. *Left*: Raw vectors after first evaluation step. *Right*: Validated vector field after full analysis and validation. The crescent-shaped area at the top is the reflection of the laser light sheet on the hub

Due to the highly turbulent and unsteady nature of the propeller wake this instantaneous velocity field varies between consecutive revolutions. To get a representative velocity distribution for one rotational offset a set of shots of this angular position is averaged.

4. Results

A selected example of the results of the open water tests is shown in Figure 7. Vectors (top) show the transversal velocity components, and the contours show the axial velocity component, all at $x/D = 0.2$. The advance ratio was $J = 0.3$. The tip vor-

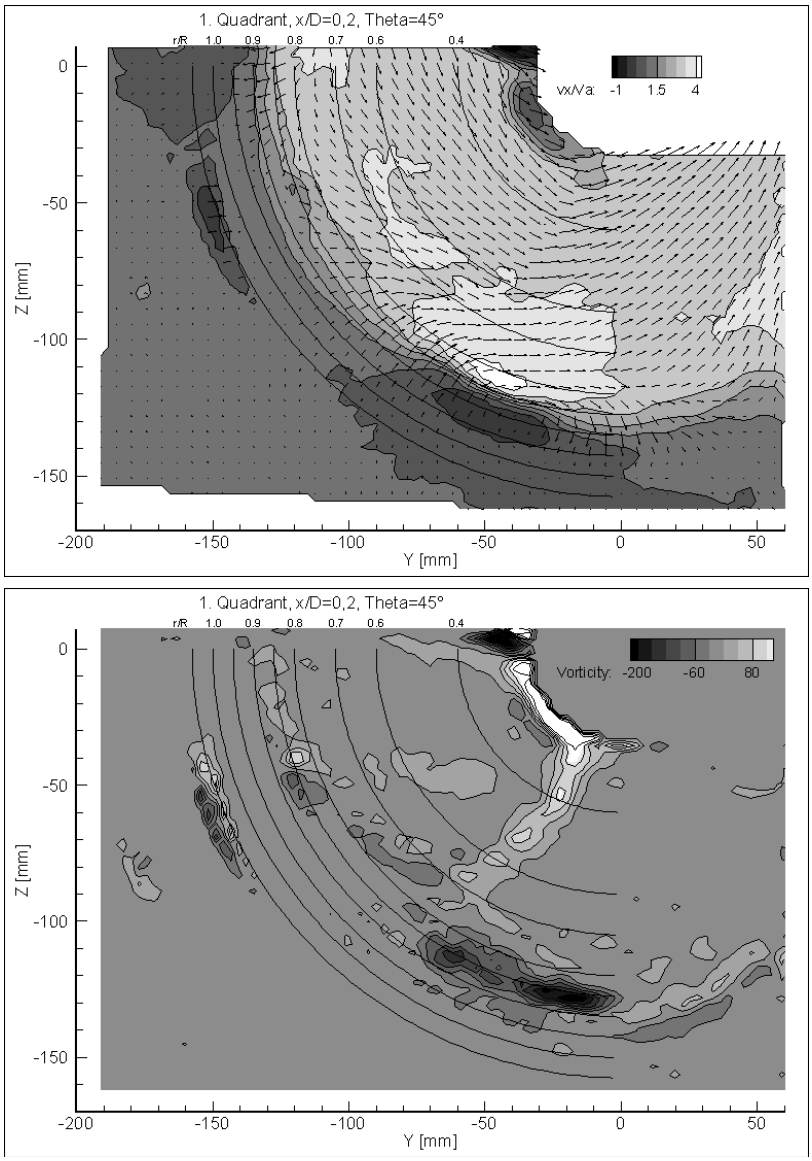

Fig. 7. *Top*: Resulting axial velocity field from open water test. $J = 0.3$, $x/D = 0.2$, rotational offset *Theta* = 45°, $n = 10\ s^{-1}$. *Bottom*: Vorticity distribution

tex is very well distinguishable, and at the upper left corner (0°) the beginning of another tip vortex becomes apparent. Figure 8 shows the smoothed velocity distribution along the marked radii for the normalized axial (*vx*), tangential (*vt*) and radial (*vr*) velocity components. *vx*/*Va* clearly shows the segregation between the inner (smaller radii) and outer (larger radii) parts of the tip vortex at 0.85 *R*, which in a way marks the centerline of the vortex.

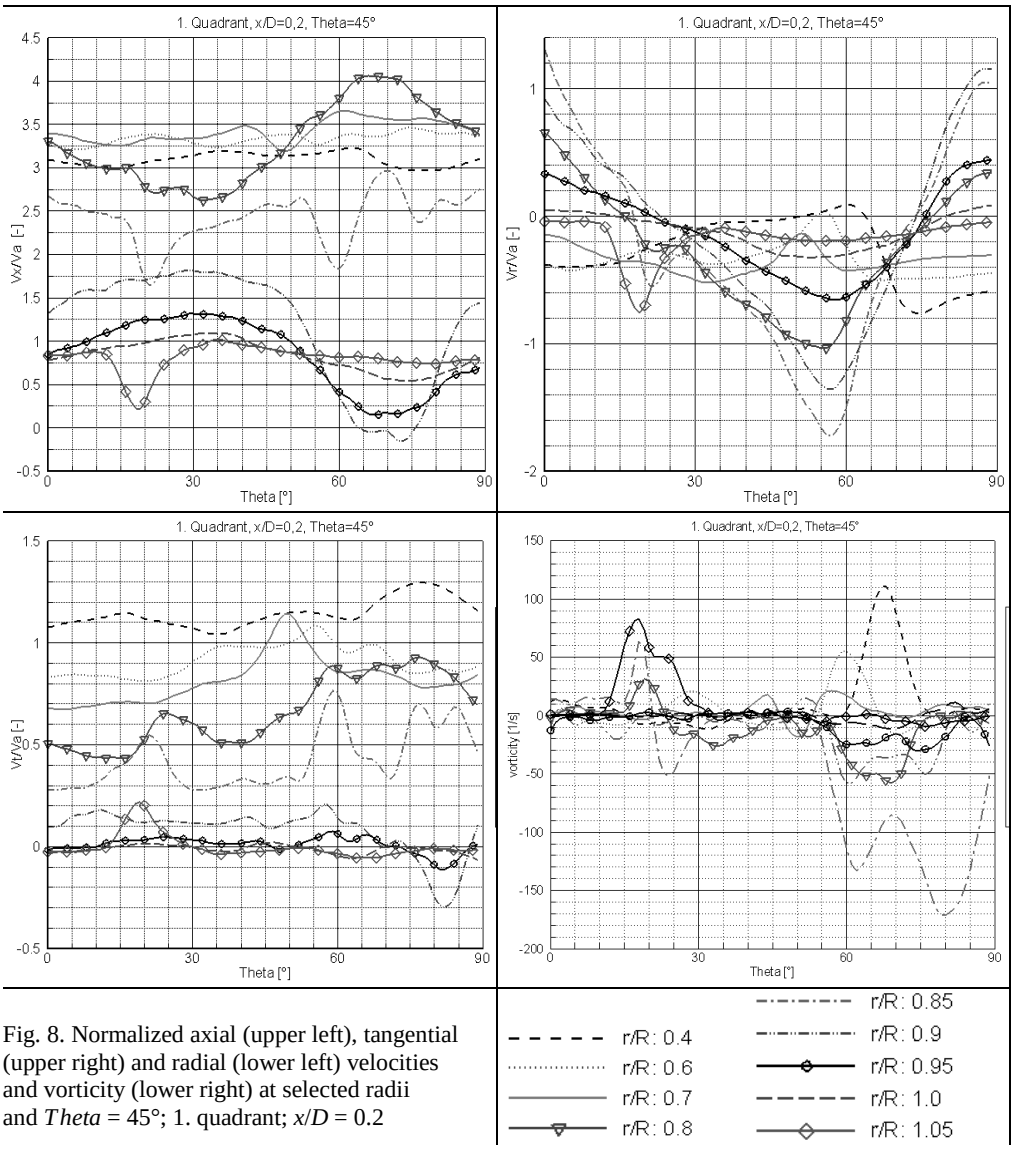

Fig. 8. Normalized axial (upper left), tangential (upper right) and radial (lower left) velocities and vorticity (lower right) at selected radii and *Theta* = 45°; 1. quadrant; *x*/*D* = 0.2

Vorticity is defined by the partial derivative of the velocity components:

$$\Omega = \frac{\partial Vy}{\partial x} - \frac{\partial Vx}{\partial y}$$

and its distribution can be seen in Figure 7 (bottom). The effects induced by the tip vortex and the velocity defect following the trailing edge of the blade can be easily identified; even the shape of the blade becomes visible from the edge vortices (lower right). Figure 8 also shows the smoothed vorticity distribution along the specified radii. The slightly curved shape of the maximum's ridge in Figure 7 can be found again in the distribution of the peaks between 60° and 80°. As pictures were taken via the tilted mirrors, the rotational offset increases from 9 o'clock to 6 o'clock position, though the propeller is actually right-handed.

In Figure 9 an example of the vorticity distribution in the cavitation tunnel experiment is displayed for an advance coefficient of $J = 0.7$. The strong gradients in the tip vortex and, directionally inverted, in the hub vortex can be seen clearly. Moreover the directionally inverted remaining of the trailing edge vortices can be identified above the vorticity cores.

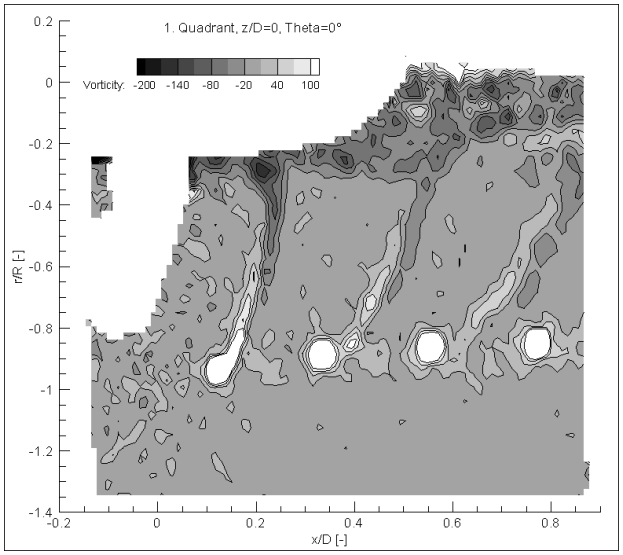

Fig. 9. Vorticity distribution in the cavitation tunnel $J = 0.7$

Finally, a series of images showing the angular resolved propeller slipstream is presented in Figure 10. Each of the images results from averaging 10–40 single captures. By averaging these 9 vector fields a mean velocity distribution for the propeller wake can be retrieved, similar to what one gets for example from LDV measurements.

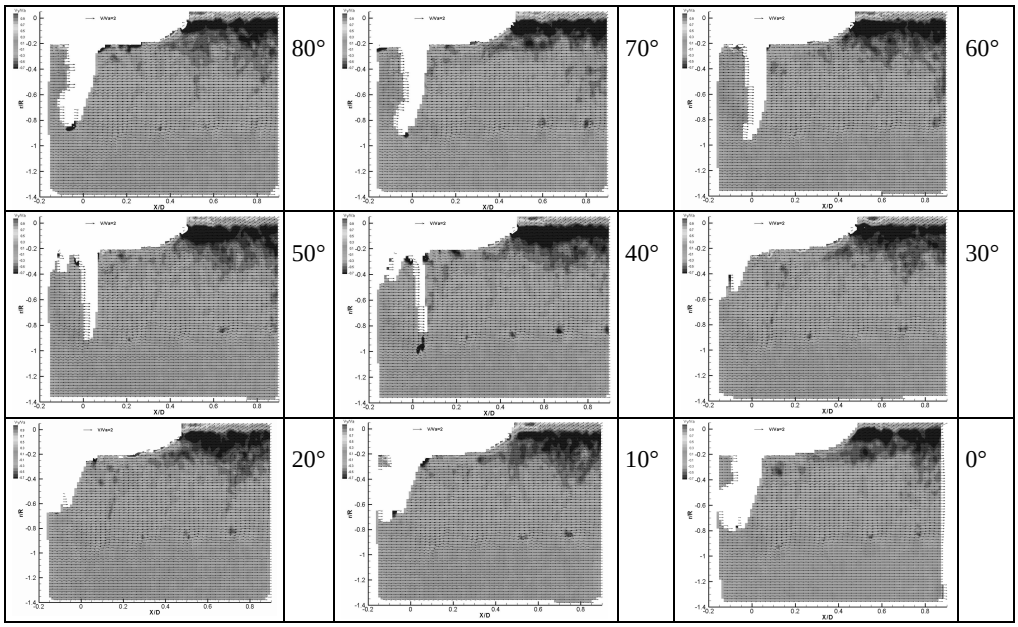

Fig. 10. Angular resolved propeller wake; every picture is phase-averaged from 10–40 pictures. 1. quadrant (positive inflow and rotation); $J = 0.7$

5. PIV and CFD

Since the analysis of the SPIV measurement provides most of the interesting variables of the flow (3 velocity components, turbulence intensity, vorticity, strain rate), this technique can well be used for validation of CFD (Computational Fluid Dynamics) calculations, both stationary and unsteady. However, a very fine spatial resolution is required in order to keep up with the detailed results of the measurements. As the investigated volume is large compared to the scale of the vortical structures of interest, the number of grid elements can quickly exceed several million cells, which poses high requirements on the computer hardware. Both experiments were investigated numerically using CFD to solve the RANS equations [5]. A block structured, multi domain grid was developed with about 2×10^6 control volumes. To close the set of Reynolds Averaged Navier Stokes Equations the SST approach was used and additionally a curvature correction method was applied. The curvature correction adjusts the turbulent production depending on the curvature of the streamlines. Unfortunately, the open water test simulation failed to render the details of the helicoidal tip vortex structure further downstream than about $0.05D$. At $x/D = 0.2$ hardly any traces of the tip vortices are to be found in the velocity distribution. One reason could be the combination of turbulence model and grid spacing, as turbulence models in general dissipate turbulent kinetic energy. Following Rung [6], the SST model constant

$C_{\varepsilon 1} = 1 + 0.44 \cdot \max(1,\ 0.3S)$, $S = \left(\frac{k}{\varepsilon}\right)\sqrt{2S_{ij}S_{ij}}$ being the shear rate tensor, can result in a negative production term for the turbulent viscosity for $C_{\varepsilon 1} > 2$:

$$P_{vt} \sim v_t\left(\frac{k}{\varepsilon}\right)S_{ii}^2\left[\left(\frac{\varepsilon}{P}\right)\left(C_{\varepsilon 2} - 2\right) + \left(2 - C_{\varepsilon 1}\right)\right].$$

This can rapidly lead to a total decay of turbulence in areas of high shear rates.

The simulation of the cavitation tunnel experiment was more promising. Figure 11 shows an example of the calculated flow field for the 4. quadrant (negative inflow from right, positive rotation, turbine state) in the cavitation tunnel experiment.

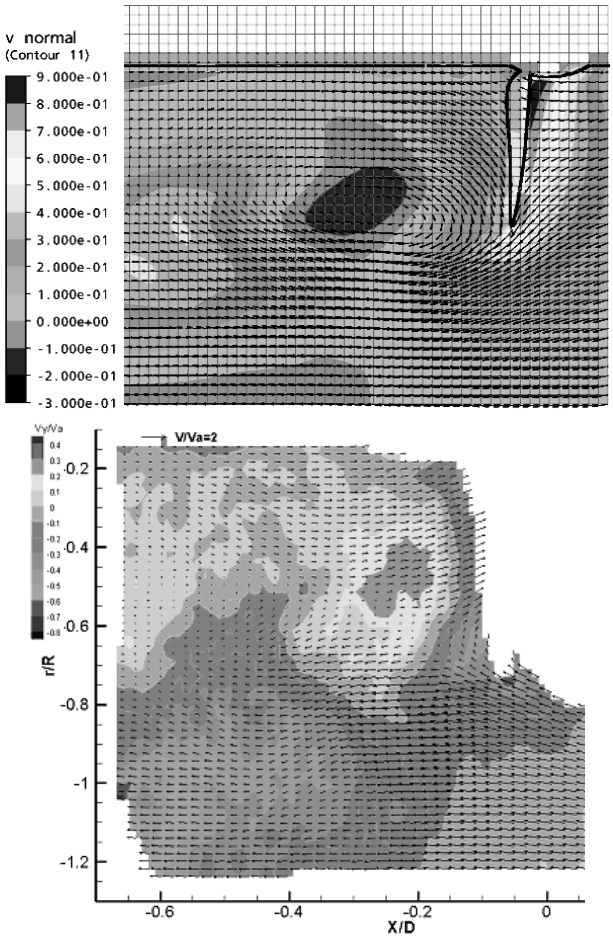

Fig. 11. Velocity field around a propeller in a turbine state, 4. quadrant (negative inflow, positive rotation) in the cavitation tunnel. *Top*: CFD calculation. *Bottom*: PIV measurements. Mind the different scales

The separating vortices are quite similar, though the simulation places them further downstream. The expansion of the slipstream is slightly stronger in the measurement than in the calculation.

6. Conclusions and outlook

A newly installed submersible stereoscopic Particle Image Velocimetry system at Potsdam Model Basin was introduced. The system can provide detailed insight into flow phenomena which are of vital interest for successful ship and propulsion design and optimization. Selected results were presented for both the experiments in the towing tank and in the cavitation tunnel. While the measurements revealed vertical structures in great detail in the propeller wake, the CFD calculations did only partly reproduce these structures in the flow. Further investigations have to be done to be able to simulate the flow closer to the conditions measured in the experiment.

In the near future the system will be utilized to measure the wake field behind a model ship with full appendages in various propulsion, inflow and rudder conditions. The measurements will be done in many planes behind the propeller on both sides of the rudder and will hopefully show the flow separation at the inclined rudder. In another experiment the wake behind a wing will be measured in the stationary frame of reference. This requires an extensive conversion of the system, because a very large field of view is requested in a greater operating depth.

Acknowledgement

This research project was funded by the German Ministry of Education and Research, BMBF.

References

[1] Mach, K.-P.: *Experimentelle Geschwindigkeitsuntersuchungen mittels PIV und LDA in 4 Quadranten für den Modellpropeller VP1455*, Bericht Nr. 3326, Schiffbau-Versuchsanstalt Potsdam, April, 2007.

[2] Courtesy TSI, from personal communication.

[3] Lee S.J., Paik B.G., Yoon J.H., Lee C.M.: *Three-component velocity field measurements of propeller wake using a stereoscopic PIV technique*, in: Experiments in Fluids, Vol. 36, 2004, pp. 575–585.

[4] van Doorne C.W.H., Westerweel J., Nieuwstadt F.T.M.: *Measurement uncertainty of stereoscopic-PIV for flow with large out-of-plane motion*, in: Particle Image Velocimetry: Recent Inprovements, Proceedings of EUROPIV 2, 2003, Springer, Berlin, 2004.

[5] Rieck, K.: *Berechnung der viskosen Umströmung eines Propellers in 4 Quadranten*, P1423/VP1455, Bericht Nr. 3313, Schiffbau-Versuchsanstalt Potsdam, Januar 2007.

[6] Rung, Th.: *Statistische Turbulenzmodellierung*, Lecture Notes, http://www.cfd3.cfd.tu-berlin.de/Lehre/TURB/script/script_vollstaendig.pdf, 2003.

Zastosowanie stereowizyjnego systemu PIV do badania pola przepływu w basenie holowniczym i w tunelu kawitacyjnym

Opisany został niedawno uruchomiony podwodny system stereowizyjny PIV (Particle Image Velocimetry), przeznaczony do pomiarów w basenie holowniczym i pracujący prostopadle do głównego kierunku przepływu. System pozwala na bezkontaktowy pomiar trójwymiarowego pola prędkości w basenie holowniczym i w tunelu kawitacyjnym. Przepływ może być analizowany z rozdzielczością kilku tysięcy punktów jednocześnie, z częstotliwością do 15 klatek na sekundę, co daje dobry wgląd w pole prędkości bez zakłócania przepływu. Referat opisuje dwa przypadki zastosowania (pędnik odosobniony w basenie holowniczym i w tunelu kawitacyjnym), oraz zalety i wady nowego systemu. Krótko omówione zostały możliwości weryfikacji obliczeń CFD. Przedstawiono plany zastosowania systemu w przyszłości.

ARCHIVES OF CIVIL AND MECHANICAL ENGINEERING

Vol. VII 2007 No. 3

Full Scale Identification Method of Four-Quadrant Hull Hydrodynamic Coefficients in Ship Manoeuvring

J. ARTYSZUK
Szczecin Martime University, Wały Chrobrego 1-2, 70-500 Szczecin, Poland, artyszuk@am.szczecin.pl

A new identification method of four-quadrant hull manoeuvring hydrodynamics (temporarily called a "2×LT method"), as essentially based on recording the manoeuvring motions excited by two fixed-point lateral forces, is presented in detail, including the concept formulation and simulated results (proving the method's potential). There is, namely, a significant lack of published data in this context, which are necessary e.g. to run the low-speed harbour manoeuvring and berthing simulation. This rather simple and cheap solution can be easily used for full scale ships, that are intended to be the primary field of application, where two fore and aft pushing tugs are required. Also free-running models, after installing two mobile lateral thrusters, are a successful option, though being subject to some scale effects.

Keywords: *ship manoeuvring, mathematical model, identification, four-quadrant hull hydrodynamics*

1. Introduction

One of the latest scientific efforts within ship manoeuvring problems is connected with a validation range (application limits) of ship manoeuvring mathematical models – see e.g. [1], [5]. This range, in terms of allowable drift angles and nondimensional yaw velocities, and their mutual combinations, is of course dependent on the background input data for the model parameters identification or estimation. Those data can be either of a kinematic nature (as related to ship motion behaviour in full or physical model scale), or of a dynamic type (as comprising various force measurements in towing tanks on a physical model or fluid mechanics computations).

However, for harbour low speed manoeuvring it is necessary to have a model with the so-called four-quadrant hydrodynamics in any of the following aspects – hull, propeller, or rudder. The four-quadrant hull hydrodynamics, that means nondimensional hull force and moment coefficients given as two-variable functions of arbitrary (both in magnitude and sign) drift angle and nondimensional yaw velocity, plays anyhow the most important part. Namely, it represents the only passive (resistive) forces in ship manoeuvring, all other excitations or environmental factors can be called active (or steering) forces. In this way the four-quadrant hull hydrodynamics essentially affects among others the modes of low-speed ship operation like: ship manoeuvring with tug(-s) assistance only, ship drifting behaviour in wind and waves, combined operation of stern (conventional or high lift) rudder and bow lateral thruster units.

The mentioned two-argument functions, comfortably stored in appropriate lookup tables, can be next visualised by a "surface". The ship in her arbitrary manoeuvre ex-

periences always a certain time history of the drift angle and nondimensional yaw velocity, and thus a certain sequence of the respective hydrodynamic coefficient. Such triples form a curve on the coefficient surface (with time as the parameter), which is specific to a particular manoeuvre. A set of manoeuvres can "draw" a region (patch) on such a surface. The wider is such a region, the more widespread of the model validation range is, or its identification (by analogy) as based on the kinematic motion analysis. A multiple regression concept to identify the lookup tables of the hydrodynamic coefficients was presented in [2]. It shall be mentioned that typical stern rudder manoeuvres, even accompanied by high propeller loading (temporary increase of the main engine rpm or propeller pitch as to give the effect of the so-called "kick ahead"), do not provide a huge contribution to the domain region of hull hydrodynamic coefficients, thus limiting the more extensive usage of the mathematical model. The efficiency of accelerated turns and zigzag tests at various rudder angles was demonstrated in [3].

In the present work, from the perspective of four-quadrant hull hydrodynamics identification, the effort is focused on the efficiency of a rather simple procedure, as relying on the application of two different lateral forces (of known but varying magnitude and sign) at fixed longitudinal locations, which can be produced in the real-life by tugs and/or lateral thruster units (the full scale potential), or by lateral thrust generators as installed on free running physical models. The latter are often used to emulate the tugs or lateral thruster units in manned scaled physical models for shiphandling training. The name "2×LT method" is proposed for the procedure. The basic purpose of generating two different lateral forces is to create an arbitrary value of steering yaw moment while keeping the same lateral steering force. This means that the "virtual" application point of the lateral force can be continuously moved along and even out off the ship, hence extending the lever arm of lateral force over the ship's physical dimensions. Dual lateral forces also overcome the usual restrictions on a full-scale ship that regard the discrete/fixed locations of fairleads (for pulling tugs) and bulkheads (for pushing tugs, suitable tug attachment points are generally marked on a ship's side).

Two cases of computed four-quadrant hull hydrodynamic coefficients are used for testing purposes, since there is a significant lack of published model test results (nondimensional force measurements) from towing tanks for arbitrary ship motions. The main and direct goal of this contribution is to verify whether or not it is possible to cover the whole range of the drift angle – nondimensional yaw velocity domain of the hull hydrodynamic coefficients while moving continuously the application point of a single constant lateral force along the ship's length. The aforementioned case of dual lateral forces will allow a practical implementation/execution of such a test.

2. Ship manoeuvring motions and hull hydrodynamics

In the case of a single external steering excitation (in terms of lateral force and its lever arm) the ship manoeuvring differential equations in body axes can look like:

$$\begin{cases} \dfrac{dv_x}{dt}\left(m+m_{11}\right)=+\left(m+c_m m_{22}\right)v_y\omega_z+F_{xH} \\ \dfrac{dv_y}{dt}\left(m+m_{22}\right)=-\left(m+m_{11}\right)v_x\omega_z+F_{yH}+F_{y0} \\ \dfrac{d\omega_z}{dt}\left(J_z+m_{66}\right)=-\left(m_{22}-m_{11}\right)v_x v_y+M_{zH}+x_{Fy0}F_{y0} \end{cases} \tag{1}$$

where:

v_x, v_y, ω_z – longitudinal, lateral, and yaw velocities,

m, J_z – ship's mass and moment of inertia,

m_{11}, m_{22}, m_{66} – added masses and inertia,

c_m – empirical constant,

F_{xH}, F_{yH}, M_{zH} – hull resistance, lateral force, and yaw moment,

F_{y0}, x_{Fy0} – external lateral force and its application point.

The underlined term in (1) means the Munk moment, so one shall be cautious to keep it separately, as shown, and hence to convert some hull yaw moment formulas or data, if such have the Munk moment already included. The latter approach is for some reasons more frequently observed in the worldwide literature.

The hull generalised forces can be expressed without any physical consequences in the standard (the first one) or modified (the other one) form:

$$\begin{bmatrix} F_{xH} \\ F_{yH} \\ M_{zH} \end{bmatrix} = 0.5\rho LTv_{xy}^2 \begin{bmatrix} c_{fxh}\left(\beta,\Omega_m\right) \\ c_{fyh}\left(\beta,\Omega_m\right) \\ Lc_{mzh}\left(\beta,\Omega_m\right) \end{bmatrix} = 0.5\rho LT\left(v_{xy}^2+\omega_z^2L^2\right) \begin{bmatrix} c_{fxhm}\left(\beta,\Omega_m\right) \\ c_{fyhm}\left(\beta,\Omega_m\right) \\ Lc_{mzhm}\left(\beta,\Omega_m\right) \end{bmatrix} \tag{2}$$

where:

ρ – water density,

L, T – ship's length and draft,

c_{fxh}, c_{fyh}, c_{mzh} – lookup table stored hull hydrodynamic standard coefficients,

c_{fxhm}, c_{fyhm}, c_{mzhm} – lookup table stored hull hydrodynamic modified coefficients,

v_{xy}, β, Ω_m – total linear velocity, drift angle, modified dimensionless yaw velocity according to:

$$v_{xy}=\sqrt{v_x^2+v_y^2}\,, \qquad \operatorname{arctg}\beta=\frac{-v_y}{v_x}\,, \qquad \beta\in\left(-180°,+180°\right\rangle \tag{3}$$

$$\Omega_m=\frac{\omega_z L}{\sqrt{v_{xy}^2+\omega_z^2L^2}}\,, \qquad \Omega_m\in\left\langle -1,+1\right\rangle \tag{4}$$

With regard to the standard form, instead of the modified dimensionless yaw velocity Ω_m, the traditional definition of dimensionless yaw velocity $\overline{\omega_z}$ (sometimes marked as r') is more often used in such expressions:

$$\overline{\omega_z} = \frac{\omega_z L}{v_{xy}}, \qquad \overline{\omega_z} \in \langle -\infty, +\infty \rangle \tag{5}$$

However, both dimensionless yaw velocities and both types of hull hydrodynamic coefficients are compatible and convertible by the following relationships:

$$\Omega_m = \frac{\overline{\omega_z}}{\sqrt{1+\overline{\omega_z}^2}}, \qquad \overline{\omega_z} = \frac{\Omega_m}{\sqrt{1-\Omega_m{}^2}} \tag{6}$$

$$\begin{bmatrix} c_{fxh}(\beta,\Omega_m) \\ c_{fyh}(\beta,\Omega_m) \\ c_{mzh}(\beta,\Omega_m) \end{bmatrix} \cdot \left(1-\Omega_m^2\right) = \begin{bmatrix} c_{fxhm}(\beta,\Omega_m) \\ c_{fyhm}(\beta,\Omega_m) \\ c_{mzhm}(\beta,\Omega_m) \end{bmatrix} \tag{7}$$

Introducing the below relationships:

$$k_{11} = \frac{m_{11}}{m}, \quad k_{22} = \frac{m_{22}}{m}, \quad \overline{r_{66}}^2 = \frac{m_{66}}{mL^2}, \quad \overline{r_z}^2 = \frac{J_z}{mL^2}, \quad \overline{F_{y0}} = \frac{F_{y0}}{\rho c_B LBT}, \quad x'_{Fy0} = \frac{x_{Fy0}}{L} \tag{8}$$

where c_B and B are the ship's block coefficient and breadth, one can obtain more convenient and readable form of differential equations (1):

$$\begin{cases} \dfrac{dv_x}{dt}(1+k_{11}) = +(1+c_m k_{22}) v_y \omega_z + \dfrac{1}{2Bc_B}\left(v_{xy}^2 + \omega_z^2 L^2\right) c_{fxhm}(\beta,\Omega_m) \\ \dfrac{dv_y}{dt}(1+k_{22}) = -(1+k_{11}) v_x \omega_z + \dfrac{1}{2Bc_B}\left(v_{xy}^2 + \omega_z^2 L^2\right) c_{fyhm}(\beta,\Omega_m) + \overline{F_{y0}} \\ \dfrac{d\omega_z}{dt}\left(\overline{r_z}^2 + \overline{r_{66}}^2\right) = \dfrac{-(k_{22}-k_{11}) v_x v_y}{L} + \dfrac{1}{2Bc_B L}\left(v_{xy}^2 + \omega_z^2 L^2\right) c_{mzhm}(\beta,\Omega_m) + x'_{Fy0} \cdot \overline{F_{y0}} \end{cases} \tag{9}$$

If the Munk moment is included (combined) with the hull yaw moment, it is purposeful to differently mark the latter, e.g. with an asterisk:

$$M_{zH}{}^* = -(m_{22} - m_{11}) v_x v_y + M_{zH} \tag{10}$$

$$c_{mzh}{}^* = \frac{M_{zH}{}^*}{0.5\rho L^2 T v_{xy}^2}, \qquad c_{mzhm}{}^* = \frac{M_{zH}{}^*}{0.5\rho L^2 T (v_{xy}^2 + \omega_z^2 L^2)} \tag{11}$$

Hence, for example

$$c_{mzhm}{}^{*} = c_{mzhm} + \left(k_{22} - k_{11}\right) c_B \frac{B}{L} \sin 2\beta \cdot \left(1 - \Omega_m^2\right) \tag{12}$$

Because the ship's hull is symmetric against the centre plane, it is enough during the identification or validation of the four-quadrant hull hydrodynamics to consider only positive drift angles β, i.e. $\beta \in \langle 0°, +180° \rangle$, but with both signs (full range) of the nondimensional yaw velocity Ω_m, i.e. between –1 and 1. For negative drift angles the following relationships can be here yielded:

$$\begin{bmatrix} c_{fxhm}\left(-|\beta|, \Omega_m\right) \\ c_{fyhm}\left(-|\beta|, \Omega_m\right) \\ c_{mzhm}\left(-|\beta|, \Omega_m\right) \end{bmatrix} = \begin{bmatrix} c_{fxhm}\left(+|\beta|, -\Omega_m\right) \\ -c_{fyhm}\left(+|\beta|, -\Omega_m\right) \\ -c_{mzhm}\left(+|\beta|, -\Omega_m\right) \end{bmatrix} \tag{13}$$

3. The computation setup

Two ships, A and B, for purpose of the present work have been selected. Respective data are summarised in Table. The ship A corresponds to a tanker of [6], while the ship B is a quite abstract full body ship. The hydrodynamic coefficients for ship A are presented in Figures 1 and 2 and follow directly the original theoretical formulas published in [6]. Having a look at both charts and comparing them with other published experimental data, it can be concluded that some future revision is needed, especially with regard to the hull yaw moment coefficient.

Table. Main particulars of exemplary ships

Parameter	Ship A	Ship B
k_{11}	0.074	0.03
k_{22}	0.781	1.00
$\overline{r_z}$	0.2288	0.2
$\overline{r_{66}}$	0.1985	0.2
c_m	0.83	0.3
L	290	250
B	47.5	30
c_B	0.805	0.8

Ship B in the below computations is subject, by contrast, to simple but more readable (thus suitable for a future improvement) rules for hydrodynamic coefficients (one should notice that fore and aft symmetry of the hull is thus implied):

$$\begin{cases} c_{fyhm} = \sin\beta \sin|\beta| \cdot \left(A + B|\omega_z|\right) \cdot \left(1 - \Omega_m^2\right) \\ c_{mzhm}{}^{*} = \left(C \sin 2\beta + D\omega_z|\omega_z|\right) \cdot \left(1 - \Omega_m^2\right) \end{cases} \tag{14}$$

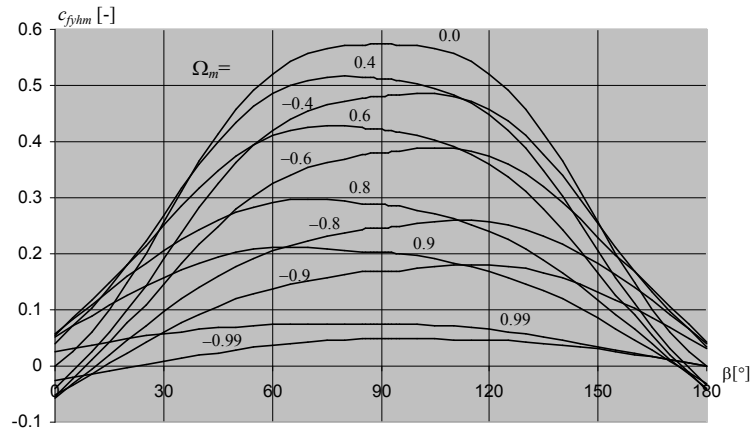

Fig. 1. Hull sway force coefficient by [6] formulas for ship A

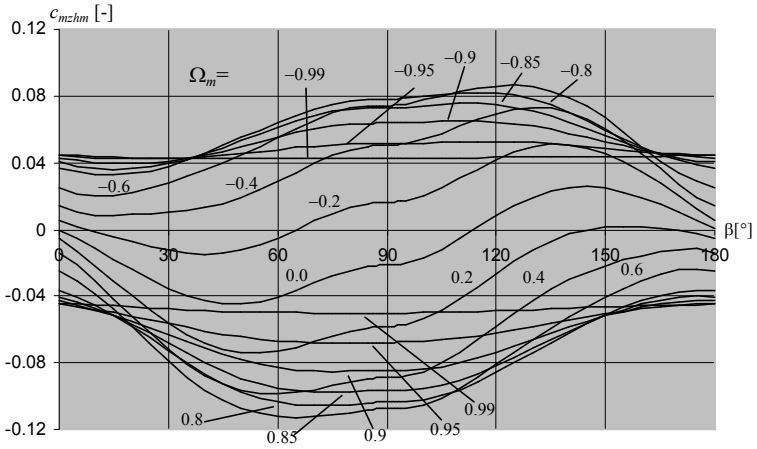

Fig. 2. Hull yaw moment coefficient by [6] formulas for ship A

Based on (14), as inspired to some extent by experimental data from [4], the charts shown in Figures 3 to 7 were adopted for ship B. They contain various forms of the coefficients presentation, since there is no solid standard in the literature.

For both ships it has been also assumed that

$$c_{fxhm} = -0.01\cos\beta \cdot \left(1 - \Omega_m^2\right) \tag{15}$$

The implication of (14) in relation to the hull yaw moment is that, while adjusting accordingly the C parameter, the chart of c_{mzhm} in Figure 7 could only consist of hori-

zontal straight lines specific to particular modified nondimensional yaw velocity Ω_m. Additionally, when *D* parameter is much lowered against the *C* parameter, the "oscillations" of c_{mzhm}* with the drift angle for comparatively low Ω_m will violate and go over the straight line corresponding to $\Omega_m = 1$ (the spot turning).

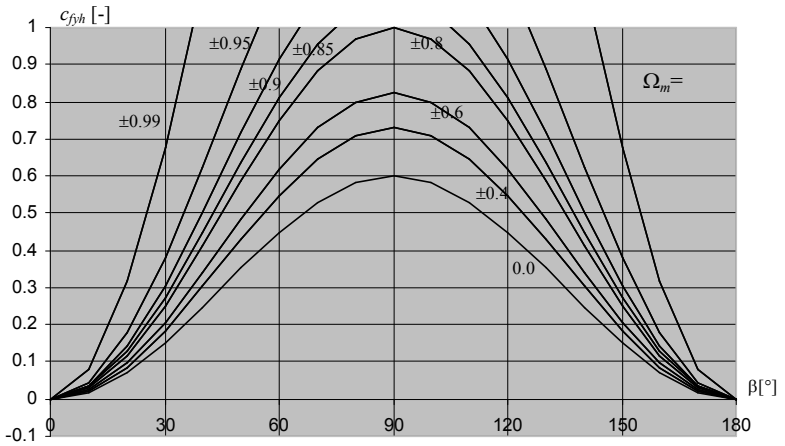

Fig. 3. Simplified hull sway force coefficient for ship B

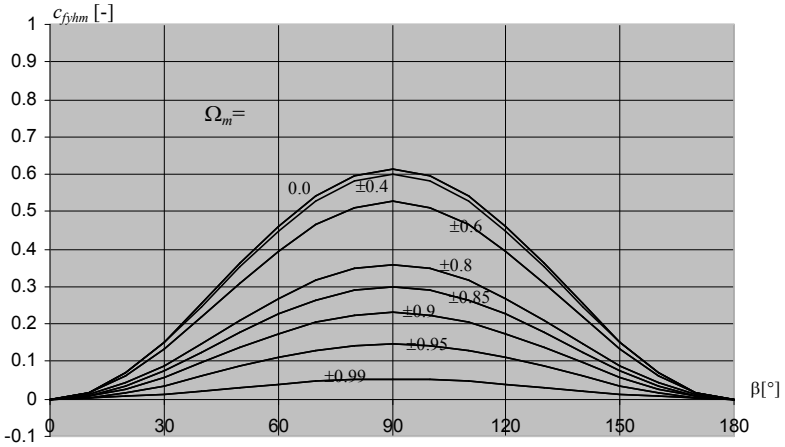

Fig. 4. Simplified hull sway force coefficient for ship B – modified style of nondimensioning

Both ship A and B have been next exposed to applying a constant lateral force to portside, $\overline{F_{y0}} = -0.01$, at forward locations x'_{Fy0} discretised every 0.05 up to 1.0. The computation time limit has been set to 1200 seconds.

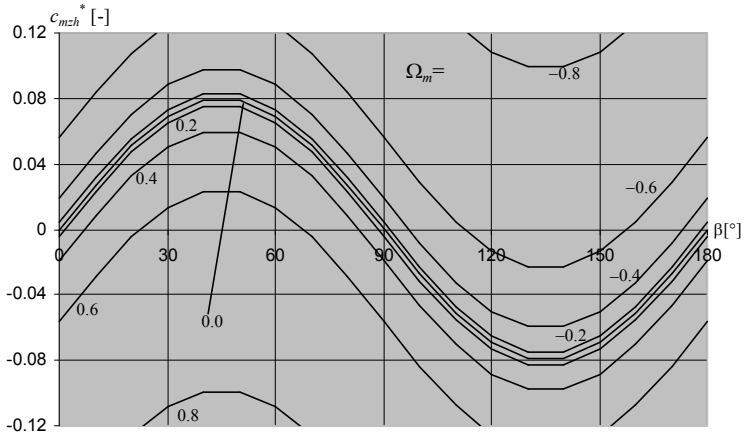

Fig. 5. Simplified hull yaw moment coefficient for ship B (the Munk moment included)

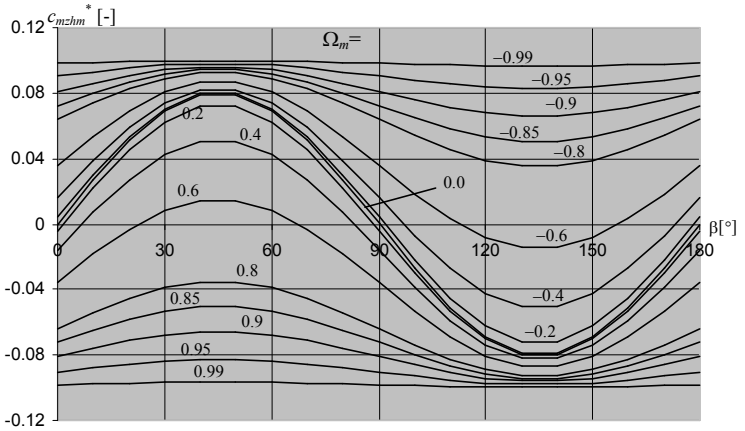

Fig. 6. Simplified hull yaw moment coefficient for ship B
(the Munk moment included) – modified nondimensioning

In practice, such a dense discretisation of x'_{Fy0} may be only achieved using the mentioned dual lateral forces (negative or positive ones), F_{yo1} and F_{y02}, spaced at fixed relative longitudinal locations x'_{Fy01} and x'_{Fy02}, but technically limited now to the range $\langle -0.5,+0.5 \rangle$. The following expressions, which are the basis of the "2xLT" method, give the mutual relationship of both lateral forces:

$$F_{y0} = F_{y01} + F_{y02}\,, \tag{16}$$

$$F_{y0} \cdot x'_{Fy0} = F_{y01} \cdot x'_{Fy01} + F_{y02} \cdot x'_{Fy02}\,. \tag{17}$$

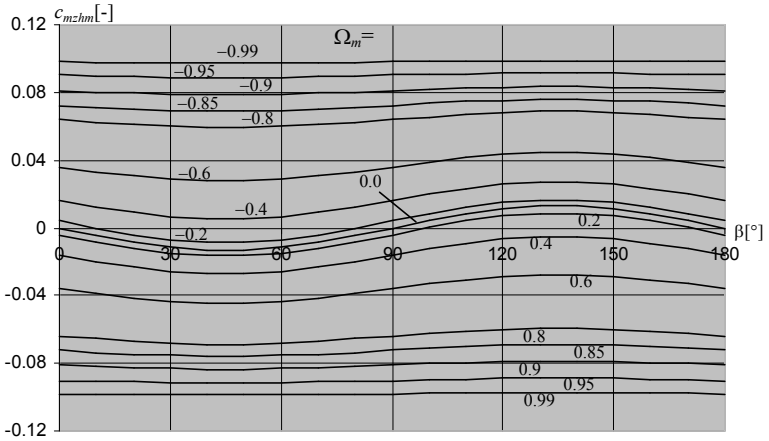

Fig. 7. Simplified hull yaw moment coefficient for ship B
(the Munk moment excluded) – modified nondimensioning

Therefore:

$$\frac{F_{y01}}{F_{y02}} = \frac{\dfrac{x'_{Fy02}}{x'_{Fy0}} - 1}{1 - \dfrac{x'_{Fy01}}{x'_{Fy0}}} \quad \text{and} \quad F_{y01} + F_{y02} = F_{y0}\,. \tag{18}$$

4. The numerical results

Figure 8 (ship A) and Figure 9 (ship B), show the drift angle – nondimensional yaw velocity pattern yielded when ships are set initially to the rest. Only drift angles up to +90° can be realised (as accompanied by negative nondimensional yaw velocities), since the ships start to increase the forward velocity due to the centrifugal term in the surge motion Equation of (1) or (9). The similar situation happens when making a turn with the bow lateral thruster. The most interesting and promising from both figures seems to be almost the whole area up to this 90° drift angle limit that is uniformly covered. However, this is still one quarter of the area in our concern. The second unique quarter could be reached when the application point of the negative (directed towards the portside) lateral force would move astern of the midship section – the domain region defined by $\beta \in (+90°,+180°)$ and $\Omega_m \in (0,+1)$ is here yielded.

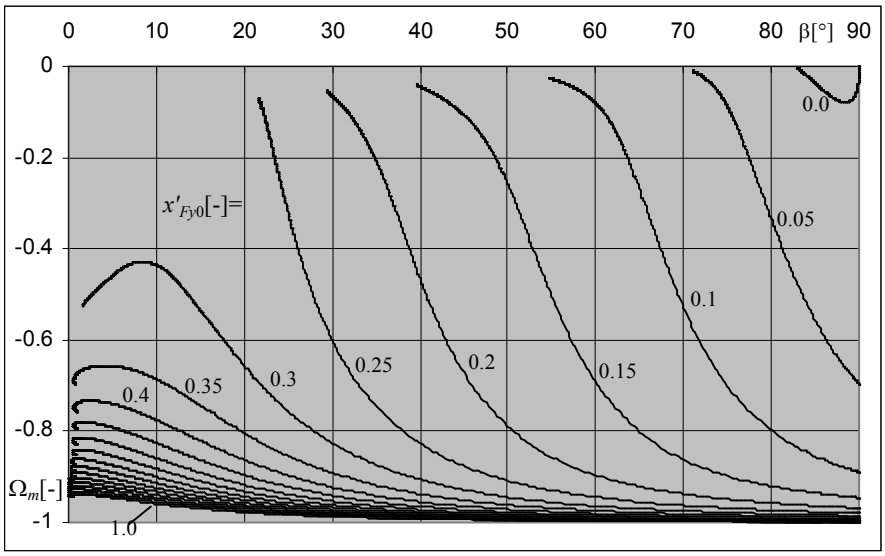

Fig. 8. Relation between Ω_m and β, for ship A (no initial motions)

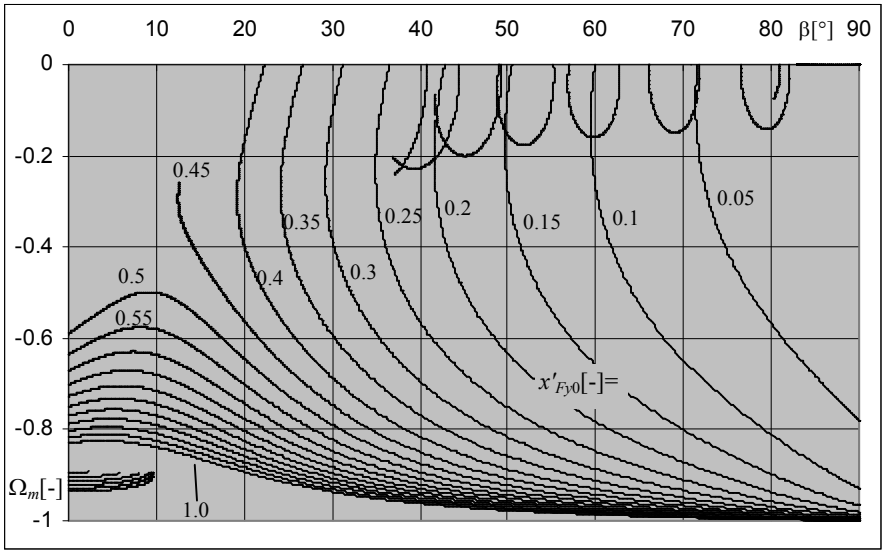

Fig. 9. Relation between Ω_m and β, for ship B (no initial motions)

In view of the above it is recommended to set initially the ship at negative forward speed while the application point is positive, or at positive speed when the lateral force

is exerted aft. In the first case, when the initial velocity is 0.5m/s astern, the chart presented in Figure 10 is received.

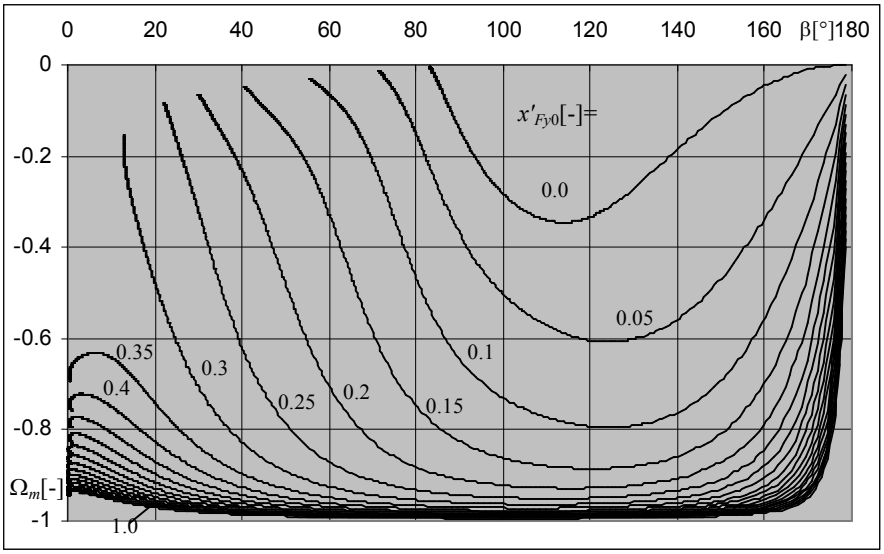

Fig. 10. Relation between Ω_m and β, for ship A (initial astern velocity of order 0.5m/s)

The effect of applying a longitudinal force (e.g. an additional tug) in this context, i.e. for extending the (β, Ω_m) region as a similar action to imposing the nonzero initial velocity, is put aside for the future research. It shall be also mentioned that, unless the initial forward velocity is zero, the magnitude of the lateral force has some influence on the relation between Ω_m and β – this does not take place when the ship initially starts from the rest.

5. Final remarks

It has been proved through the performed simulation research that the four-quadrant hydrodynamics is essential e.g. for tug operation simulation. For the same reasons, the four-quadrant hull hydrodynamic can be identified (estimated), even in the full scale, when two tugs are available.

This identification is carried out in three steps: 1 – recording the ship manoeuvring motions for the continuously varying application point of the lateral force, however a separate run of the manoeuvre is necessary for each discrete (by nature) application point, 2 – determining the time history of particular hull hydrodynamic coefficients for each run from the analysis of ship motions (a simple transformation of differential equations and some knowledge/guess on added masses are required), 3 – approximating the obtained 3D curves of hydrodynamic coefficients (as defined versus the drift

angle β and nondimensional yaw velocity Ω_m, the time is the parameter for each point on such curves) with a surface as explicit function of the both arguments. Various numerical algorithms can be used for the latter task.

It is believed that the tug inertia is negligible, since in fact, one should consider the whole system ship-tug(-s) as a rigid body. This can be verified in next studies.

Using the investigated procedure, one can also verify the mathematical models in shiphandling simulators, which are often in a closed and encoded format. The author's practical experience with these models indicates that some unjustified simplifications or even errors can be suspected, that are hardly to be discovered. The latter is mainly due to the fact that the model motion behaviour is only "exposed" to the user, while the very useful hydrodynamic coefficients are often confidential.

References

[1] Artyszuk J.: *Drift-Yaw Correlation in Ship Manoeuvring Model Identification and Validation*, Scientific Bulletin, no. 3, Vol. 75, Maritime University, Szczecin, 2004.

[2] Artyszuk J.: *An Identification Method of Hull Forces Based on Sea Manoeuvring Trials for Ship Control*, 11th IEEE International Conference on Methods and Models in Automation and Robotics MMAR'05, CD-ROM (ISBN: 83-60140-90-1), 29/VIII–1/IX, Miedzyzdroje, 2005a, pp. 177–182.

[3] Artyszuk J.: *Ship Manoeuvring Auxiliary Differential Equations for Optimal Sea Trials Programme Design*, Scientific Bulletin, no. 6, Vol. 78, Marine Traffic Engineering MTE'05, Maritime University, Szczecin, 2005b, pp. 11–20.

[4] Kose K., Misiag W.A., Hashizume Y., Nogami S., Ishioka Y.: *A Practical Approach to the Mathematical Model of Ship Maneuvering in Harbours*, Manoeuvrability '95, Vol. 2, International Symposium on Manoeuvrability of Ships at Slow Speed, October 16–19, Ilawa, Poland, 1995.

[5] Lebedeva M.P. et al.: *Development of Criteria for Certification of the Mathematical Models Used by Marine Simulators*, International Conference on Marine Simulation and Ship Manoeuvrability – MARSIM 2006, Jun 25–30, Paper no. M-25, Terschelling (NL), 2006.

[6] Oltmann, P., Sharma, S.D.: *Simulation of Combined Engine and Rudder Maneuvers Using an Improved Model of Hull-Propeller-Rudder Interactions*, 15th Symposium on Naval Hydrodynamics, September 2–7, Hamburg, 1984.

Identyfikacja w skali rzeczywistej pełnych (4-ćwiartkowych) charakterystyk hydrodynamicznych kadłuba statku w manewrowaniu

Praca przedstawia potencjał zastosowania dwóch źródeł siły poprzecznej (np. holowników) do wyznaczania bezwymiarowych współczynników hydrodynamicznych sił i momentu kadłuba statku w pełnym zakresie kąta dryfu i względnej prędkości kątowej. Pozwala to na symulację dowolnych manewrów jednostki pływającej, szczególnie przy małej prędkości linio-

wej i na akwenach portowych. Dwa źródła siły poprzecznej, przy zachowaniu jednakże ich wypadkowej wartości, dają możliwość realizacji dowolnego momentu sterującego, tym samym punktu przyłożenia (ramienia) siły poprzecznej. W efekcie, jak przedstawiono w referacie, można osiągnąć dowolne kombinacje kąta dryfu i względnej prędkości kątowej, tym samym objąć całą dziedzinę funkcji reprezentowanych przez poszczególne współczynniki hydrodynamiczne. Określenie wspomnianych charakterystyk hydrodynamicznych odbywa się poprzez rejestrację parametrów ruchu statku przy systematycznie zmienianym ramieniu wypadkowej siły poprzecznej i obliczenie z równań ruchu hydrodynamicznych współczynników kadłuba jako funkcji czasu. Ostatnim etapem jest aproksymacja otrzymanych trójwymiarowych krzywych (składających się z punktów definiowanych kątem dryfu, względną prędkością kątową oraz danym współczynnikiem hydrodynamicznym – czas jest parametrem takiej krzywej) za pomocą powierzchni reprezentującej współczynnik hydrodynamiczny i będącej jawną funkcją kąta dryfu oraz względnej prędkości kątowej.

ARCHIVES OF CIVIL AND MECHANICAL ENGINEERING

Vol. VII 2007 No. 3

An analytical and experimental study on dynamic stability of a vessel

M. ASGHARI, H. ZERAATGAR
Department of Marine technology, Amirkabir University of Technology, 424 Hafez Ave., Tehran, Iran

F. BAKHTIARI-NEJAD
Department of Mechanical Eng., Amirkabir University of Technology, 424 Hafez Ave., Tehran, Iran

Many researchers have studied the roll stability of ships since it is the most critical case of capsizing for conventional vessels. In this study external exerted forces from waves or winds on a vessel are modeled as a step exciting moment. Calculation of dynamic angle of stability Φ_{dy}, which is the first overshoot angle of vessel response to exciting moment, is the main objective of this paper. For this purpose two methods are used. The first one, so-called traditional method, determines Φ_{dy} by equalizing the external heeling moment energy and righting moment energy; while the other solves the rolling equation assuming step exciting moment and linear damping.

Additionally, a model experiment is carried out with a step exciting moment then model rolling responses are registered. The results of both theoretical methods are compared with experimental results. The comparison shows that for large rolling amplitude such as 35 degrees, inclusion of linear damping does not have any considerable effect dynamic angle of stability. It means that the traditional method is reliable.

Keywords: *Forced rolling, dynamic angle of stability, exciting moment, damping*

Notations

A_{XX}: [Kgm^2] – Roll added moment of inertia
B_{44}: [Kgm^{2}Sec^{-1}] – Linear damping coefficient
D: [m] – Dynamic lever of stability
g: [mSec^{-2}] – Gravitational acceleration
$f(t)$: [Nm] – Exciting moment
$\overline{GM}$: [m] – Metacentric height
$\overline{GZ}$: [m] – Righting arm
I_{XX}: [Kgm^2] – Ship longitudinal mass moment of inertia
M_0: [Nm] – Step exciting moment
M_{44v}: [Nm] – Nonlinear damping moment
t: [Sec] – Time
W: [Nm] – Potential energy of vessel
W': [Nm] – External work of exciting moment
ω_d: [Sec^{-1}] – Roll damped frequency
ω_n: [Sec^{-1}] – Roll natural frequency
ς: – Linear damping ratio
ε – Relative error
Φ: [Rad] – Roll angle

$\dot{\Phi}$: [RadSec^{-1}] – Roll velocity
$\ddot{\Phi}$: [RadSec^{-2}] – Roll acceleration
Φ_{dy} : [Rad] – Dynamic angle of stability
Φ_{st} : [Rad] – Static angle of stability
Δ : [Kg] – Ship displacement
Hint: Parameters whose units are not mentioned are dimensionless.

1. Introduction

Large rolling and losing transverse stability is a known reason of ship capsizing. Severe casualties have been still reported due to severe rolling. Hence, studying of the phenomenon of ship rolling has become an interesting subject for researchers.

One of these cases may be considered as excitation of a vessel by external forces of sea waves or winds. Such an exciting force is modeled as step moment in this study. Questioned force leads to an overshoot heeling angle, which is called dynamic angle of stability, as the most important and hazardous part of transient response of a ship. To evaluate Φ_{dy} two methods have been introduced in this study.

Although most of these studies focus on frequency-domain, time-domain solutions of both linear and non-linear rolling equation have its own enthusiasts. Odabasi and Vince (1982) studied the effects of initial angle variations and roll damping on the roll response of a ship under the sudden action of a wind [1]. Various models of roll motion including nonlinear damping terms have been studied by Bass and Haddara (1988). These models have been curve fitted on experimental results and their validity was compared with each other [2]. In 1998 Taylan determined steady response of a vessel to sinusoidal wave for four types of ships assuming nonlinear damping and restoring. He also studied the effect of different forms of nonlinear damping and restoring moment in resonant condition [3].

2. Formulation and mathematical model

In this section two methods for assessing of dynamic angle of stability are presented. The first one is the traditional method which is also used in some rule books. The main feature of traditional method is disregarding of damping during of rolling that leads to over estimation of Φ_{dy}. On the contrary, the second method solves the rolling equation where the damping is included by assumption of a linear damping.

2.1. Energy method

Righting moment opposes the roll motion of a vessel. This leads to absorbing and storing of potential energy whose amount is a function of heeling angle. When the ship is inclined from zero up to a given heeling angle "Φ", the amount of potential energy can be calculated as follows:

$$W = \Delta\, g \int_0^{\Phi} \overline{GZ}(\Phi)\, d\Phi\,, \tag{1}$$

where:

– W represents the potential energy,
– Δ is the displacement of ship,
– g is gravitational acceleration,
– $\overline{GZ}$ denotes righting arm and Φ is heeling angle.

The integral in Equation (1) is called dynamic lever of stability "*D*" [4]. Figure 1 shows typical static and dynamic lever of stability of a barge.

$$D(\Phi) = \int_0^{\Phi} \overline{GZ}(\Phi)\, d\Phi\,. \tag{2}$$

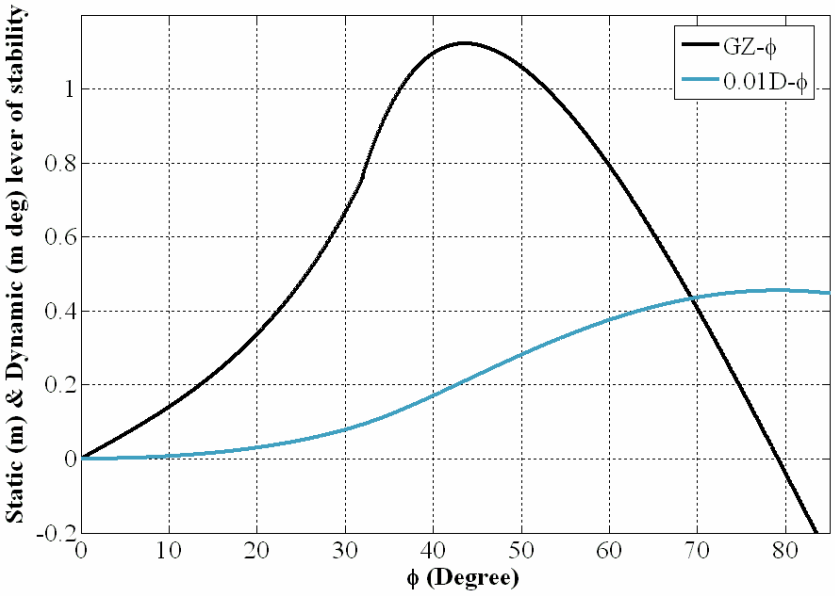

Fig. 1. Typical static and dynamic lever of stability

On the other hand, inclining of a vessel needs external work from exciting moment. This work leads to both kinetic and potential energy on vessel. By supposing a constant exciting moment one can calculate the external work as follows:

$$W' = \int_0^{\Phi} M_0\, d\Phi = M_0\, \Phi\,, \tag{3}$$

where:

– W' represents work due to exciting moment,

– M_0 stands for the step exciting moment.

Work due to exciting force partly changes to potential and kinetic energy and partly is consumed by damping moments, which is neglected in this method. When the roll angle reaches Φ_{dy}, the kinetic energy of the vessel instantly gets zero. Moreover, the work due to damping moment is disregarded. Therefore, exciting energy is assumed to be totally stored as potential energy in this method. On this basis, dynamic angle of stability may be evaluated by equaling Equation (1) and (3):

$$D(\Phi) = \frac{M_0\,\Phi_{dy}}{\Delta\, g}\,. \tag{4}$$

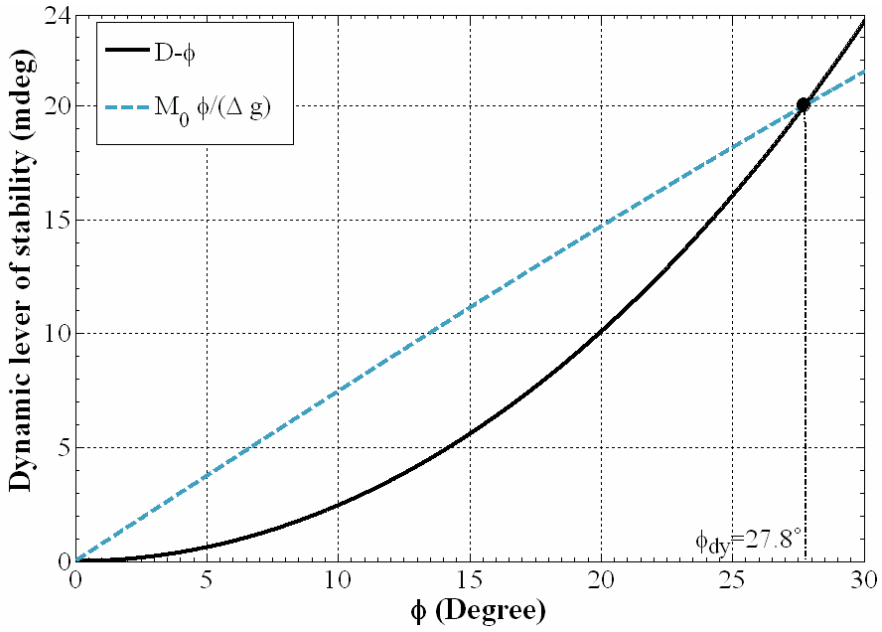

Fig. 2. Use of energy method in determination of Φ_{dy}

Equation (4) is used traditionally for calculation of Φ_{dy}. By drawing either sides of Equation (4) in the same diagram and finding their intersection as in Figure 4, dynamic angle of stability easily is determined.

2.2. Analytical solution of rolling motion

The typical differential equation of roll motion can be expressed as:

$$\left(I_{xx}+A_{xx}\right)\ddot{\Phi}+B_{44}\,\dot{\Phi}+M_{44v}\left(\Phi,\dot{\Phi}\right)+\Delta\, g\,\overline{GZ}\left(\Phi\right)=f\left(t\right), \tag{5}$$

where:

– I_{xx} is ship longitudinal mass moment of inertia,

– A_{xx} is roll added moment,

– $I_{xx} + A_{xx}$ is equivalent moment of inertia. Dots represent differentiation with respect to time.

– B_{44} is the linear damping coefficient,

– M_{44v} is nonlinear damping moment,

– $\overline{GZ}$ denotes righting arm,

– $f(t)$ is external exciting moment which is modeled as step function M_0 in this article.

Linear damping is the dominant damping for roll motion. In this study the nonlinear damping is disregarded. On the other hand righting arm shows a linear behavior up to a certain heeling angle $\Phi_{critical}$:

$$\overline{GZ}=\Delta\, g\,\overline{GM}\,\Phi \quad \left(\Phi\le\Phi_{critical}\right) \tag{6}$$

where $\overline{GM}$ is transverse metacentric height.

In the case of large roll angle a polynomial of order three or five is used to model the further part [3]. In this study the experiment is done by a model where the linear behavior of restoring moment is pretty large. Taking into account all above discussions, the Equation (5) takes the following form:

$$\left(I_{xx}+A_{xx}+m\,r^2\right)\ddot{\Phi}+B_{44}\,\dot{\Phi}+\Delta\, g\,\overline{GM}\,\Phi=M_0\,, \tag{7}$$

$\Phi(0)=0,\qquad \dot{\Phi}(0)=0$: as initial condition

where:

– m is the mass of suspended weight to exert sudden exciting moment,

– r is the radius of the apparatus where the mass m is suspended from.

In fact, the term mr^2 in Equation (7) refers to effect of an apparatus which generates the exciting moment and it is small in comparison to equivalent moment of inertia. Strictly speaking, in ideal condition this term does not exist. Solution of Equation (7) yields:

$$\begin{aligned}\Phi(t)&=[\overline{\Phi}_1\,Sin\omega_d t+\overline{\Phi}_2\,Cos\omega_d t]\,e^{-\zeta\omega_n t}\\&+\left(I_{xx}+A_{xx}\right)^{-1}\omega_d^{-1}\int_0^t M_0\,Sin\omega_d\left(t-\lambda\right)e^{-\zeta\omega_n\left(t-\lambda\right)}\,d\lambda\end{aligned}\,, \tag{8}$$

where:

– $\overline{\Phi}_1$ and $\overline{\Phi}_2$ are constant values,

– ζ denotes damping ratio, which increases as the damping increases,

– ω_d and ω_n are damped and natural frequencies respectively which are defined as follows:

$$\zeta = B_{44} \Big/ 2\sqrt{(I_{xx} + A_{xx})\,\Delta\, g\, \overline{GM}}\,, \tag{9}$$

$$\omega_n^2 = \Delta\, g\, \overline{GM} \Big/ \left(m\, r^2 + I_{xx} + A_{xx}\right), \tag{10}$$

$$\omega_d = \omega_n\, \sqrt{1-\zeta^2}\,. \tag{11}$$

In Equation (8) the first term on right hand side of equation is the homogeneous solution of Equation (7) while the convolution integral is the particular solution. Substitution of initial condition in Equation (8) yields constant values to be zero. Thus, the explicit solution for Equation (7) takes the following form:

$$\Phi(t) = \frac{M_0}{\Delta\, g\, \overline{GM}} \left[1 - \left(1-\zeta^2\right)^{0.5} \sin\left(\omega_d t + \tan^{-1}\left(\sqrt{1-\zeta^2}\,\Big/\zeta\right)\right) e^{-\zeta\omega_n t}\right]. \tag{12}$$

Experiments show that the linear damping ratio of ships range from 0.02 to 0.2 [5]. Therefore, the term $\sqrt{1-\zeta^{\,2}}$ can be well approximated by unity. Using some simplification the final form of roll response becomes as follows:

$$\Phi(t) = \Phi_{st}[1 - e^{-\zeta\omega_n t}\, Sin(\omega_d t + \arctan\zeta^{-1})]\,, \tag{13}$$

where:

Φ_{st} – represents static angle of stability in which ship rests on steady state condition.

By the same token ω_n and ω_d practically are the same.

3. Tests

A bulk carrier model with following specifications was set up:

Table 1. Main specifications of bulk carrier model

Draft (m)	Breadth (m)	LBP (m)	Displacement (Kg)	Block Coefficient	$\overline{GM}$ (m)
0.0635	0.205	1.040	10.3	0.76	0.0080

An experiment is conducted stepwise as follows:

1 – The model stability characteristics $\overline{GZ} - \Phi$ curve (Figure 3) and $\overline{GM}$ were determined by means of inclining test. As one can see in Figure 3 righting arm is a linear function of roll angle up to $\Phi_{critical} \approx 20°$.

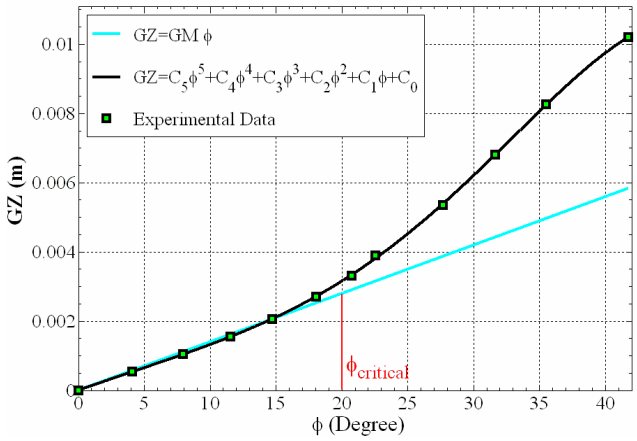

Fig. 3. Experimental righting arm of model

2 – A 5th order polynomial was fitted on $\overline{GZ} - \Phi$ curve (Figure 3) and by integration the dynamic lever of stability $D - \Phi$ was determined.

Table 2. Main results of tests

No.	Load (Nm)	Φ_{dy} (°)	Φ_{st} (°)	ω_d (Rad Sec^{-1})
1	1.03	12.53	7.55	2.78
2	2.54	26.81	16.54	3.24
3	3.57	32.98	21.08	3.63

3 – Three different step exciting moments were exerted on model, as shown in Table 2, and all roll peak amplitudes were recorded. For higher accuracy all tests were repeated several times. By using Chauvenet criterion the deviant data from mean values of data set were recognized and disregarded. Very small roll amplitudes are also neglected due to decline of period of oscillations which is a sign of interference of laboratories apparatus damping with natural damping of model.

4. Results and analysis

The right sides of Equation (4), for three different exciting moments, are drawn in dynamic lever curve (D – Φ). For evaluating the dynamic angles of stability, intersections of dynamic lever with corresponding lines are determined in Figure 4. In fact, Figure 4 shows the results of traditional method based on calculations.

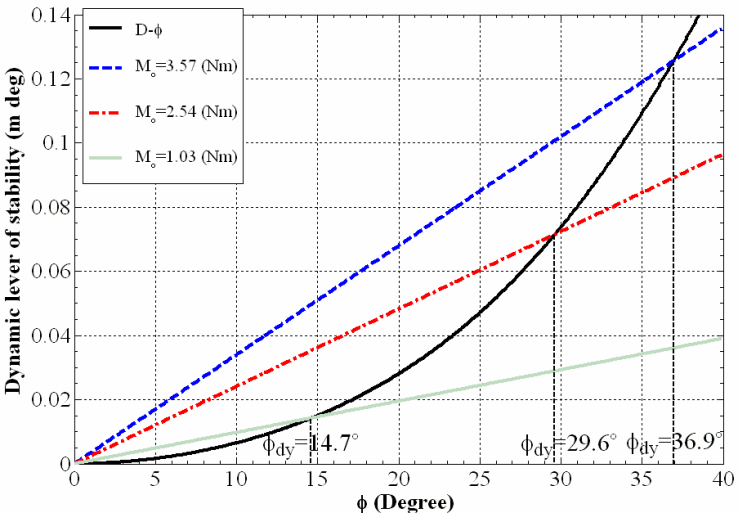

Fig. 4. Determination of Φ_{dy} by means of energy method

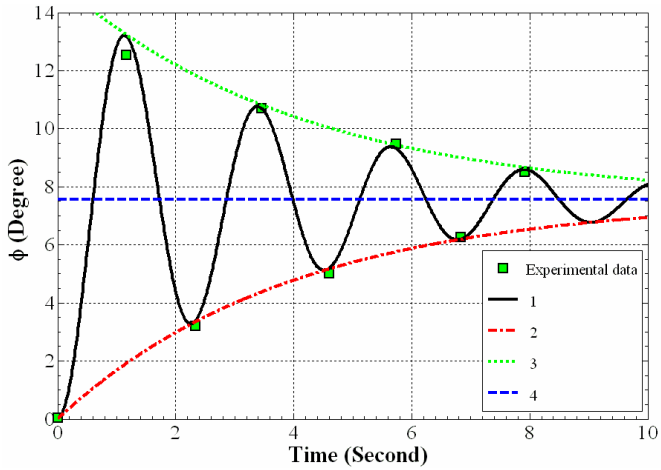

Fig. 5. Identification of linear damping ratio (Exciting moment = 1.03 (Nm)): Where in this figure solid line "1" is plotted by Equation 13, dashed line "2" is lower envelope (Equation 14), dashed line "3" is upper envelope (Equation 14) and dashed line "4" shows static angle of stability (Φ_{st} = 7.55°)

On the other hand it is assumed that Equation 13 governs entire experimental results. As one may see in this equation Φ_{st} and ω_n are both known (see Table 2), while the damping ratio is unknown. On this basis, the method of least square error is used to find the best curve which envelops the experimental data. By determination of this curve the damping ratio and Φ_{dy} would be calculated. Figures 5, 6 and 7 show the best curves, which can be fitted on experimental data with respect to Equation 13. The

value of ζ may be also assessed by fitting of upper and lower envelopes on data. By use of Equation 13 the equation of upper and lower envelopes can be written as follows:

$$\Phi(t) = \Phi_{st}\left(1 \pm e^{-\zeta\omega_n t}\right) \tag{14}$$

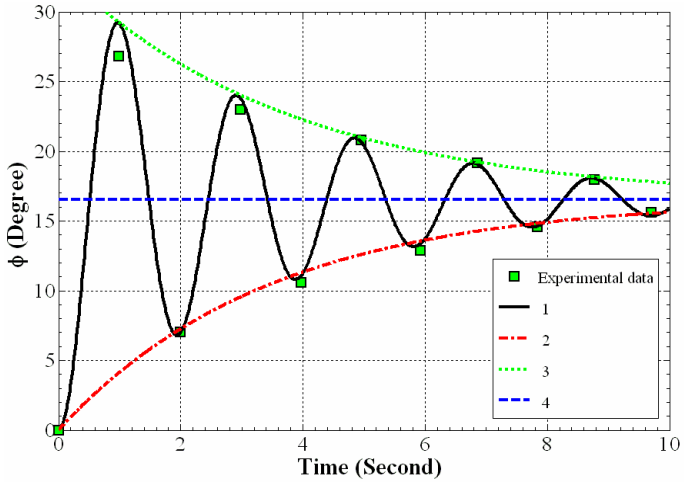

Fig. 6. Identification of linear damping ratio (Exciting moment = 2.54 (Nm)): Where in this figure solid line "1" is plotted by Equation 13, dashed line "2" is lower envelope (Equation 14), dashed line "3" is upper envelope (Equation 14) and dashed line "4" shows static angle of stability (Φ_{st} = 16.54°)

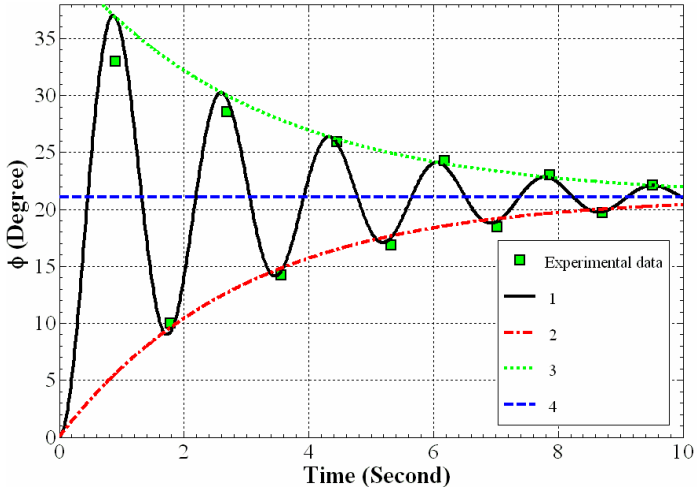

Fig. 7. Identification of linear damping ratio (Exciting moment = 3.57 (Nm)): Where in this figure solid line "1" is plotted by Equation 13, dashed line "2" is lower envelope (Equation 14), dashed line "3" is upper envelope (Equation 14) and dashed line "4" shows static angle of stability (Φ_{st} = 21.08°)

On Figures 5, 6 and 7 different curves are fitted to figure out a damping ratio ζ for the vessel. Except for Φ_{dy}, Equation 13 may be used for modeling of roll motion quite well. This may be confirmed according to minimum root mean square error for fitted curves and convergence of ζ in different identifications as in Table 3.

Table 3. Identified damping ratio in tests

Load (Nm)	ζ : (Eq. 13)	ζ : Upper envelope	ζ : Lower envelope	$\zeta_{average}$
1.03	0.090	0.090	0.087	0.089
2.54	0.084	0.089	0.082	0.085
3.57	0.088	0.094	0.088	0.090

where:

– $\zeta_{average}$ denotes average of ζ.

Knowing the fitted curve, the first over shoot angle of curve is regarded as dynamic angle of stability. Table 4 compares results of two theoretical methods with experiment:

Table 4. Comparison of results

Test	Φ_{dy} Experiment	Energy method		Analytic method	
		Φ_{dy}	$\varepsilon(\%)$	Φ_{dy}	$\varepsilon(\%)$
1	12.53º	14.66º	17.0	13.21º	5.4
2	26.81º	29.64º	10.6	29.20º	8.9
3	32.98º	36.92º	11.9	36.58º	10.9

where:

– ε represents relative error.

Although the analytical method has resulted in a lower Φ_{dy} than the energy method, it is still apart from the reality. As it can be seen in Table 4 this is much considerable in severe forced rolling. More over without considering the first over shoot angle, Equation 13 models the remained part of experimental results with excellent accuracy. Therefore, it can be concluded that damping power and quality from beginning of motion up to first peak "Φ_{dy}" is completely different from the rest of rolling process. Considering above mentioned, Equation 13 is used to identifying a curve, with a certain ζ, which begins from origin and exactly crosses practical Φ_{dy}. By applying this method, regardless of rest of data, a local damping ratio can be determined for first half period. Figure 8 shows the identification of local damping ratio in this range for third test.

Figure 8 implies that there is a dominate damping in first half period which is ignored in this study. Strictly speaking, because of high mean angular velocity at the beginning of motion, the term of nonlinear damping in Equation 5 must be taken into account in determination of Φ_{dy}. It seems that nonlinear damping acts strongly at the first half period of rolling and vanishes sharply on the other parts. An attempt has been made to find an average linear damping ratio that is shown in Table 5. It seems to author that using the average damping ratio could leads to better compliance with experimental results than the previous approach.

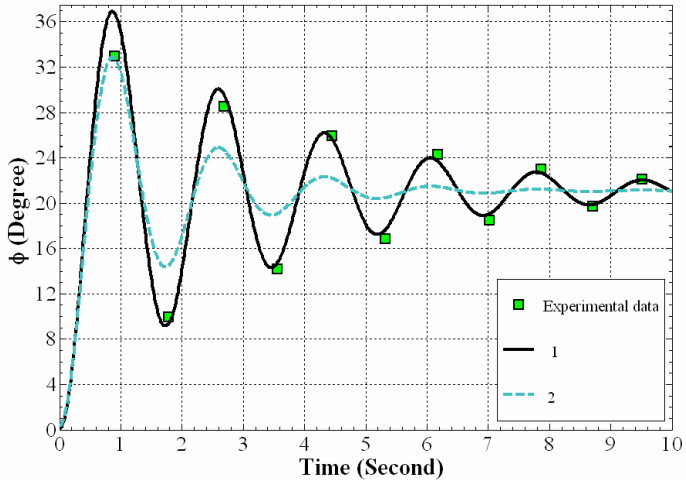

Fig. 8. Comparison of damping ratio in first half period and rest of results: Where in this figure Solid line "1" is plotted by Equation 13 ($\zeta = 0.090$) and dashed line "2" is plotted by Equation 13 ($\zeta = 0.18$)

Table 5. Local damping ratio in first half period

Test	$\zeta_{average}$	ζ_{0-1}
1	0.089	0.130
2	0.85	0.150
3	0.090	0.180

5. Conclusions

Dynamic angle of stability of a ship is an important parameter for analyzing ship stability. Traditionally, the method applied to calculate the dynamic angle of stability neglects the effect of damping forces. In this study, for a given ship model the traditional method as well as a method which takes into account the effect of damping by assumption of linear model are used to calculate the dynamic angle of stability for ship.

An experiment has been conducted to measure the dynamical angle of stability. Table 4 compares the result of with two other methods. Certainly, the inclusion of damping shows better results than traditional method but there is an error of about 5 up to 11 percents. The difference between experiment and theoretical methods increases as the amplitude of roll angle increases. The reason for such behaviour is that the modeling of damping by constant linear damping coefficient is not correct.

The following may be concluded from this study:

There is not much difference between the results of traditional method and analytical method. In the other words, in severe roll motion with roll amplitude of 30 degrees or more, inclusion of linear damping does not have any considerable effect on dynamical angle of stability.

Use of Equation 13 is recommended for modeling of forced rolling with low amplitudes less than 12 degrees.

Nonlinear damping plays a major role to damp the roll motion at the first half period of rolling. Hence, modification of Equation 13, for evaluating dynamic angle of stability, seems to be essential.

Despite of exclusion of damping in traditional method it have 10 up to 20 percents of safety margin for ships.

Acknowledgements

The authors would like to thank from Mr. Houman Etesamifar for his valuable comments in edition of this paper.

Reference

[1] Odabasi A.Y., Vince J.: *Roll response of a ship under the action of sudden excitation*, Int. Shipbuilding Prog. 29, 1982, pp. 327–333.
[2] Bass D.W., Haddara M.R.: *Nonlinear models of ship rolling damping*, Int. Ship building Prog. 35, 1988, No. 401, pp. 5–24.
[3] Taylan M.: *The effect of nonlinear damping and restoring in ship rolling*, Ocean Engineering 27, 2000, pp. 921–932.
[4] H Semyonov-Tyan-Shansky V.: *Statics and dynamics of ship*, Moscow, Peace publishers, Translated from Russian by Konyaeva M.
[5] Asghari M.: *A study on ship's free rolling in calm water by means of model test*, Bsc. thesis, Dept. Marine Eng., Amirkabir Univ. of technology, 2006.

Analityczne i eksperymentalne badanie dynamicznej stateczności statku

Wielu badaczy studiowało stateczność poprzeczną statku, ponieważ przechyły boczne są krytyczne dla wywracania konwencjonalnego statku. W badaniach zewnętrzne siły od falowania i wiatru działające na statek są modelowane jako skokowy moment wymuszający. Obliczanie dynamicznego kata przechyłu Φ_{dy} w odpowiedzi statku na działanie momentu wymuszającego, jest głównym tematem niniejszego referatu. W tym celu zostały zastosowane dwie metody. Pierwsza, tak zwana metoda tradycyjna, wyznacza Φ_{dy} przez porównanie energii zewnętrznego momentu przechylającego i energii momentu prostującego. Druga polega na rozwiązaniu równania kołysań bocznych ze skokowym momentem wymuszającym i tłumieniem liniowym.

Dodatkowo zostały wykonane badania modelowe ze skokowym momentem wymuszającym. Rejestrowana były kołysania modelu w odpowiedzi na wymuszenie. Wyniki obu metod teoretycznych zostały porównane z wynikami badań doświadczalnych. Porównanie pokazuje, że dla dużej amplitudy kołysań bocznych rzędu 35 stopni uwzględnienie liniowego tłumienia nie ma znaczącego wpływu na kąt przechyłu dynamicznego. Oznacza to, że metoda tradycyjna jest wiarygodna.

ARCHIVES OF CIVIL AND MECHANICAL ENGINEERING

Vol. VII 2007 No. 3

3D Form analysis of rope deformation with long towed underwater hydroacoustic antenna

J. BIELAŃSKI
Gdańsk University of Technology, ul. Gabriela Narutowicza 11/12, Gdańsk

The article describes a possible solution of the boundary problem for the long rope and underwater hydroacoustic antenna system with density insignificantly greater than the density of the water and small rigidity. There is only known a point of rope connection to the ship and depth on which the end of the towed object is placed. The paper presents the analysis of the towed antenna system with rope and calculation form of the system, forces of weights, buoyancy force and lift with changeable longitudinal rope's tension. The results of calculations give us information about the depth of dip of the antenna end point in function of ship speed and lengths of ropes towing. Other results of antenna bending in horizontal plane allow us to define an error in measurements of antennas. Taking into account this error if will give us better accuracy of the executed measurement by the underwater hydroacoustic antenna towed by a maneuvering ship.

Keywords: *hydroacoustic antenna, hydrodynamic forces, internal forces and form of rope for towing*

1. Introduction

The growing employment of rope in techniques of research and exploitation of sea causes that the precision of calculations of rope forms and rope tenses from hydrodynamic loads and from towed objects must grow too. The article presents description of the force as over acting on the system towing rope with antenna and short rope braking. It formulates, in a three-dimensional area, an equation of balance of power. The formulated boundary value problem is solved in numeric way with finite element method. It performs verification of account of antenna form with rope only in vertical plane behind assistance of measurement result rendered accessibly by US Navy.

2. Problem formulation

The ship towed under water a rope with hydroacoustic antennas. The rope length is near 1700m and antenna length is about 250m length. There are very important questions: are bendings of the antenna and rope in vertical and horizontal plane big? The answer for the first question concerns bending of the rope with antenna in vertical plane limits use of antenna on shallow water. The answer for the second question concerns bending of the antenna in horizontal plane and, if it is possible, an increase of accuracy of the measurement by the towed antenna of maneuvering ship.

In order to answer on the above-mentioned questions there have been formulated equilibrium equations for the load and internal longitudinal force in the rope which are used later to execute programs with numeric calculations.The static equilibrium state of the rope is sought, without considering its load imposed by possible movements of the water particles caused by waves. Any elastic strain in the rope is omitted too. The equilibrium state of the rope is reached by the following types of loads:

The weight of the rope and the antenna;

The buoyancy;

The hydrodynamic forces.

As a result of the above-mentioned foundation there has been received balance equation of power acting on the element of the rope.

The figure below presents geometry of towed array.

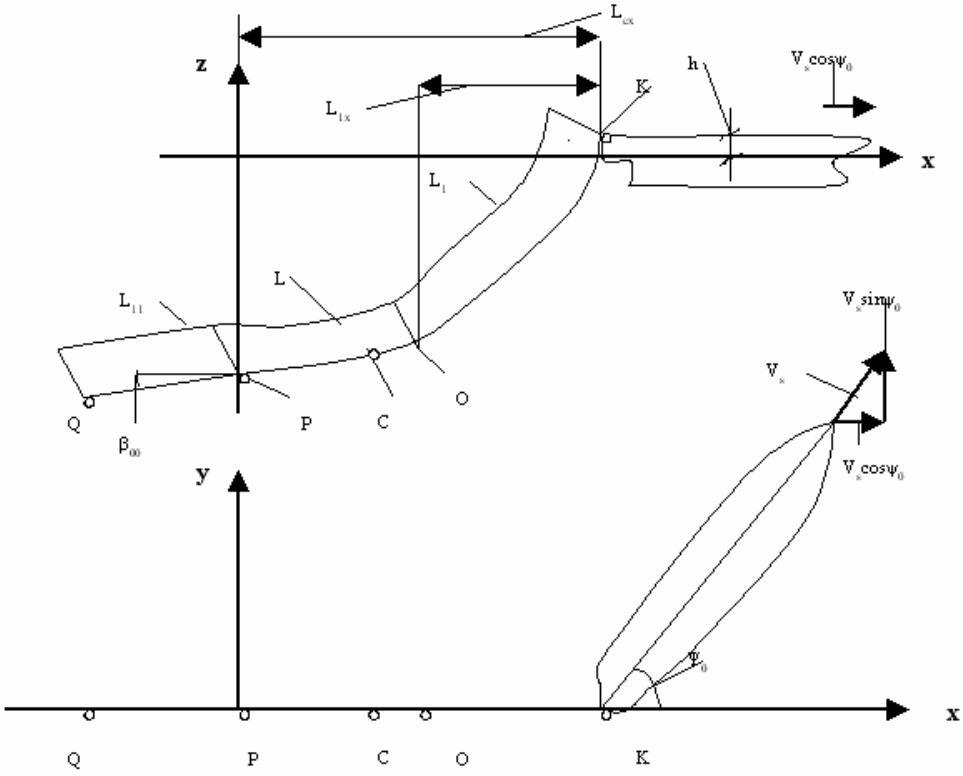

Fig. 1. Coordinate system Oxyz for the ship and the rope with antenna

The formulated balance equations of power acting on the element of the rope came into existence on base of Figure 2.

The hydrodynamic forces are calculated behind assistance of Morison's equation:

$$\begin{aligned} F_n &= \frac{1}{2}\rho C_n V_n |V_n| d, \\ F_t &= \frac{1}{2}\pi\rho C_t V_t |V_t| d \end{aligned} \quad , \tag{1}$$

where:

F_n – the continuous load in the rope acting along the axis '*n*', directed as the flow speed vector projected on the plane perpendicular to the rope's axis;

F_t – the continuous load acting tangentially to the rope's axis;

ρ_W – the water density;

C_n, C_t – the dimension-less coefficients depending on the cross-section of the rope;

V_n – the co-ordinate of the flow speed vector projection on the axis normal to the rope;

V_t – the co-ordinate of the flow speed vector projection on the axis tangential to the rope;

d – the characteristic dimension of the cross-section of the rope (the rope diameter for a rope with a round cross-section), (D – for the antenna).

It is possible to define relationships between the parts of the hydrodynamic continuous load and horizontals and vertical warehouse vector of internal tension of the rope. Dependences behind assistance Figure 2 received:

$$\begin{aligned} &\frac{dH}{dx} = h; \frac{dQ}{dx} = q; \frac{dT}{dx} = t \\ &\frac{dy(x)}{dx} = \frac{T}{H} = tg\psi(x) \approx \sin\psi(x), \\ &\frac{dz(x)}{dx} = \frac{Q}{H} = tg\beta(x) \approx \sin\beta(x) \end{aligned} \tag{2}$$

where:

H – the horizontal component of an internal tension in the rope;

Q – the vertical component of an internal tension in the rope;

h – the horizontal component of the hydrodynamic continuous load;

q – the vertical component of the hydrodynamic continuous load;

t – the second part the horizontal component of the hydrodynamic continuous load for direction of movement traverse;

$\beta(x)$, $\psi(x)$ – angles between tangential direction of the rope element and x axis in vertical and horizontal plane respectively, see Figure 2.

It set up except it, that change of direction of the ship movement will not be greatest than 30deg. From the foundation of small change of ship movement direction we get results which say that the horizontal part of hydrodynamic load of the ropes h has the same value as during simple movement of the ship.

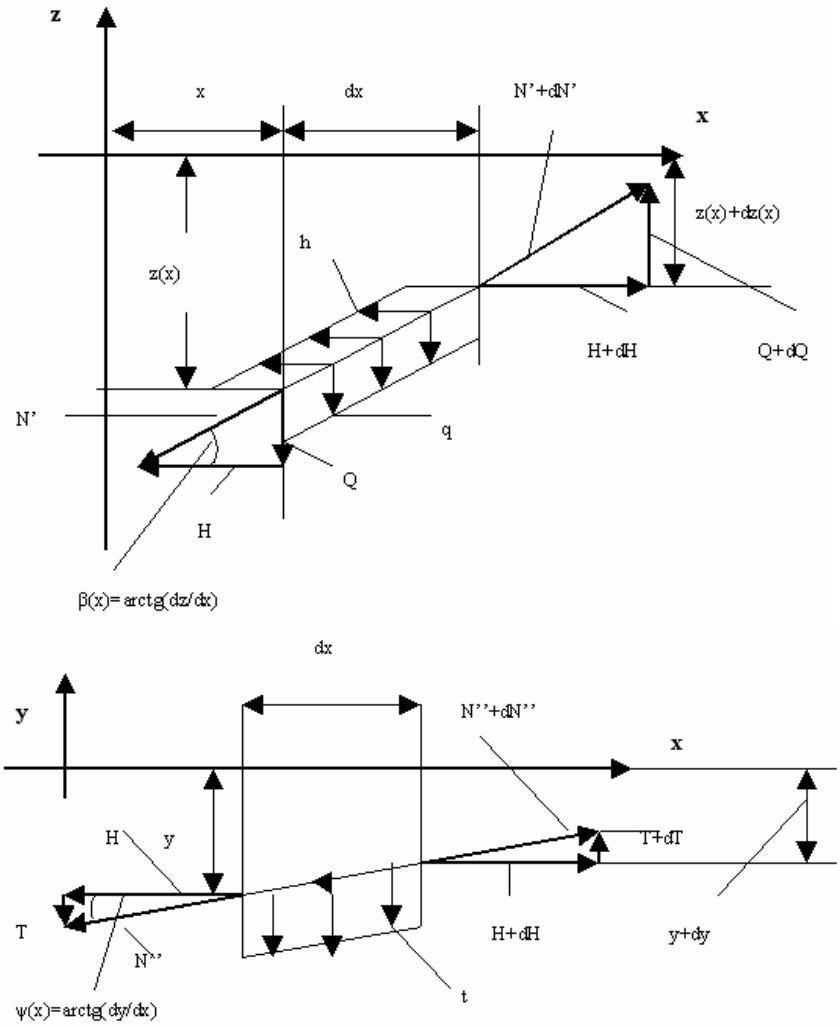

Fig. 2. The continuous horizontal and vertical load and internal longitudinal force impact on the element of the rope or on the element of the antenna

Dependences will accept form as lower:

$$N^2 = H^2 + Q^2 + T^2 = H^2\left(1+\left(\frac{dy}{dx}\right)^2+\left(\frac{dz}{dx}\right)^2\right),$$
$$N = H\sqrt{1+\left(\frac{dy}{dx}\right)^2+\left(\frac{dz}{dx}\right)^2}, \quad N' = H\sqrt{1+\left(\frac{dz}{dx}\right)^2}, \quad N'' = H\sqrt{1+\left(\frac{dy}{dx}\right)^2}. \tag{3}$$

The Equations (2) can be presented in following form:

$$\begin{aligned} \frac{d}{dx}\left(H\frac{dz}{dx}\right) &= q \\ \frac{d}{dx}\left(H\frac{dy}{dx}\right) &= t \end{aligned}, \tag{4}$$

and after differentiation in other form:

$$\begin{aligned} H\frac{d^2z}{dx^2} + A_{Fn}\left(\frac{dz}{dx}\right)^4 + A_{Fn}\left(\frac{dz}{dx}\right)^2 - q_o &= 0 \\ H\frac{d^2y}{dx^2} + A_{Fn1}\left(\frac{dy}{dx}\right)^4 - A_{Fn1}\left(\frac{dy}{dx}\right)^2 &= 0 \end{aligned}, \tag{5}$$

where:

$A_0 = ½\ \rho_W\ V_s^2$;

$A_{Fn} = A_0\ d\ C_n\ [\cos(\psi_0)\ f_0(x)]^2$;

$A_{Ft} = A_0\ \pi\ d\ C_t\ [\cos(\psi_0)\ f_0(x)]^2$;

$F_n = A_{Fn}\ \sin^2(\beta)$, – the normal parts of hydrodynamic force acting on element of the rope in vertical plane;

$F_t = A_{Ft}\ \cos^2(\beta)$, – the tangential parts of hydrodynamic force acting on element of the rope in vertical plane;

$q_0 = (\rho_L - \rho_W)\ S_L\ g$;

V_s – ship velocity;

$f_0(x)$ – the linear function of x, $f_0(x = x(Q)) = 0$, $f_0(x = x(K)) = 1$, K – is the point on the stern of the ship, Q – end-point of towed array;

$A_{Fn1} = A_0\ d\ C_n\ [\sin(\psi_0 - \psi)\ f_0(x)]^2$;

$A_{Ft1} = A_0\ \pi\ d\ C_t\ [\sin(\psi_0 - \psi)\ f_0(x)]^2$;

$F_{n1} = A_{Fn1}\ \sin^2(\psi)$, – the normal parts of hydrodynamic force acting on element of the rope in horizontal plane;

$F_{t1} = A_{Ft1}\ \cos^2(\psi)$, – the tangential parts of hydrodynamic force acting on element of the rope in horizontal plane.

The antenna bending stiffness can be calculated from following relationship:

$$EI = \frac{q_{00} l^4}{384 f}, \tag{6}$$

where:

f – the deflection of the antenna axis from experiment;

l – distance between points of supporting antennas in water, from experiment also;

$q_{00} = (\rho_O - \rho_W) \times g \times \pi \times D^2/4$;
ρ_O – the average density of the antenna material;
D – diameter of the antenna;
EI – the antenna bending stiffness.

3. Problem solution method

The problem was solved with utilization of personal procedures for boundary value problem.

The boundary and initial conditions defined in following manner:

– K – initial point of the rope on the stern of the ship where x, y, z are known coordinate – power of tension is measured here;

– O – point of initial antenna where the angles inclination of the rope β and ψ are equal to the angles of the antenna deflection β and ψ;

– tension of the rope in point O is equal to the resisting force of antenna and ropes braking;

– P – end-point of antenna – pressure is measure here and it defines simultaneously the depth of dip.

4. Results of calculations for exemplary object data

The calculations of the rope shape were performed for data in Table 1.

It presents results of these calculations in vertical surface in the form of the function H_p. This function presents dependence of the dip depth of the antenna end point P of rope length and ship velocity and coefficients of these functions – presented in Table 2.

Table 1. The data of the rope with antenna

Description of largeness	Symbol	Unit of measure	Value
Height of point of rope grapple over surface of water	h	m	2
Length of rope towing	$L1$	m	100–1722
The diameter of the rope	d	m	12.7e–3
Length of antenna	L	m	263.65
The diameter of the antenna	D	m	90e–3
The average density of the antenna material	ρ_O	kg/m^3	1092.5
The antenna bending stiffness	EI	Nm^2	1.2e4
Length of rope braking antenna	$L11$	m	22.86
Ship velocity	V_w	kn	12
Water density	ρ_w	kg/m^3	1020
The dimension-less coefficients of the forces depending on the cross-section of the rope	C_n C_t	[-] [-]	1.2 2e–2
The dimension-less coefficients of the forces depending on the cross-section of the antenna	C_{na} C_{ta}	[-] [-]	1.2 1.013355×C_t

Table 2. The results of the dip depth of the antenna end point *P*

$H_p(x = L1) = a\,x^3 + b\,x^2 + c\,x + d$				
	A	*B*	*c*	*d*
V_w = 5 kn	0	–5.2e–5	0.385	–40
V_w = 10 kn	2.1(3)e–8	7.2e–5	0.127(3)	–18
V_w = 15 kn	–2.6672659270e–8	9.2133085722e–5	4.0430516914e–2	–7.7029104699
V_w = 20 kn	–2.5068546517e–8	8.9475657793e–5	5.4233008690e–3	–2.8778165291
V_w = 25 kn	1.1499860866e–8	7.6377268650e–6	3.4929082027e–2	–7.6664502365

These functions have graphic form as on the following drawing.

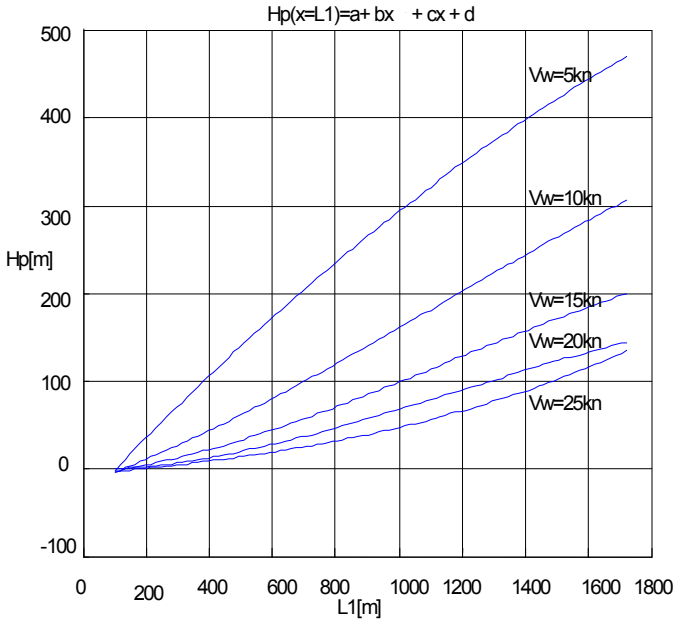

Fig. 3. The function H_p describing dips depth of the antenna end-point (*P*) depending on the speed of the ship towing V_w and lengths of the towed ropes *L*1

Results of calculations have been presented on following drawings in horizontal plane.

The Figures 4, 5 and 6 illustrate lines outlined by points in time underway for ship velocity V_w = 12kn and ψ_0 = 30deg and ψ_0 = 40deg, respectively. Whole process of antenna turning lasts 5 minutes, Figure 4.

Deformation of antenna has a parabolic form in horizontal surface and maximum dart of bending achieves value in initial stages of turning back 0.1m with ship velocity 12knots and course change angle ψ_0 = 30deg, Figure 5. Value of dart of relative bending achieves value 0.04%. Similar value of relative bending of antenna takes a stand at the greatest value of executioner of kink.

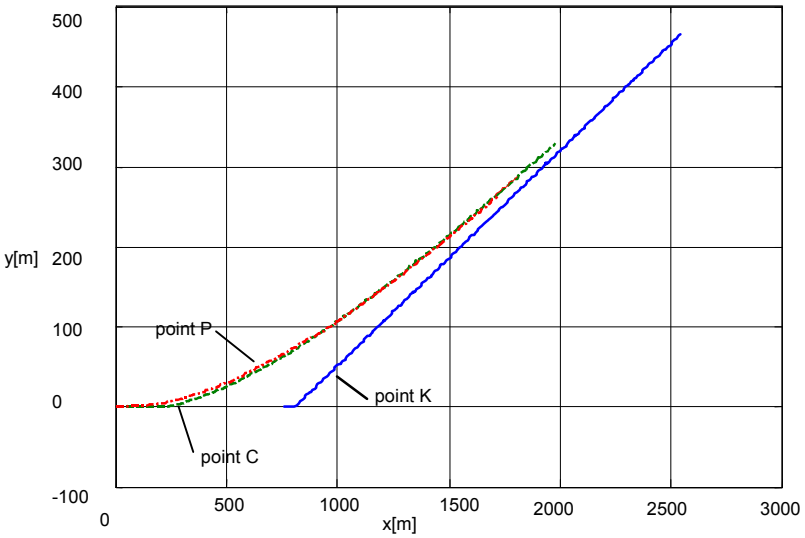

Fig. 4. Presentation of relocation points *C*, *P* of antenna and point *K* of fastening towed rope to the ship in time

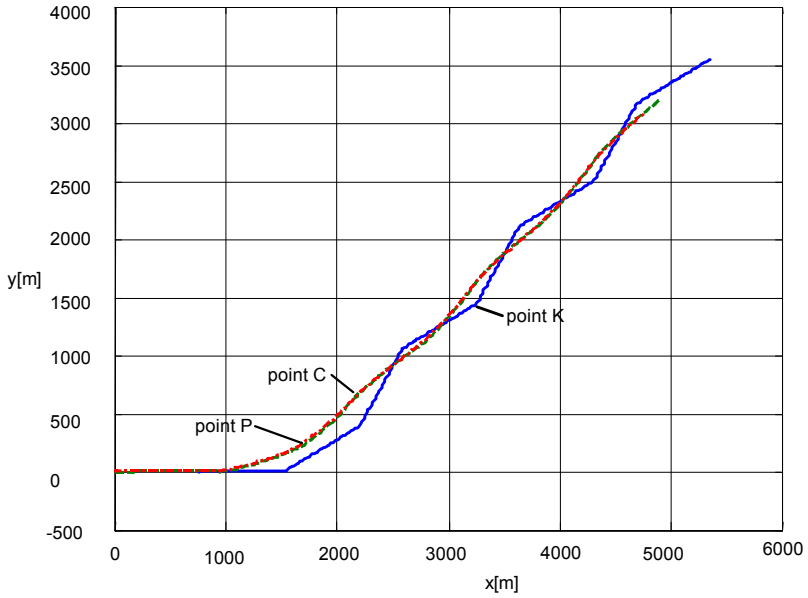

Fig. 5. The way in time of antenna points – *C*, *P* and point *K* on ship during maneuvers of the ship with changes of course angle of the ship about $\psi_0 = 30$deg

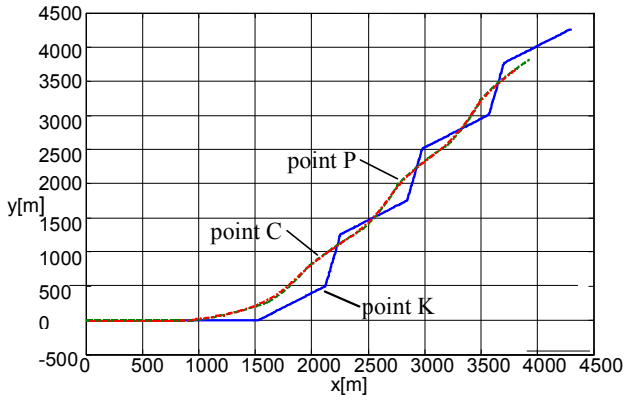

Fig. 6. The way in time of antenna points – *C*, *P* and point *K* on ship during maneuvers of the ship with changes of course angle of the ship about $\psi_0 = 40$deg

5. Conclusions

- On the basis of calculations with described mathematical model there was prepared simple algorithm for fast scaling of antenna site in area without time-consuming calculations of boundary value problem;
- The above-mentioned algorithm allows to calculate site of antenna also after interrupt of data transmission caused by failure. The error of antenna site decreases with time.

References

[1] Bielański J.: *The analisys of the system towing rope with long underwater object*, Hydroacoustics, Gdynia, 2006, Vol. 9.
[2] Bielański J., Bogdaniuk M.: *The iterative method in search for the state of equilibrium in anchor ropes*, Marine Technology Transactions, Polish Academy of Sciences, 2003, Vol. 14, pp. 5–18.
[3] Ronghua Li, Zhongying Chen, Wei Wu: *Generalized difference methods for differential equations*, Marcel Dekker, Inc., New York, 2000, pp. 1–442.
[4] Jaan Kiusallaas: *Numerical methods on engineering with Matlab*, Cambridge University Press, Cambridge, 2005, pp. 1–426.

Trójwymiarowa analiza deformacji kształtu liny holującej i długiej podwodnej anteny hydroakustycznej

Artykuł opisuje rozwiązanie zagadnienia brzegowego dla zestawu długiej liny holującej i podwodnej anteny hydroakustycznej o gęstości tej ostatniej nieznacznie większej od gęstości

wody i małej sztywności. Znane jest tylko położenie punktu zamocowania liny do okrętu (p-kt początkowy holowanego zestawu) oraz głębokość, na której znajduje się koniec anteny. Przedstawiono analizę sił działających na holowany zestaw, ich równania równowagi oraz obliczenia kształtu liny i anteny pod wpływem sił masowych, wyporu hydrostatycznego i hydrodynamicznego z uwzględnieniem zmiennego wzdłużnego napięcia w linie. Wyniki obliczeń pozwalają na predykcję głębokości zanurzenia końca anteny w funkcji prędkości okrętu i długości liny holującej. Ponadto wyniki obliczeń określające deformację kształtu anteny (ugięcie) w płaszczyźnie poziomej umożliwiają określenie błędu pomiaru anteny. Uwzględnienie tego błędu umożliwia uzyskanie dokładniejszych namiarów hydroakustycznej anteny holowanej pod wodą przez manewrujący okręt.

ARCHIVES OF CIVIL AND MECHANICAL ENGINEERING

Vol. VII 2007 No. 3

An overview of the selected results of the European Union Project EFFORT

T. BUGALSKI
Ship Design and Research Centre S.A., Ship Hydromechanics Division, ul. Szczecińska 65, 80-392 Gdańsk, Poland

The European-Union EFFORT (European Full-Scale Flow Research and Technology) project focuses on validating and introducing innovative Computational Fluid Dynamics (CFD) prediction methods for the performance of the ship/propeller combination at the full scale, instead of the usual model scale. Within the project existing CFD codes have been extended, extensive full scale and model-scale (PIV) flow measurements have been conducted, and validation of the CFD predictions has been carried out. In this paper an overview of the EFFORT project results is given and the innovations that have been implemented by EFFORT consortium group are shown. The model scale PIV experiments that have been carried out on two vessels are also discussed. In the paper there are shown some of the validation results based on these experiments. Finally there are selected examples of the calculations that have been carried out by CTO S.A. in which the validated CFD computations have been used as a design tool replacing the model tests which are normally carried out.

Keywords: *EFFORT, CFD, model and full scale tests , Wake-Field*

1. Introduction

A challenging new European cooperative project EFFORT (European Full-scale Flow Research and Technology) has been recently finished. Principal objectives are the refinement and validation of Computational Fluid Dynamics (CFD) prediction methods for the viscous flow around a ship hull at the full scale, and their introduction into practical ship and propeller design.

Hydrodynamic aspects play an important role in the quality of a ship. Dominant criteria in the hull form design are often the resistance and powering performance; in addition, the occurrence of noise and vibrations, important for the comfort level of crew and passengers, often has a hydrodynamic cause, stemming from the operation of the propeller in the disturbed flow field behind the ship hull.

Therefore, the detailed knowledge of the flow around the aft-part of a ship is critical: In this area, flow separation may occur, with important consequences for the resistance and power; and the flow field felt by the propeller should be determined. Unfavourable characteristics of this flow field (e.g. large spatial variations of the velocity) may result in performance loss, propeller cavitation leading to noise, vibrations and erosion, etc. The viscous flow can be computed using Reynolds Averaged Navier Stokes (RANS) codes. This is becoming a common component in the ship design

process, and good agreement with model-scale wake field measurements can be achieved today.

The real purpose is to predict the full-scale flow, wake field and hull/propeller interaction. RANS computations offer that possibility, and such full-scale viscous-flow computations start to be used in the practical ship design; but how accurate these predictions are, and to what extent they depend on the turbulence modelling used, is not really known. A validation of the full-scale ship viscous flow predictions has generally been insufficient so far, mainly due to the virtual absence or difficult accessibility of the suitable full-scale experimental wake field data. This is the fundamental point that EFFORT aims to address.

The following steps have been made in the project:

A full-scale measurement campaign in which extensive flow measurements onboard of two vessels – hopper dredger "UILENSPIEGEL" (Dredging International), and the research vessel "Nawigator XXI" operated by the Maritime University of Szczecin – have been done by MARIN (Netherlands) using Laser-Doppler Velocimetry (LDV) techniques. In addition, also existing full-scale flow data was collected. Corresponding model-scale measurements using Particle Image Velocimetry (PIV) and other techniques have been done by Ship Design and Research Centre S.A. (CTO, Poland).

A joint CFD development phase, in which limited refinements have been made (that play a central role in full-scale flow predictions): advanced turbulence modelling, propeller/hull interaction, free-surface modelling.

There have also been made the extensive validation studies, to establish the level of accuracy and improve the modelling. Finally, the CFD tools, extended and validated in the project, have been used in design studies proposed by the industrial participants.

The project, supported by the 5th Framework "GROWTH" programme of the European Union and by the industry, has been run for three and half years. The consortium consists of the institutes MARIN, CTO, HSVA, and Bassin d'Essais des Carènes; the universities of Helsinki (HUT), Athens (NTUA), Szczecin, Chalmers University and Ecole Centrale de Nantes (ECN); and the industrial participants Rolls-Royce, IHC Holland, Kvaerner Masa Yards, Lloyd's Register, and Van Voorden Propellers. The project has been coordinated by MARIN. An important step forward in the use and usefulness of viscous flow computations in European ship design, and thereby in the quality and efficiency of the design process, is expected owing to completion of this challenging project.

More information about this project can be found on the EFFORT website: http://www.marin.nl/projects/effort

2. Basic and non-standard experiments

One important task of the project has been extensive full-scale flow measurements on board of two vessels at sea and corresponding model test measurements in the

towing tanks. The full scale measurements have been done by MARIN using LDV techniques. Corresponding model scale measurements of the total wake have been done by CTO using the PIV technique. Furthermore, basic model tests have been carried out by CTO and HUT, completed by measurements of the nominal wake using PIV and a five-hole Pitot tube (Nawigator) and a six-hole Pitot tube (Uilenspiegel). NTUA have performed wave-pattern measurements of a smaller model of the Nawigator.

Nawigator XXI

IHC – Uilenspiegel

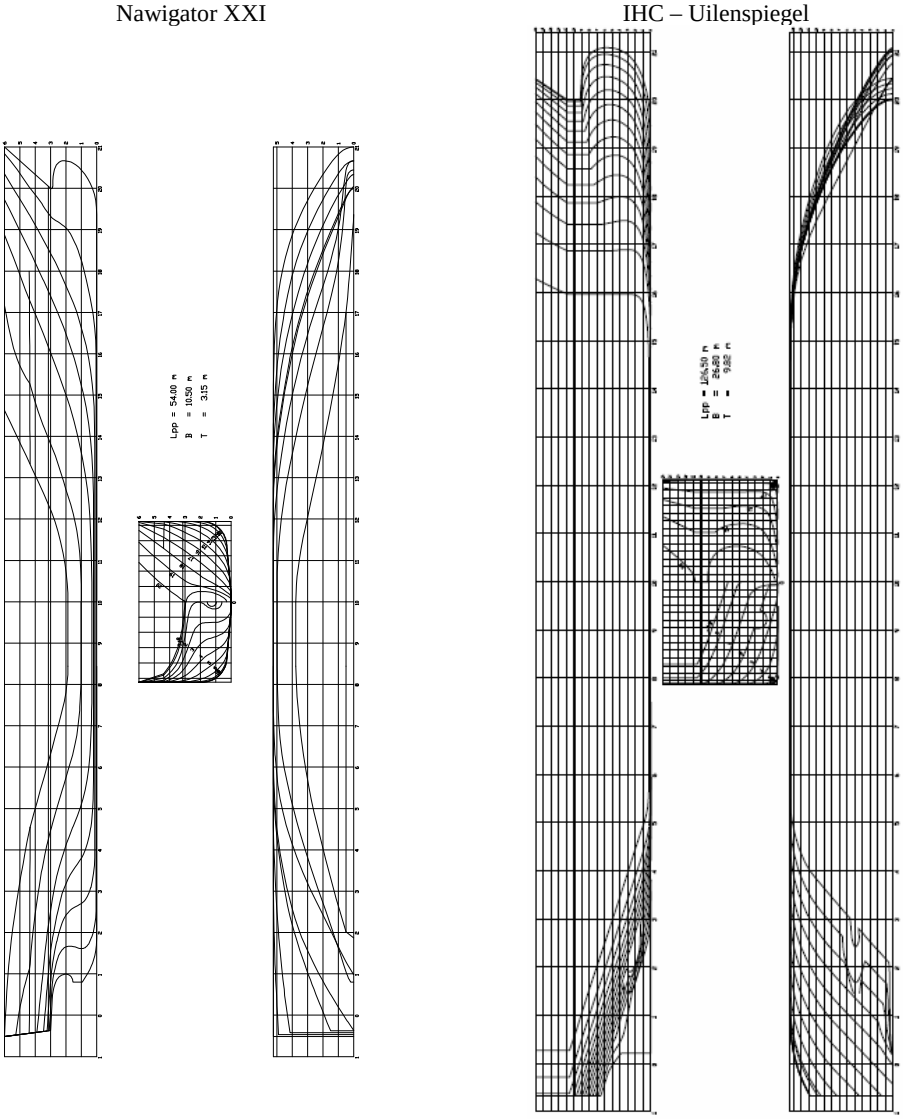

Fig. 1. Lines of vessels have been tested in EFFORT project

The non-standard model tests, for training/research vessel Nawigator XXI and for hopper dredger Uilenspiegel, have been performed at the Ship Hydrodynamics Division of Ship Design and Research Centre S.A. (CTO). For Nawigator, the following tests have been performed: PIV measurements of nominal and total wake field, Pitot probe measurements of the nominal wake field, longitudinal wave cut test and the manoeuvring tests. For Uilenspiegel, PIV measurements of the total wake field and the longitudinal wave cut tests have been performed.

The full scale measurements have been done on the research vessel "Nawigator XXI" operated by the Maritime University of Szczecin and hoper dredger "Uilenspiegel" constructed by IHC Holland (Figure 1). The "Nawigator XXI" vessel has the following main particulars: length overall 60.30 m, breadth moulded 10.47 m, depth to the main deck 4.20 m, draught 3.15 m, deadweight abs. 300 t. The main destination of the ship is training of students for the future work as deck officers, engineers and ship electricians. For this purpose she is provided with the most modern electronic navigation, communication and automation equipment. The "Uilenspiegel", second vessel, has the following main particulars: length between perpendiculars 126.50 m, breadth moulded 26.80 m, design draught 5.00 m.

Fig. 2. View of Nawigator XXI vessel stern

Fig. 3. View of model of Nawigator XXI screw propeller

The measurements at model scale are unique as they have been performed according to the full-scale conditions of the ship allowing an examination of the influence of the different Reynolds numbers on the flow field without the necessity of performing major corrections. The main task has not been performing a full-scale prediction of the performance of the ship, but providing experimental data for the validation of the computations carried out within the EFFORT project. Therefore the results are slightly different from the standard ones. Fairing of the obtained curves has not been carried out in order to keep the information about the standard deviations of the measured values. In order to have an idea about the repeatability of the measurements, repeated

measurements performed on different days where the model has been put into the water again (HUT) and ITTC – UA analysis have been performed by CTO.

3. Wake-Field model scale PIV experiments

A large task realized in the framework of the EFFORT project has been the application of PIV method for the velocity field measurements near the ship model, with or without the working propeller. As the method is relatively new, the results have been treated more carefully than those obtained with the Pitot probe. Despite some problems faced during taking the measurements and processing the results, the obtained results look promising and show large potential of the PIV method for research purposes.

The principle of PIV measurements allowing to measure three components of the velocity in chosen plane is presented in Figure 4. The cameras were located in the streamlined body (torpedo), towed together with the model as shown in Figures 5 and 6. The velocity field was measured in the sectional planes located close to the propeller disc plane. For Nawigator, the measurements were taken both with and without working propeller, for Uilenspiegel – only with working propeller.

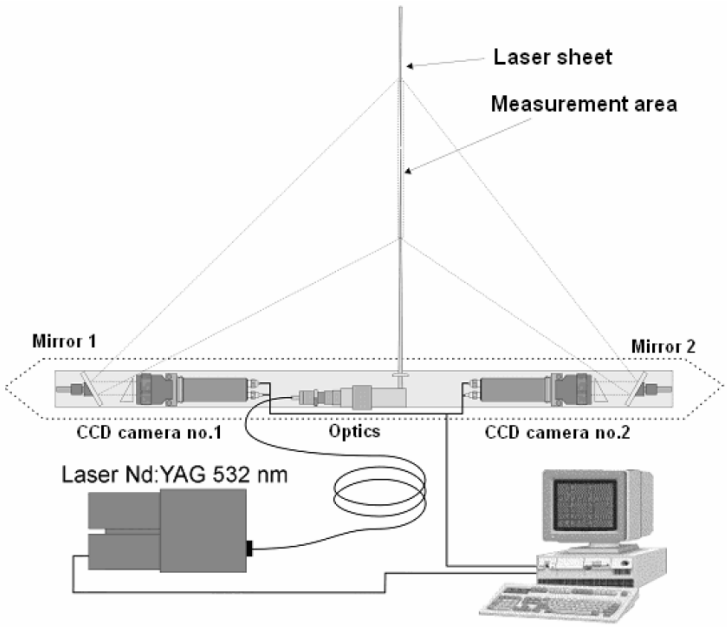

Fig. 4. PIV measurements – scheme of the equipment

Some obvious advantages of PIV method, compared to the Pitot probe measurements, are:

- smaller intrusiveness,
- possibility of taking measurements in some regions not available for the Pitot probe measurements (e.g. a region close before the working propeller),
- a velocity field in a relatively large area can be measured in a short period of time, which makes the method usable for the measurements of an unsteady flow. The Pitot probe measurements are usable only for a steady flow.

As the measurements were taken around the model towed in the towing tank, the PIV equipment had to be located in a device moving together with the model. This device houses two cameras and a laser light source. The photographs of the measurement stand are shown below.

Fig. 5. PIV measurements on Nawigator XXI model – the measurement stand

Fig. 6. PIV measurements on Uilenspiegel model

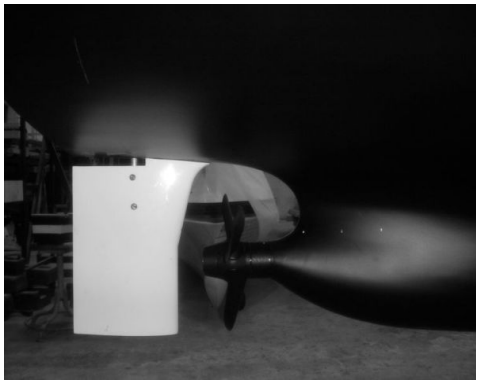

Fig. 7. Aft part of the training vessel

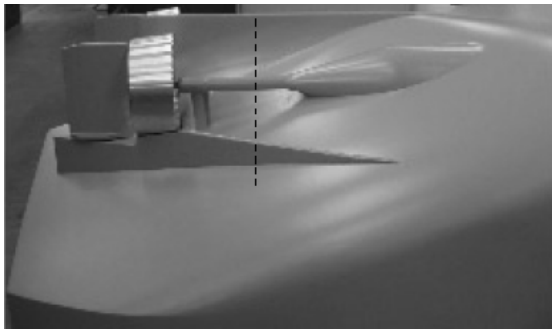

Fig. 8. Aft part of the dredger

The photographs in Figures 6 and 8 show the model of the second example vessel – the hopper dredger. The PIV measurements have been carried out for fully appended

hull with working propeller. The velocity field has been measured in two planes perpendicular to the symmetry plane and the base plane – one of these planes is marked in the photograph with the dashed line.

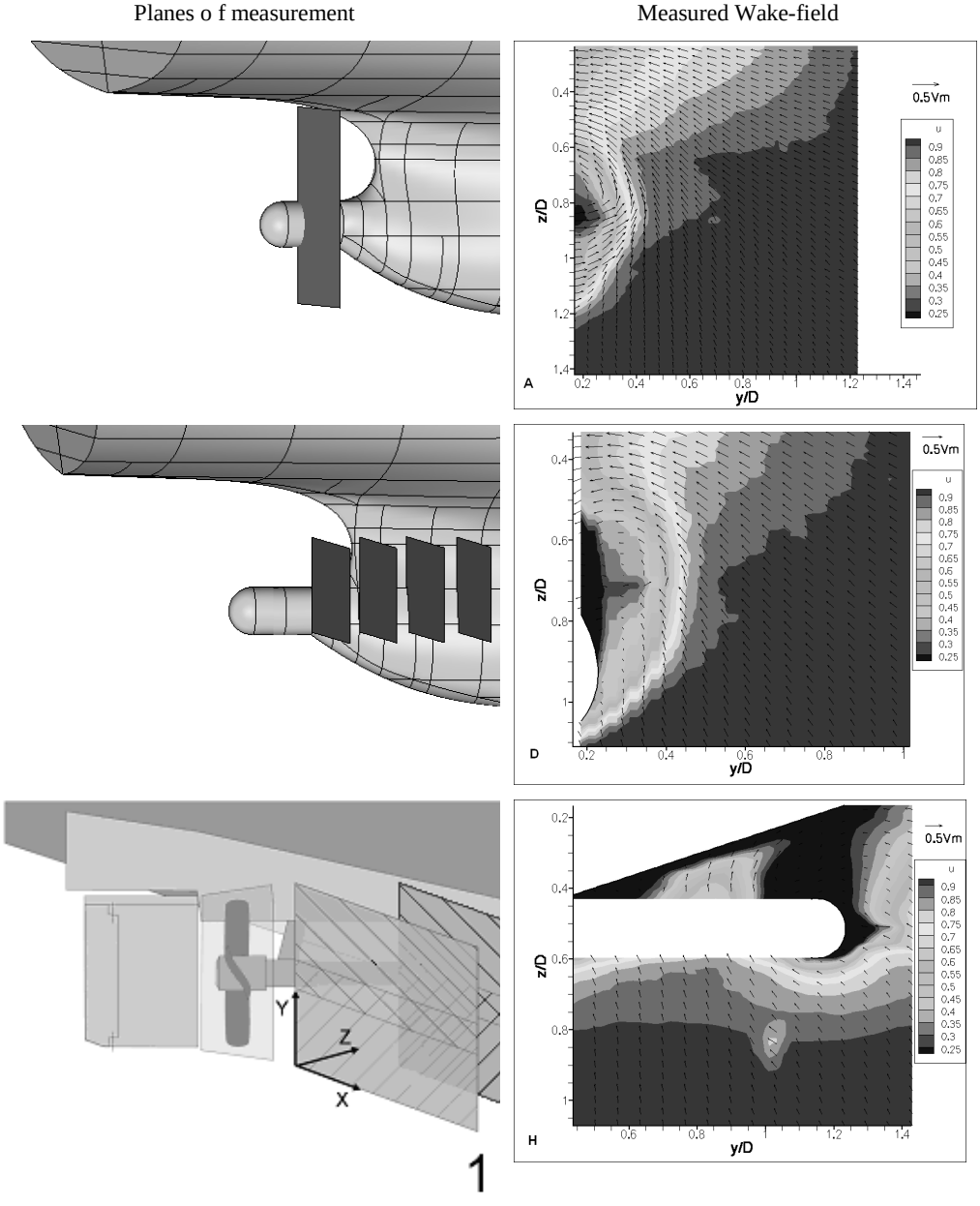

Fig. 9. Planes of PIV measurements with examples of measurement results

As can be seen in the picture showing the arrangement of the measurement stand, the laser sheet points in the direction perpendicular to the symmetry plane. This implies that a small part of the measurement plane shown in Figure 8 is hidden in the shade of the propeller shaft and it is not possible to measure the velocity field in this region at the assumed arrangement of the measurement equipment.

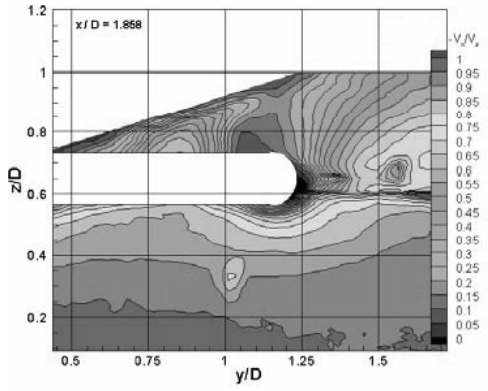

Fig. 10. Axial velocity component – PIV (CTO)

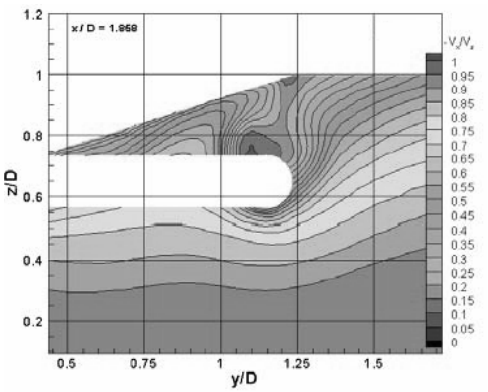

Fig. 11. Axial velocity component – CFD (ECN)

The velocity field measured in the remaining part of this plane shows an outstanding conformity with the CFD results which has been obtained by ECN – the comparison is presented in Figure 9.

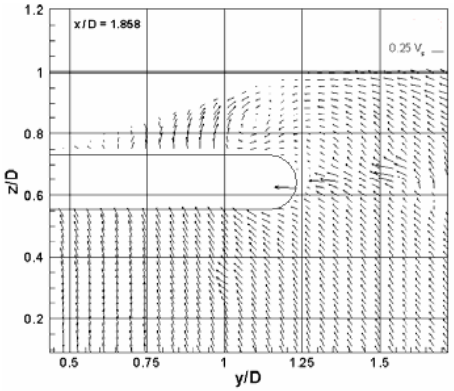

Fig. 12. Transversal velocity component – PIV (CTO)

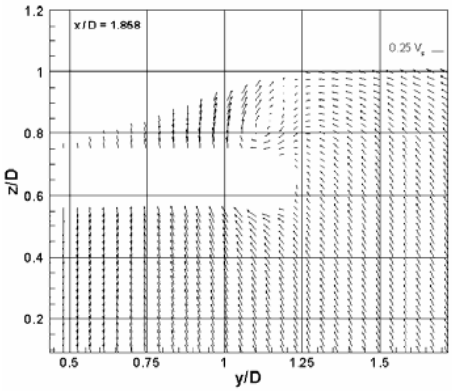

Fig. 13. Transversal velocity component – CFD (ECN)

In Figures showing the PIV results, a narrow horizontal strip of non-physical velocity can be observed at z/D ~ 0.6. It comes from the fact that the measurements have been taken in two stages on different heights in order to cover the entire measurement

area, and then the pictures from CCD cameras, overlapping in a small part, have been merged.

A conclusion can then be made for the future that if the measurements have to be taken in few stages, the boundaries between the measurement areas in single stages should not be located in regions where complex flow can be expected.

4. CFD computations of wake-field

The validation of the wake filed computations for two vessels, first in the model scale second in the full scale, have been one of the main tasks of the European EFFORT project. The results obtained from RANSE solvers have been compared with the following experimental data:

- Pitot probe measurements – at the model scale,
- Particle Image Velocimetry (PIV) measurements – at the model scale,
- Laser – Doppler Velocimetry (LDV) measurements – at full scale.

Ship Design and Research Centre S.A. participating in EFFORT has engaged primarily in the model tests; however, some comparative computations have been carried out, using the experience of other partners, in order to implement an effective procedure for the computations of the wake field.

Although different measurement methods have been used and the experiment has been carried out also at the full scale, the correctness of the CFD results have been assessed basing mainly on the most standard test results: the Pitot probe measurements at the model scale. Other experimental results have been used to assess the usability of alternative measurement techniques.

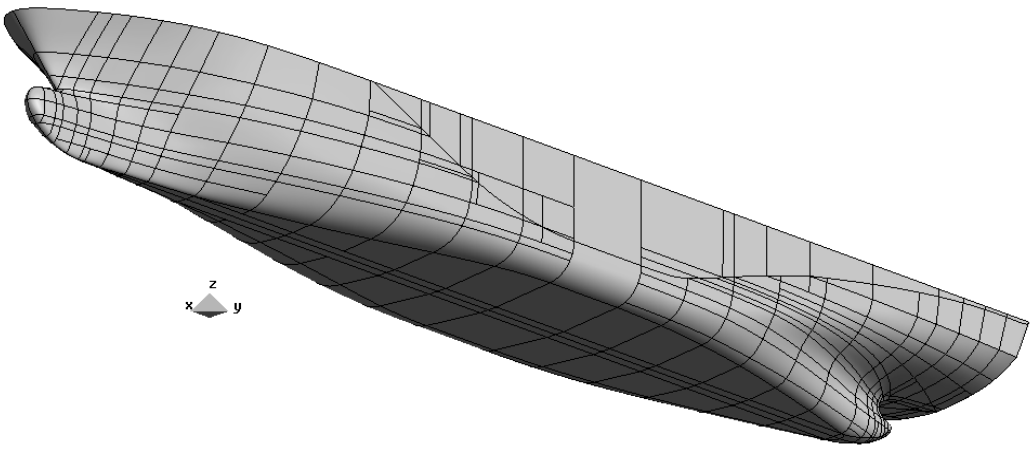

Fig. 14. Nawigator XXI: underwater shape (grid for CFD calculations)

Figure 15 presents some examples of the comparison of measured and computed wake field for one of the database vessels: the training vessel "Nawigator XXI". The shape of Nawigator is presented in Figure 14.

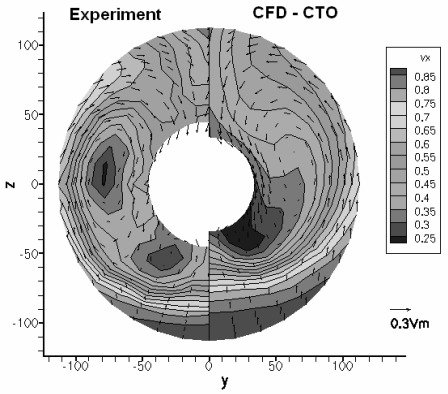

Turbulence model: standard k-ε

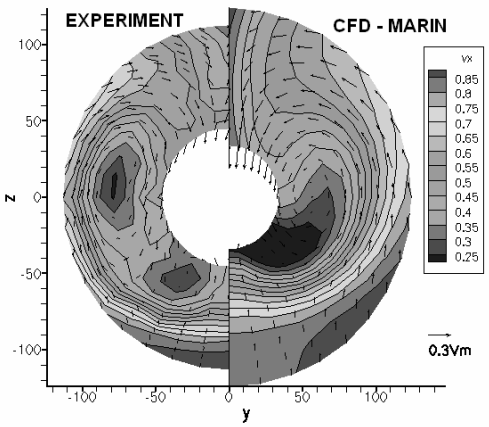

Turbulence model: Menter's k-ω

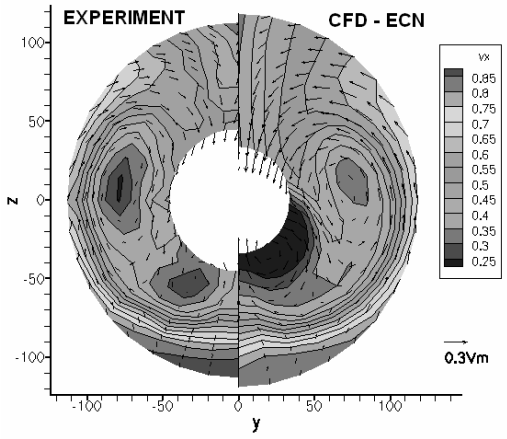

Turbulence model: RSM

Fig. 15. Comparison of measured and computed wake field for "Nawigator XXI"

The following conclusion can be drawn basing on the above comparison:

- a general tendency can be observed to underestimate the axial velocity in a narrow region in the upper part of the propeller disc,
- the experiment reveals a separated region of low axial velocity, to the side from the propeller hub ($y \sim -75$, $z \sim 0$). This phenomenon has been predicted correctly only in ECN's computations, where RSM turbulence model and a very dense mesh has been used,

• the computations of CTO have been carried out with the use of a relative coarse mesh (700 000 cells). The mesh, consisting of less than 1 million cells, is CTO's standard for the free surface ship flow computations. The free surface shape and the resistance value obtained for such mesh revealed to be accurate enough for comparative studies of different versions of the hull, and this is the most frequent computational task in CTO. However, the comparison presented above shows that such a rough model is not sufficient for correct prediction of the wake field. On the other hand, accurate results obtained by ECN show that the RANSE model is able to capture the wake flow phenomena if only the mesh resolution is sufficient and proper turbulence model is applied. This encouraged CTO to carry out some additional computations in order to work out an affordable procedure for accurate prediction of the wake field.

The following observations have been taken into account:

• a modification of the standard model for free surface flows simply by increasing the mesh density and changing the turbulence model to obtain an accurate wake field would result in unacceptable computational time,

• the time required to obtain a convergence of the free surface flow is even few times longer than the convergence time for the flow without free surface. For a displacement ship, sailing at low or moderate Froude number, the influence of the free surface on the wake field can be often neglected. It is then reasonable to compute the wake field separately, without taking the free surface into account.

It has been also assumed that the flow can be computed accurately for the aft part of the hull only, using the velocity field computed on the coarse mesh as the inlet boundary condition. The domain for computing the free surface flow is rectangular and ranges one ship length upstream, two lengths downstream and to the side and one length downward. To compute the wake field, the domain dimensions have been greatly reduced, as shown above, and the domain shape has been changed to cylindrical (the cylinder radius was 0.55 of the model length).

The hull has been cut in the middle and the inlet boundary condition has been applied there, using the velocity field computed with the coarse mesh (it has been then assumed that the flow in this region is still relatively simple and the coarse mesh is sufficient to evaluate it accurately). Similarly, the velocity field computed with the coarse mesh has been imposed on the cylindrical wall bounding the domain. The outlet has been located closer to the hull.

The block-structured, hexahedral mesh has been generated with the use of ANSYS ICEM CFD Hexa. The number of cells has been about 2 000 000.

The computations have been carried out using the FLUENT solver with two turbulence models: SST k-ω and RSM. The results are show in Figure 16.

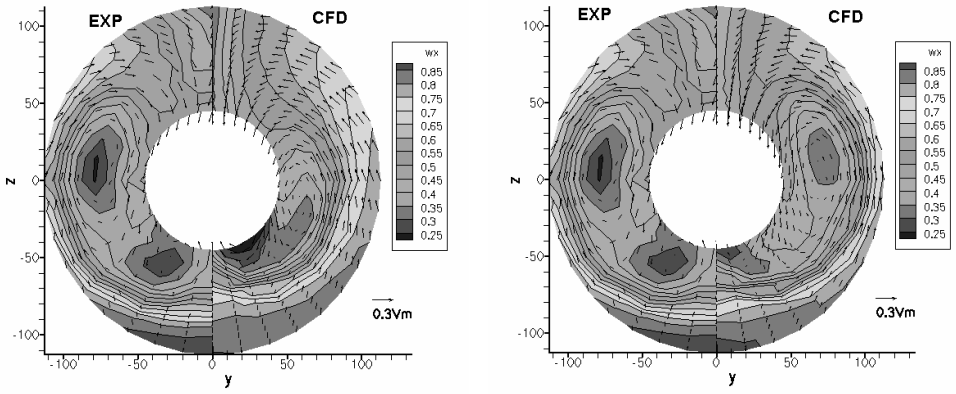

Turbulence model: SST *k-ω* Turbulence model: RSM

Fig. 16. Comparison of computed and measured wake field

The results of the wake field computations with the mesh of high density yield the following conclusions:

- the results obtained with the two-equation SST k-ω model are better than the results obtained with the coarse grid, but are still poor,
- the results obtained with the RSM model are satisfactory, so this model of turbulence seems to be a good choice for the accurate wake field computations,
- the numerical prediction in both cases tends to underestimate the velocity in the upper part of the propeller disc. This effect is stronger for the SST k-ω turbulence model,
- in case when the computer resources are limited and the results from the coarser mesh for entire hull are available, the proposed method for wake field computations can be considered attractive as the results are sufficiently accurate. However, the problem of overestimation of the hull shade in the upper part of the propeller disc remains unsolved.

Realization of The EFFORT project resulted in accumulation of large amount of valuable data both for model scale and full scale flow. According to EFFORT consortium agreement and EU rules this data will be made a public in few years.

Acknowledgements

This paper presents selected results of the project EFFORT supported by the 5th Framework 'GROWTH' program of the European Union and by the industry. This financial support is gratefully acknowledged.

Sketches of comparisons of PIV measurements and CFD computations have been generated by B. Starke (MARIN). CFD computations presented here have been done by M. Kraskowski (CTO), B. Starke (MARIN), M. Visonneau (ECN).

The Particle Image Velocimetry tests were conducted and the results processed thanks to the cooperation with the scientific team from the Institute of Fluid Flow Machinery of Polish Academy of Science conducted by Prof. J. Mizeraczyk.

The author would like to thank all the partners for their patience and the remarkable work.

References

[1] Raven H., Verkuyl J-B.: *New EFFORT in full–scale CFD validation*, MARIN Report, Wageningen, December, 2002, No.78, pp. 18.

[2] Bugalski T., Czyżewski W, Szulc M.: *EU and Polish EFFORT for validation of full – scale viscous – flow predictions*, Proceedings of the sixth International Workshop on Methods for Development and Evaluation of Maritime Technologies (DeMAT'2003), Rostock, 2005, Vol. 3, pp. 261.

[3] Kraskowski M., Bugalski T.: *CFD and EFD tools for ship flow prediction*, 16th International Conference on Hydrodynamics in Ship Design (HYDRONAV'05), Gdańsk, Ostróda, 2005, pp. 467.

[4] Bugalski T.: *UA in ship model tests*, Jurata Scientific Session of CTO Jubilee, 2001.

[5] The Resistance Committee – *Final Report and Recommendations to the 23rd ITTC*, 2002.

Przegląd rezultatów europejskiego projektu badawczego EFFORT

Celem europejskiego projektu badawczego o akronimie EFFORT pt.: „*Europejskie badania i technika pomiaru opływu okrętu w pełnej skali*", był rozwój metod Numerycznej Mechaniki Płynów (CFD) poprzez stworzenie unikalnej bazy wyników pomiarów, w skali naturalnej (rzeczywistej skali statku) podczas rejsów na otwartym morzu i na modelach badanych w basenach holowniczych. W ramach projektu przeprowadzono pomiary parametrów opływu kadłubów, w szczególności pól prędkości,(w skali pełnej, techniką laserową LDV) i równoważne, w skali modelowej (techniką PIV oraz klasyczną sondami Pitota, dla dwu statków: szkolno – badawczego statku Akademii Morskiej w Szczecinie – Nawigator XXI o długości *Lpp* = 54.13 m, oraz pogłębiarki oceanicznej IHC – Uilenspiegel, o długości *Lpp* = 126.0 m. Praca omawia sam projekt badawczy oraz prezentuje nową technikę pomiarową PIV. Wyniki pomiarów posłużyły jako podstawa do oceny wyników obliczeń opływu statków za pomocą systemów rozwijanych w ramach projektu.

ARCHIVES OF CIVIL AND MECHANICAL ENGINEERING

Vol. VII 2007 No. 3

To the problem of designing of board coverings that receive intensive local load

E. BURAKOVSKIY, P. BURAKOVSKIY, V. PROKHNICH
Kaliningrad state technical university, Sovetski prospect 1, 236000 Kaliningrad

This paper is devoted to the development of refined methods of locally loaded board coverings bearing strength evaluation. In domestic practice it is shown, for the first time, that taking into account rigidity of a plate changes not only deforming nature of a tie, but it dramatically varies qualitative characteristics of a loading strength of a tie.

Keywords: *plate, framework, hull structure, locally- distributed loads, elasto–plastic deformation*

Design of a hull structure with minimum weight is linked mainly with metal distribution between plating which makes up 70–80% of whole weight, and covering framework. Nowadays we face this acute problem too.

It is clear that excessive reduction of tie dimensions leads to depreciation period reducing and damaging increase, but at the same time it leads to an increase of useful carrying capacity and economic efficiency. On the other hand increase of dimensions will reduce economic indexes, etc. So we understand that choosing of tie dimensions is optimization problem, but this problem is not completely solved. It is well known that damaging of hull structure is caused mainly by intensive locally-distributed loads. That means that the development of methods which will calculate hull ties in elasto-plastic stage is topical.

Let us consider locally loaded hull covering with principal direction joisting. To simplify analysis we consider that covering is infinite in two directions. Such idealization does not have an influence on deformation picture, because strongly localized plastic deformations, caused by intensive local loads, fade rapidly while moving away from loading spot. On the other hand this idealization dramatically simplifies the whole the analysis.

Let us suppose local load moving about the covering (or it's appointed area) loading plate or rib in turn. We assume pressure on a square spot $a_1 \times b_1 = 200 \times 200$ mm as a local load. Question about actual area of operational load localization is quite difficult and needs original research.

It follows from covering structure that locally loaded plate and rib branch deformation examination is necessary and enough to satisfy solidity requirement. We should bear in mind that only plates and ribs of equal solidity will ensure minimum weight of covering. We use probability of element destruction as a most advisable balanced life criterion. As applied to covering destruction probability on reaching some normative

deflection is probability of two independent occurrences and determined as probability product (formula 1):

$$Q_{qp} = \int_0^\infty Q_p(w) dQ_q(w) = \int_0^\infty Q_p(w) q_q(w) dw, \tag{1}$$

where:

$Qp(w)$ – covering destruction probability on normative deflection;

$Qq(w)$– probability of reaching of normative deflection;

$$Q'_q(w) = q_q(w), \qquad Q_q(w) = \int_0^w q_q(w) dx. \tag{2}$$

Generally $Qq(w)$ can be determined using Kolmogorov's evolutionary equation of the first kind. Determination scheme for stationary and non-stationary cases are shown in [1].

Covering destruction probability in case deflection exceeds W_1 level can be written as:

$$Q_p = \int_0^{W_1} \varphi(W_p) dW, \tag{3}$$

where:

Q_p – covering destruction probability;

W_1 – deflection, corresponding fixed destruction probability;

$\varphi(W_p)$ – destructing deflection frequency distribution function, which can be found experimentally.

For beam structure destruction probability criterion can be written in the following way. Maximum plastic deformation value can be defined by approximation of plastic deformation distribution in plastic hinge area under certain loading function. Integral of this function is equal to plastic extension value defined according to plane section hypothesis.

For symmetrical load of a beam we can write:

$$u_{пл_i} = 2 \cdot \int_0^{c_m} \frac{\varepsilon_{\max}}{2} \cdot \left(1 + \cos\frac{2\pi x}{c_m}\right) dx, \tag{4}$$

where:

c_m – coordinate of a point corresponding fiber fluidity moment value;

$\varepsilon_{\max}$ – desired maximum plastic deformation value.

So it is no difficulty to determine desired maximum plastic deformation value from above equation ($\varepsilon_{\max}$).

By increasing load in ΔP_{i+1} beam receives deflection of f_{i+1}. That leads to plastic deformation value increase and removal of fiber fluidity points. By defining new coordinates of fiber fluidity points we approximate plastic deformation growth using same cosine function. Dividing whole deformation process into phases and defining maximum deformation growth on each it is easy to find desired quantity

$$\varepsilon_{\max} = \sum_{i=1}^{n} \Delta\varepsilon_{\max_i} , \tag{5}$$

where:

n – number of phases.

We should notice that increasing of number of phases will make result more accurate.

Disposing of specified maximum plastic deformation values we can judge about margins of safety of construction. Comparing these values to pattern destruction frequency function depending on plastic deformation phase $\psi(\varepsilon_{\max})$ [1] it is possible to find construction destruction probability depending on deformation phase of its ties, defining $\varepsilon_{\max}$ from (5)

$$P_P = \int_0^{\varepsilon_{\max}} \psi\varepsilon_{\max} d\varepsilon . \tag{6}$$

In fact such interrelation is realization of probability criterion of deformed beam structure solidity. Providing equal destruction probability for plates and ribs we bring about equal solidity condition. It is necessary to have “force-deflection” dependences for all covering elements. Locally loaded plate calculation was viewed above and has no fundamental difficulties and can be carried out in accordance with [1].

While evaluating rib branch bearing strength traditionally limit balance theory is used with assumption made that board plating supporting force is insignificant. Validating was that rib was much more rigid then plate. Chain stains are significant in plate with advanced deflections that can influence rib branch bearing strength. Attention was paid [2] on problem of plate rigidity accounted for rib deflection consideration. So, rib branch analytical model is brought to consideration of elasto–plastic bend of beam loaded with point force and lying on elasto–plastic foundation with linear strengthening [3].

Rib foundation characteristics can be found from consideration of deflection of fascia-beam two spaces long and loaded with point force in the middle of span.

Such solution can be found using “plastic hinge momentary opening” hypothesis which is quite developed for fascia-beam [1]. Using piecewise-linear approximation of “force-deflection” dependence we can find elasto–plastic foundation characteristics (Figure 1).

Found:

$$K_1 = \frac{P_1}{w_1}, \qquad K_2 = \frac{P_2 - P_1}{w_2 - w_1}. \tag{7}$$

Problem should be solved in appointed consecution because thrust coefficient for fascia-beam is not known. On the first phase assigning some Kp_1 value we consider rib branch deflection like elasto–plastic beam deflection lying on elasto–plastic foundation with linear strengthening [3] to kinematic variable beam type mechanism. After that it is possible to refine Kp value in accordance with [1, (8)] and correct foundation rigidity parameters.

$$Kp = \frac{0.08 + 0.06\dfrac{b_1}{l_1}}{1.08 + 0.06\dfrac{b_1}{l_1}}, \tag{8}$$

where:

l, b – failure area dimensions (Figure 2).

Calculating process continues till failure area dimensions will vary less then 5% between previous and following cycles.

Varying rigidity of ribs and plates this method allows estimate its influence on ribs bearing strength and refine efficient ratio in rigidity of ribs and plates.

Thus for flexible plates $\frac{a}{t}$ = (60–120) (Figure 3) rib bearing strength increases (5–20%) with decrease of space (a) and is conditioned mainly by beam rigidity. For rigid plate $\frac{a}{t}$ = (30–60) and $\frac{a}{t}$ = (20–40) plate rigidity increase leads to rib bearing strength decrease (10–15%). It is conditioned by changing of beam destruction area and thrust coefficient of plates, which provide rib beam maintenance by foundation reaction creation. Decrease of thrust coefficient of rigid plate simultaneously with rib destruction area decrease leads to rib beam bearing strength decrease.

Such rib behavior prevents from its solidity reserve estimation because load, which makes a kinematic mechanism of rib, depends much of plate rigidity. It is clear that main factor leading to beam destruction is extension in extreme fibers of plastic hinge, which proportionate to beam destruction angle in it. With plate rigidity increase destruction angle in central plastic hinge falls (up to 60%), as a result maximum plastic

extensions in plastic hinge remain much lower than that for beams lying on flexible foundation. Thus margin of safety for the same beam, changed into kinematic variable mechanism and lying on plates of same thickness but different spaces, can differ up to 1.5 times.

It should be noted that destruction angle in plastic hinge does not changes greatly with plate rigidity change but is defined by thickness and space of boarding.

Data showing efficient increase of rib bearing strength by its rigidity increase are of certain interest. Thus for flexible plate $\frac{a}{t}$ = (60–120) 4.5 times rib rigidity increase leads to only 70% increase in rib bearing strength (here we consider bearing strength as kinematic variable mechanism formation). For more rigid plate $\frac{a}{t}$ = (30–60) 4 times rib rigidity increase leads to 20% increase in bearing strength. Note that these conclusions are made in assumption of bend destruction mechanism realization. Figures can vary if shear deformations considered.

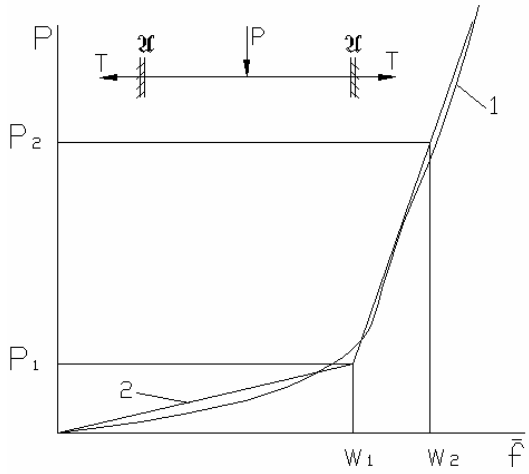

Fig. 1. Foundation characteristics definition scheme

While trimeric hinge mechanism forms rib branch does not lose its bearing strength but become able to receive load much greater then load of trimeric hinge formation. This effect is caused by increase of boarding maintenance force with increase of deflection. Besides longitudinal forces plays more evident part. Let us view rib branch deformation after kinematic variable mechanism in “beyond-extreme” condition. We consider that rib branch destruction area is known and defined by distance between two external non-stationary hinges in longitudinal direction and double space in transverse direction in accordance with [3]. Also consider destructed units are rigid.

Taking into account that destruction area dimensions are known to define longitudinal force we use method linked with conventional division into rigid and flexible ties, in accordance with [1]. That leads to thrust rib branch rigidity characteristic expressed in rib thrust coefficient $Kp_{ш}$. For that matter in formula (8) interchange l_1 and b_1.

Having construction thrust rigidity it is easy to describe destructed units deformation process. Compile system of deformation equilibrium and compatibility equations for rib destructed units:

$$\frac{P}{2} - \int_0^l r(x)dx = 0\,, \tag{9}$$

$$P \cdot l - T \cdot f - 2M_0(T) - M(r) = 0\,, \tag{10}$$

$$u_f - u_{упр} - u_{пл} = \Delta_{расп}\,, \tag{11}$$

where:

$\int_0^l r(x)dx$ – sum of foundation reaction acting on destructed unit;

$M(r)$ – reaction force moment relative to beam point where crosscutting force equals null;

$u_f = \frac{1}{2}\int_0^l (w'(x))^2 dx$ – beam end bearings rapprochement with the assumption of beam axis non-tensility;

$u_{упр} = \frac{T \cdot l}{F_{ш} \cdot E}$ – beam axis elastic lengthening;

$u_{пл} = \sum \theta_i \frac{\partial M(T)}{\partial T}$ – beam axis plastic lengthening in plastic hinges;

$\Delta_{р.ш} = \frac{T \cdot l}{F_{р.ш} \cdot E}$ – hold-down beam shortening;

$Kp_{ш} = \frac{F_р}{F_р + F_{ш}}$ – rib thrusting coefficient.

Solving this equation system we obtain “force-deflection” dependence. It should be noted that with outside load increase plastic hinge moves toward the force and leaves plastic deformation area behind (Figure 2). Thus if outside non-stationary plastic hinge is in 1 position while increasing outside force P plastic hinge will move to 2, 3, 4 positions and so on. Consistent increase of P load leads to foundation reaction increase

and rise of longitudinal force T to its limiting value T_0. After that theoretically beam becomes a plastic string. Scheme of beam destructed unit movement with consistent outside load increase is represented on Figure 4.

Rib destructed unit deflection calculation results are represented on Figure 5. Calculations were made taking into consideration longitudinal forces T up to reaching limiting value.

Taking into consideration covering rigidity influence on rib bearing strength we can refine side stringer elasto-plastic foundation characteristics. That allows to describe locally loaded stringer deformation characteristics more accurate. Approximating rib "force-deflection" curve (Figure 2) with linear functions we find refined side stringer elasto-plastic foundation characteristics. Which model represents an infinite beam lying on elasto-plastic foundation with linear variable rigidity characteristics [3].

According to [3] stringer deformation process can be divided into stages. Changing from one stage to another is carried out in accordance with "momentary plastic hinge opening" hypothesis. On each stage we have system of deformation equilibrium and compatibility equations. After appearance of outside non-stationary plastic hinges it is necessary taking into account longitudinal forces while load increasing.

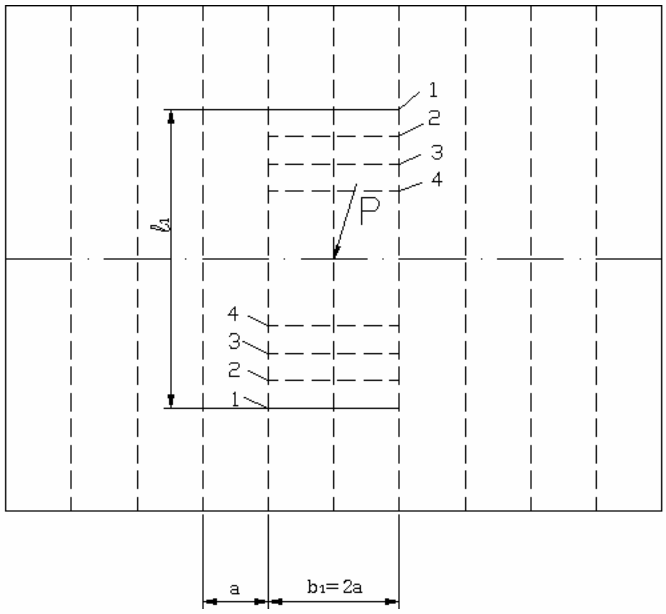

Fig. 2. Covering destruction area transformation scheme

It should be noted that with a load increase simultaneous movement of plastic hinges in ribs and in stringers that leads to stringer thrust coefficient continuously change.

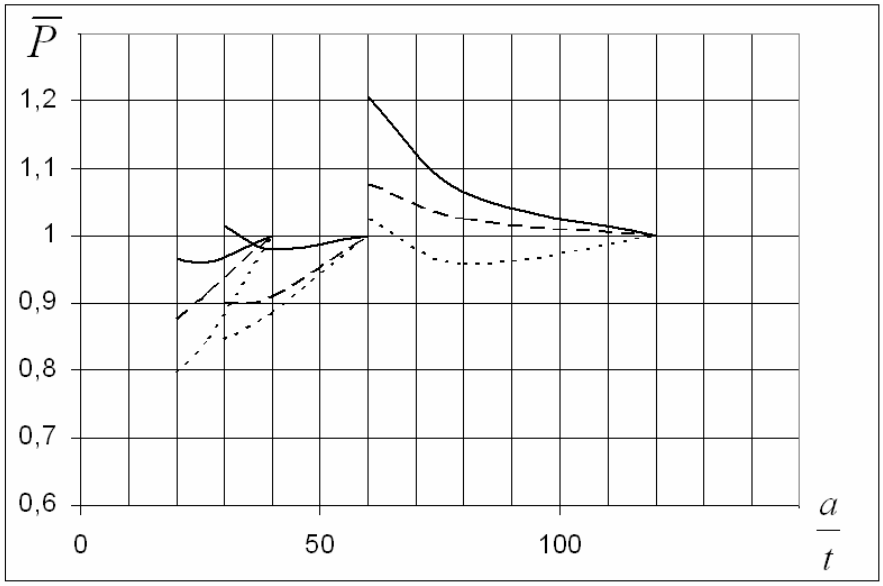

Fig. 3. Beam bearing strength change depending on plate rigidity

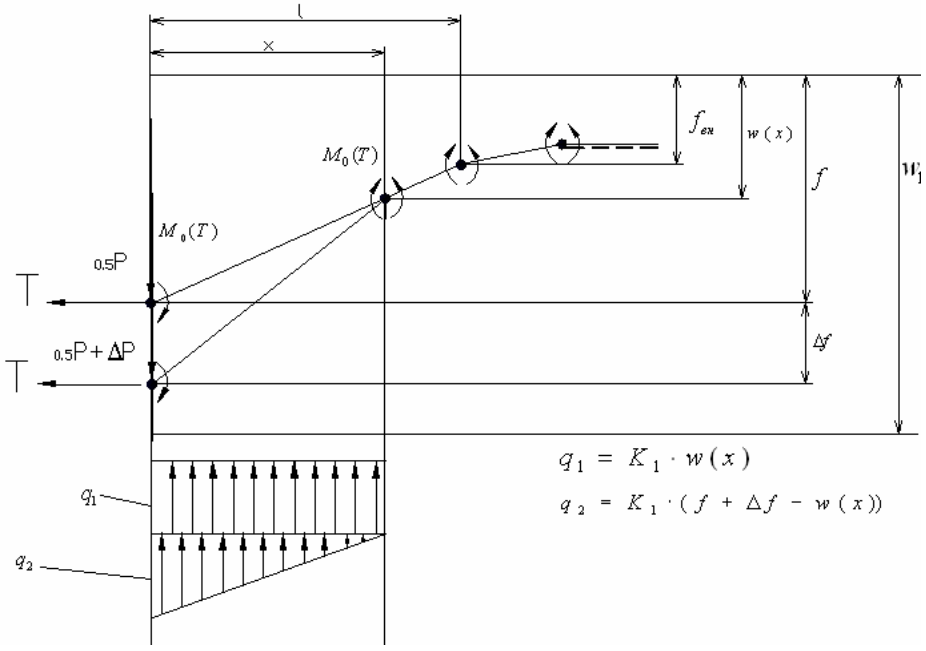

Fig. 4. Rib destructed unit deformation scheme and foundation reaction distribution scheme in first stage of deformation

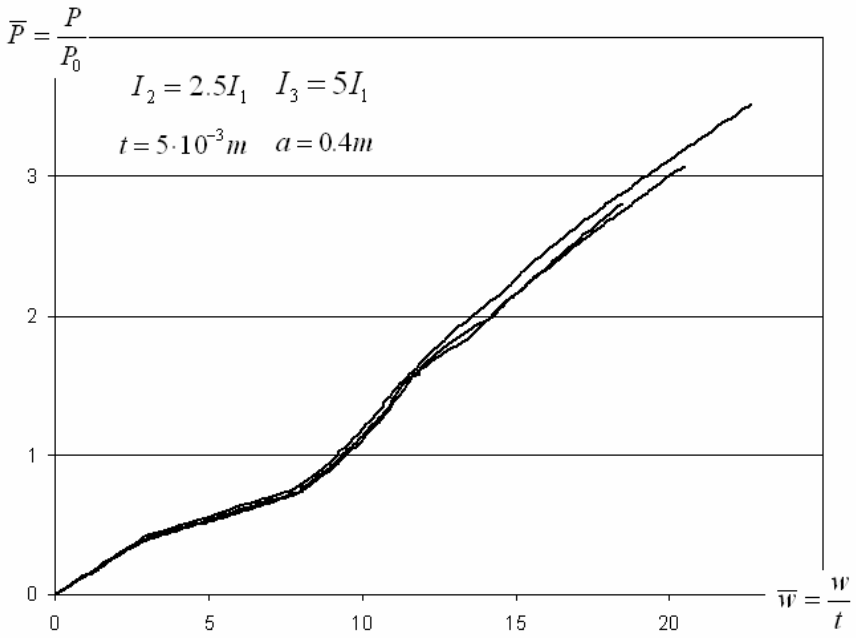

Fig. 5. Destructed unit deflection change depending on its rigidity with constant space

Obtained solutions allow to define locally loaded board covering deformation character, find extra solidity reserves, lower steel intensity, choose dimensions and find optimum scheme of board covering tie arrangement according to balanced life criterion. Therefore designing ship hull lighter and economically preferable at the same time without lowering its reliability is allowed.

References

[1] Бураковский Е.П.: *Совершенствование нормирования параметров эксплуатационных дефектов корпусов судов*, –Калининград, КГТУ, 2005, pp. 339c.

[2] Папкович П.Ф.: *Труды по строительной механике корабля т. 1*. –Л.: Судпромгиз, 1962, pp. 576c.

[3] Бураковский П.Е.: *Изгиб упруго- пластических балок, лежащих на основании с характеристиками прандтлевского типа с линейным упрочнением*, Труды научной конференции «Инновации в науке и образовании, 2006, ч. 2.

[4] Бураковский П.Е.: *Исследование поведения локально загруженных шпангоутов в запредельном состоянии*, Труды научной конференции «Инновации в науке и образовании, 2006, ч. 2.

Projektowanie mocnicy burtowej w przypadku dużego obciążenia miejscowego

Referat jest poświęcony rozwijaniu zaawansowanych metod projektowania mocnicy burtowej poddanej obciążeniom miejscowym, na podstawie oceny obciążenia. Pokazano, że po uwzględnieniu zmiany sztywności płyty zmienia się znacznie nie tylko charakter odkształcenia wzdłużnicy pokładowej, ale również jej jakościowa charakterystyka wytrzymałości na obciążenia.

ARCHIVES OF CIVIL AND MECHANICAL ENGINEERING

Vol. VII 2007 No. 3

To the question of navigation safety at ship collisions

E. BURAKOVSKIY, V. DMITROVSKIY, I. JAKUTA
Kaliningrad state technical university, Sovetski prospect 1, 236000 Kaliningrad

A great number of papers dedicated to ships collision on. The basic difficulty is a complex probable nature of this phenomenon on the one hand and considerable influence of the human factor (difficult to be formalized by mathematical methods) on the other. This paper suggests one of such models, simplified to a great extent. It doesn't, for example, describe dangerous situations when ships are going in one direction overtaking each other. Its practical importance is the matter to be discussed. But in any case the authors think that its getting more precise and complicated will give an impetus to a new approach to the problem. It will make possible to avoid subjectiveness and mistakes in the future at forecasting catastrophes.

Keywords: *navigation safety, mathematical model, ship collisions*

Collisions of vessels are one of the most wide spread and heavy types of damages, occurred on the sea. For a perennial period a share of collisions in general amount of emergency navigational events forms 29.6%. As for as losses are concerned this type of navigational damages enjoys the position no. 1 [1–5].

A great number of papers dedicated to ships collision appear on late. One version of mathematical model of ship collision is presented in this article. The basic difficulty is a complex probable nature of this phenomenon on the one hand and considerable influence of the human factor (difficult to be formalized by mathematical methods) on the other.

This paper suggests one of such models, simplified to a great extent. It doesn't, for example, describe dangerous situations when ships are going in one direction overtaking each other. Its practical importance is the matter to be discussed. But in any case the authors think that it's getting more precise and complicated will give an impetus to a new approach to the problem. It will make possible to avoid subjectiveness and mistakes in the future at forecasting catastrophes.

The whole analysis will be carried out from the point of view of one vessel which we'll call for simplicity ours, or our vessel. All the other ships we shall call opposing, i.e. the influence of all the other ships going in the same direction with us upon the situation is ignored.

Let us suggest that all the ships (ours and opposing) move in parallel courses in such a way, that their centres are always within a limited corridor (the sides may extend beyond its borders). We shall designate half of the corridor breadth – K. The mean number of opposing ships in the corridor at the distance of one mile we'll designate Δ.

For the sake of simplicity we'll call half the breadth of our vessel *W*. Trough in reality it is a half breadth of dangerous ships closing due to the "sucking" effect (in practice it is approximately 3 times half-breadth of ship's hull). *V* is the speed of our vessel. Random half-breadth of opposite ships we shall designate ω, and their random speed v. We'll introduce a movable coordinates system, the beginning of which is always in the middle of the corridor, *y*-axis is oriented towards our ship's movement. But the beginning of the coordinates system is being shifted together with our ship in such a way that its coordinate $y_0 = 0$. *X*-axis is our ship's coordinate, x_0 is known and constant. Random coordinate x of an opposite vessel we'll designate ξ.

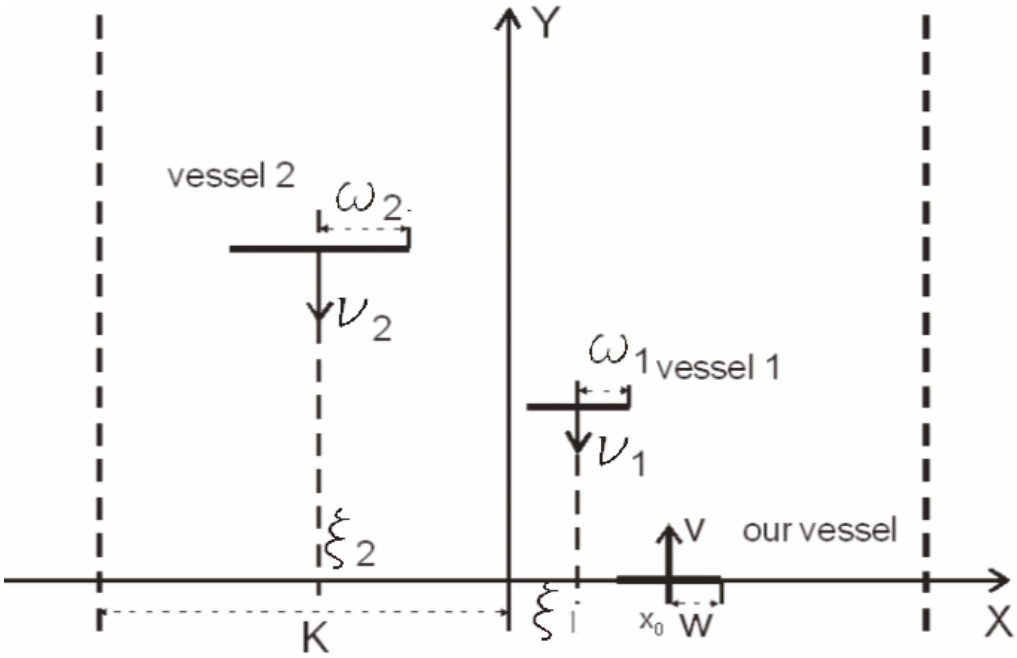

Fig. 1. Schema of ship moving without manoeuvring

The following table gives the summary of all random values, describing opposite vessels and their characteristics.

Table. Summary of the random values, describing opposite vessels

Random value	Designation	Distribution function	Distribution thickness	Mathematical anticipation
X-coordinate	ξ	F_ξ	f_ξ	Ξ
Speed	v	F_v	f_v	N
Breadth	ω	F_ω	f_ω	Ω
Distance at detection	ρ	F_ρ	f_ρ	P

By collision we'll understand segments overlapping of these two ships when the opposing vessel crosses *x*-axis, i.e. situation when $|\xi - x_0| \le W + \omega$.

It is vital to discuss the task in the simplest definition, when the collision danger is being ignored, i.e. no attempts are made to avoid it. Naturally such definition will unavoidable bring about collision, but currently we are being interested in its probability for some quite limited period of time. Further, by making the model more complicated, we'll try to take into account the manoeuvring attempts to avoid collision.

The moments when the opposing vessels cross *x*-axis form the Poisson flow with the intensiveness $\Lambda(V+N)$. All the random values, describing the situation, are independent in statistical population.

The probability of our vessel's collision with one of the opposing when it crosses *x*-axis in the above mentioned definition equals:

$$P_1(x_0) = \int_0^{\infty} f_{\omega}(w) \int_{x_0-(W+w)}^{x_0+W+w} f_{\xi}(x)\,dx\,dw. \tag{1}$$

Note that the broader the vessel the greater the probability. We'll designate

$$\overline{P_1}(x_0) = 1 - P_1(x_0). \tag{2}$$

The probability that during the period of time [0, T] equals k, k = 0, 1, 2… of opposing vessels will cross *x*-axis equals

$$\frac{(\Lambda T(V+N))^k}{k!} e^{-\Lambda T(V+N)}. \tag{3}$$

So, the probability of no collision within period of time [0, T] in this definition according to the full probability formula equals

$$\overline{P_{\infty}}(x_0, V, N, \Lambda, T) = e^{-\Lambda T(V+N)} \sum_{k=0}^{\infty} \frac{\left(\Lambda T(V+N)\overline{P_1}(x_0)\right)^k}{k!} = \exp\left\{-\Lambda T(V+N)P_1(x_0)\right\}. \tag{4}$$

And probability that such collision will occur, equals correspondingly

$$P_{\infty}(x_0, V, N, \Lambda, T) = 1 - \overline{P_{\infty}}(x_0, V, N, \Lambda, T). \tag{5}$$

Taking into account that we are interested in probabilities values $\overline{P_{\infty}}(x_0, V, N, \Lambda, T)$ close to 1, formulas (4) and (5) with a mistake to a safer side may be substituted by

$$\overline{P_\infty}(x_0, V, N, \Lambda, T) = 1 - \Lambda T(V + N) P_1(x_0), \tag{6}$$

$$P_\infty(x_0, V, N, \Lambda, T) = \Lambda T(V + N) P_1(x_0). \tag{7}$$

Let's make the model more complicated by taking into consideration attempts to avoid collision by means of manoeuvring.

Let's suppose that our vessel detects opposing one at random distance ρ, after which both vessels start manoeuvring, trying to avoid collision. In this situation we have no right to suggest independence of ρ, ξ, ω and v. So we suppose that we known probability $P_0(x_0, V_0, r, x, w, v)$ of our vessel's avoiding collision with the opposing one at the condition that we detected it at the r distance, its X coordinate equals x, its breadth – w, speed – v. Our vessel's speed is equal to V.

Note, that at $|x - x_0| > W + w$ this probability equals 1 independently of other parameter values, because no manoeuvring is necessary in this situation to avoid collision.

In this case the obtained probability $P_1(W, x_0)$ is getting less

$$P_1(V, x_0) = \int_0^\infty f_v(v) \left(\int_0^\infty f_\rho(r) \left(\int_0^\infty f_\omega(w) \left(\int_{x_0 - (W+w)}^{x_0 + W + w} P(V, r, x, w, v) f_\xi(x) dx \right) dw \right) dr \right) dv. \tag{8}$$

The probability of no collision within period $[0, T]$

$$\overline{P_\infty}(x_0, V, N, \Lambda, T) = \exp\{-\Lambda T(V + N) P_1(V, x_0)\}, \tag{9}$$

is getting larger correspondingly.

For the practical use of the obtained result it is necessary to make more specific distributions being involved in the model.

At first we shall discuss a degenerate example when the breadths of all opposing vessels are equal to 2Ω. Through such model may sum to have no practical interest, but as a matter of fact its analysis helps to facilitate understanding the behaviour laws of more complex models. Moreover it will turn out that in a typical case when K is much greater then W and Ω it gives the same result as the more complex models.

For this model formula (1) is expressed

$$P_1(x_0) = \int_{x_0 - (W + \Omega)}^{x_0 + W + \Omega} f_\xi(x) dx, \tag{10}$$

and probability $\overline{P_1}(x_0)$ will take the form

$$\overline{P_1}(x_0) = 1 - \int_{x_0-(W+\Omega)}^{x_0+W+\Omega} f_\xi(x)dx = \int_{-K}^{x_0-(W+\Omega)} f_\xi(x)dx + \int_{x_0+(W+\Omega)}^{K} f_\xi(x)dx\,. \tag{11}$$

The first integral of this formula is equal to probability to pass the opposing vessel by the port, and the second one- by the starboard.

Taking into account that $f_\xi(x) = 0$ at $x < -K$ and $x > K$, the final formulas for this probability depend on relations between K, W and x_0:

$$\overline{P_1}(\Omega, W, x_0) = \begin{cases} \int_{x_0+(W+\Omega)}^{K} f_\xi(x)dx, & -K \le x_0 \le -K+W+\Omega \\ \int_{-K}^{x_0-(W+\Omega)} f_\xi(x)dx + \int_{x_0+(W+\Omega)}^{K} f_\xi(x)dx, & -K+W+\Omega < x_0 < K-W-\Omega \\ \int_{-K}^{x_0-(W+\Omega)} f_\xi(x)dx, & K-W-\Omega \le x_0 \le K \end{cases} \tag{12}$$

The loss of integrals close to the corridor sides is easily accounted for by the following figure:

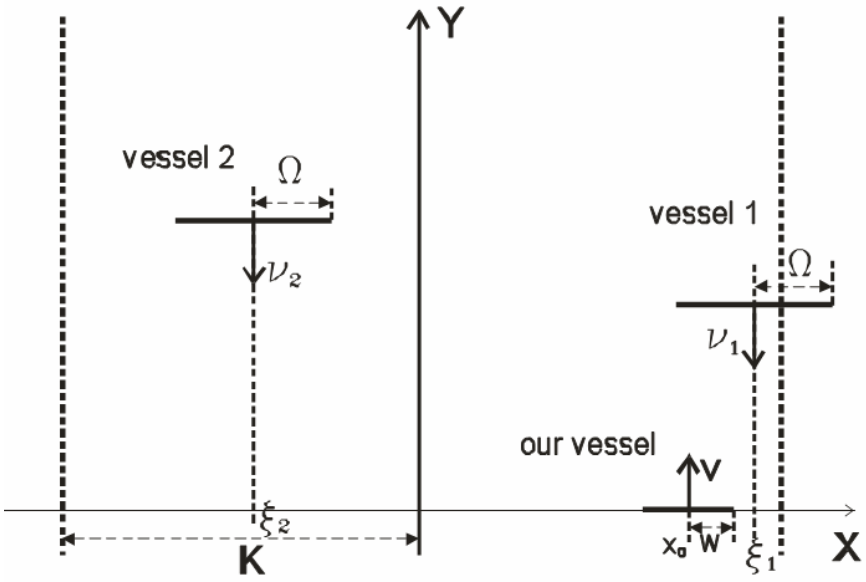

Fig. 2. Mathematical schema of ship manoeuvring

Here $K - W - \Omega < x_0 > K$, and opposing vessels can not pass our vessel by starboard, so formula (10) possesses the only integral, equal to probability to pass our vessel safely by on our port. The analogues probabilities behaviour is observed in even more complex models.

In a particular case of equal distribution of opposing vessel by the corridor breadth, i.e.

$$f_{\xi}(x) = \begin{cases} 1/2K, & |x| < K \\ 0, & |x| \geq K \end{cases}. \tag{13}$$

The formula (10) is simplified:

$$\overline{P_1}(\Omega, W, x_0) = \begin{cases} \left(K + |x_0| - W - \Omega\right)/2K, & K - W - \Omega \leq |x_0| \leq K \\ \left(K - W - \Omega\right)/K, & |x_0| < K - W - \Omega \end{cases}. \tag{14}$$

Let opposing vessels breadth have the gamma-distribution:

$$f_{\omega,a,b}(w) = \frac{b^a}{\Gamma(a)} w^{a-1} e^{-bw}, \qquad w \geq 0, \tag{15}$$

where:

$\Gamma(a)$ – gamma-function:

$$\Gamma(a) = \int_0^{\infty} x^{a-1} e^{-x} dx. \tag{16}$$

The physical meaning of a and b parameters is that $\Omega = ab^{-1}$, and opposing vessels breadth dispersion equals ab^{-2}. For simplicity we again suggest that opposing vessels are evenly spread along the corridor breadth, i.e. $f_{\xi}(x)$ is defined by formula (12).

Since the model is symmetrical against y-axis, then $P_1(-x_0) = P_1(x_0)$, and it is sufficient to find these probabilities only for non-negative x_0.

Taking into account that W is much less than K, we'll get:

$$\overline{P_1}(x_0) = 1 - \frac{b^a}{\Gamma(a)} \int_0^{\infty} w^{a-1} e^{-bw} \left(\int_{-(W+w)}^{W+w} f_{\xi}(x - x_0) dx \right) dw =$$

$$1 - \frac{b^a}{2K\Gamma(a)} \int_0^{\infty} w^{a-1} e^{-bw} \min\left(K + x_0, W + w\right) dw -$$

$$\frac{b^a}{2K\Gamma(a)}\int_0^{\infty} w^{a-1}e^{-bw}\min(K-x_0,W+w)dw=$$

$$\frac{b^a}{2K\Gamma(a)}\int_0^{\infty} w^{a-1}e^{-bw}\left(K+x_0-\min(K-x_0,W+w)\right)dw+$$
$$\frac{b^a}{2K\Gamma(a)}\int_0^{\infty} w^{a-1}e^{-bw}\left(K-x_0-\min(K-x_0,W+w)\right)dw=$$
$$\frac{b^a}{2K\Gamma(a)}\int_0^{\infty} w^{a-1}e^{-bw}\max(0,K+x_0-W-w)dw+$$

$$\frac{b^a}{2K\Gamma(a)}\int_0^{\infty} w^{a-1}e^{-bw}\max(0,K-x_0-W-w)dw= \qquad (17)$$
$$\frac{b^a}{2K\Gamma(a)}\left(\begin{array}{l}\int\limits_0^{K+x_0-W} w^{a-1}e^{-bw}\left(K+x_0-W-w\right)dw+\\ \int\limits_0^{\max(0,K-x_0-W)} w^{a-1}e^{-bw}\left(K-x_0-W-w\right)dw\end{array}\right)$$

The first integral of this formula corresponds to probability to pass the opposing vessel by port, and the second one by starboard. The final formulas for these probabilities depend on relations between K, W and x_0.

At $x_0 < K - W$ we get

$$\overline{P_1}(x_0)=\frac{b^a\left(K+x_0-W\right)}{2K\Gamma(a)}\int_0^{K+x_0-W} w^{a-1}e^{-bw}dw-\frac{b^a}{2K\Gamma(a)}\int_0^{K+x_0-W} w^{a}e^{-bw}dw+$$
$$\frac{b^a\left(K-x_0-W\right)}{2K\Gamma(a)}\int_0^{K-x_0-W} w^{a-1}e^{-bw}dw-\frac{b^a}{2K\Gamma(a)}\int_0^{K-x_0-W} w^{a}e^{-bw}dw=$$
$$\frac{\left(K+x_0-W\right)\Gamma\left(a,b\left(K+x_0-W\right)\right)}{2K\Gamma(a)}-\frac{\Gamma\left(a+1,b\left(K+x_0-W\right)\right)}{2bK\Gamma(a)}+$$
$$\frac{\left(K-x_0-W\right)\Gamma\left(a,b\left(K-x_0-W\right)\right)}{2K\Gamma(a)}-\frac{\Gamma\left(a+1,b\left(K-x_0-W\right)\right)}{2bK\Gamma(a)}=$$

$$\begin{aligned}&(2K\Gamma(a))^{-1}\left((K+x_0-W-ab^{-1})\Gamma(a,b(K+x_0-W))+b^{a-1}(K+x_0-W)^a e^{-b(K+x_0-W)}\right)+\\&(2K\Gamma(a))^{-1}\left((K-x_0-W-ab^{-1})\Gamma(a,b(K-x_0-W))+b^{a-1}(K-x_0-W)^a e^{-b(K-x_0-W)}\right)=\\&(2K\Gamma(a))^{-1}\left((K+x_0-W-\Omega)\Gamma(a,b(K+x_0-W))+b^{a-1}(K+x_0-W)^a e^{-b(K+x_0-W)}\right)+\\&(2K\Gamma(a))^{-1}\left((K-x_0-W-\Omega)\Gamma(a,b(K-x_0-W))+b^{a-1}(K-x_0-W)^a e^{-b(K-x_0-W)}\right)\end{aligned} \quad (18)$$

where:

$\Gamma(a, x)$ – is a not-full gamma-function.

$$\Gamma(a,y)=\int_0^y x^{-1}e^{-x}dx\,. \quad (19)$$

At $x_o = 0$ this formula is simplified:

$$\begin{aligned}&\overline{P_1}(0)=(K\Gamma(a))^{-1}\left((K-W)\Gamma(a,b(K-W))-b^{-1}\Gamma(a+1,b(K-W))\right)=\\&(K\Gamma(a))^{-1}\left((K-W-\Omega)\Gamma(a,b(K-W))+b^{a-1}(K-W)^a e^{-b(K-W)}\right)\end{aligned}\,. \quad (20)$$

At $K - W \le x \le K$ the second integral in the formula for probabilities is equal to 0, since at $x_0 = K - W$ our vessel touches the corridor border by the starboard, after which passing the opposite vessel is possible by port only. So

$$\begin{aligned}&\overline{P_1}(W,x_0)=(2K\Gamma(a))^{-1}\left((K+x_0-W)\Gamma(a,b(K+x_0-W))-\Gamma(a+1,b(K+x_0-W))\right)=\\&(2K\Gamma(a))^{-1}\left((K+x_0-W-\Omega)\Gamma(a,b(K+x_0-W))+b^{a-1}(K+x_0-W)^a e^{-b(K+x_0-W)}\right)\end{aligned} \quad (21)$$

The described model, in spite of its simplicity, is flexible enough and allows to adjust it very precisely to the statistic characteristics of some definite flow of vessels. If we know the values of mathematical expectation M and dispersion D of half-breadth of vessels on some definite route, we may provide exact equation of corresponding model parameters to them by varying parameters a and b if we resolve the simple equations systems:

$$\begin{cases}ab^{-1}=M\\ab^{-2}=D\end{cases}, \quad (22)$$

which gives us

$$\begin{cases}a=M^2/D\\b=M/D\end{cases}. \quad (23)$$

Suppose, we discuss two routs, where mean values of vessel's half- breadth are equal – 20 meters. On the first rout these half- breadth have a very big spread (D = 9) and in the second-they are practically the same (D = 1). The following two graphs of gamma-distribution thickness of vessels half-breadth for these routs illustrate how the model may be formed in these cases:

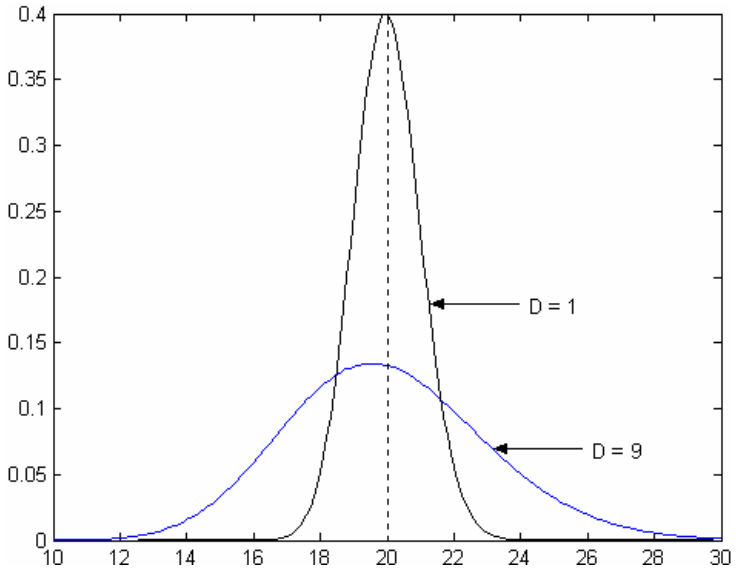

Fig. 3. Result of illustration of mathematical model

Let's have a look at how these probabilities behave in the following example.
Suppose
$K = 5 \cdot$ *miles* $= 9260 \cdot$ *meters*,
$T = 1 \cdot$ *hour*,
$\Lambda = 3 \cdot$ *mile*$^{-1} = 3/1852 \cdot$ *meter*$^{-1}$,
$N = 14 \cdot$ *knots*,
$a = 16$,
$b = 4/3 \cdot$ *meter*$^{-1}$,
$V = 12 \cdot$ *knots*,
$W = 10 \cdot$ *meters*,
$x_0 = 0$,
i.e. corridor breadth is equal to 10 miles, our vessel follow the middle of the corridor with 12 knots speed, and its breadth – 20m. Opposite to us move the vessels with the mean speed of 14 knots, their mean breadth $2\Omega = 2a/b = 24$ meter, random breadth are in general within 10 to 40 m. On average there are 3 vessels in the corridor within 1 mile length. Our subject of interest is probability to avoid collision for an hour on the condition, that all the vessels take no effort to avoid collision.

In this case according to formulas (4) and (21)

$$\overline{P_1}(0) = (K\Gamma(a))^{-1}\left((K-W-\Omega)\Gamma(a, b(K-W)) + b^{a-1}(K-W)^a e^{-b(K-W)}\right) =$$
$$\frac{(9260м - 10м - 12м)\Gamma\left(16,4/3м^{-1} \times (9260м - 10м)\right) - \left(4м^{-1}/3\right)^{15} \times (9260м - 10м)^{16} \times e^{-(9260м-10м)\left(4м^{-1}/3\right)}}{9260м \times \Gamma(16)} \approx$$
$$\frac{9238 \times \Gamma(16,37000/3)}{9260 \times \Gamma(16)} \approx \frac{9238}{9260} \approx 0.99762419,$$
$$P_1(0) = 0,00237581,$$

Approximated equalities here are as a matter of fact very precise- calculating abilities of the modern computers do not afford to discriminate $\overline{P_1}(0)$ and $\frac{9238}{9260}$. And, finally,

$$\overline{P_\infty}(x_0, V, N, \Lambda, T) = \overline{P_\infty}(0,3,14,3,1) = \exp\{-3 \cdot 1 \cdot (12+14)P_1(0)\} = \exp\{-78 \cdot P_1(0)\} \approx$$
$$\exp\{-0.18531318\} \approx 0.830844$$

We emphasize that such low probability of our vessel's "survival" is accounted for by the lack of vessel's steering.

It is to be noted that "monobreadth" model, according to formula (14) gives in this situation the same result:

$$\overline{P_1}(10,0) = (K - W - \Omega)/K = \frac{9238}{9260},$$

since K (9260 meters) is much more than w (10 m) and Ω (12 meters). If these parameters could be compared to each other, the influence of breadth scatter of opposite vessels on $\overline{P_1}(0)$ l of not steered vessels would have lost all the meaning- the probability of $\overline{P_\infty}(x_0, V, N, \Lambda, T)$ would be close to zero, through it would differ by times for "monobreadth" and gamma models.

The analysis of the suggested models shows that at comparatively general suppositions as to the character of opposite vessels' flow, we can get simple formulas, describing probabilities of wreck-free floating.

Numerical example showed that even a very short period of time and at low intensity of opposite vessels flow the collision probability of "non-managed" model is very high. But it also allowed to make a supposition that in a typical situation when K is much greater then W and Ω, in a "managed" model it will be possible to be limited by its "monobreadth" variant, which will simplify all the calculations. Whether this hypothesis will prove to be true remains to be showed by further analysis.

References

[1] Yudovich A.B.: *Prevention of navigational damages of sea counts*, M.: Transport, 1988.
[2] Gluder H., Olsen D.: *Current practice in risk analysis of ship collisions to bridges*, [in:] Gluder H., Olsen D.: *Editors, Ship collision analysis*, Rotterdam, Balkena, 1999.
[3] Petersen M.J., Pedersen P.T.: *Collisions between ships and offshore platforms*, Offshore Technology, Conference, Houston, USA, 1981.
[4] Petersen M.J.: *Dynamics of ship collisions*, Ocean Engineering, Vol. 9, 4, 1982, pp. 295–329.
[5] Sven O., Pedersen P.T., Samuelides M.: *Elements of risk analysis for collision and grounding of a RO-RO passenger ferry*, Marine Structures, Vol. 15, No. 4–5, July–October, 2002, pp. 461–474.

Zagadnienie bezpieczeństwa nawigacji w przypadku kolizji statków

W ostatnim czasie pojawia się wiele artykułów poświęconych kolizjom statków. W niniejszym referacie prezentowany jest model matematyczny opisujący kolizję statków. Zasadniczą trudnością jest, z jednej strony, złożony charakter tego zjawiska, a z drugiej strony, znaczny wpływ czynnika ludzkiego, który trudno opisać metodami matematycznymi. W referacie proponowany jest pierwszy taki model. Jest on w dużym stopniu uproszczony i nie opisuje, na przykład, niebezpiecznych sytuacji, gdy statki wyprzedzają się płynąc w jednym kierunku. Omówiona została kwestia praktycznej użyteczności opisanego modelu. Zdaniem autorów, rozszerzenie zakresu i zwiększenie dokładności modelu zainicjuje nowe podejście do zagadnienia. W przyszłości będzie możliwe uniknięcie subiektywizmu i błędów przy przewidywaniu katastrof.

ARCHIVES OF CIVIL AND MECHANICAL ENGINEERING

Vol. VII 2007 No. 3

A methodology for evaluating the controllability of a ship navigating in a restricted channel

K. ELOOT
Flanders Hydraulics Research (FHR), Flemish Government, Antwerp, Belgium

J. VERWILLIGEN, M. VANTORRE
Maritime Technology Division, Ghent University, Ghent, Belgium

A methodology is presented for evaluating the controllability of a ship navigating in a restricted channel by means of a hydrodynamic force analysis. This method is applied to assess the controllability of a container vessel in straight channel reaches and in bends in two practical cases. By comparing different initial conditions and bottom configurations the influence of different ship characteristics (main dimensions, draft, rudder and propeller characteristics), operational parameters (such as speed, propeller commands, and bank clearance), environmental parameters (such as current and tidal level), and channel characteristics (water depth, bank slope, bend radius) on this controllability can be evaluated. For estimating the components of the force analysis, use is made of results of captive model tests in shallow and restricted waters.

Keywords: *Controllability of a ship, bank effects, structural and operational measures*

Notations

A_{RT}: [m^2] – lateral rudder area,
C_{YR}: – non-dimensional lateral rudder force
C_{Th}: – thrust loading coefficient:

$$C_{Th} = \frac{T_P}{\frac{1}{8}\rho\pi D_P^2 u_A^2}$$

D_P: [m] –propeller diameter
Fr: – ship length related Froude number
Fr_h: – water depth related Froude number
h: H [m] – water depth at the ship
h_1: [m] – water depth outside waterway
h_{eff}: [m] – effective water depth
k_m: – propeller race contraction factor
L: [m] – ship length
L_{PP}: [m] – ship length between perpendiculars
m: [kg] – ship mass
n: [rpm] – propeller rate
$n_{\max}$: [rpm] – reference propeller rate
N_{ur}: – hydrodynamic coefficient
N_R: [Nm] – yawing moment generated by the rudder
N_C: [Nm] – moment generated by current
R: [m] – bend radius
T: [m] – draft

T_P: [N] – propeller thrust
u: [m/s] – longitudinal ship speed
u_A: [m/s] – advance speed at the propeller
u_R: [m/s] – average inflow velocity at the rudder
V_C: [m/s] – current velocity
V_T: [m/s] – reference speed in the propeller race

$$V_T = \sqrt{\left|\frac{8T_P}{\rho\pi D_p^2}\right|}$$

w: – wake fraction
x_G: [m] – longitudinal position of the centre of gravity
y_B: [m] – bank clearance
Y_R: [N] – lateral rudder force
z_m: [m] – mean sinkage
β_{ik}: – bank effect coefficients
ρ: [kg/m³] – water density

1. Introduction

Manoeuvring simulation, either controlled by an autopilot (fast time) or by a human operator (real time), is an approved tool for evaluating the feasibility and safety of ship manoeuvres and transits. In both control modes, the characteristics and quality of the controller may considerably affect the results and conclusions of the simulation study. On the other hand, regardless of the control system, it is impossible to keep the ship under control if the available control forces generated by the rudder are exceeded by the forces disturbing the ship (e.g. bank effects, current) or required to perform a given trajectory (e.g. bends). Due to inertia, a temporary unbalance (e.g. due to wind gusts, meetings, …) may be acceptable in particular cases, but a permanent exceeding of the control forces inevitably results into an uncontrollable ship.

In order to evaluate the inherent safety of a considered manoeuvre, a methodology can be used for comparing the available control forces with the forces that have to be counteracted. This hydrodynamic force analysis will only take yawing moments into consideration. This methodology can be applied to determine operational limits, to investigate the sensitivity of ship controllability with respect to parameter variations, and to compare existing situations to new conditions.

With respect to parameter variations, generally a large number of parameters affecting a manoeuvre can be identified. In the case of a ship taking a bend in a river with longitudinal current, following non-exhaustive distinction can be made:

- ship dependent characteristics such as draft, geometric dimensions (scale factor), and manoeuvring behaviour;
- environmental parameters such as water depth variations, current and tide;
- channel characteristics such as bank geometry, water depth and bend radius;
- operational parameters such as propeller rate, ship speed and bank clearance.

In this paper two situations will be considered based on practical case studies. Firstly, a ship navigating in a canal, following a straight course parallel to the centre line will be considered, which is typically the case in a two-way traffic situation. As a second example, the force balance for a ship taking a bend to starboard on an eccentric course on a river will be investigated.

2. Hydrodynamic Forces

2.1. Control forces

If external forces (e.g. exerted by tugs) are not taken into account, the available control forces are supplied by the rudder. If available, a full mathematical manoeuvring simulation model for the considered vessel can be used; however, a first approximation can be obtained by using following formula for the lateral force Y_R and the yawing moment N_R at the rudder:

$$Y_R = \frac{1}{2} \rho C_{YR} u_R^2 A_{RT} , \tag{1}$$

$$N_R = -\frac{L_{pp}}{2} Y_R . \tag{2}$$

The flow at the rudder is visualised in Figure 1 and depends particularly on the forward ship speed u and the thrust loading coefficient C_{Th}.

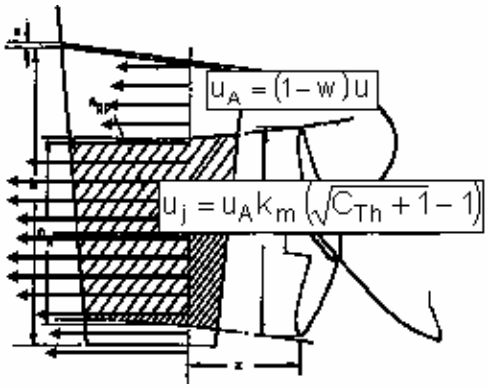

Fig. 1. Flow at the rudder

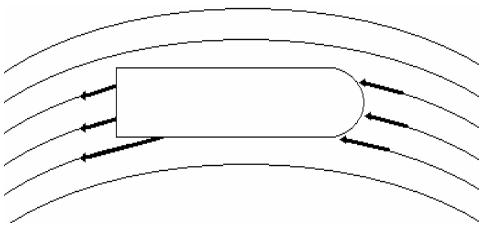

Fig. 2. Yawing moment caused by the curvature of the streamlines of the longitudinal current

2.2. Curvature of the current

The current in a bend is assumed to follow the curvature of the waterway. Consequently, a ship taking a bend will be subject to a yawing moment N_C caused by the different flow orientation at the stern and the bow (Figure 2), that can be calculated by means of:

$$N_C = \left(N_{ur} - mx_G\right) u \frac{V_C}{R} . \tag{3}$$

N_{ur} being the linear yaw velocity hydrodynamic coefficient for the yaw moment, which depends on the water depth to draft ratio. When a ship takes a bend to starboard the current will cause a yaw moment to port side when the when the ship is sailing upstream.

2.3. Bank effects

In general, a ship following a course parallel to a bank will be subject to a lateral force towards the nearest bank, and a yawing moment that tends to turn the ship towards the centre line of the waterway.

This effect is caused by an asymmetric flow due to the ship speed and the action of the propeller. If the flow due to ship speed is isolated, however, the lateral force may be repulsive if the under keel clearance is very small (e.g. 10% of draft). The yawing moment, on the other hand, always acts in the same sense, but is also very sensitive to water depth changes. Propeller action always causes a lateral force aft acting towards the bank.

Because the yawing moment generated by the bank always acts towards the centre of the waterway, and a ship normally sails at the starboard side of this waterway, the bank will hinder a bend to starboard.

For the estimation of the yawing moment induced by a bank, a regression model described in [1] has been applied. The yawing moment N_{bank} is subdivided into three contributions: $N^{(H)}$ due to the ship speed (pure towing condition), $N^{(P)}$ due to the propeller loading (bollard pull condition), and $N^{(HP)}$ due to a combination of ship speed and propeller loading:

$$N^{(H)} = \frac{1}{2}\rho L^2 T u^2 \sum_{i=1}^{2} \sum_{k=0}^{2} \beta_{ik}^{(H)} y_B^i \left(\frac{T}{h_{eff} - T} \right)^k , \tag{4}$$

$$N^{(P)} = \frac{1}{2}\rho L^2 T V_T^2 \sum_{i=1}^{2} \sum_{k=0}^{2} \beta_{ik}^{(P)} y_B^i \left(\frac{T}{h_{eff} - T} \right)^k , \tag{5}$$

$$N^{(HP)} = \frac{1}{2}\rho L^2 T V_T^2 Fr \sum_{i=1}^{2} \sum_{k=0}^{2} \beta_{ik}^{(HP)} y_B^i \left(\frac{T}{h_{eff} - T} \right)^k . \tag{6}$$

The effective water depth h_{eff} is calculated accounting for the mean sinkage z_m:

$$h_{eff} = h - z_m , \tag{7}$$

with

$$z_m = T \left[c_1 + c_2 \left(\frac{n}{n_{\max}} \right)^2 + c_3 y_B + c_4 \left(\frac{n}{n_{\max}} \right)^2 y_B \right] \frac{Fr_h^2}{\sqrt{1 - Fr_h^2}} . \tag{8}$$

The coefficients c_i and β_{ik} in these formulas are deduced from comprehensive captive model test programs, carried out in the *Towing tank for manoeuvres in shallow water (co-operation FHR – Ghent University)* in Antwerp, with a ship loaded within a range of drafts interacting with different banks, [2], [3]. The bank configurations differ in slope, water depth, and the level of a horizontal submerged bank.

2.4. Bend initiation

Based on the results of (simulated) turning circle manoeuvres, an estimation can be made of the fraction of the available rudder capacity required to perform a bend with given characteristics (i.e. radius), taking account of the ship's forward initial speed and the propeller rate. Although these two parameters are not fully independent, for bend initiation they can be considered as such in practice.

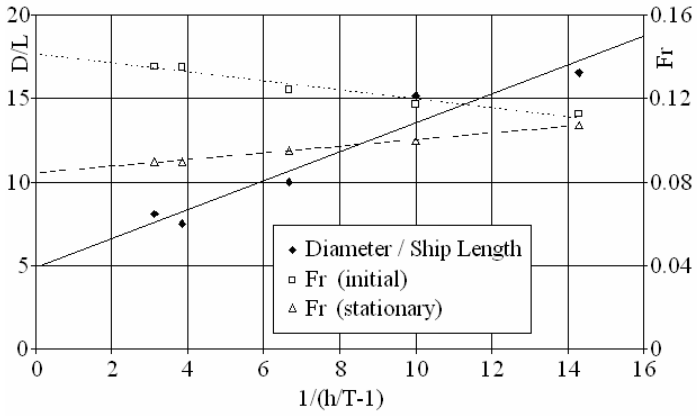

Fig. 3. Turning circle characteristics in function of under keel clearance for a container carrier model

The present calculations will be based on captive manoeuvring test series carried out at FHR with container carrier models at different drafts and under keel clearances [4], [5]; typical results are shown in Figure 3. As deep water conditions were not tested, the model may be less reliable at large under keel clearances. In deep water, the manoeuvring performance of the vessel in Figure 3 is rather poor compared to the IMO standards, which results in conservative conclusions.

3. Approach to a meeting in a straight reach of a two-way traffic channel

Before a meeting situation in a restricted channel, the vessels are lined up along their meeting lines, and are therefore subject to bank effects. For a specific ship in a given loading condition with a specified under keel clearance, the rudder angle required to compensate for bank induced forces depends on the ship speed, the applied propeller rate and the ship-bank distance. Graphs are generated for a specified engine setting, indicating zones of required rudder capacity as a function of speed and bank clearance.

Panamax container vessel	
Length between perpendiculars	294.0 m
Breadth	32.2 m
Draft	10.5 m
Max. speed	24.0 kn
Propeller diameter	7.4 m
Max. Propeller revs	80 rpm
Rudder surface	72.9 m²

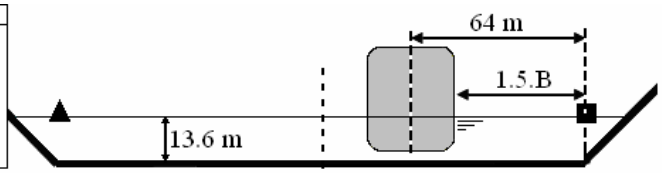

Fig. 4. Panamax container vessel sailing on her meeting line in the Gaillard Cut

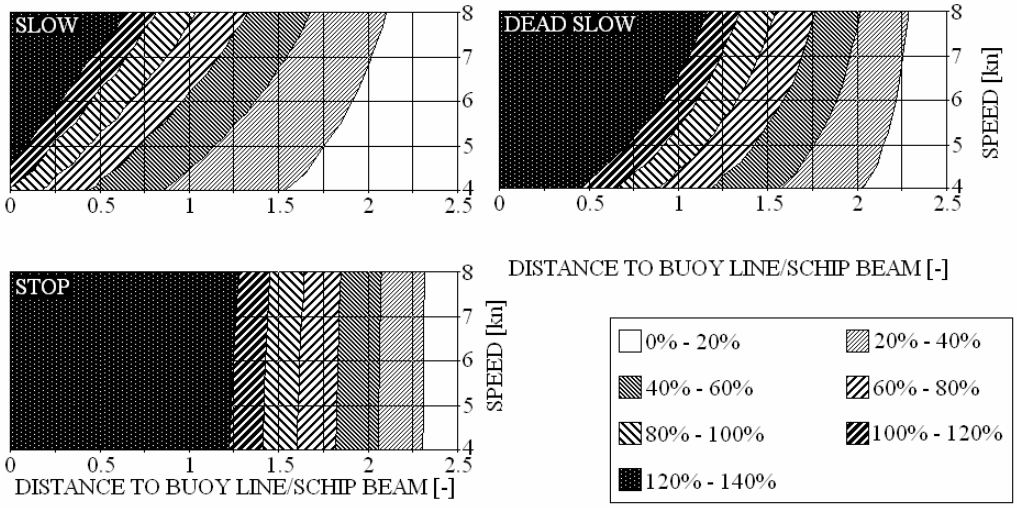

Fig. 5. Required rudder capacity at different propeller rates

As an example, a typical panamax container carrier meeting another ship in the Gaillard Cut, the narrowest reach of the Panama Canal, is discussed. At this location a ship preparing for a meeting situation will leave a clearance of about 1.5 times the ship beam to the buoy line (see Figure 4).

In Figure 5 the influence of the propeller rate on the controllability of a ship is illustrated. It can be concluded that the ship, sailing on her meeting line with a speed of 6.5 knots requires 38% of the rudder capacity to counteract the bank effects with propulsion slow, increasing to 70% at dead slow, and 85% with the propeller stopped.

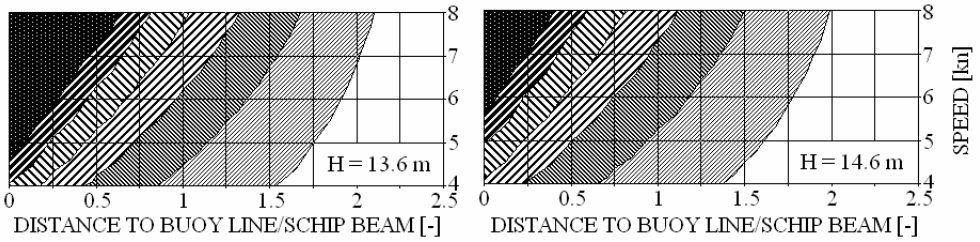

Fig. 6. Required rudder capacity: effect of deepening

In Figure 6 the initial situation is compared with an enhanced situation after deepening of the channel. For a ship with engine slow ahead, the required rudder capacity drops from 38% to about 25% if the depth is increased to 14.6 m. This can be explained by the fact that bank induced forces are very sensitive to under keel clearance variations.

4. Bend initiation on a river

4.1. Situation

The Western Scheldt, the river connecting the Port of Antwerp to the North Sea over a distance of 63 km, is characterised by an important tidal regime. Presently, ships with a draft larger than 11.85 m – planned to be increased to 13.1 m in the near future – are tide dependent, and regulations limit the draft of the vessels as a function of overall length. The methodology described above has been applied to assess the effect of increasing dimensions of container carriers on the controllability of the vessels at several critical locations in the fairway. One of these locations is the bend of Bath (Figure 7), combining a rather limited bend radius of 1200 m with a restricted width (350 m between the buoys) and thus a limited bank distance.

In order to initiate the bend successfully, the rudder capacity of the vessel, ascending the river, will have to counteract the influence of the ebb tide current and the banks, while a certain rudder capacity is also necessary for course changing and sailing along the bend. The influence of wind, which can nevertheless be important in this area, will be neglected in the following example.

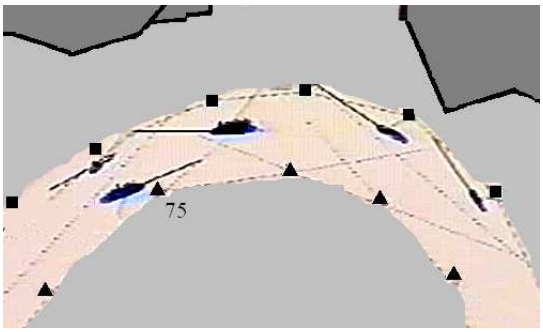

Fig. 7. Meeting situation in the bend of Bath

The evaluation of the bend manoeuvre on the Western Scheldt is considered for a container carrier with dimensions as shown in Table 1. Moreover this table contains the reference situation for tide height, current velocity and bend radius.

Table 1. Reference situation: ship in arrival in bend of Bath

		Length over all	352.2 m
		Beam	42.8 m
Tide height to MLLWS	1.16 m	Draft	14.0 m
Current speed (ebb)	1.73 knots	Maximum speed	25.0 kn
Bend radius	1200 m	Propeller diameter	8.5 m
		Maximum propeller rate	104 rpm
		Rudder surface	83.1 m^2

In Figure 8 the bathymetry is displayed monitored in 2005. The cross section is approximated by a bank with a slope of 1/8 investigated in the towing tank. At a certain distance the bottom becomes horizontal at a water depth equal to $h_1 = -2.0$ m referred to MLLWS. The effect of this submerged bank is discussed in [2].

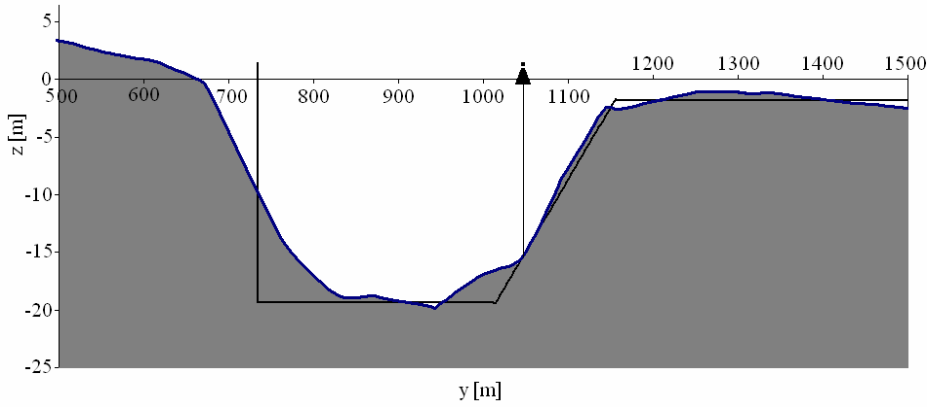

Fig. 8. Real (2005) and approximated bottom profile (water depth referred to MLLWS)

The required rudder capacity is displayed in Figure 9. For example, a ship with speed through the water equal to 14 knots, propeller rate harbour full and leaving a clearance of 2 times the ship's beam to the buoy line, needs 66% of the rudder capacity to perform a bend and to counteract the effects of banks and current.

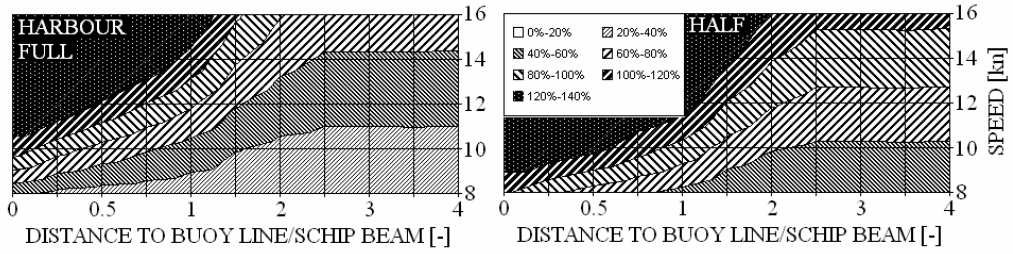

Fig. 9. Required rudder capacity at different propeller rates

4.2. Structural measures

The force balance methodology can be applied to assess the effectiveness of several possible structural measures that can be considered to improve the controllability of a ship in the situation described above. Preferably the structural measures can be accomplished by dredging outside the waterway, as in that case the dredging works do not hinder the shipping traffic. The following structural measures are considered (Figure 10):

- increasing the original bank slope (1/8) to steeper values (1/5–1/3);
- increasing the level h_1 of the submerged bank from –2 m to –3 m;
- dredging the toe of the bank.

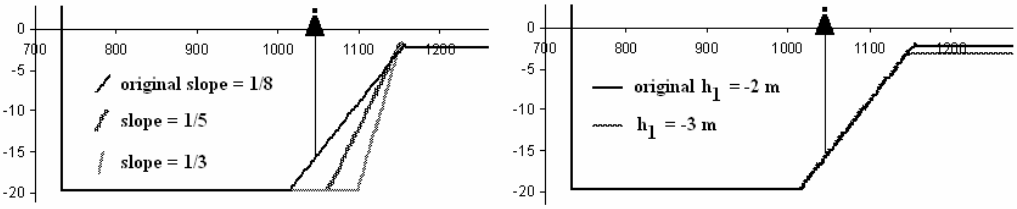

Fig. 101. Different bottom configurations to evaluate the influence of structural measures on the controllability of ships

4.2.1. Effect of steeper slopes

The results for the bottom configurations with different slopes sketched in Figure 10, are shown in Figure 11. At higher ship speeds the influence of a steeper slope is significant. The required rudder capacity for a ship at a speed of 14 knots, leaving

a clearance of 2 times the ship's beam to the buoy line, drops from originally 66% to 63% for a slope of 1/5, and to 60% for a slope of 1/3.

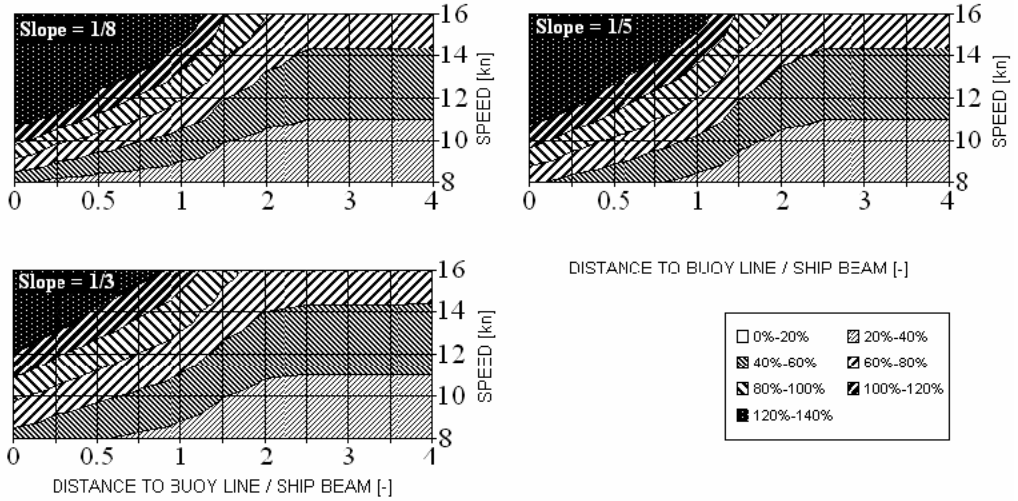

Fig. 11. Required rudder capacity at different slopes (harbour full)

Another way to evaluate the influence of steeper slopes is the comparison of the distances to the buoy line for which the ship, sailing at 14 knots, becomes incontrollable. Initially the ratio of the controllable distance to the buoy to the ship beam is 1.2. This value decreases to 1.1 for a slope of 1/5, and to 0.8 for a 1/3 slope.

4.2.2. Effect of a different h_1

The results for the bottom configurations with different h_1 sketched in Figure 10, are shown in Figure 12. The effect is negligible: after deepening the horizontal bank the required rudder capacity becomes 0.5% smaller for a ship with V = 14 kn and y_B/B = 2.

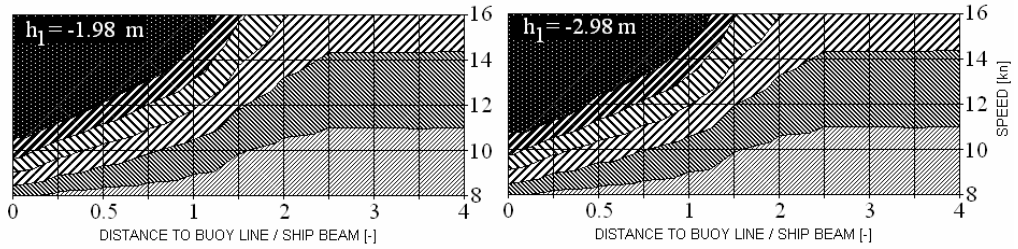

Fig. 12. Required rudder capacity with different values of h_1 (harbour full)

4.2.3. Dredging the toe of the bank

Figure 8 shows an accumulation of sediments at the toe of the starboard bank. In this case the required rudder capacity is shown for the same bottom as in Figure 8, but the toe is dredged. From the evaluation in Figure 13 it is clear that this modification positively influences the controllability of a ship sailing at a small distance to the buoy line, due to the increase of the local under keel clearance, which has an important effect on both manoeuvrability and bank effects.

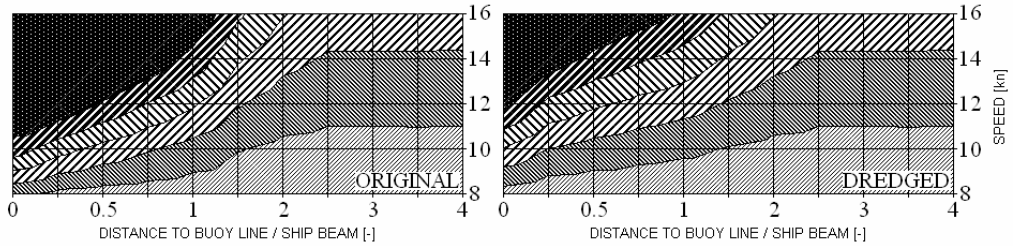

Fig. 13. Required rudder capacity with and without the toe at the starboard bank (harbour full)

4.3. Operational measures

Besides structural measures to improve the controllability, effective measures can also be taken by a conscious choice of different operational parameters such as ship speed, clearance to the buoy line, tide height, current speed and draft.

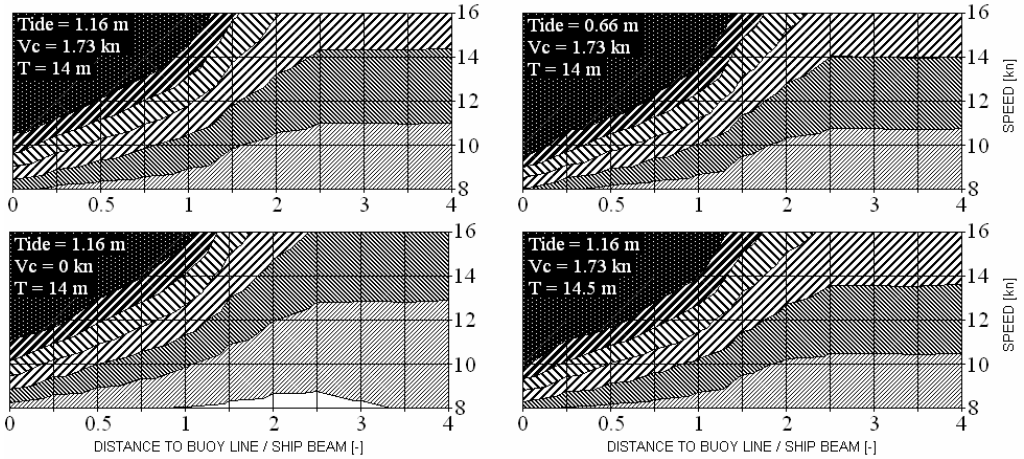

Fig. 14. Required rudder capacity to evaluate operational measures

The effect of speed and clearance is clear from the previous figures. An increase of the ship speed and a decrease of the clearance to the bank will require a larger rudder capacity. Indeed, often only a moderate decrease of speed or a slight increase of the bank clearance is required to obtain an effect that is comparable to the structural measures discussed above.

To evaluate the influence of tide height, current speed and draft, following variations of these parameters are examined:

- increase of tide height with 0.5 m (causing an increase of the under keel clearance);
- zero current speed;
- increase of draft with 0.5 m.

In Figure 14 the required rudder capacities are shown for the reference conditions and the variations on these conditions as listed above. For a ship with V = 14 kn and y_B/B = 2 the required rudder capacity is outlined in Table 2.

Table 2. Required rudder capacity for speed V = 14 kn and bank clearance y_B/B = 2.0

Draft (m)	14.0	14.0	14.0	14.5
Tide (m above MLLWS)	1.16	0.66	1.16	1.16
Current speed (kn)	1.73	1.73	0.00	1.73
Required rudder capacity	65.8%	69.8%	54.5%	70.9%

5. Conclusion

A hydrodynamic force analysis methodology has been presented, based on the comparison of the available control capacity that can be induced by the rudder and the yawing moments that are required to compensate for external disturbances such as bank and current effects or to initiate a defined bend. This method allows an evaluation of the effect of variations of the governing parameter on ship controllability, and may be used as a tool to compare new situations with known ones.

The influences of propeller rate, speed, bank clearance, under keel clearance, current velocity, and draft on the controllability of a ship in straight and curved reaches of a channel have been illustrated. A comparison was made to evaluate possible structural and operational measures to improve the controllability of the ship in a bend.

Although this methodology may be very useful to provide a quantitative assessment of the feasibility of proposed manoeuvres, and to quantify the effect of certain measures on the controllability in a channel, one should keep in mind that a successful operation not only depends on the available rudder capacity, but also on dynamic effects, the swept path, interaction between ships, transit strategy, visibility, human factors, etc. On order to account for these elements, other tools such as fast time simulation and full mission bridge simulator runs are required. Nevertheless, the methodology described in this paper may give a useful indication.

6. Summary

The controllability of a ship can be evaluated by the comparison between the required yawing moment and the maximum yawing moment generated by the rudder. In this paper the method is illustrated by two manoeuvres. The first evaluation consideres a ship sailing a straight course parallel to the canal centre line, the second evaluation handles a ship taking a bend to starboard on an eccentric course. In the first condition the ship is only subject to bank effects. A ship taking bends is further subject to the influence of the curvature of the current and requires a yawing moment to initiate the bend.

The proposed method offers an objective evaluation of the contrallibility of a ship. This evaluation can be used as a tool for fairway design or for defining traffic limits by calculating the beneficial effect of structural and operational measures on the controllability of ships.

The structural measures discussed in this paper are the influence of deepening, steeper slopes, deepening outside the waterway and dredging the bank toe. It can be concluded that dredging at the buoy line is much more effective than dredging outside the waterway.

Operational parameters investigated in this paper are ship speed, propeller rate, bank clearance, tide height, current speed and draft. In general, minor variations of ship speed and bank clearance may result into important effects on ship controllability. Also the under keel clearance, affecting both ship manoeuvrability and bank effects, appears to be a very important parameter.

References

[1] Vantorre M., Delefortrie G., Eloot K., Laforce E.: *Experimental investigation of ship-bank interaction forces*, International Conference on Marine Simulation and Ship Maneuverability, MARSIM 2003, Kanazawa, August, 2003.

[2] Lataire E., Vantorre M., Laforce E., Eloot K., Delefortrie G.: *Navigation in confined waters: influence of bank characteristics on ship-bank interaction*, International Conference on Marine Research and Transportation, ICMRT 2007, Naples, June, 2007.

[3] http://www.bankeffects.ugent.be/

[4] Eloot K, Vantorre M., Delefortrie G.: *Prediction of ship manoeuvrability of an 8000 TEU containership in deep and shallow water: mathematical modelling and captive model testing*, International Conference on Marine Simulation and Ship Maneuverability, MARSIM 2006, Terschelling, June, 2006.

[5] Delefortrie G.: *Manoeuvring behaviour of container vessels in muddy navigation areas*, PhD Thesis, Ghent University, May, 2007.

Metoda oceny sterowności statku w kanale

Przedstawiona jest metoda oceny sterowności statku płynącego w kanale, przy pomocy analizy sił hydrodynamicznych. Metoda została zastosowana do oceny sterowności kontene-

rowca w kanale na odcinku prostym i na zakolu, w dwóch przypadkach o znaczeniu praktycznym. Wpływ różnych charakterystyk statku (wymiarów głównych, zanurzenia, charakterystyk steru i pędnika), parametrów eksploatacyjnych (takich jak prędkość, nastawy śruby i odległość od brzegu kanału), czynników środowiskowych (takich jak prąd wody i pływy), i charakterystyki kanału (głębokość wody, nachylenie brzegu, promień zakola) na sterowność może zostać oceniony przez porównanie różnych warunków początkowych i konfiguracji dna. W celu oszacowania sił hydrodynamicznych potrzebnych do analizy wykorzystano wyniki badań modelowych na uwięzi na wodzie płytkiej i ograniczonej.

ARCHIVES OF CIVIL AND MECHANICAL ENGINEERING

Vol. VII 2007 No. 3

The effect of ship's impact on sea bed in shallow water

W. GALOR
Maritime University of Szczecin, ul. Wały Chrobrego 1/2, 70-500 Szczecin

The main goal of navigation is to lead the ship amount of port of destination. The main limitation of ship handling is the depth of port water area. The ship's movement on such area is connected with problems like shallow waters in which it is possible to impact on sea bed. The consequence of such event can results in the ship hull damage. The kind and degree of hull damage mainly depend on the energy absorbed by the hull during its impact against the sea bottom. The paper presents the bass of a model which describes the ground. A general algorithm of ship movement parameters determination during contact with sea bed is determinate.

Keywords: *safety of navigation, port water area, ship impact on the sea bed*

1. Introduction

The marine navigation is the process of planning and realisation of a safe movement of ship from one place to another (port of destination).The main goal of navigation is to handle the ship in accordance with the aim of its motion when required parameters of this process should be retained. Realization of this goal depends on assurance of suitable level of ships safety during their manoeuvring in water area. This is achieved by controlling ship movement along a planned trajectory. However, various factors may affect ship motion. The process of safe movement in water area is called safe navigation. The world fleet tends to expand in terms of total capacity, with vessels growing in size, while their number is maintained on a similar level. The existing ports are expected to service bigger ships than those for which they were designed. The building of new ports is restricted on the one hand by natural conditions of sea areas, and necessary large financial effort on the other hand. As economic and geopolitical conditions change, directions of cargo transport (bulk in particular) also change, sometimes in a cycle lasting a few years. This in turn, makes building new ports a risky enterprise for investors, as the invested capital return amounts to at least twenty years. The goal of entering larger ships into the port can be achieved through changes in operating conditions within ports and modernization of certain components of port basins and areas. These actions should result in ports handling ships as large as possible on condition that specified safety level is maintained. Safe manoeuvring of a ship within a given area requires that the manoeuvring area of a ship with a specific draft is comprised within available port water area having a required depth.

This purpose of ship's manoeuvring is put into practice by steering the ship movement on a planned trajectory. The ship, however, may be affected by various factors

during that process, which sometimes make it difficult. This means that in certain conditions just any trajectory cannot be planned for the ship, and on the other hand, steering the traffic on a properly planned trajectory is not always possible. The occurrence of factors affecting the ship's movement causes its free way limitation. The ship's leading should be safe first of all, which means it should not cause any navigational accident. A navigational accident is an undesirable occurrence which can cause different losses. Mainly there are lives or health, loss or damage to ship or cargo, pollution of natural environment, damage to the port structure, economical loss due to blocking of the port or its part, cost of salvage operation and other. Among water areas there are those where ship manoeuvring is limited more then in other sea areas. These areas are called limited waters. There are many definition and names of such type of waters [2]. The universal definition of limited waters may be that it is area, where the ship can't choose the free way. This limitation is caused by factors that affect the ship manoeuvring. One of such kind of waters is port water areas.

2. Port water areas

The port approach and port areas are characterised by limited depth (shallow water) and various port structures. These man-made structures comprise surface or submerged structures which together with installations, construction arrangements associated with these structures, technical equipment and other equipment relevant to function given structure make up one technical-functional object. From the point of view of limitations of traffic in an area, hydro technical structures, the port water area generally include the following structures:

- objects formed due to dredging and silting work, particularly harbour and shipyard water areas, such as outer harbours, basins, sea and inland fairways, approach channels, passing and turning areas,
- channels,
- wharves making up enclosures of the shore and generally allowing ships to berth and lie alongside,
- shore protecting structures, mainly breakwaters, bottom strengthening, dredged fairway slope strengthening structures,
- structures of fixed aids to navigation, especially lighthouses situated in a sea area, land- and water-based beacons, leading marks and navigational lights, dolphins,
- structures situated within sea harbours, particularly mooring cargo handling islets, landing stages,
- port buildings situated in sea ports, particularly breakwaters, wave breakers, cargo-handling and lying alongside, others,
- structures connected with the seabed exploitation (oil rigs, platforms and pipelines).

Besides, they comprise structures of floating navigational marks, particularly moored navigational buoys. Figure 1 presents an example of water area restricted by port structures.

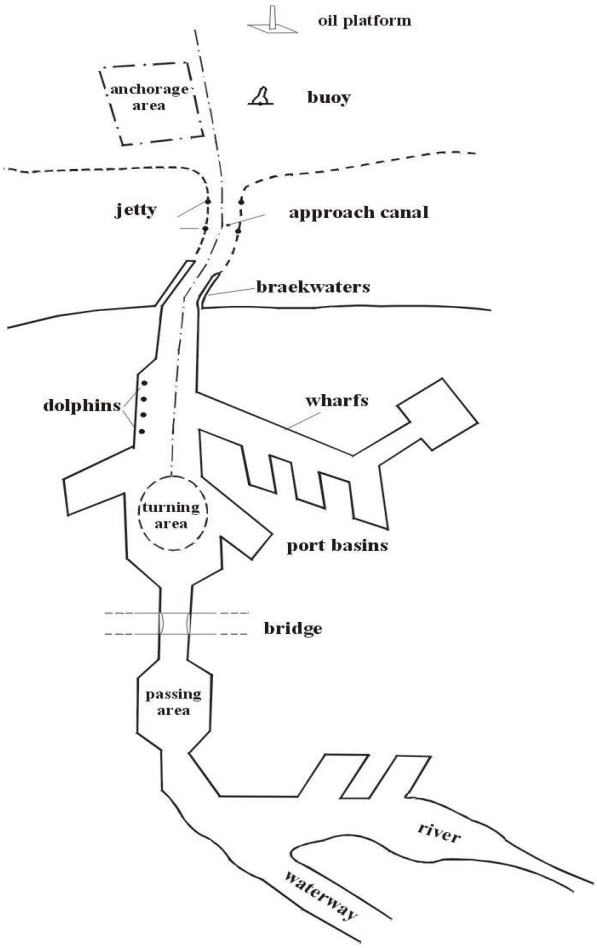

Fig. 1. An example of port water areas

Safe manoeuvring of a ship within a given area requires that the manoeuvring area of a ship with a specific draft is comprised within available port water area having a required depth. There are two undesired types of events [4] that can lead to a navigational accident within a port area:

- impact on the shore (or another port structure),
- contact with the sea bed.

The accessible port water area (for given depth) warrants safety manoeuvring if fulfills condition:

$$\omega \in \Omega, \tag{1}$$

where:

ω – requisite area of ship's manoeuvring,
Ω – accessible port water.
The second condition given the realizing of safe manoeuver on area is:

$$H_i \geq T + R_B, \tag{2}$$

where:
H_i – the depth in i-th point of area,
T – ship's drought,
R_B – safe under keel clearance (UKC).
R_B is the value of minimum under keel clearance of a ship manoeuvring within a given area to assure the ship safety that is no contact of ship's hull with the bottom should occur [3]. This clearance is also called the required or safe water clearance.

3. The risk of ship' impact on sea bed

The situation when a ship's hull impacts the sea bed often results in serious damage. The damage may be of various kinds:

- tearing of bottom plating,
- crushing of deck,
- folding of web frames,
- stretching of shell plating.

That is why the evaluation of ship's movement safety should allow for its impact against the bottom, on condition that the effects of the impact (losses) do not exceed the accepted level (hull damage). That incident can be described as follows:

$$R_{dop} = P_U [Z_c \leq R_B] \text{ for } C \leq c_{\min}, \tag{3}$$

where:
Z_c – the list distance between ships hull and bottom during manoeuvring,
R_B – under keel clearance,
C – losses,
$c_{\min}$ – acceptable level of losses.
The level of losses sustained from the impact against the ground depends on many factors, the most important of which is the type of bottom (ground). If the bottom is soft penetration to a certain depth does not cause any hull damage.
The conditions of ship's safe impacting on sea bed are as follows.

$$E \leq E_{\mathrm{d}} \text{ dla } p \leq p_{\mathrm{dop}}, \tag{4}$$

where:
E – ship's maximum kinetic energy absorbed by the berth-fender-ship,
E_d –ship's admissible kinetic energy absorbed by the berth-fender-ship,

p – maximum pressure of individual fender on ship's hull plating,

p_{dop} – admissible pressure of individual fender on ship's hull plating.

The energy absorbed by the ship's hull hitting the sea bed is equal to the work done by the ship during the impact. The energy mainly depends on the force appearing between the hull and the bottom. It is difficult to define the force and its curve as the function of time by analytical methods. Therefore, simpler methods based on empirical research data are used. The empirical equation given below presents the energy of impact dependent on ship's mass and the velocity at the moment of impact. The vertical component of ship's velocity should be taken into account in these calculations:

$$E_v = m_s V_v^2 /2, \tag{5}$$

where:

E_v – energy absorbed during impact,

m_s – ship's mass,

V_v – vertical components of ships velocity.

The consequences arising from the fact that a ship hits the ground while moving, such as hull damage or, possibly, loss of cargo (particularly liquid cargo, which may pollute the marine environment) depend on a number of factors which can be expressed by a variety of measures [1].

The kind and degree of hull damage depends mainly on the energy absorbed by the hull when hitting the bottom. The measure of hull damage used for the assessment of the impact is the volume of damaged hull material. The relationship combining the absorbed energy and the degree of damage has been empirically worked out [6]:

$$E = 47.2 \times R_T - 37.2, \tag{6}$$

where:

E – energy absorbed by the hull during impact,

R_T – degree of damage of hull material.

This empirical relation has been determined from the observations of the effects of numerous collisions and is used for the assessment of collision effects. The value of coefficient in formula (6) is results of its carried out of research.

Admissible pressure of an individual fender on the ship's hull depends on her size and design. And according to the type of vessel (a general cargo carrier, a container ship, a tanker, a bulk carrier, a gas carrier) it can range from 200–700 kN/m^2 [5]. It is determined on the basis of the analysis of deflections during the stresses of the shell plating structure which takes into account an adequate distribution of fender pressure on the shell, longitudinal girders, and frames. At the same time a phase of elasticity of ship's shell structure is assumed. There are situations in which work of deflection of a given part of the shell plating is taken into consideration and where a plastic strain in the form of dents of the shell is accounted for.

4. Probability of the hull damage

$$P_{\mathrm{k}}(P_{\mathrm{u}}) = P\,[Q_{sgr} \geq Z_G], \tag{7}$$

where:

Q_{sgr} – admissible pressure on ship's hull,

Z_G – passive earth pressure.

While determining the probability of ship hull damage during the impact one should take into account that not every such impact ends in a serious accident. Therefore risk of ship's impact on sea bed can be determined as:

$$P_{uw} = P_u \times P_k(P_u), \tag{8}$$

where:

P_{uw} – probability of an accident during ship's manoeuvres,

P_u – probability of a ship's touching the bottom.

The risk of ship impact against the sea bottom may be assumed as a criterion for the evaluation of the safety of ship manoeuvres within port waters.

5. The ship's movement during impact of sea bed

During a ship's striking the bottom of an area built of sandy or argillaceous ground, for a vessel in progressive movement, there occurs a gradual sinking of the hull into the ground (until the ship stops). The mechanism of the ship's striking the area's bottom depends on the ship's draft, namely whether the vessel is trimmed by the bows, the stern or if it is loaded on an even keel. During a ship's striking the bottom of an area of fragmented ground, for a vessel in progressive movement, there occurs gradual sinking of the hull into the ground (until the vessel's stoppage). During this process there can be distinguished the plough-in phase bound with longitudinal motion and the penetration (sinking) in a vertical direction. Figure 2 presents this movement in the case of a vessel being trimmed by the bows. A similar phenomenon will occur in the case of being trimmed by the stern.

The penetration of the ship into the ground depends on the relation between the horizontal V_H and vertical V_v components of the ship's speed V_S. The ship will stop in a certain distance I_P from the point of the hull's first contact with the bottom and the penetration to a particular depth Z_K. In the initial stage of the ship's penetration into the ground is mainly affected by horizontal forces. Stopping of the ship takes place on a horizontal plane until the ship stops, which is described as stopping distance I_P from the first contact point to the stopping of the vessel.

On the basis of considerations presented there has been prepared an algorithm of calculating vessel movement parameters when striking the port water area ground and of forces impacting on the vessel's hull. It has been applied in a computer simulation

model of the vessel's movement in the area. The model works in real time and serves the purpose of preparing navigational analyses. This permits risk determination of the vessel striking the area bottom and its results (likelihood of hull damage). The stopping of ship will be fulfills when the initial kinetic energy (in moment of first contact with sea-bed) became completely lost:

$$mV^2_{Ho}/2 - \int P_{RT}dl - \int P_B dl - \int P_{RK}dl = 0, \tag{9}$$

where:

m – ships mass and water added mass,

V_{Ho} – horizontal component of ships velocity in moment of contact with sea-bed,

$\int P_{RT}dl$ – work performed for overcoming friction force of the hull's bottom part,

$\int P_B dl$ – work performed for overcoming the resistance of friction of the lateral parts of the hull,

$\int P_{RK}dl$ – work performed for overcoming soil wedge.

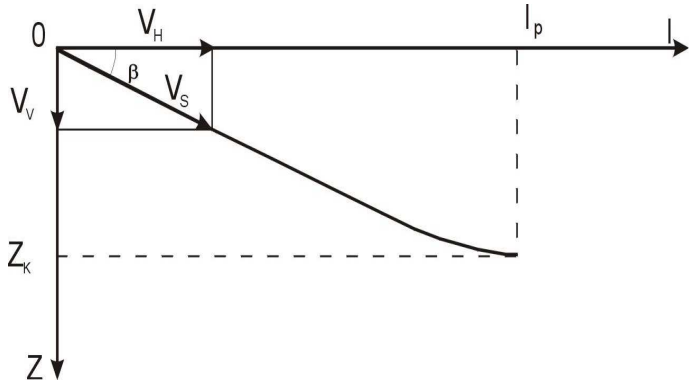

Fig. 2. Penetration of the ship's hull into the bottom

The ship's velocity during contact with ground of sea-bed will be decrease until stopping. The way of ship's stopping will be equal:

$$L_K = \int V_{Hi}\,dt \quad \text{for} \quad t \in (t_0 - t_K), \tag{10}$$

where:

L_K – way of ship's stopping,

t_K – time to ship's stopping,

V_{Hi} – horizontal component of ship's velocity during phase of ploughing.

$$V_{Hi} = (2 \times \Delta E_{Ki} / m)^{½}, \tag{11}$$

where:

ΔE_{Ki} – decreasing of ship's kinetic energy due to movement to contact with sea bed, which it alters on work performed for hull resistances during ploughing.

The pressure of the ship on ground:

$$\sigma = \frac{N}{S}, \tag{12}$$

where:

N – the push force of ship's hull,

s – area of hull contact with ground.

The ship's push on the ground is an effect of decreasing of ship's draft. The greater emergence bear witness about greater pushing. The magnitude of push force will alter depending on ship's draft and trim. The pushing for even keel will be equal:

$$\sigma_i = \frac{\Delta T_i \cdot Lp_p \cdot B \cdot \delta}{S} \cdot \gamma, \tag{13}$$

where:

ΔT_i – currently draft decreasing,

L_{pp} – length between perpendiculars,

B – breadth of ship,

δ – ship's block coefficient,

γ – water weight specific gravity,

S – surface area of hull contact with ground.

6. Determination of the effect of ship's impact

In successive steps ship movement parameters during contact with the ground are calculated, what permits the determination of its results. The following steps are accomplished:

- calculating initial kinetic energy,
- calculating pressure of the vessel on the area bottom, to decrease the water level or the vessel's draft,
- checking whether passive earth pressure (the ground's reaction) does not exceed the permissible value,
- calculating the friction force of the bottom part of the vessel's hull against the ground, taking into account the friction coefficient,
- calculating the depth of the vessel's penetration into the ground,
- calculating work performed for overcoming friction force of the hull's bottom part,
- calculating work performed for overcoming the resistance of friction of the lateral parts of the hull for a specified depth of the vessel's penetration into the ground,

- calculating work performed for overcoming soil wedge,
- calculating the decrease of the vessel's kinetic energy caused by contact with the ground,
- calculating the decrease of the vessel's speed components.

The example of calculation using algorithm is presented below.

Basic dates:

- length between perpendiculars L_{pp} = 260.0 m,
- breadth of ship B = 42.0 m,
- ship's draft T = 12.8 m,
- ship's block coefficient δ = 0.83,
- initial horizontal component of ship's speed V_H = 5.5 m/s,
- initial vertical component of ship's speed V_V = 0.01 m/s.

The results of calculations are following:

- over 265 sec from first contact of ship with sea-bed its speed stopped up to zero,
- the length of ship's stopping distance I_p = 295.0 m,
- the admissible pressure on ship's hull there wasn't overdoing in this case.

7. Conclusions

The under keel clearance should ensure ship's safe manoeuvring in a port area on the one hand, and may restricted the maximal ship's draft on the other hand, particularly in port areas. It is possible to predict of maximum sailing draft for entering ships into the port by proper method of calculation. This result can be achieved through the minimization of under keel clearance value while risk is kept at an acceptable minimum. A ship can touch the bottom of a navigable area due to the reduction of its keel clearance. Such an event no has to necessaribily results of damage of ship's hull. The kind and degree of hull damage mainly depend on the energy absorbed by the hull during its impact against the sea bottom. The effect of ship's impacting i.e. contact of a floating body with sea bottom consisting of different types of soils. It is possible to determine of results of shp impact on sea bed. It permits to assess of navigational risk and thus to improve the safety of ship movement in shallow water.

References

[1] Galor W.: *The managing of the navigational safety of ships in port water areas,* Editors C.A. Brebbia et al., WITPRESS Southampton, Boston, 2005.

[2] Galor W.: *The movement of ship in water areas limited by port structures,* Annual of Navigation, No. 10, Gdynia, 2005.

[3] Galor W.: *Analiza określania zapasu wody pod stępką,* Materiały XI Międzynarodowej Konferencji Naukowo–Technicznej „Inżynieria Ruchu Morskiego", Szczecin, 2005.

[4] Galor W.: *Wybrane problemy bezpieczeństwa żeglugi na akwenach portowych*, TRANSPORT pod redakcją Z. Strzyżakowskiego, Prace Naukowe, No. 3, 23, 2005 Politechniki Radomskiej, Radom, 2005.
[5] *Morskie budowle hydrotechniczne. Zalecenia do projektowania i wykonania Z1-Z41*,
[6] *Fundacja Promocji Przemysłu Okrętowego i Gospodarki Morskiej*, pod redakcją B. Maurkiewicza, Wyd. IV, Gdańsk, 2006.
[7] Pedersen, T.P., Zhang, S.: *Absorbed energy in ship collision and grounding, revision Minorsky's Empirical Method*, Journal of Ship Research, Vol. 44, No. 2.

Skutki uderzenia statku w dno akwenu portowego a płytkowodziu

Głównym celem nawigacji jest bezpieczne prowadzenie statku do portu przeznaczenia. Ograniczeniem realizacji tego celu jest głębokość akwenu. Ruch statku po takim akwenie jest związany z problemami płytkowodzia, które mogą być przyczyną uderzenia statku w dno akwenu. Konsekwencją takiego zdarzenia może być uszkodzenie kadłuba statku. Rodzaj i wielkość uszkodzenia zależą głównie od energii absorbowanej przez kadłub podczas uderzenia w dno akwenu. Referat przedstawia podstawy budowy modelu takiego uderzenia, przy czym przedstawiono ogólny algorytm określenia parametrów ruchu statku podczas kontaktu z dnem akwenu.

ARCHIVES OF CIVIL AND MECHANICAL ENGINEERING

Vol. VII 2007 No. 3

A desktop ship manoeuvrability prediction system

T. GÓRNICZ
Wrocław University of Technology, Wybrzeże Wyspiańskiego 25, 50-370 Wrocław

This paper presents low-cost, reasonable accurate system for model design factors influencing a ship's manoeuvrability. The presented system is based on modified Abkowitz's mathematical model, with both linear and non-linear differential equations.

Keywords: *ship manoeuvrability, ship simulation, movement prediction, Abkowitz's model*

Notations
I_z – mass moment of inertia of ship about an axis through centre of gravity,
M – mass,
x_G – distance along longitudinal direction, between the centre of gravity and origin of reference axes fixed in the ship,
u_0 – initial speed of a ship,
u – ship's longitudinal speed, v – ship's transverse speed,
r – yaw rate, δ – rudder deflection angle,
$\Delta u = u\text{-}u_1$
X – total force in x direction, parallel to plane of symmetry of a ship,
Y – total force in y direction, perpendicular to plane of symmetry of a ship,
N – total moment about an axis through centre of gravity,
X^0, Y^0, N^0 – forces and moment acting on a ship at the equilibrium condition,
X_u, X_v, etc. – partial derivatives of X with respect to u, v, etc.
Y_u, Y_v, etc. – partial derivatives of Y with respect to u, v, etc.
N_u, N_v, etc. – partial derivatives of N with respect to u, v, etc.

1. Introduction

A ship's manoeuvrability is a major design factor when choosing a specific construction. Nowadays there are couple of common methods to predict ships manoeuvrability. The computational power of the typical home computer is sufficient to support some computer ship manoeuvrability prediction systems (CSMPS). Based on Abkowitz's mathematical model this paper describes such a system, its structure and crucial elements.

2. Application specification

A good computer ship manoeuvrability prediction system (CSMPS) should be universal, accurate, and easy to use. Figure 1 shows the proposed structure of the system, its main elements and their hierarchy.

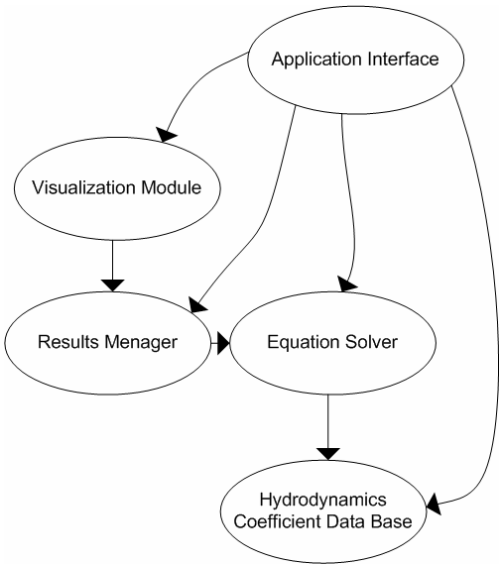

Fig. 1. General structure of CSMPS

2.1. Hydrodynamics coefficient data base

The ship designer typically will need to make a fast calculation for different sets of coefficients. Because of this fact, the way, how we will hold the coefficients is significant. From one side, the database should be easy to manage electronically. From another it should be transparent to the user. An "XML" file system was chosen for this database. The structure of this file system is easy to understand and there is variety of software libraries ready to read and write such files. These libraries were used to provide reading XML functionally inside the CSMPS. Finally all values are held as text variable with desired precision, making them easy to read and to manipulate.

2.2. Equation solver

This block provides the two most important parts of the CSMPS: equations (linear and non-linear) and the solver of a differential equation set. Both of them are described in chapter 3 and 3.1 of this paper.

2.3. Results manager

All results received from the solver are saved in a specific file. Such results are usually analysed using a professional calculation computer application. A reasonable first cut of the behaviour can be determined by performing a preliminary recalculation of results to extract important parameters, within the resulting manager module, and to send them to the visualization module.

2.4. Visualization

The visualisation module is not strictly necessary to implement in a CSMPS model, but it greatly simplifies the whole process of predicting and testing ship manoeuvrability. It allows a designer to perform fast analysis of current results, catching problems and errors before the main analysis will be performed.

An OpenGL is a free graphic library, which supports 2D as well as 3D graphics. It was used as the basis of the visualisation module, because it is a well-documented standard, it is easy to find a lot of examples, and finally it is supported by companies, producing graphics software and hardware.

2.5. Interface

The last part of the system, which has access to all other elements is the application interface. The graphical interface is best for this type of application. It is fast, intuitive and easier to use than text interface. It allows a designer to easily manipulate all of the parameters of the application like equations sets, coefficient values and results.

3. Mathematical model

The proposed CSMPS uses the Abkowitz's mathematical model. There are two versions of it: linear and non-linear. The difference between them is the number of elements taken into account for the Taylor expansion. The Equation from (1) to (7) presents the linear model transformed into suitable form for the numerical calculation. The linear model is usually used to determine course stability, ship's manoeuvrability for small rudder angle and in first stages of designing autopilots.

Linear equation:

$$\dot{u} = \frac{f_1}{m - X_{\dot{u}}}, \tag{1}$$

$$\dot{v} = \frac{1}{f_4}[f_2(I_z - N_{\dot{r}}) - f_3(m \cdot x_G - Y_r)], \tag{2}$$

$$\dot{r} = \frac{1}{f_4}[f_3(m - Y_{\dot{v}}) - f_2(m \cdot x_G - Y_r)], \tag{3}$$

where:

$$f_1(u, v, r, \delta) = X_u \Delta u + X_\delta \delta, \tag{4}$$

$$f_2(u, v, r, \delta) = Y_\delta \delta + Y_v v + (Y_r - m u_0) r, \tag{5}$$

$$f_3(u,v,r,\delta) = N_\delta \delta + N_v v + (N_r - mx_G u_0) r \,, \tag{6}$$

$$f_4(u,v,r,\delta) = (m - Y_{\dot v})(I_z - N_{\dot r}) - (mx_G - Y_{\dot r})(mx_G - N_{\dot v}) \,. \tag{7}$$

The core of the equations are four main variables: the ship's longitudinal speed (u), transverse speed (v), yaw rate (r) and the rudder angle (δ).

The non-linear model is usually based on first three elements of the Taylor expansion. It is much more accurate than the linear one, which is why it is widely used in predicting ship's manoeuvrability. This model is also recommended by the ITTC.

The basic movement equations (1, 2, 3) are the same for linear and for the non-linear theory. The difference lies in the formulas for f_1, f_2, f_3, which are:

$$\begin{aligned} f_1(u,v,r,\delta) &= X^0 + X_u \Delta u + \frac{1}{2} X_{uu} \Delta u^2 + \frac{1}{6} X_{uuu} \Delta u^3 + \frac{1}{2} X_{vv} v^2 + \\ &(\frac{1}{2} X_{rr} + m \cdot x_G) r^2 + \frac{1}{2} X_{\delta\delta} \delta^2 + \frac{1}{2} X_{vvu} v^2 \Delta u + \frac{1}{2} X_{rru} r^2 \Delta u + \frac{1}{2} X_{\delta\delta u} \delta^2 \Delta u \,, \\ &+ (X_{vr} + m) vr + X_{v\delta} v\delta + X_{r\delta} r\delta + X_{vru} vr\Delta u + X_{v\delta u} v\delta\Delta u + X_{r\delta u} r\delta\Delta u \end{aligned} \tag{8}$$

$$\begin{aligned} f_2(u,v,r,\delta) &= Y^0 + Y^0{}_u \Delta u + Y^0{}_{uu} \Delta u^2 + Y_v v + \frac{1}{6} Y_{vvv} v^3 + \frac{1}{2} Y_{vrr} v r^2 + \frac{1}{2} Y_{v\delta\delta} v\delta^2 \\ &+ Y_{vu} v\Delta u + \frac{1}{2} Y_{vuu} v u^2 + (Y_r - m u_0) r + \frac{1}{6} Y_{rrr} r^3 + \frac{1}{2} Y_{rvv} r v^2 + \frac{1}{2} Y_{r\delta} r\delta^2 \\ &+ Y_{ru} ru + \frac{1}{2} Y_{ruu} r\Delta u^2 + Y_\delta \delta + \frac{1}{6} Y_{\delta\delta\delta} \delta^3 + \frac{1}{2} Y_{\delta vv} \delta v^2 + \frac{1}{2} Y_{\delta rr} \delta r^2 + \\ &Y_{\delta u} \delta\Delta u + \frac{1}{2} Y_{\delta uu} \delta\Delta u^2 + Y_{vr\delta} vr\delta \end{aligned} \,, \tag{9}$$

$$\begin{aligned} f_3(u,v,r,\delta) &= N^0 + N^0{}_u \Delta u + N^0{}_{uu} \Delta u^2 + N_v v + \frac{1}{6} N_{vvv} v^3 + \frac{1}{2} N_{vrr} v r^2 \\ &+ \frac{1}{2} N_{v\delta\delta} v\delta^2 + N_{vu} v\Delta u + \frac{1}{2} N_{vuu} v u^2 + (N_r - mx_G u_0) r + \frac{1}{6} N_{rrr} r^3 + \frac{1}{2} N_{rvv} r v^2 \\ &+ \frac{1}{2} N_{r\delta} r\delta^2 + N_{ru} ru + \frac{1}{2} N_{ruu} r\Delta u^2 + N_\delta \delta + \frac{1}{6} N_{\delta\delta\delta} \delta^3 + \frac{1}{2} N_{\delta vv} \delta v^2 \\ &+ \frac{1}{2} N_{\delta rr} \delta r^2 + N_{\delta u} \delta\Delta u + \frac{1}{2} N_{\delta uu} \delta\Delta u^2 + N_{vr\delta} vr\delta \end{aligned} \,. \tag{10}$$

3.1. Drift angle modification

One of the most spectacular advantages of Abkowitz's model is that it can be easily modified. New hydrodynamic effects can be taken into account and negligible parts can be removed from the equations.

One of the methods to improve the accuracy of this model it is to recalculate drift angle for the at rudder at each calculation step and use this information to determine the real force of the rudder. The standard Abkowitz's model assumes that the force on a rudder is a function only of the rudder angle. Estimating this force by taking into consideration the angle of the real flow around the rudder greatly reduces the approximation error. The results using these calculations are shown in chapter 4.

3.2. Solution of the manoeuvrability equation system.

There are several numerical ways to solve proposed sets of differential equations of motion. The simple methods, like Euler's are not recommended. The general reason is poor accuracy, but Euler's method is also considered not very stable as well.

The simplest reasonable solving method is the fourth order Runge-Kutta algorithm. The main idea 4th order method is showing (11)

$$\begin{aligned} k_1 &= hf(x_n, y_n), \\ k_2 &= hf(x_n + a_2 h, y_n + b_{2,1}k_1), \\ k_3 &= hf(x_n + a_3 h, y_n + b_{3,1}k_2 + b_{3,2}k_2), \\ k_4 &= hf(x_n + a_4 h, y_n + b_{4,1}k_1 + b_{4,2}k_2 + b_{4,3}k_3), \\ y_{n+1} &= y_n + c_1 k_1 + c_2 k_2 + c_3 k_3 + c_4 k_4 + O(h^5) \end{aligned} \tag{11}$$

where:

a_n, $b_{n,n}$, c_n, – parameters,

h – stepsize,

y_{n+1} – new function value,

y_n – previous function value.

Usually the most powerful tools to solve ordinary differential equations are the adaptive step size control methods. The main purpose of using such methods is to achieve a predetermined accuracy with minimum computational effort [3].

One of the adaptive step size methods is the combination of two different order Runge-Kutta methods. This is well tuned to the mathematical model applied in section 3. Really accurate results can be achieved by using the combination fifth and fourth order method (Cash-Karp parameters for embedded Runge-Kutta methods were taken from [3]). However there are other combinations for this method, like Prince – Dormand (1981). This solver uses a combination of sixth and seventh order method, however for chosen mathematical model and accuracy at the level of 1E–4 it doesn't produce much better results than the lower order methods. Moreover, this method is more computational complicated and thus it was rejected.

4. Results verification

All of the results presented in this chapter are computed by using hydrodynamic coefficients for the Esso Osaka tanker. The full-scale trials and hydrodynamic coefficients were taken from [5].

Figure 2 shows a comparison of a predicted trail (linear model) and full-scale sea trials. The agreement between them is rather poor. Only the first part of the path is close to sea trial results. Adding the drift angle test data didn't improve the accuracy of the results, either. Moreover, even though the ship made full circle the drift angle didn't yet reach the stable phase, see Figure 3.

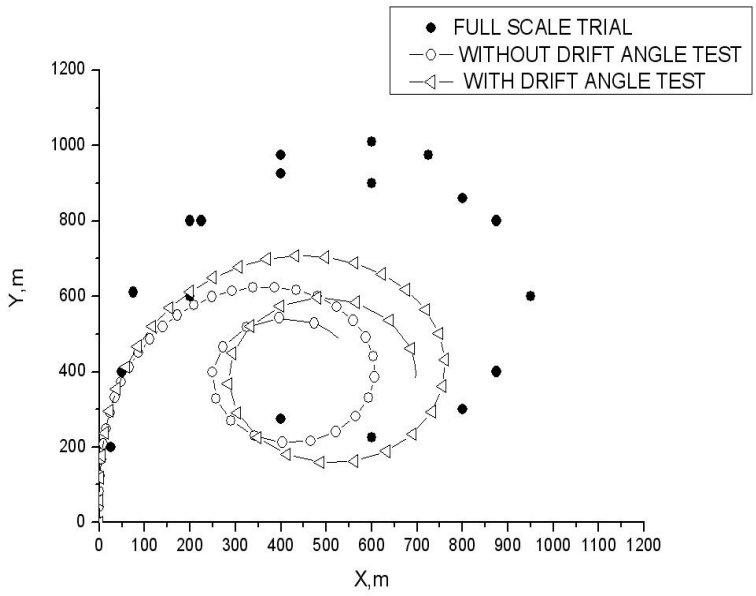

Fig. 2. Turning trajectory for linear equations (V = 10 kts, rudder angle +35°)

The low accuracy of the results from the linear model principally due to an incomplete set of the hydrodynamic coefficients of Esso Osaka. The second reason is the oversimplification of the linear model.

The agreement between full-scale trails and results from the non-linear model are rather good, especially when taking into account the drift angle correction. This greatly improves the accuracy of the results, shown on Figure 4.

The diameter of turning circle from the computation that includes the drift angle correction is larger than the one measured on the full-scale trail, but the same tendency has the mathematical model proposed by the SNU professional laboratory [5].

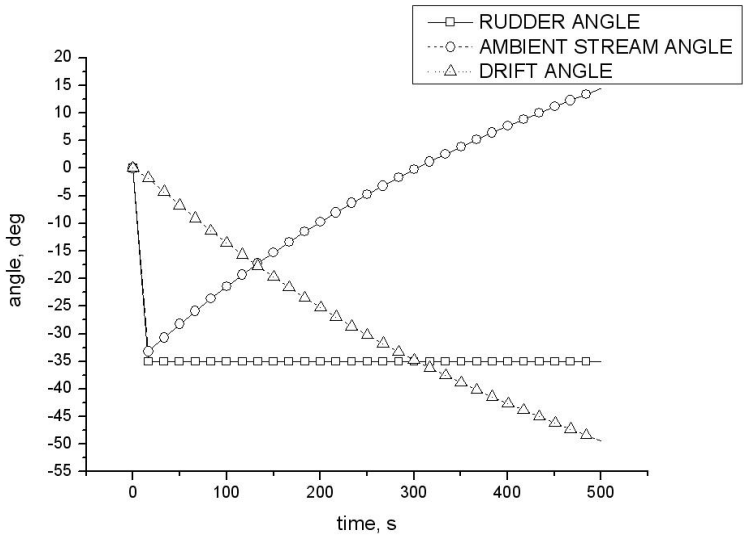

Fig. 3. Time history for angle at rudder (linear equations)

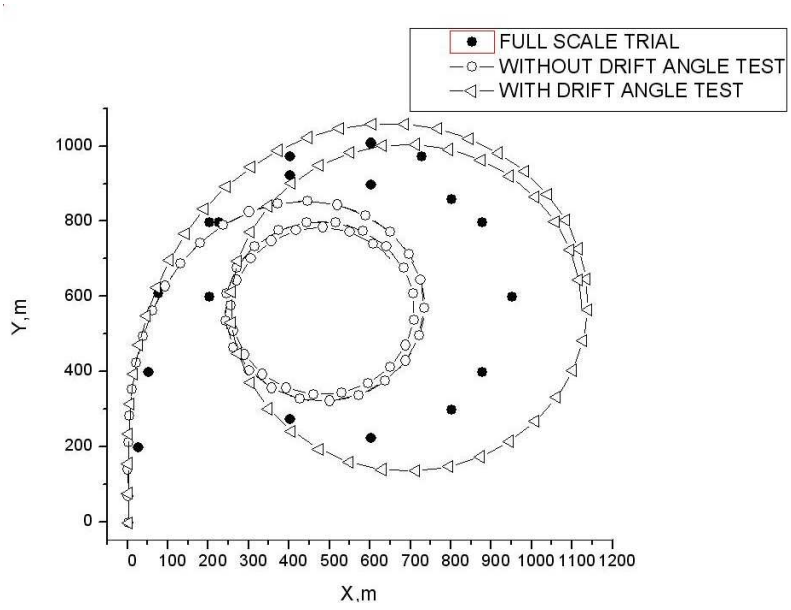

Fig. 4. Turning trajectory for non-linear equations (V = 10kts, rudder angle +35°)

Figure 5 shows that the drift angle stabilized at value 23° and falling into the range presented in [5], from 13° to 25°. This figure demonstrates that recalculation of the drift angle at every calculated time step is important. Although the rudder angle set is

at 35°, the angle of the actual stream around the rudder is reduced to only 12°. This is the reason for the decrease of force generated by the rudder.

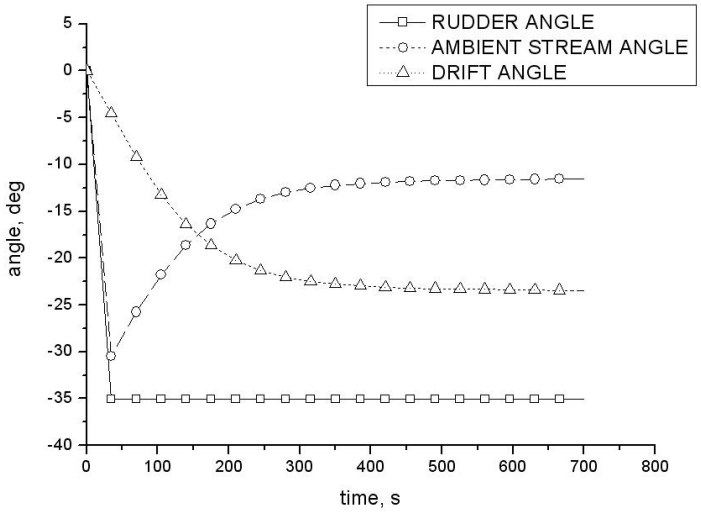

Fig. 5. Time history for angle at rudder (non-linear equations)

As mentioned in chapter 3, one of the advantages of the chosen model is the ability to complement this model with new elements. By adding the new effects we may improve the accuracy of the model and the whole prediction of ship manoeuvrability.

5. Conclusion

A well-designed CSMPS must be clear, useful and accurate. The solution presented here is a good starting point to design a modelling system. Its main advantage is its low cost. At the heart of the application is a set of differential equations. The system has ability to easily modify the mathematical model and its solver demonstrates high speed of computation. Finally this system doesn't need immense computational power, so can be run on PC.

The results from the first non-linear model verification are very promising.

References

[1] Abkowitz M.A.: *Lectures on Ship Hydrodynamics – Steering and Manoeuvrability*, Lungby, Denmark, 1964.

[2] Comstock J. P.: *Principles of Naval Architecture*, The Society of Naval Architects and Marine Engineers, New York, 1967.

[3] Press W.T., Teukolsky S.A., Vetterling W.T., Flannery B. P.: *Numerical Recipes in C*, Cambridge University Press, New York, USA, 1992.
[4] Kincaid D., Chenney W.: *Numerical Analysis*, Mathematics of Scientific Computing, The University Texas at Austin, 2002.
[5] *Proceedings of the 23rd INTERNATIONAL TOWING TANK CONFERENCE*, The Specialist Committee on Esso Osaka.

Komputerowy system predykcji właściwości manewrowych statków.

W pracy przedstawiono strukturę niedrogiego, umiarkowanie dokładnego systemu do określania parametrów, mających kluczowy wpływ na właściwości manewrowe statków. Zaproponowane rozwiązanie zostało opracowane na podstawie zmodyfikowanego modelu Abkowitza, zarówno dla liniowych i nieliniowych równań ruchu.

ARCHIVES OF CIVIL AND MECHANICAL ENGINEERING

Vol. VII 2007 No. 3

Mathematical models in description of capsizing scenarios

T. HINZ
Foundation for Safety of Navigation and Environment Protection

Nowadays, although the knowledge of the causes of capsizing is more and more vast, still the large quantities of ships sink as a result of capsizing accidents. Therefore, this particular subject is widely discussed in the paper as a major issue among many prominent research centres. Presently, the results of the numerical simulations represent the most important part in these debates. This paper is my first attempt to demonstrate some of the main mathematical models used in hydrodynamics to describe different scenarios of capsizing. Generally, the article concentrates on non-linear models due to the fact that they are widely employed to practical calculations. These models are used both for capsizing tests and, very often, for judging design parameters, such as slamming, green-water-on-deck, etc. The choice of mentioned scenarios was made according to their frequency in real circumstances.

Keywords: *water on deck, parametric roll, broaching, model*

1. Introduction

The most common reasons for capsizing of ships are the following phenomena:

- parametric roll resonance,
- broaching,
- water on deck,
- extreme and fricke waves,
- poor stability lost,
- free surface.

Both the estimation of free surface influence and assessment of poor stability lost have been utilized for many years. There is no need for complicated mathematical models to examine these scenarios. On the other hand, the first four scenarios are distinguished by much more complex physical background, what is described in details in this paper.

IMO in its work on supplementing stability regulations, presents three most significant scenarios, which should be included into IS Code according to opinion of distinguished experts in this area [1]:

- parametric roll resonance,
- broaching,
- dead-ship condition.

This article provides the description of scenarios connected with following phenomena:

- broaching,
- parametric roll resonance,
- water on deck.

Another scenario the so-called “dead-ship condition” will not be presented in this work because it is still in the initial level of research.

Broaching is defined by Umeda as “the phenomenon whereby the ship cannot maintain her course despite maximum steering effort” [2], [3].

The state that is characterized as “If the encounter period is a multiple of half of the roll period, the roll motion develops with a period equal to the natural roll period” Umeda calls the parametric roll resonance [3].

2. Existing computational models

The mathematical model is a description of real conditions that is usually prepared for using complicated mathematical methods.

In order to examine more complicated scenarios of the ship’s capsizing, the more advanced mathematical models are used for solving hydrodynamics of phenomena. The base for all these models is the second Newton’s Law. To obtain the solution of the motion equation is not so complex. There are many computational libraries that are capable of integrating the systems of ordinary differential equations. The features that distinguish one model from another are the different ways of determining hydromechanical forces and coefficients that appear in the motion equations.

The models that are employed to describe the scenarios have the non-linear character because the hydromechanical coefficients, which are conformed in them, are dependent on time.

It is extremely challenging to separate the mathematical models from the software where these models are used. Due to that, in this paper the division of scenarios is replaced by the division of software. This particular layout is also sensible in the case when the software (mathematical models) has more general character and describes different scenarios.

2.1. LAMP

The “LAMP” model has wide applications. It can be used to examine the stability of ships and the issues related to the ship structure behaviour in waves.

The model that is included in the LAMP software is based on six degrees of freedom (DOF) and potential flow. The model is non-linear. There are two kinds of approaches used in the model: one related to the mixed source formulation and another one connected with the IRF-based formulation (Impulse Response Function).

The first formulation is based on the division of the computation domain into two parts: inner domain and outer domain (Figure 1). In the inner domain the Rankine sources distributed over the wetted surface of the hull is used, the matching surface

and the free surface between the hull and matching surface [4]. The outer domain is solved with Green functions distributed only over an arbitrarily shaped matching surface, because these particular functions meet both the linear condition of free surface and the radiation condition. In the case of the matching surface, the conditions connected with the velocity potential and the continuity of derivatives are imposed. These assumptions allow to conduct further calculations according to the boundary elements method.

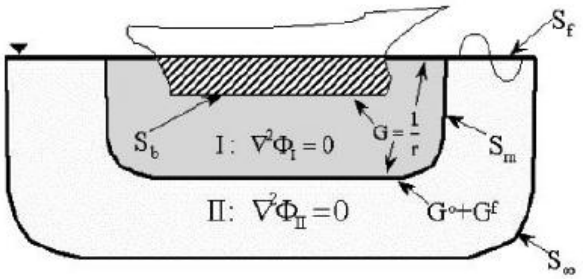

Fig. 1. Computational domain in mixed source formulation [4, 5]

In the IRF formulation, velocity potentials are pre-computed for steady forward speed [P006]. Further computations are reduced to the combination of the potentials of IRF with the actual ship motions and wave height.

Despite the forces connected with the pressures that are determined according to above conceptions, this method uses the non-pressure forces for instance [5]:

- forces generated by anti-rolling fins,
- forces generated by the positioning systems,
- forces generated by the propellers and rudders,
- viscous roll damping.

There are four approaches used to conduct the computations related to the green water on deck phenomena.

3. Hydrostatic and Froude-Krylov forces

The deck pressure is computed from the linear condition for the wave for each submerged deck element. Such an approach is a combination of hydrostatical pressure and Froude-Krylov forces [6].

4. Semi-empirical model

In this model the computations are calculated using an empirical expression derived from Zhou [7], aside from it, the approach proposed by Buchner is applied here as well [8].

5. Shallow water flow calculation [6]

In this case a finite-volume method is applied. The calculation is done only for the longitudinal and transverse motions assuming that these calculations are conducted for the shallow water conditions.

In the shallow water method, the equations of conservation of mass (1) and momentum (2) are calculated in the time domain using the approach that is used in shallow water's computations. Simultaneously, the effects connected with stickiness are not taken into account in the calculations. This method was offered by Stoker. The acceleration normal to the deck is omitted in the computations, whereas the tangential velocity and pressure are constant in the case of the whole height. In this method, 3D calculations are reduced to the calculations in 2D space. The division of computational domain is demonstrated in Figure 2 [6]. The axis Z in configuration, which is connected with the deck, is placed parallel to the direction of gravitational acceleration. The area is divided into cuboids with the surface of base C_e and the surface of sides A_S.

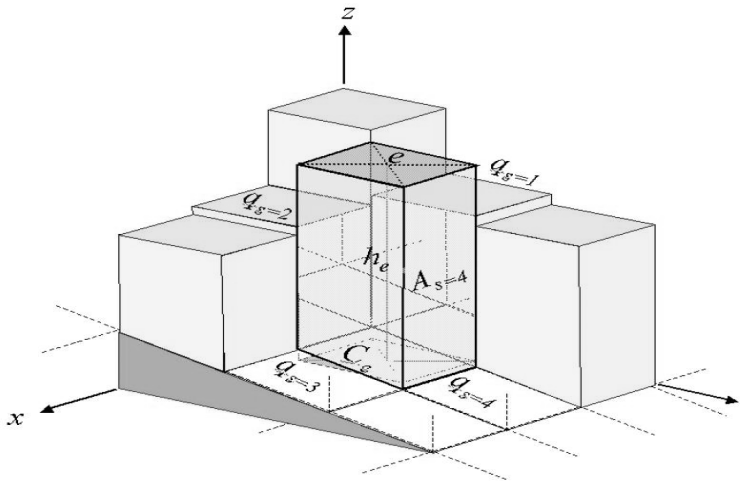

Fig. 2. Fluid's element in shallow water method [6]

$$\frac{dm}{dt} = \frac{\partial}{\partial t}\int_{CV} \rho dVol + \int_{CS} \rho(v_r \cdot n) dS = 0\,, \tag{1}$$

$$\frac{d(mv)}{dt} = \frac{\partial}{\partial t}\int_{CV} v\rho dVol + \int_{CS} v\rho(v_r \cdot n) dS = \\ = \int_{CS_e} p(-n dS) - \int_{CV_e} b dVol\,, \tag{2}$$

After appropriate transformations are done, the equation of conservation of mass takes the form that can be used to attain the numeral solutions (3), similar form is taken by the equation of conservation of momentum (4) [7].

$$M_{ee}^{j} h_{e}^{k_j+1} + \sum_{s=1}^{4} M_{eq_s}^{j} h_{q_s}^{k_j+1} = W_{e}^{j} \ , \tag{3}$$

$$R_{ee}^{j} v_{e}^{k_j+1} + \sum_{s=1}^{4} R_{eq_s}^{j} v_{q_s}^{k_j+1} = S_{e}^{j} \ . \tag{4}$$

This particular approach is used as the main method in order to calculate the influence of water on the deck in the LAMP system [6].

6. Full Computation Fluid Dynamics (CFD) Calculation

The flow calculation is computed using a finite-volume method (FEM) and a 3-D volume grid. In comparison to shallow water, flow calculation is done for three motion directions: vertical, longitudinal and transverse flow [6].

Figures 3, 4 and 5 present results of regular wave roll calculation for 3 cases [6]:

- without Effect of Water on Deck (Figure 3),
- with Hydrostatic Forces of Deck (Figure 4),
- including Finite-Volume Water on Deck (Figure 5).

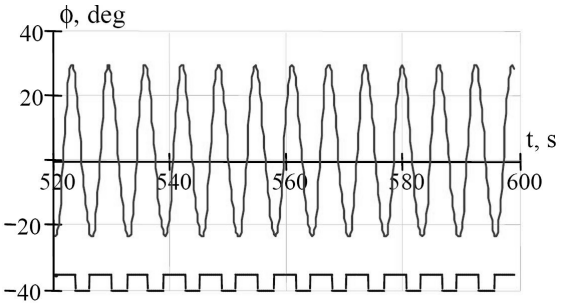

Fig. 3. Regular wave roll without Effect of Water on Deck – roll angel [6]

The computation of parametric roll resonance in LAMP system is performed as a part of the numerical simulation of the ship motion. The roll damping coefficient is computed using the method [9]:

- an empirical method derived from the Kato,
- methodology coefficients adapted from model tests.

Figure 6 presents comparisons of effects of roll damping computed with different methods.

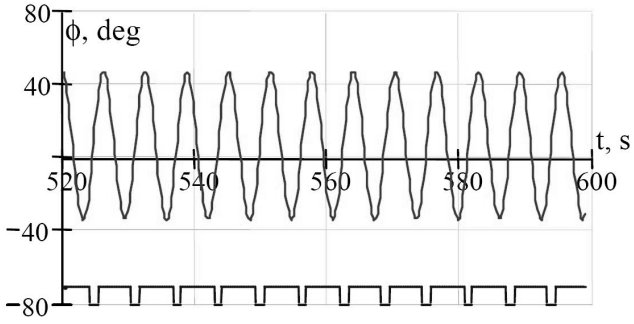

Fig. 4. Regular wave roll Regular wave roll without Effect of Water on Deck – roll angel [6]

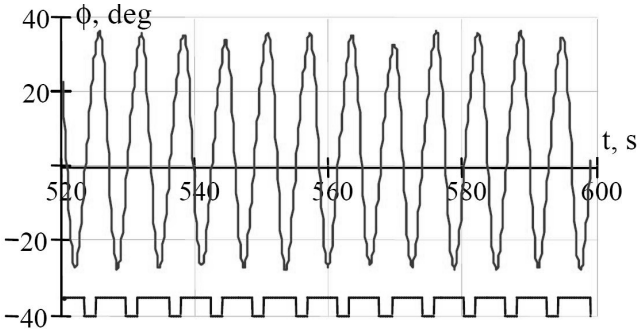

Fig. 5. Regular wave roll Regular wave roll including Finite-Volume Water on Deck – roll angel [6]

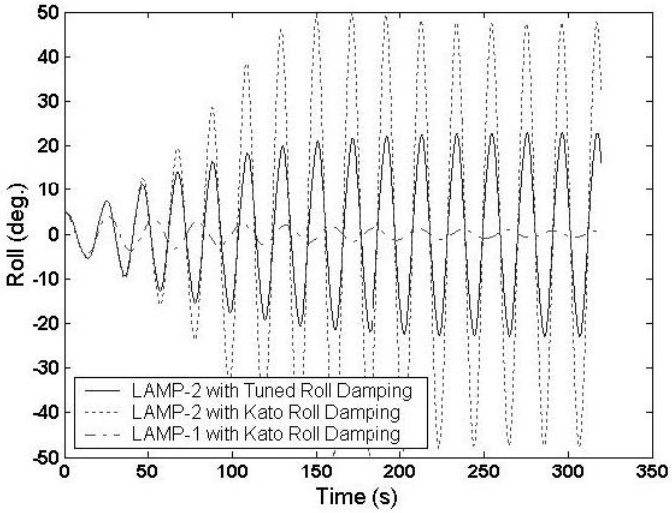

Fig. 6. Comparisons of effect of roll damping model on regular wave [9]

7. OU-Broach

This model was mainly developed for computing the broaching and surf-riding phenomena. It is based on 4 DOF related to the surge-sway-yow-roll motions [2]. As the broaching phenomenon is related to manoeuvring [1], this particular model can be also used to calculate the manoeuvring properties. Currently, the non-linear wave forces are used in this model [2] (originally the linear approach was applied here).

The model is based on the state equation (5) [2].

$$\dot{x} = F(x;b) = \{f_1(x;b), f_2(x;b), \ldots, f_8(x;b)\}. \tag{5}$$

The wave forces and moments are defined as a sum of lift force (Figure 7) and Froude-Krylov force and Smith effect [10].

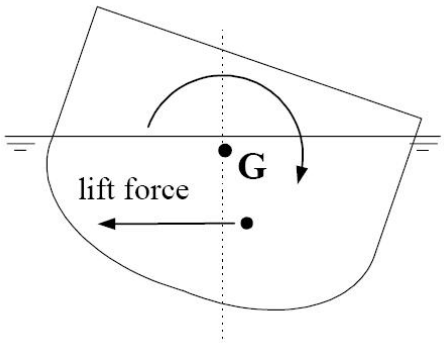

Fig. 7. Schematic view induced lift force and moment [10]

The wave effect on restoring arm is determined by the expression that is obtained in empirical way [10]. Equations 6 presents component of the wave effect on restoring arm [10]. Figure 8 shows comparisons of righting arm between the calculation based on Froud-Krylov assumption and the experiment [10].The transverse restoring moment is computed using the hydrostatic method [3]. The forces and moments connected with manoeuvring are defined in the non-linear way for calm water [3]. Equations 8–11 shows nonlinear manoeuvring forces and moments [10].

$$\begin{aligned} GZ^{WL} = [\{(7.4 \cdot e^{-7.9 \cdot Fn})(-\zeta_a \cos(2\pi\xi_G / \lambda + 0.314)) + (18.6 \cdot e^{-9.2 xFn}) \cdot \\ (2\zeta_a)^2 / L\} \cdot \phi \cdot \frac{1}{2} \rho L d u^2\}] \cdot H_{eff} \cdot (\frac{d}{2} - OG) / W \end{aligned} \tag{6}$$

where

$$H_{eff} = \sqrt{\frac{2\pi \frac{L}{\lambda}\cos(\chi)\sin(\pi \frac{L}{\lambda}\cos(\chi))}{\pi^2 - (\pi \frac{L}{\lambda}\cos(\chi))^2}}\,, \tag{7}$$

$$X_{NL} = X_{vr}(u) + X_{vv}(u)v^2 + X_{rr}(u)r^2 + (m + m_y)vr\,, \tag{8}$$

$$Y_{NL} = Y_{vvv}(u)v^3 + Y_{rrr}(u)r^3 + Y_{vvr}(u)v^2 r + Y_{vrr}(u)vr^2\,, \tag{9}$$

$$N_{NL} = N_{vvv}(u)v^3 + N_{rrr}(u)r^3 + N_{vvr}(u)v^2 r + N_{vrr}(u)vr^2\,, \tag{10}$$

$$K_{NL} = K_{vvv}(u)v^3 + K_{rrr}(u)r^3 + K_{vvr}(u)v^2 r + K_{vrr}(u)vr^2\,. \tag{11}$$

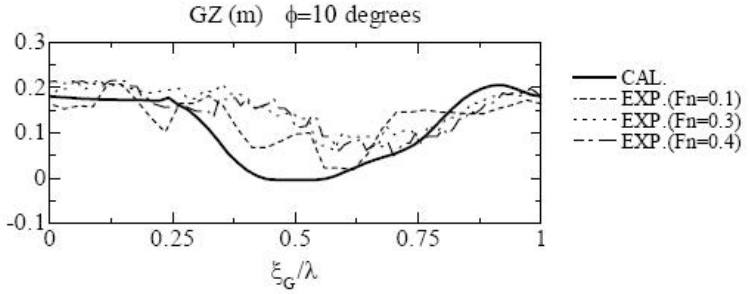

Fig. 8. Comparisons of righting arm between the calculation based on Froud-Krylov assumption and the experiment for the ship with H/λ = 1/15, λ/L = 1.5, χ = 30 degrees

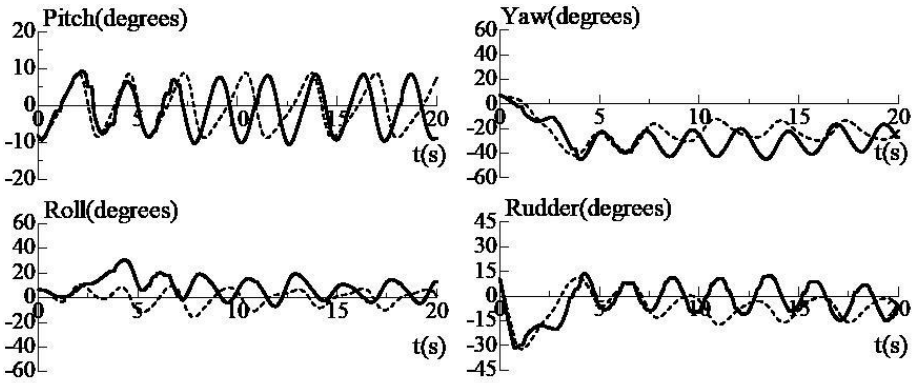

Fig. 9. Comparison between the numerical results and experimental results; continuous line – experimental, dotted line – calculation [10]

Figure 9 shows comparison between the numerical results and experimental results with $H/\lambda = 1/10$, $\lambda/L = 1.637$, $\chi = -30$ degrees and $Fn = 0.3$ [10].

8. Future

At present, the models, that are being used, allow to forecast the probability of the ship's capsizing in a quite detailed way, of course according to the quality approach.

The present models are mainly based using the potential methods. They seem still to be derived from the strip theory. A man should aim to the widest usage of CFD in computations. It is possible that FEM with the usage of turbulence model would cause the improvement in the accuracy of results [11].

Currently, the models for simulating the parametric roll resonance, broaching and green-water-on-deck are still being under development. However, according to the IMO recommendations, there is a need for developing computational models that simulate also different scenarios of ship's capsizing [1]. It also concerns the models such as the dead-ship condition model or others, which shut be developed even from the statistics point of view.

9. Conclusion

This study focuses on two models only that are used to simulate the scenarios of the ship's capsizing. It is a tiny part of numerous computational models. There are models dedicated to particular scenarios. On the other hand, there are models, general ones, which are encased in the different additional elements in order to enlarge the accuracy of calculations.

References

[1] Umeda N., Hashimoto H., Paroko D., Hori M.: *Recent developments of theoretical prediction on capsize of intact ships in waves*, Marine Systems & Ocean Technology, Vol. 2, 2006, No. 1–2.

[2] Umeda N., Hashimoto H.: *Qualitative aspects of nonlinear ship motions in following and quartering seas with high forward velocity*, Journal of Marine Science and Technology, Vol. 6, 2002.

[3] Umeda N., Peters A.: *Recent Research Progress on Intact Stability in Following/Quartering Seas*, Proc. 6th International Ship Stability Workshop, Webb Institute, New York, September, 2002.

[4] Lin W.M., Zhang S.: *A mixed source formulation for nonlinear ship-motion and wave-load simulations*, 1999.

[5] Weems K., Zhang S., Lin W.M., Shin Y.S, Bennett J.: *Structural Dynamic Loadings Due to Impact and Whipping*, Proceedings of the Seventh International Symposium on Practical Design of Ships and Mobile Units, 1998.

[6] Belenky V., Liut D., Weems K., Shin Y.S.: *Nonlinear ship roll simulation with water-on-deck*, Proc. 6th International Ship Stability Workshop, Webb Institute, New York, September, 2002.
[7] Zhou Z.Q., De Kat J.O., Buchner B.: *A Nonlinear 3-D Approach to Simulate Green Water Dynamics on Deck*, Proc. 7th Numerical Simulation Hydrodynamics, 1999.
[8] Buchner B.: *On the Impact of Green Water Loading on Ship and Offshore Unit Design*, Proc. 6th Symposium on Practical Design of Ships and Mobile Units.
[9] France W., Levadou M., Treakle T., Pauling J., Michel R., Moore C.: *An Investigation of Head-Sea Parametric Rolling and its Influence on Container Lashing Systems*, SNAME Annual Meeting, 2001.
[10] Hashimoto H., Umeda N.: *Enhanced Approach for Broaching Prediction with Higher Order Terms Taken into Account*, Proc. 6th International Ship Stability Workshop, Webb Institute, New York, September, 2002.
[11] J. Gorski: *A Perspective on the Progress and Role of RANS Codes for Predicting Large Amplitude Ship Motions*, Proc. 6th International Ship Stability Workshop, Webb Institute, New York, September, 2002.

Matematyczne modele w opisie scenariuszy przewracania

Współcześnie, chociaż coraz lepiej znamy mechanizmy przewracania się statków, nadal dużą ich część tonie w wyniku różnego rodzaju wypadków statecznościowych. Dlatego też ta tematyka ciągle zajmuje główne miejsce wśród zagadnień, którymi zajmują się główne ośrodki naukowe. Obecnie coraz większą role odgrywa symulacja numeryczna. Niniejszy artykuł jest próbą przedstawienia modeli matematycznych stosowanych obecnie w hydromechanice do opisu scenariuszy przewracania się. Wybór scenariuszy podyktowany jest ich najczęstszym występowaniem. Każdy z prezentowanych modeli w jakiś sposób opisuje zjawiska występujące podczas przewracania się.

ARCHIVES OF CIVIL AND MECHANICAL ENGINEERING

Vol. VII 2007 No. 3

Comparison of EFD and CFD investigations of velocity fields for selected body–propeller configurations

P. HOFFMANN, S. JAWORSKI, A. KOZŁOWSKA
Ship Design and Research Centre S.A., Ship Hydromechanics Division, Szczecińska 65, 80-392 Gdansk

Purpose of this paper is to analyse correlation between CFD calculation and experiments on axisymmetric body with working propeller. Model tests were conducted in 1981–1986 in the cavitation tunnels of Ship Propeller Department of the Institute of Fluid Flow Machinery of the Polish Academy of Sciences and in Ship Hydromechanics Division Ship Design and Research Centre in Gdańsk [1–6]. CFD calculations were made in 2007 in Ship Hydromechanics Division Ship Design and Research Centre in Gdańsk.

Keywords: *CFD, axisymmetric body, actuator disc*

1. Introduction

Knowledge about the velocity field around the axisymmetric body with working propeller is important for designing submarine propulsion, torpedoes, semi submerged ships, pod propellers. It is also important for theoretical analysis of propeller-hull interaction to obtain ship wake prognosis. The purpose of this paper is to analyse current CFD methods and to answer the question: "Can experimental methods be used only for verification of end result?"

2. Experimental Equipment and Techniques

Basic experimental tests were conducted in cavitation tunnel (test section dimensions of 0.425 m × 0.425 × 1.3) in Ship Propeller Department of the Institute of Fluid Flow Machinery (IFFM) of the Polish Academy of Sciences. During the test some axisymmetric bodies were analysed – each had different waterline exit angle on stern (from 19° to 40°).

The comparison of experiment and CFD calculations was made with three axisymmetric bodies (waterline exit angle on stern: β = 19°, 30°, 40°). Placing of axisymmetric body in the measuring space of cavitation tunnel is shown on Figure 1.

The following tests were made:

- measurements of the nominal velocity field (V_n) in cross-sections with constant velocity of undisturbed flow (V_∞),
- measurements of the total velocity field (V_t) with constant thrust coefficient (K_T) in the same cross-sections,

• measurements of the total velocity field (V_t) in the cross-section near the propeller plane in whole range of thrust coefficient (K_T),

• measurements of the suction and pressure distribution on the body caused by change of load of the propeller [1, 4, 5]. Velocity field measurement was made by miniature Prandtl probe. The probe measured only the axial velocity,

• part of the tests was repeated in bigger measuring space of cavitation tunnel in Ship Hydromechanics Division of Ship Design and Research Centre in Gdańsk [2, 3, 6].

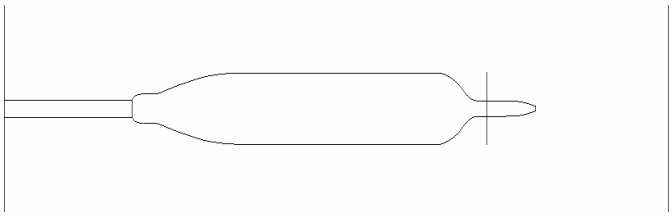

Fig. 1. Placing of radial-symmetric body in the test section

Table 1: Propeller data

r/R	m/l	t/l	l/D	P/D
0.2	0.0230	0.2250	0.2210	0.853
0.3	0.0199	0.1880	0.2383	0.840
0.4	0.0173	0.1506	0.2537	0.831
0.5	0.0150	0.1162	0.2685	0.823
0.6	0.0130	0.0861	0.2812	0.821
0.7	0.0113	0.0605	0.2913	0.822
0.8	0.0099	0.0393	0.2973	0.819
0.9	0.0089	0.0259	0.2999	0.825
1.0	0.0080	0.0150	0.2993	0.825

where:
r – radius of blade section,
m – profile camber,
t – maximum thickness,
l – profile chord length,
P/D – pitch ratio.

Propeller data is follow:
– Propeller no: 082
– Profile type: NACA 16/NACA 08
– $A_E/A_0 = 0.565$
– $D = 0.147$ m
– $D_p = 0.2D = 0.0294$ m

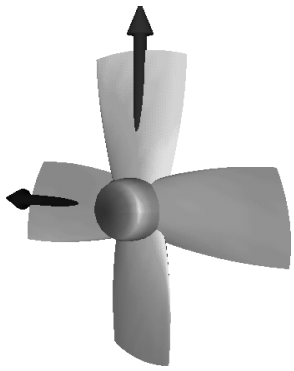

Fig. 2. Propeller used in experiments

Table 2. Working propeller parameters in cavitation tunnel (IFFM)

Pos.	K_T		Jt Propeller on shaft	Jt *K*-19	Jt *K*-30	Jt *K*-40
1	0.12	Jt	0.635	0.690	0.755	0.828
		$10K_Q$	0.204	0.211	0.198	0.186
2	0.16	Jt	0.555	0.595	0.645	0.703
		$10K_Q$	0.250	0.254	0.244	0.236
3	0.20	Jt	0.468	0.498	0.536	0.579
		$10K_Q$	0.293	0.294	0.289	0.284

3. CFD analysis

The computations were carried out at the same scale as the model test using the RANSE method. The flow was computed in the domain of the following dimensions: 0.425 m × 0.425 × 1.3. The flow solver Fluent was used.

The propeller was approximated by an actuator disc with the same diameter as the real propeller.

The mesh of hexahedral type was used. The number of mesh cells was about 850 000. The pictures below show the mesh on the bodies surface and placing of the actuator disc in one of axisymmetric bodies.

Validation of CFD calculations was done by comparing with velocities measured during experiments for the all studied body–propeller configurations in two different planes near the working propeller.

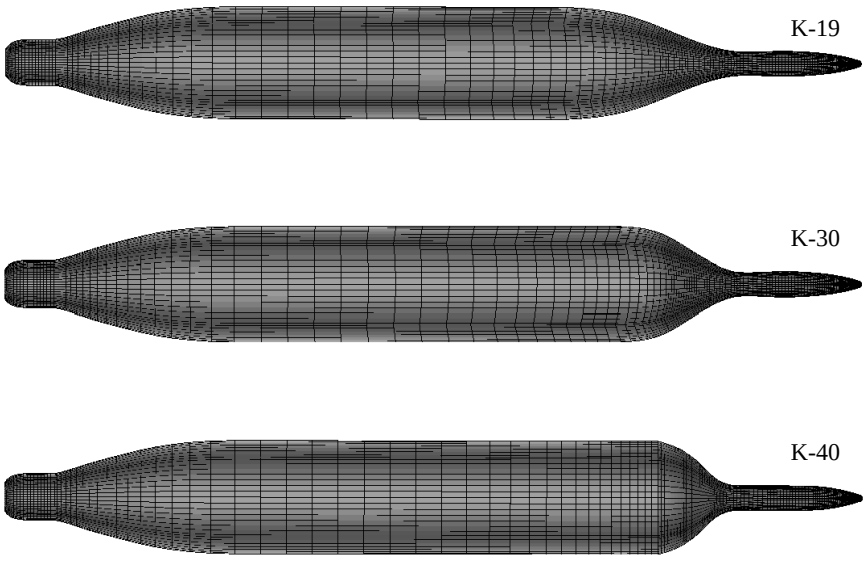

Fig. 3. Hexahedral mesh on the body surface

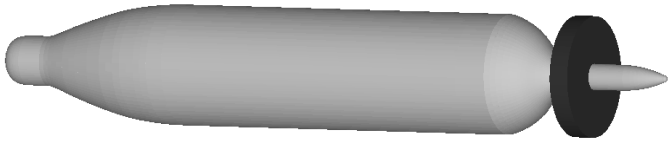

Fig. 4. Actuator disc (darker object on right) simulating propeller in CFD calculations

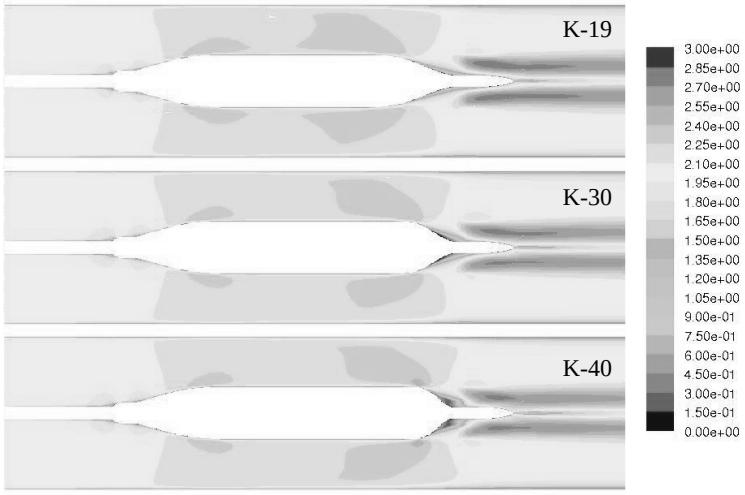

Fig. 5. Total velocity V_t field distribution for $K_t = 0.12$

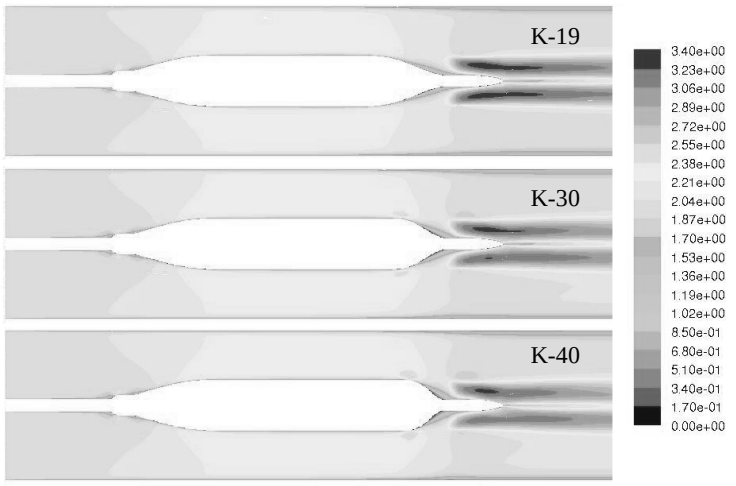

Fig. 6. Total velocity V_t field distribution for $K_t = 0.16$

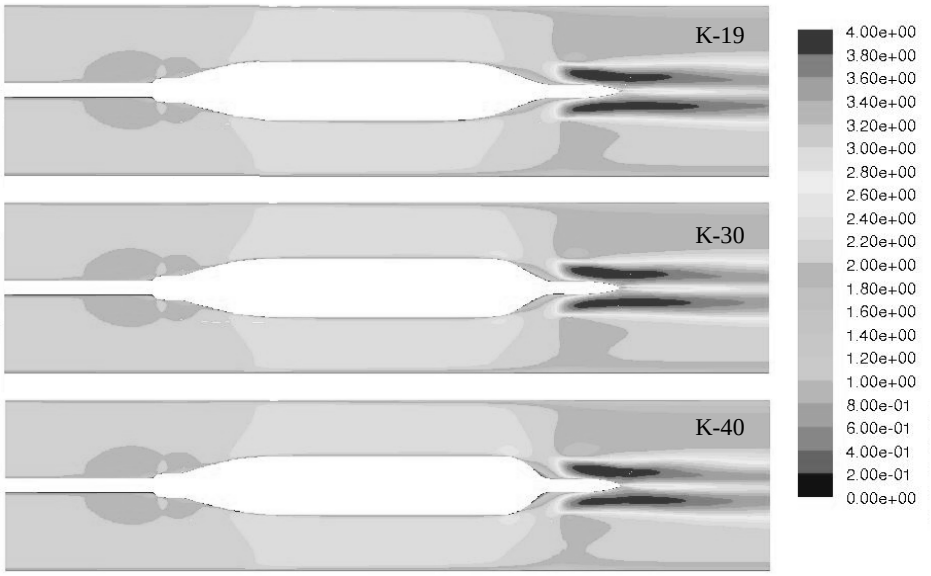

Fig. 7. Total velocity V_t field distribution for $K_t = 0.20$

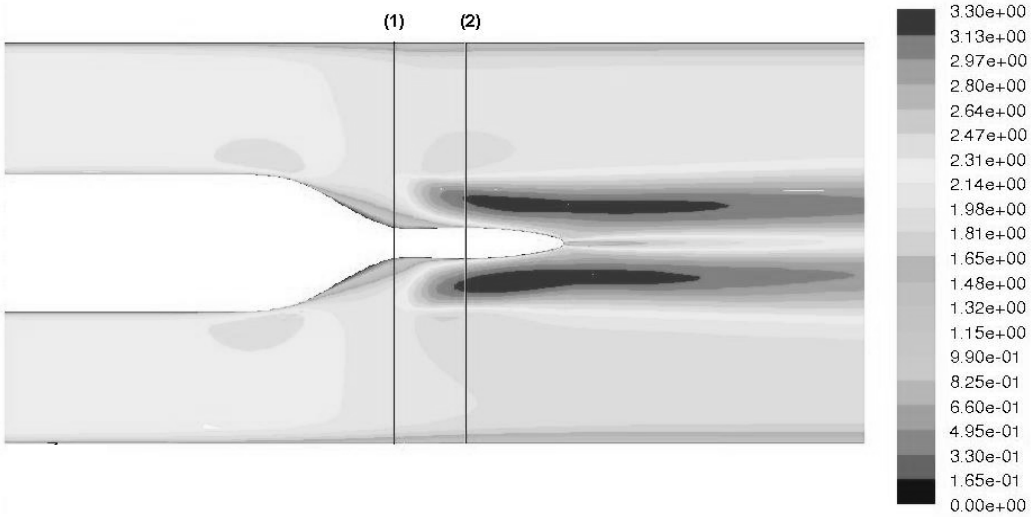

Fig. 8. Axial position of measuring planes for *K*20 body and 082 propeller (plane 1, $x = -0.19D$; plane 2, $x = +0.29D$, where D – propeller diameter)

Figures 9 and 10 present example results of this validation task which was done for *K*20 body and 082 propeller.

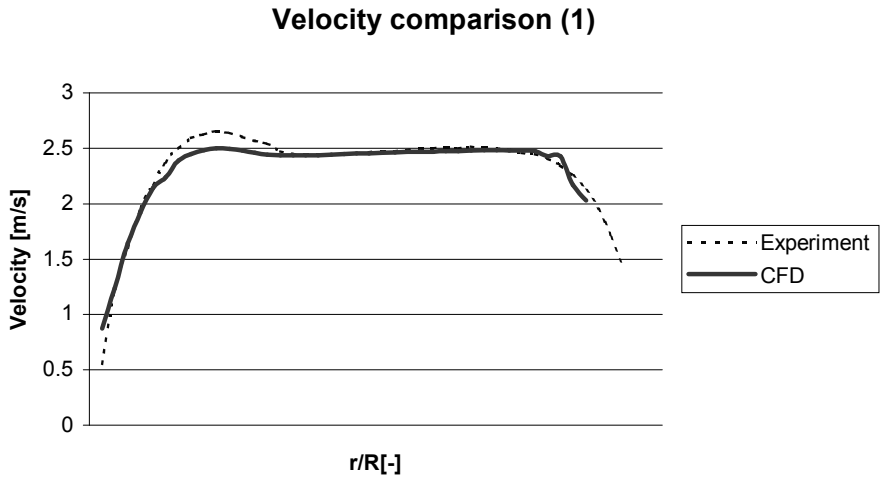

Fig. 9. Radial distribution of total velocity measured and calculated on plane 1, see Figure 8

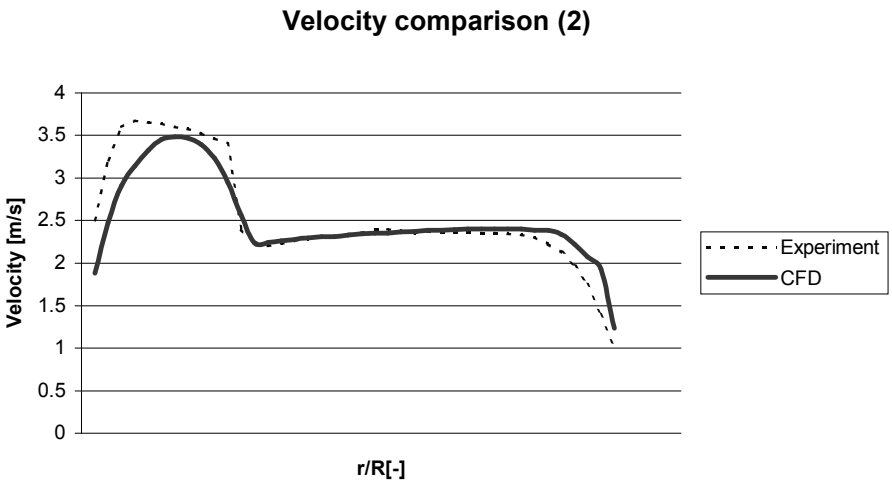

Fig. 10. Radial distribution of total velocity measured and calculated on plane 2, see Figure 8

4. Conclusion

The comparison shows that CFD calculations of velocity field behind the axisymmetric body with working propeller gives a good approximation of experiment from quantitative and qualitative approach. It is necessary to broaden our knowledge by conducting more experiments and computations to achieve better approximation of

working propeller in CFD. This could be achieved by replacing actuator disc with computer model of real propeller. Results are generally promising and the work will be continued.

References

[1] Jaworski S.: *Complex measurements interaction between propeller and axisymmetric body in cavitation tunnel*, Technical Report IMP PAN, No. 148, 1981.
[2] Jaworski S., Iwanicki R., Malińska J.: *Model test in cavitation tunnel, measured interaction between propeller no. 153 and axisymmetric body S10*, Technical Report OHO CTO, No. RH–83/Z–173.
[3] Jaworski S., Iwanicki R., Malińska J.: *Model test in cavitation tunnel. Model Analysis of the interaction between the Propeller and axisymmetric body*, Raport OHO CTO, No. RH–84/Z–143.
[4] Bugalski T., Jaworski S.: *Computer Analysis of the Interaction between the Propeller and an Axisymmetric Body*, XIII Seminar on Ship Hydrodynamics, Varna, 1984.
[5] Bugalski T., Jaworski S.: *Analysis of the interaction between the propeller and axisymmetric body*, VI Symposium on Ship Hydromechanics, Gdańsk, 1985.
[6] Iwanicki R.: *Model test in cavitation tunnel, measurements of nominal and real velocity field behind axisymmetric body; Finding new methods to determine effective velocity field*, Report OHO CTO, No. RH–86/Z–171.

Porównanie wyników badań modelowych (EFD) i obliczeń numerycznych (CFD) pól prędkości dla wybranych układów ciało osiowosymetryczne – pędnik śrubowy

W pracy przeanalizowano korelację między obliczeniami, za pomocą numerycznej hydromechaniki (CFD), a wynikami badań modelowych pól prędkości wokół serii ciał osiowosymetrycznych z pracującym pędnikiem (modelem śruby okrętowej). Badania modelowe prowadzono w latach 1981–1986 w tunelu kawitacyjnym Instytutu Maszyn Przepływowych PAN w Gdańsku oraz Ośrodku Hydromechaniki Okrętu Centrum Techniki Okrętowej w Gdańsku [1–6]. Natomiast obliczenia numeryczne metodami CFD przeprowadzono w 2007 roku w Ośrodku Hydromechaniki Okrętu Centrum Techniki Okrętowej S.A. w Gdańsku.

ARCHIVES OF CIVIL AND MECHANICAL ENGINEERING

Vol. VII 2007 No. 3

Selection of the most suitable method to split the resistance increment into components related to individual propellers of double-ended ferry

H. JARZYNA
The Szewalski Institute of Fluid-Flow Machinery PASci, ul. Fiszera 14, 80-952 Gdańsk

The resistance increment ΔR_{D+R} measured in model propulsion tests of a double-ended ferry with the pushing aft propeller SR and the pulling fore propeller SD is to be split into two components: ΔR_R and ΔR_D related to each of the propellers. The splitting procedure based on the measured magnitudes is possible only when additional assumptions are made.

Two procedures are presented in this paper. The first procedure, $i = 1$, is directly related to the components of resistance increment ΔR_R and ΔR_D. The second procedure, $i = 2$, is related to the components $(R_0 - F_D)_R$ and $(R_0 - F_D)_D$ attributed to individual propellers. In both procedures the same assumptions are used for splitting. Proposed assumptions are based on the proportion of propeller thrust T_R and T_D, or on the proportion of the delivered power P_{DR} and P_{DD}. Procedures combined with assumptions define the methods and are denoted K_{ij} where subscript j refers to the assumption.

Two prerequisites were formulated. Both have to be satisfied by methods of practical importance:

1. $\Delta R_R + \Delta R_D = \Delta R_{D+R}$,
2. $\Delta R_{R1j} = \Delta R_{R2j}$ and $\Delta R_{D1j} = \Delta R_{D2j}$.

Above prerequisites are satisfied only by the K_{11} and K_{21} methods. The methods K_{13} and K_{23} satisfy only the first prerequisite.

Keywords: *self-propulsion test, double-ended ferry, resistance increment due to propeller action*

Notations

F_D – skin friction correction in self propulsion test,
n_R, n_D – rate of propeller revolution of SR and SD propeller respectively,
P_{DR}, P_{DD} – power delivered to SR and SD propeller respectively, in case of the simultaneous action of SR and SD propellers,
P_D – total delivered power, $P_D = P_{DR} + P_{DD}$,
$P_{D(0+R)}$ – power delivered to the SR propeller, in case of the alone action of SR propeller,
$P_{D(D+0)}$ – power delivered to the SD propeller, in case of the alone action of SD propeller,
P_{Dm} – mean delivered power, $P_{Dm} = \dfrac{P_{D(0+R)} + P_{D(D+0)}}{2}$,
R_0 – model ship resistance,
SD – fore propeller (pulling propeller),
SR – aft propeller (pushing propeller),
t_D – coefficient of resistance increment due to SD propeller, in case of the simultaneous action of SR and SD propellers,
t_R – coefficient of resistance increment due to SR propeller, in case of the simultaneous action of SR and SD propellers,
t_{D+R} – coefficient of resistance increment due to SR and SD propellers in simultaneous action,

t_{0+R} – coefficient of resistance increment due to SR propeller in alone action,
t_{D+0} – coefficient of resistance increment due to SD propeller in alone action,
T_R, T_D – thrust of SR and SD propeller respectively, in case of the simultaneous action of SR and SD propellers,
T_{D+R} – total thrust of SD and SR propellers in simultaneous action, $T_{D+R} = T_D + T_R$,
T_{0+R} – thrust of SR propeller, in case of the alone action of SR propeller,
T_{D+0} – thrust of SD propeller, in case of the alone action of SD propeller,
T_m – mean propeller thrust, $T_m = \frac{T_{0+R} + T_{D+0}}{2}$,
V_M – speed of model ship,
ΔR_R, ΔR_D – resistance increments due to SR and SD propeller respectively, in case of the simultaneous action of SR and SD propellers,
ΔR_{D+R} – resistance increment due to the simultaneous action of SR and SD propellers,
Upper index t^R or t^T indicates that coefficient was defined using R_0 or T_{D+R} respectively.

1. Introduction

1.1. The problem to be solved based on the model of self-propulsion test

The double-ended ferry with the pushing propeller SR and the pulling propeller SD is put in the self-propulsion model test. There are no problems in measuring some magnitudes such as:

T_R, $T_D \rightarrow T_{D+R} = T_R + T_D$

n_R, n_D, V_M,

R_0 is provided from resistance tests. Some other magnitudes are calculated, namely F_D and $\Delta R_{D+R} = T_{D+R} - (R_0 - F_D)$.

The resistance increment ΔR_{D+R} due to the simultaneous action of the SD and SR propellers is to be split into the components ΔR_R and ΔR_D related to each of these propellers. The determination of these components is the only problem to be solved in this paper. The task will be completed by definition and examination of procedures and additional assumptions.

1.2. Procedures

Resistance increment can be written in two different forms:

$$\Delta R_{D+R} = \Delta R_R + \Delta R_D, \tag{1}$$

or

$$\Delta R_{D+R} = T_{D+R} - (R_0 - F_D) = T_R - (R_0 - F_D)_R + T_D - (R_0 - F_D)_D. \tag{2}$$

The first notation can be transferred to:

$$1 = \frac{\Delta R_R}{\Delta R_{D+R}} + \frac{\Delta R_D}{\Delta R_{D+R}}. \tag{3}$$

The components ΔR_R and ΔR_D in Equation (1) can be determined according to the following formulae:

$$\Delta R_R = \Delta R_{D+R} \times (A_j)_R, \tag{4}$$

$$\Delta R_D = \Delta R_{D+R} \times (A_j)_D, \tag{5}$$

where:

$(A_j)_D$ and $(A_j)_R$ denote the factors corresponding to assumptions.

According to the second notation (2):

$$\begin{aligned} R_0 - F_D &= (R_0 - F_D)_R + (R_0 - F_D)_D \\ 1 &= \frac{(R_0 - F_D)_R}{R_0 - F_D} + \frac{(R_0 - F_D)_D}{R_0 - F_D}. \end{aligned} \tag{6}$$

The components $(R_0 - F_D)_D$ and $(R_0 - F_D)_R$ can be determined according to the following formulae:

$$\Delta R_R = T_R - (R_0 - F_D) \times (A_j)_R, \tag{7}$$

$$\Delta R_D = T_D - (R_0 - F_D) \times (A_j)_D. \tag{8}$$

This way two procedures were defined. The first procedure ($i = 1$):

$$\Delta R_{R1} = \Delta R_{D+R} \times (A_j)_R, \tag{9}$$

$$\Delta R_{D1} = \Delta R_{D+R} \times (A_j)_D. \tag{10}$$

and the second one ($i = 2$):

$$\Delta R_{R2} = T_R - (R_0 - F_D) \times (A_j)_R, \tag{11}$$

$$\Delta R_{D2} = T_D - (R_0 - F_D) \times (A_j)_D. \tag{12}$$

1.3. Proposed assumptions

The considered assumptions are listed in Table.

Table. Assumptions

	$(A_j)_R$ =	$(A_j)_D$ =	
j = 1 based on thrust ratio	$\frac{T_R}{T_{D+R}}$	$\frac{T_D}{T_{D+R}}$	(13)
j = 2 based on thrust ratio	$\frac{T_R}{T_{0+R}}$	$\frac{T_D}{T_{D+0}}$	(14)
j = 3 based on power ratio	$\frac{P_{DR}}{P_D}$	$\frac{P_{DD}}{P_D}$	(15)
j = 4 based on power ratio	$\frac{P_{DR}}{P_{D(0+R)}}$	$\frac{P_{DD}}{P_{D(D+0)}}$	(16)
j = 5 based on thrust ratio	$\frac{T_R}{T_m}$	$\frac{T_D}{T_m}$	(17)
j = 6 based on power ratio	$\frac{P_{DR}}{P_{Dm}}$	$\frac{P_{DD}}{P_{Dm}}$	(18)

The factors A_1 and A_3 can be calculated using the measured values of T_R, T_D, P_{DR} and P_{DD} from the model self-propulsion test with SR and SD propellers in simultaneous action. The fractions A_2, A_4, A_5 and A_6 can be calculated using the measured values of T_{0+R} and $P_{D(0+R)}$ from self-propulsion test with SR propeller in action, and values of T_{D+0} and $P_{D(D+0)}$ from self-propulsion test with SD propeller in action.

1.4. Possible combinations of procedures and assumptions

The first group of splitting methods is related to the procedure i = 1. These methods were composed by combining the procedure with six assumptions which allow to determine the components ΔR_R and ΔR_D of the total resistance increment ΔR_{D+R}:

$$\Delta R_{R1j} = \Delta R_{D+R} \times (A_j)_R, \tag{19}$$

$$\Delta R_{D1j} = \Delta R_{D+R} \times (A_j)_D, \tag{20}$$

where:

j – relates to each of the six assumptions.

The second group of methods is related to the procedure i = 2. These methods were composed alike by combining the second procedure with individual assumptions:

$$\Delta R_{R2j} = T_R - (R_0 - F_D) \times (A_j)_R, \tag{21}$$

$$\Delta R_{D2j} = T_R - (R_0 - F_D) \times (A_j)_D. \tag{22}$$

There are altogether 12 methods (i.e. procedures combined with assumptions K_{ij}) that will be evaluated in this paper from the point of view of usefulness in propeller design, investigation and verification.

1.5. Prerequisites for selection of valid assumptions

First of all the methods have to be examined if they fulfil the basic prerequisite:

$$\Delta R_{D+R} = \Delta R_{Rij} + \Delta R_{Dij}, \tag{23}$$

for *i*-th procedure and for *j*-th assumption. This condition states, that the sum of the components ΔR_D and ΔR_R must be equal to resistance increment ΔR_{D+R}.

Next another prerequisite has to be analyzed. It can be written as follows:

$$\Delta R_{R1j} = \Delta R_{R2j}, \qquad \Delta R_{D1j} = \Delta R_{D2j}. \tag{24}$$

It means that the ΔR_R (or ΔR_D) components determined according to the same assumption „*j*" in both procedures ($i = 1$ and $i = 2$) have to be equal to each other either unconditionally or conditionally.

Another question is if the component ΔR_R (or ΔR_D) calculated using the same procedure ($i = 1$ or $i = 2$) and various assumptions has the same value:

$$\Delta R_{Rij} = \Delta R_{Ri(j+n)}$$

$$\Delta R_{Dij} = \Delta R_{Di(j+n)} \tag{25}$$

1.6. Nondimensional form of the resistance increment

The nondimensional coefficients are introduced similar to the thrust deduction fraction. They relate each resistance increment ΔR with a magnitude that is constant in the considered problem. The most suitable magnitudes are the ship resistance R_0 and the total thrust T_{D+R} in the case where it is constant. The proposed coefficients are listed bellow:

$$t^R_{Rij} = \frac{\Delta R_{Rij}}{R_0}, \qquad t^T_{Rij} = \frac{\Delta R_{Rij}}{T_{D+R}}, \tag{26}$$

$$t^R_{Dij} = \frac{\Delta R_{Dij}}{R_0}, \qquad t^T_{Dij} = \frac{\Delta R_{Dij}}{T_{D+R}}, \tag{27}$$

$$t^R_{D+R} = \frac{\Delta R_{D+R}}{R_0}, \qquad t^T_{D+R} = \frac{\Delta R_{D+R}}{T_{D+R}}, \tag{28}$$

$$t^R_{D+0} = \frac{\Delta R_{D+0}}{R_0}, \qquad t^T_{D+0} = \frac{\Delta R_{D+0}}{T_{D+0}}, \tag{29}$$

$$t_{0+R}^{R} = \frac{\Delta R_{0+R}}{R_0}, \qquad t_{0+R}^{T} = \frac{\Delta R_{0+R}}{T_{0+R}}. \tag{30}$$

The values T_R and T_D can not be used as reference magnitudes because they are variable in the domains $0 \le T_R \le T_{D+R}$ and $T_{D+R} \ge T_D \ge 0$ in the considered problem.

2. Resistance increment split using the K_{11} and K_{21} methods

When the assumption ($j = 1$) is applied the sum of resistance increments ΔR_R and ΔR_D is equal to the global resistance increment ΔR_{D+R} in both procedures $i = 1$ and $i = 2$:

$$\Delta R_R + \Delta R_{D11} = \Delta R_{D+R}, \qquad t_{R11}^{R} + t_{D11}^{R} = t_{D+R}^{R}, \qquad t_{R11}^{T} + t_{D11}^{T} = t_{D+R}^{T}, \tag{31}$$

$$\Delta R_{R21} + \Delta R_{D21} = \Delta R_{D+R}, \qquad t_{R21}^{R} + t_{D21}^{R} = t_{D+R}^{R}, \qquad t_{R21}^{T} + t_{D21}^{T} = t_{D+R}^{T}. \tag{32}$$

In the case where the assumption $j = 1$ is used also the same values of ΔR_R and ΔR_D are received in both procedures $i = 1$ and $i = 2$.

$$\Delta R_{R11} = \Delta R_{R21}, \qquad t_{R11}^{R} = t_{R21}^{R}, \qquad t_{R11}^{T} = t_{R21}^{T}, \tag{33}$$

$$\Delta R_{D11} = \Delta R_{D21}, \qquad t_{D11}^{R} = t_{D21}^{R}, \qquad t_{D11}^{T} = t_{D21}^{T}. \tag{34}$$

3. Resistance increment split using the K_{13} and K_{23} methods

When the assumption ($j = 3$) is applied the sum of resistance increments ΔR_R and ΔR_D is equal to the global resistance increment ΔR_{D+R} in both procedures $i = 1$ and $i = 2$.

$$\Delta R_{\mathrm{R13}} + \Delta R_{D13} = \Delta R_{D+R}, \qquad t_{R13}^{R} + t_{D13}^{R} = t_{D+R}^{R}, \qquad t_{R13}^{T} + t_{D13}^{T} = t_{D+R}^{T}, \tag{35}$$

$$\Delta R_{\mathrm{R23}} + \Delta R_{D23} = \Delta R_{D+R}, \qquad t_{R23}^{R} + t_{D23}^{R} = t_{D+R}^{R}, \qquad t_{R23}^{T} + t_{D23}^{T} = t_{D+R}^{T}. \tag{36}$$

However, the shares of components from methods K_{13} i K_{23} are the same only conditionally. The condition $P_{DR}/P_{DD} = T_R/T_D$ usually does not hold. The values ΔP_P calculated using the assumption $j = 3$ in both procedures $i = 1$ and $i = 2$ are then different. Consequently, different are also the values of ΔR_D:

$$\Delta R_{\mathrm{R13}} \neq \Delta R_{R23}, \qquad t^{R}_{R13} \neq t^{R}_{R23}, \qquad t^{T}_{R13} \neq t^{T}_{R23}, \tag{37}$$

$$\Delta R_{\mathrm{D13}} \neq \Delta R_{D23}, \qquad t^{R}_{D13} \neq t^{R}_{D23}, \qquad t^{T}_{D13} \neq t^{T}_{D23}. \tag{38}$$

4. Conclusions

- The prerequisite $\Delta R_{Rij} + \Delta R_{Dij} = \Delta R_{D+\mathrm{R}}$ (or $t_{Rij} + t_{Dij} = t_{D+R}$ in terms of nondimensional coefficients) is fulfilled unconditionally only when the assumption $j = 1$ or $j = 3$ is used in any procedure $i = 1$ or $i = 2$.
- In both procedures $i = 1$ and $i = 2$ the same values of ΔR_R are received ($\Delta R_{R11} = \Delta R_{R21}$ or $t_{R11} = t_{R21}$) and the same values of ΔR_D are received ($\Delta R_{D11} = \Delta R_{R2}$ or $t_{D11} = t_{D21}$) only when the assumption $j = 1$ is used.
- When the assumption $j = 3$ is used the values of ΔR_R and ΔR_D are usually different in both procedures $i = 1$ and $i = 2$ ($\Delta R_{R13} \neq \Delta R_{R23}$ and $\Delta R_{D13} \neq \Delta R_{D23}$, or $t_{R13} \neq t_{R23}$ and $t_{D13} \neq t_{D23}$).
- Considering the prerequisites (23) and (24) it can be concluded that both of them are satisfied simultaneously only when the assumption $j = 1$ in the procedure $i = 1$ or $i = 2$ is used.

References

[1] Jarzyna, H.: *Możliwe hipotezy podziału globalnej zmiany oporu kadłuba na składniki związane ze śrubą pchającą SR i ciągnącą SD przy ich jednoczesnej pracy*, to be published in CTO-Gdańsk.

[2] Jarzyna, H.: *The possible hypotheses of global hull resistance change division in two parts connected with pushing SR and pulling SD propellers in simultaneous action*, to be published in CTO-Gdańsk.

[3] Jarzyna, H.: *Podstawy oceny przydatności projektowej, badawczej i weryfikacyjnej kryteriów podziału mierzalnej całkowitej zmiany oporu kadłuba ΔR_{D+R} na składniki ΔR_R i ΔR_D przypisane śrubom ciągnącej SD i pchającej SR pracującymi jednocześnie*, Część I. Treść prezentacji seminaryjnej w CTO-OHO, Część II. Podsumowanie ustaleń.

[4] Jarzyna, H.: *The model ship hull resistance change due to simultaneous action of aft and bow screw propeller*, Proceeding of Hydronav'05, Gdańsk–Ostróda, Sept., 2005.

Rezultaty wyboru kryterium podziału globalnej zmiany oporu kadłuba na składniki związane z obu śrubami promu symetrycznego

Pomierzoną w modelowych badaniach napędowych promów symetrycznych globalną zmianę oporu kadłuba ΔR_{D+R} wskutek działania śruby rufowej SR i dziobowej SD należy podzielić na składniki ΔR_R i ΔR_D związane z każdą ze śrub. Podział taki możliwy jest pod warun-

kiem przyjęcia dodatkowych założeń. Praca analizuje możliwe założenia w dwu grupach proceduralnych.

Procedura pierwsza, $i = 1$, wiąże bezpośrednio zmiany ΔR_R i ΔR_D z hipotezami zmian. Procedura druga, $i = 2$, wiąże zmiany $(R_0 - F_D)_R$ i $(R_0 - F_D)_D$ z tymi samymi hipotezami zmian.

Hipoteza pierwsza, j=1, zakłada proporcjonalność zmian z obu procedur do mierzalnych naporów T_R i T_D. Hipoteza druga, $j = 2$, zakłada proporcjonalność zmian z obu procedur do mierzalnych mocy P_{DR} i P_{DD}.

Rozpatruje się kryteria zmian określane jako K_{ij}. Sformułowano dwa warunki, jakie spełniać winny poszczególne kryteria akceptowalne do stosowania.

1. $\Delta R_R + \Delta R_D = \Delta R_{D+R}$,

2. $\Delta R_{R1j} = \Delta R_{R2j}$, $\Delta R_{D1j} = \Delta R_{D2j}$.

Stwierdzono, że oba warunki są spełnione, gdy stosuje się kryterium K_{11} i kryterium K_{21}. Kryteria K_{13} i K_{23} spełniają jedynie warunek pierwszy.

ARCHIVES OF CIVIL AND MECHANICAL ENGINEERING

Vol. VII 2007 No. 3

Simplified RANSE simulation of a side launching

M. KRASKOWSKI
Ship Design and Research Centre S.A., Ship Hydromechanics Division, Szczecińska 65, 80-392 Gdańsk

In some Polish shipyards, building small vessels like AHTS, fishing vessels and container feeders, side launching is the basic method of launching. Due to safety reasons, in some cases Ship Design and Research Centre S.A. is asked to perform the model tests of side launching to estimate the following parameters of the hull motion during the launching:

- Heel angles – too large heel angle causes the risk of capsizing or hitting the quay.
- Minimum distance between the cribbing of the hull and the bottom of the basin.

A series of such tests for 115 m container ship were performed lately. On the other hand, a numerical method for solving the flow around moving bodies was successfully implemented by Ship Design and Research Centre S.A. – till now it was used for evaluating the flow around the ship hull free to trim and sink. Satisfactory results of these computations encouraged to apply the numerical method for the prediction of hull motion during side launching, and the first attempt of such computations is presented below.

Keywords: *CFD, side launching, fluid-structure interaction*

1. Method

The flow solver COMET, extended with the user-programmed rigid body motion module, was used for the computations. The basic features of the simulation were the following:

- the RANSE model of the flow and the finite volume method were applied,
- the VOF method was used to solve the free-surface flow,
- the dynamic mesh, moving rigidly together with the hull, was used to enable the motion of the hull,
- the forces obtained from the flow solver were used to solve the equations of motion.

Figure 1 presents the sketch of the modelled situation as well as the location of the global coordinate system *XYZ* (the *X* axis points from stern to bow).

Due to complexity of the problem, it was radically simplified in the first approach. The following assumptions were done:

- the presence of the quay was taken into account only as the constraint of the motion in the initial phase of the launching. Its influence of the flow was neglected,
- the geometry of the cribbing was greatly simplified – only the elements causing the largest damping of the rolling were considered,
- only 3 degrees of freedom were considered in the model of motion. This dramatically simplifies the computer code for solving the motion.

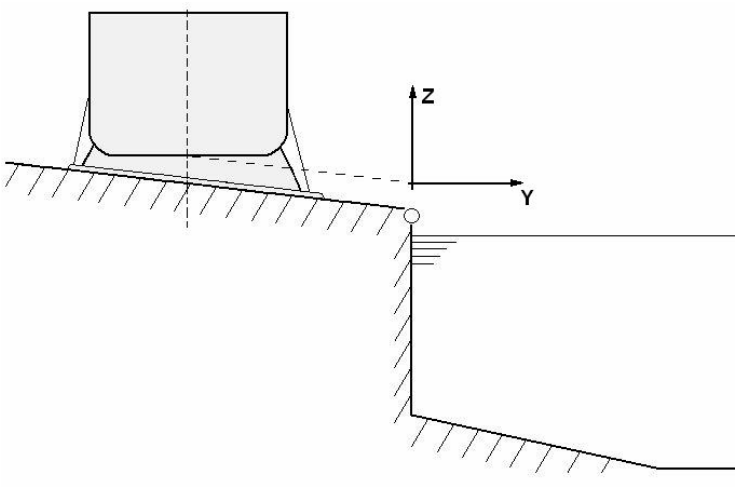

Fig. 1. Modelled situation

Figure 2 presents the mechanical model of the motion.

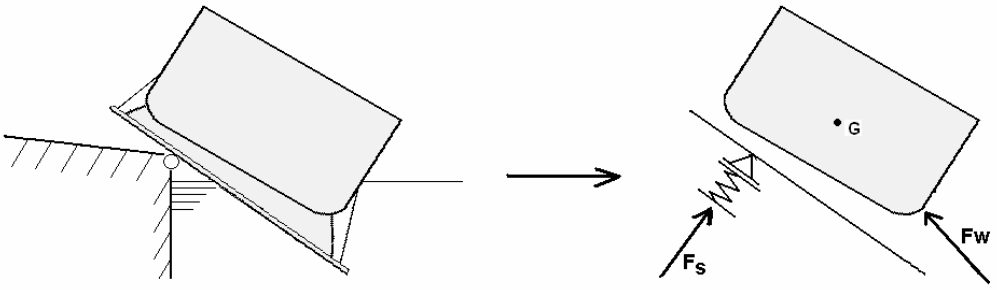

Fig. 2. Mechanical model of the motion

As shown above, the slipway is modelled with the pivot bearing of finite stiffness.

The following denotations were used in Figure 2:

F_S – force exerted on the hull by the slipway,

F_W – force exerted on the hull by the water.

Force F_W is obtained from the flow solver, and the force F_S is calculated by the rigid body motion module basing on the current location of the hull. Its location in the coordinate system connected with the slipway is fixed, and its direction is perpendicular to the skids. The value of this force is proportional to the deflection of the bearing.

The forces exerted by the slipway and the water are reduced to the gravity centre of the hull with cribbing, and thus they produce some moment M_X. The equations of the motion are solved for the gravity centre, so they can be written in the simplest form:

$$\frac{d^2Y}{dt^2}=\frac{F_Y}{m},\frac{d^2Z}{dt^2}=\frac{F_Z}{m},\frac{d^2\varphi}{dt^2}=\frac{M_X}{I_X}, \tag{1}$$

where:

φ – is the angle of heel,

m – hull mass,

I_X – hull moment of inertia,

F_Y, F_Z – components of the sum of forces exerted by the water and the slipway, reduced to the centre of gravity.

The following initial conditions were applied:

- location of the hull: the gravity centre of the hull is located directly above the end of the slipway,
- initial velocity was taken from the model test (it was assumed that it is possible to estimate the hull velocity in this location correctly and thus it is not necessary to solve the motion from the moment of release).

Numerical integration of these equations is conducted with the use of the explicit scheme. The algorithm of the motion computations can thus be described in the following way:

a) Compute the displacements in Y and Z direction using the initial velocity components:

$$\begin{aligned}\Delta Y &= V_{0Y}\times\Delta t,\\ \Delta Z &= V_{0Z}\times\Delta t.\end{aligned} \tag{2}$$

Compute the flow for the new location of the hull.

Compute the force exerted by the water and the reaction of the slipway (basing on the deflection of the bearing).

b) Compute the translational and angular acceleration basing on the old values of forces:

$$\begin{aligned}a_Y &= \frac{F_{Y\text{old}}}{m},\\ a_Z &= \frac{F_{Z\text{old}}}{m},\\ \varepsilon_X &= \frac{M_{X\text{old}}}{I_X}.\end{aligned} \tag{3}$$

Compute new values of velocity:

$$V_Y = V_{Y\text{old}} + a_Y\times\Delta t,$$

$$V_Z = V_{Z\text{old}} + a_Z \times \Delta t, \tag{4}$$

$$\omega_X = \omega_{X\text{old}} + \varepsilon_{X\text{old}} \times \Delta t.$$

Compute the displacements:

$$\Delta Y = V_Y \times \Delta t,$$

$$\Delta Z = V_Z \times \Delta t, \tag{5}$$

$$\Delta\varphi = \omega_X \times \Delta t.$$

Compute the deflection of the bearing and its reaction.

Compute the force exerted by the water. Average the water forces using the values from the current (new) and old time step (old):

$$F_{Yw} = 0.5(F_{Yw\_\text{new}} + F_{Yw\_\text{old}}),$$

$$F_{Zw} = 0.5(F_{Zw\_\text{new}} + F_{Zw\_\text{old}}), \tag{6}$$

$$M_{Xw} = 0.5(M_{Xw\_\text{new}} + M_{Xw\_\text{old}}).$$

Note: averaging the water forces in two time steps turned out to be necessary to assure the stability of the computations. On the other hand, this procedure must not be applied to the slipway forces – this would produce increasing oscillations of the hull sliding on the bearing. Each component of the force is thus computed as follows:

$$F = F_s + 0.5\,(F_{w\_\text{new}} + F_{w\_\text{old}}), \tag{7}$$

c) Repeat step 2 until desired time of simulation is reached.

As mentioned above, the numerical mesh is moving as a rigid body together with the hull – there is no relative motion between the nodes of the mesh. The idea of the computations with the dynamic mesh is presented in Figure 3.

The slipway geometry is not taken into account in the mesh, its presence is only considered in the motion model by adding its reaction to the motion equations. In Figure 3, the slipway is drawn to make the sketch clearer.

The flow in the moving domain was solved with the following settings:

- time step was set to 0.001 s,
- five iterations per time step were executed,
- the discretization scheme for the convective terms in momentum equations was Second Order Central, blended with First Order Upwind with the blending factor 0.8,
- low under-relaxation of the velocity was applied, as the time-accurate results are required.

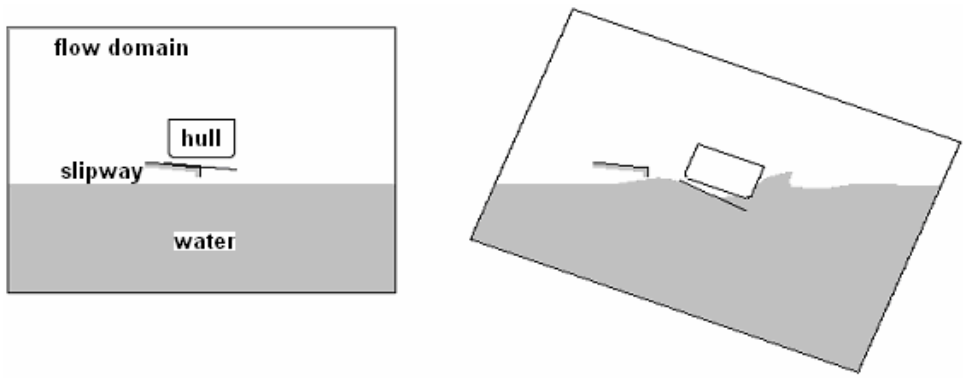

Fig. 3. Idea of the computations with the dynamic mesh

2. Results

2.1. Two-dimensional test case

Before performing the simulation of the hull launching, a 2D test case was computed in order to check the correctness of the user-coding.

The boundary conditions were:

- hydrostatic pressure on the boundaries of the domain.
- no-slip wall condition on the hull and the parts of the cribbing.

The proposed method turned out to be robust and the obtained motion of the hull section in water was looking physically.

The Figures below show the example results in two chosen time points of simulation.

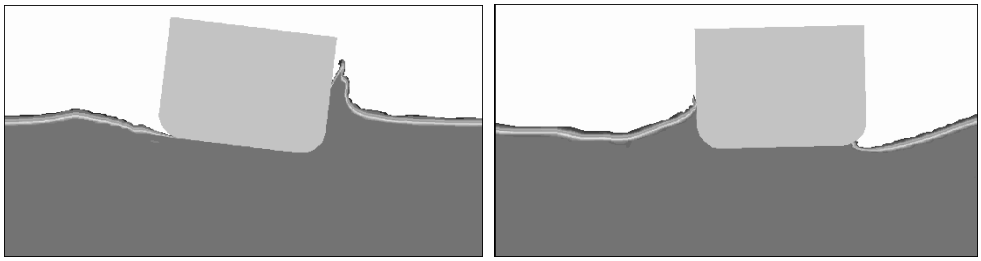

Fig. 4. Results for 2D test case

2.2. Three-dimensional case

After obtaining qualitatively correct results of the 2D analysis, the mesh for 3D hull with simplified cribbing was generated. It was a block-structured, hexahedral mesh containing about 1 million cells, and it was generated with ICEM CFD HEXA.

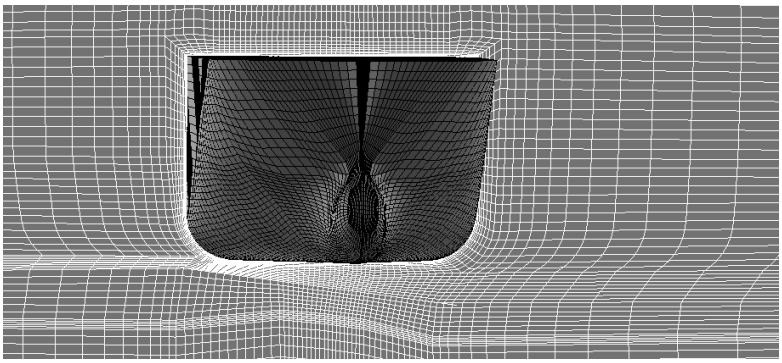

Fig. 5. Mesh for the ship

The range of the domain dimensions, in the ship coordinate system, was:

- X: $-L - 2L$ (L is the hull length),
- Y: $-L - L$,
- Z: $-L - 0.6L$.

Figure shows the surface mesh on the hull with parts of the cribbing and chosen sections of the mesh interior.

As can be seen above, the mesh of 1 million cells, covering both sides of the hull and large space above the hull, is quite coarse. It is not refined in any particular horizontal plane, as the location of the free surface changes rapidly during the simulation.

The simulation was carried out for model scale 1:40 in order to enable the direct comparison of the results. The figures below show the example results in two chosen moments of the 3D simulation.

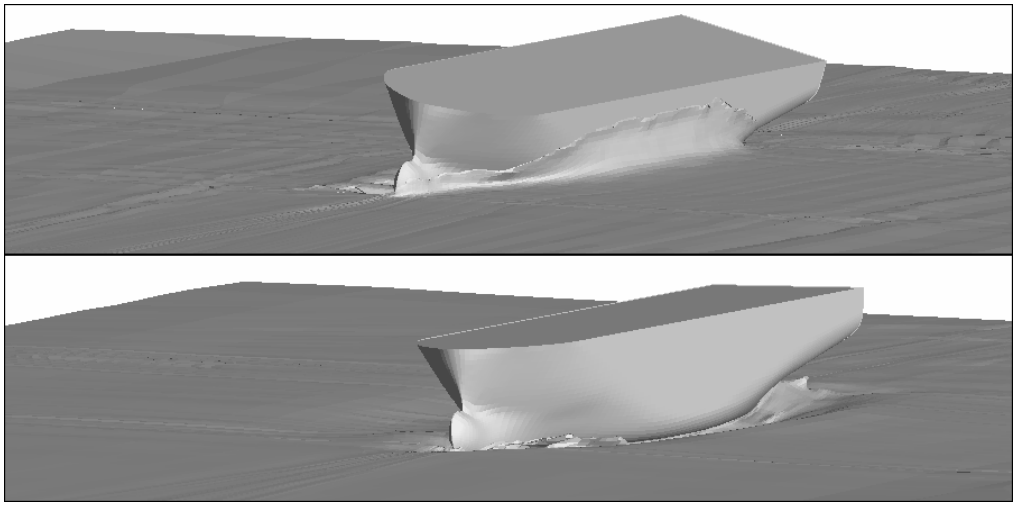

Fig. 6. Example results

Figure 8 shows the comparison of the computed and measured trajectory of two characteristic points, shown in Figure 7.

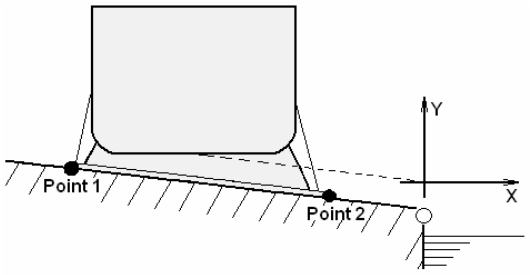

Fig. 7. Definition of the coordinate system

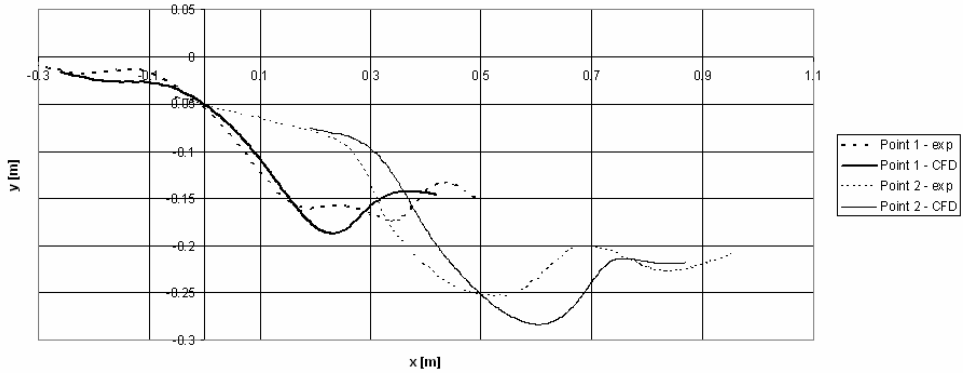

Fig. 8. Comparison of the computed and measured trajectory

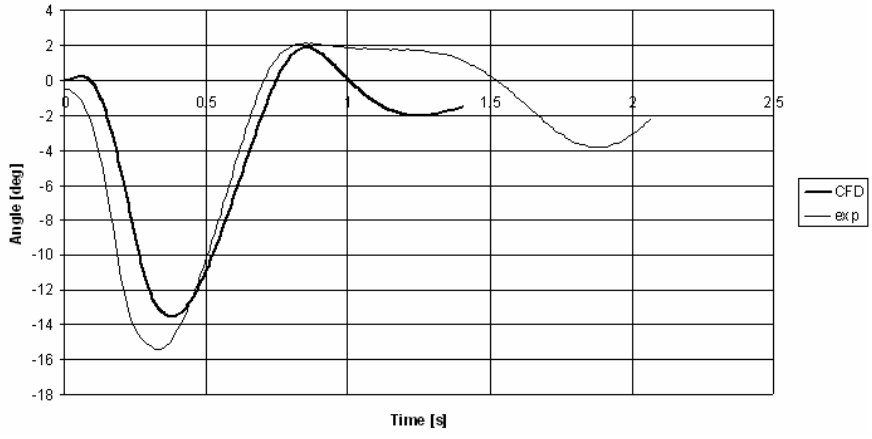

Fig. 9. Comparison of the computed and measured heel angle

The following figure presents the heel angle as a function of time. The first and second maximum of the heel angle are most important for the safety of launching.

2.3. Conclusions

Comparison of the CFD results with the experiment yields the following conclusions:

- the rotation of the hull around the edge of the slipway in the simulation, compared to the experiment, is delayed, which means that the applied model of motion introduces some unphysical inertia and has to be improved,
- qualitative comparison of the trajectories and heel angles shows that the restoring forces and damping forces are modelled quite correctly despite the coarseness of the mesh, which is shown in the comparison of the computed and measured heel angles (up to ~ 0.8 s),
- for the simulation time larger than 0.8 s, large divergence is observed between the computation and the experiment, and this is probably due to the neglecting of the quay in the simulation – after that time the wave reflecting from the quay starts to influence the hull motion,
- although the first results are not accurate enough at the moment, it seems that improving the mechanical model and increasing the mesh resolution will provide a usable method for the prediction of the very initial stage of side launching, and this stage is the most important for the safety.

References

[1] Ferziger J. H., Perić M.: *Computational Methods for Fluid Dynamics*, Springer, Berlin, 1998.
[2] Azcueta R.: *Computations of Turbulent Free-Surface Flows Around Ships and Floating Bodies*, PhD Thesis, Technical University of Hamburg–Harburg, 2001.

Uproszczona symulacja wodowania bocznego z użyciem metody RANSE

W niektórych polskich stoczniach, budujących małe statki takie jak AHTS, statki rybackie i małe kontenerowce (feedery), wodowanie boczne jest podstawową metodą wodowania. Ze względów bezpieczeństwa, w niektórych przypadkach Centrum Techniki Okrętowej otrzymuje zlecenia na wykonanie badań modelowych w celu oszacowania następujących parametrów ruchu kadłuba podczas wodowania:

- kątów przechyłu – zbyt duże kąty przechyłu stwarzają ryzyko wywrócenia statku lub uderzenia burtą w nabrzeże,
- minimalnej odległości między podbudową kadłuba a dnem basenu wodowaniowego.

Ostatnio prowadzone badania tego typu dotyczyły kontenerowca o długości 115 m. Jednocześnie Centrum Techniki Okrętowej z powodzeniem wdrożyło metodę obliczania przepływu

wokół poruszających się ciał – do tej pory używaną do obliczania opływu swobodnego kadłuba statku (z uwzględnieniem dynamicznego trymu i osiadania). Zadowalające wyniki tych obliczeń zachęciły do wykorzystania opracowanej metody numerycznej do prognozowania ruchu kadłuba podczas wodowania bocznego. Pierwsze wyniki takiej symulacji zaprezentowano w niniejszym artykule.

ARCHIVES OF CIVIL AND MECHANICAL ENGINEERING

Vol. VII 2007 No. 3

Statistical data of hull main parametersuseful for preliminary design of SWATH ships

JAN P. MICHALSKI
Gdańsk University of Technology, ul. Narutowicza 11/12, 80-952 Gdańsk
Polish Naval University, ul. Śmidowicza 69, 81-103 Gdynia

The paper presents investigations of statistical relations between main design parameters of the SWATH ship hull shapes, carried out on bibliographical data of more than eighty ships. The statistical relations are presented in the form of histograms of: ship length *L*, length to breadth ratio *L/B*, length to depth ratio *L/H*, length to pontoon diameter ratio *L/D*. Also approximated expressions are presented of the relations between the ship length and vertical clearance *Gap* and between draught *T* and pontoon diameter *D*. The presented statistical expressions, supplemented with assumptions about relations between main dimensions and derived dimensions, may be used for determination of the fast SWATH ship main design parameters at the preliminary design stage or may be a basis for rational selection of the range of variation of main dimensions in a SWATH ship hull shape series.

Keywords: *ship design, new types of ships*

1. Introduction

In the preliminary ship design two basic methodologies are used: the one based on a parent ship and that based on statistical data worked out from an appropriate number of ships of the same type as the ship being designed. The statistics based methodology is particularly useful when detailed information on the parent ship is missing.

Collecting the required statistical data, especially in the case of non-typical ships, is often difficult due to the data being scattered over the literature or not published at all. With the SWATH ships it is even more difficult as it is a new solution and relatively few ships have been built so far. The paper presents statistical relations of the main design parameters of SWATH ships, particularly main dimensions, based on data collected from the available bibliographical sources [1–24]. The statistics presented here may be used in the preliminary design of SWATH ships or in devising a series of shapes e.g. for systematic testing of resistance or seagoing qualities.

However, the set of available data on the existing ships turned out to be too small to allow statistical evaluations. The data was therefore supplemented with the information on ships, which had been a subject of design studies. The combined list, a statistical sample of SWATH ship parameters, contains data of more than eighty ships.

2. Histograms of the selected hull shape parameters

The collected data was used for statistical evaluation of selected parameters, presented in the form of histograms, in order to establish the ranges of practically used hull dimensions and their ratios.

The ship length L histogram presented in Figure 1 illustrates the frequency of appearing in the sample of ships with the length falling into a given range:

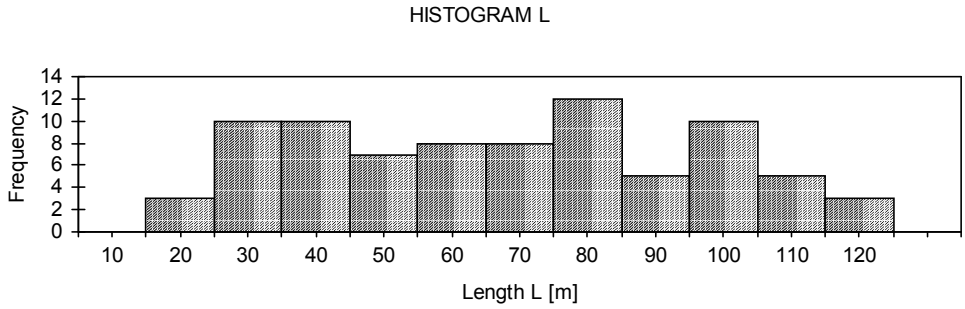

Fig. 1. Histogram of the SWATH ship length L

The histogram in Figure 1 shows that great majority of SWATH ships (if ranges with the smallest numbers are dropped) have lengths in the 20 to 100 meters range. This result coincides with similar evaluation made by the American Bureau of Shipping [2], their publication giving a maximum length of about 130 m.

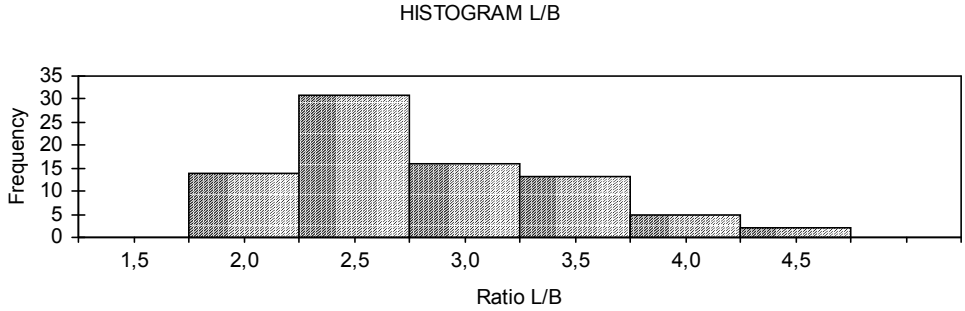

Fig. 2. Histogram of the L/B values for SWATH ships

The L/B ratio is an important parameter both for classical ships (it influences stability, resistance, cubic capacity) and for twin-hull ships. But in SWATH the value of this ratio is chosen mainly due to functional reasons – the required cargo deck arrangement. A separate question is the breadth of underwater body, i.e. the distance

between pontoons based on stability requirements. The histogram presented in Figure 2 shows the range of practically used values of *L/B* ratio.

The choice of depth is based mainly on the stability and seagoing quality requirements – for instance ensuring a sufficient vertical clearance. The histogram presented in Figure 3 shows the range of practically used values of *L/H* ratio.

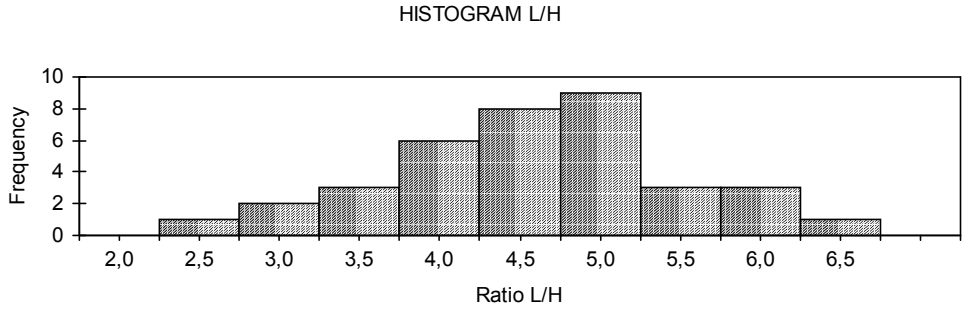

Fig. 3. Histogram of the L/H values for SWATH ships

An important design parameter for twin-hull ships is the ratio of ship breadth *B* to deck box depth *Hd* (parameter influencing the overall strength of ship). The *B/Hd* histogram obtained from the collected data cannot be a basis for statistical inference. Probably some of the causes of a considerable dispersion of the parameter values may be:

- different functional types of ships in the data list,
- different structural materials: mild steel, high tensile steel, aluminium, GRP,
- variety of ship hull structure layouts,
- differentiation of design assumptions of ships in the data list.

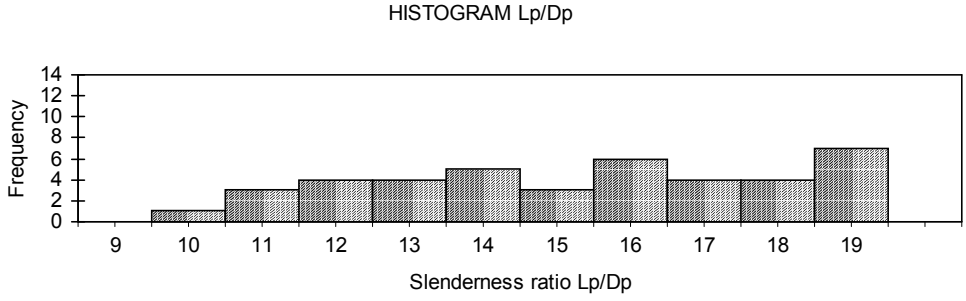

Fig. 4. Histogram of the pontoons slenderness *Lp*/*Dp* for SWATH ships

The *B/Hd* parameter value may be based only on the established mean value. The mean value of the ship breadth to deck box depth ratio *B/Hd* for ships in the data list is

about 7.5. The pontoon slenderness defined as the ratio of pontoon length to cross section area is an important design parameter of SWATH ships. The evaluation of practically used values of this parameter, presented in the form of an equivalent dimensionless ratio of pontoon length to diameter *Lp/Dp*, is shown in the histogram in

3. Auxiliary relations

Apart from the histogram presented in Figure 3, the following relation may be used to determine the ship depth *H*:

$$H = T + Hd + Gap. \tag{1}$$

The unknown values on the right hand side of the equation are draught *T* and clearance *Gap*. The size of clearance is usually determined from the design assumptions – based on the region of ship operation and the maximum sea state when the ship is allowed to leave the port. In that case *Gap* should be treated as a given value. Obviously, the size of clearance is correlated with the ship length. In order to determine the clearance versus ship length relation an approximation function was found:

$$Gap = 0.37 \cdot L^{0.56}, \tag{2}$$

which is illustrated in Figure 5.

As it can be seen from the collected data, the SWATH draught is so chosen that the pontoon draught to diameter ratio *T/Dp* fits into a narrow range of 1.2–1.5:

$$T = (1.2\text{–}1.5) \cdot Dp, \tag{3}$$

which on one side comes from limiting the maximum draught and on the other side is connected with minimizing the wave resistance in the case of fast ships.

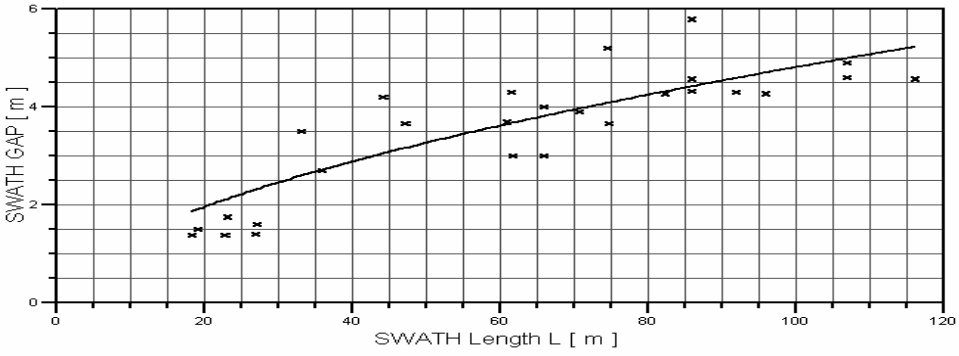

Fig.5. Approximated size of clearance *Gap* as a function of ship length

4. Conclusions

The set of parameters presented above may be used to unequivocally determine a configuration of simplified SWATH hull shape based on four independent main dimensions of the hull: *L*, *B*, *Hd*, *Dp*, draught *T* and vertical clearance *Gap*. The presented statistical expressions, supplemented with assumptions about relations between main dimensions and derived dimensions, may be used for determination of the SWATH ship main design parameters at the preliminary design stage or may be a basis for rational selection of the range of variation of main dimensions in a SWATH ship hull shape series.

References

[1] Bebor M.R., et al.: *Advenced Marine Vehicles – a Review*, Wageningen: Proceedings of Workshop on Developments in Hull Form Design, 1985.
[2] Curry R., Grove T., Mak A.: *Revised classification requirements for the design and construction of high speed ferries*, Sydney: Forth International Conference on Fast Sea Transportation 1997, BAIRD Publication.
[3] Dockter M.E., Schmitdt K.: *SWATH research vessel: the building of RV WesternFlyer*, Marine Technology, Vol. 33, 1996, pp. 3.
[4] Doerffer J.: *Studium wykonalności katamarana o małej wodnicy (SWATH). Analiza badań i wnioski projektowe*, Prace Badawcze nr 194/CPBR 9.5 – 733/89, Gdańsk: Politechnika Gdańska, Instytut Okrętowy, 1989.
[5] Doerffer J.: *Studium wykonalności katamarana o małej wodnicy (SWATH). Założenia projektowe i technologiczne*, Prace Badawcze nr 195/CPBR 9.5 – 734/89, Gdańsk: Politechnika Gdańska, Instytut Okrętowy, 1989.
[6] Dubrowskij W. A et al.: *Mnogokorpusnyje suda*, Leningrad–Sudostrojenie, 1978.
[7] Fernandez-Gonzalez F., Bazan E.N.: *Mission related preliminary design solutions for small* SWATH *ocean patrol vessels*, London: The Royal Institution of Naval Architecture, International Conference on SWATH Ships and Advanced Multi-Hulled Vessels, 1985.
[8] *First Twin-Hull Cruise Ship Enters Service*, The Motor Ship, July, 1992.
[9] Holcomb R.S.: *SWATH International's Super 4000 Class – its design, construction and performance*, Lübeck-Travemünde: Proceedings of the Third International Conference on Fast Sea Transportation FAST'95, 1995.
[10] Joo Y.R., et al.: *Development of a 1200 DWT high-speed Container Ship*, Travemünde: FAST'95 – Third International Conference on Fast Sea Transportation, 1995.
[11] Kennell C.G.: *Small waterplane area twin hull (SWATH) combatant ship parametric study*, Naval Engineers Journal, 1979.
[12] Kennell C.: *SWATH ship design trend*, London: RINA International Conference on SWATH Ships and Advanced Multi-Hulled Vessels, 1985.
[13] Kohnagel J., Bertram V.: *Conceptual Design of a Ro/Ro Catamaran Ferry for Short Sea Shipping*, Ship Technology Research, 1995.

[14] Lang T.G., Sloggett J.E.: *SWATH developments and performence comparisons with other craft*, London: The Royal Institution of Naval Architecture, International Conference on SWATH Ships and Advanced Multi-Hulled Vessels, 1985.
[15] Lee K.Y., Lee D.K, Kim V.D.: *A computer – based design model for coastal passenger SWATH ships*, Ship Technology Research, 1989.
[16] Mabuchi T., Kunitake Y. Nakamura H.: *A status report on design and operational experiences with the semi-submerged catamaran (SSC) vessels*, London: RINA International Conference on SWATH Ships And Advanced Multi-Hulled Vessels, 1985.
[17] MacGregor J.: *The Initialisation Section of Design Tool for SWATH Ships*, Gdańsk: Opracowanie Instytutu Okrętowego Politechniki Gdańskiej nr 120 CPBR 9.5, 1988.
[18] Min K.S., Lee Y.W.: *Design of a High-Speed 300 Passenger SWATH Ship*, Travemünde: FAST'95 – Third International Conference on Fast Sea Transportation, 1995.
[19] Nitz A.,Muxfeldt H.: *SUS B – first results of the German Research Project for SWATH ships conceptual design of a 90 m SWATH*, Yokohama: Proceedings of the Second International Conference on Fast Sea Transportation, FAST'93, 1993.
[20] Papanikolaou A., et al.*: Preliminary design of a high-speed SWATH passenger/car ferry*, Marine Technology, No 3, 1991.
[21] Papanikolaou A.D., et al.: *SMUCC – SWATH Multipurpose Container Carrier*, Travemünde: FAST'95 – Third International Conference on Fast Sea Transportation, 1995.
[22] Seidl L.H., Clifford W.F., Cummings J.P.: *Design and Operational Experience of the SWATH Ship NAVATEK I*, Northern California Section of SNAME, 1991.
[23] *SWATH–Cruiser RADISON DIAMOND – the world's largest twin-hull vessel ready for cruises*, Hansa nr 8, 1992.
[24] Trillo L.R.: *SWATH vessels and semisubmerged catamarans*, High Speed Marine Craft, 1990.

Ocena statystyczna głównych parametrów projektowych kształtu kadłuba statków typu SWATH

W pracy przedstawiono badania dotyczące statystycznych relacji głównych parametrów projektowych kadłuba statków typu SWATH, wykonanych w oparciu o zebrane w literaturze przedmiotu dane o ponad osiemdziesięciu statkach. Zależności statystyczne przedstawiono w postaci histogramów: długości statku L, histogramów wartości stosunków długości do szerokości L/B, długości do wysokości bocznej L/H, długości pływaków do ich średnicy L/D. Ponadto przedstawiono zależności aproksymacyjne przedstawiające relacje między długością statku, a jego prześwitem *Gap* oraz zanurzeniem T, a średnicą pływaków D.

Przedstawione zależności statystyczne, uzupełnione założeniami o relacjach pomiędzy wymiarami głównymi i wymiarami pochodnymi, mogą służyć do wyznaczania głównych parametrów projektowych statków typu SWATH na etapie projektowania wstępnego lub stanowić podstawę do racjonalnego doboru zakresu zmienności wymiarów głównych serii kształtów kadłuba statków typu SWATH.

ARCHIVES OF CIVIL AND MECHANICAL ENGINEERING

Vol. VII 2007 No. 2

The experimental studies on hydrofoil resistance

M. REICHEL, A. BEDNAREK
Ship Design and Research Centre S.A. Ship Hydromechanics Division, Szczecińska 65, 80-392 Gdańsk

This paper presents the hydrofoil resistance model tests which were performed at Ship Design and Research Centre (CTO S.A.). The measurements were carried out in the large towing tank of Ship Hydromechanics Division. A four meters long wooden hydrofoil model was tested. The model was equipped with two lifting foils and a stabilizing front foil. The measurements were conducted for a combination of three values of static trim and two foil angles of attack. A new methodology of shaft angle optimisation with vertical force simulation is presented. The simulation system is an integral extension of the standard dynamometric system for resistance measurements. This paper presents some aspects of the test methodology. The results are briefly presented in the form of standard non-dimensional coefficients in the function of volume Froude number.

Keywords: *hydrofoil resistance, model tests*

1. Introduction

Hydrofoils are nowadays not so popular like in 60's and 70's but some companies from all over the world are still interested in design, production and operation of hydrofoil vessels. Like in a standard design chain the model tests are necessary to obtain a vessel, which is hydrodynamically correct. But in the case of hydrofoil vessels not only the hull shape is important – there is also the question of foils. The designer should choose how the foils will be arranged, what shape they will have etc. Moreover an important issue is what geometrical angle of attack the foils should have. Of course attainable are mathematical models and simulators of hydrofoil performance, which include among other things the attack angles of foils as a parameter, but like all the computer results they should be validated during the model tests.

The Hydromechanics Division of the Ship Design and Research Centre also took a part in research and development of the hydrofoil vessels. In a close cooperation with the Vietnamese Shipbuilding Science and Technology Institute in Hanoi a research project was established. The project consisted of training in computer simulations of hydrofoil vessel performance and of model tests in calm and rough water.

During this project a new methodologies of model test performing and result extrapolation were invented.

2. Methodology

2.1. Model tests

The described resistance tests are in general similar to a standard resistance tests of fully displacement ships. Horizontal component of resistance was measured by extensometric dynamometer OPN-2. The value of dynamic trim angle was obtained from Crosbow – a multicomponent angle and acceleration converter.

In the case of missing full definition of propulsion geometry, particularly the angle of shaft, it is important to have a tool for quantitative estimation of the influence of lacking information on the resistance and dynamic trim angle. Inclined shaft and a larger trim angle in comparison with conventional ships are producing a vertical component of the thrust force, which is strictly connected with propeller inclination. In the hydrofoil vessel model tests an important role plays also the action of the air, which, by higher speed of the vessel, will give an apparent effect on the resistance.

Difficulties with elimination of the tunnel effect, which multiplies the air velocity in the measurement space about 1.7 times in comparison to the towing carriage speed, were the reason for an omission of the aerodynamic effect during the model tests. The short time of the research project was the reason only for the vertical component of towing force simulation, without introduction of additional mentioned factors.

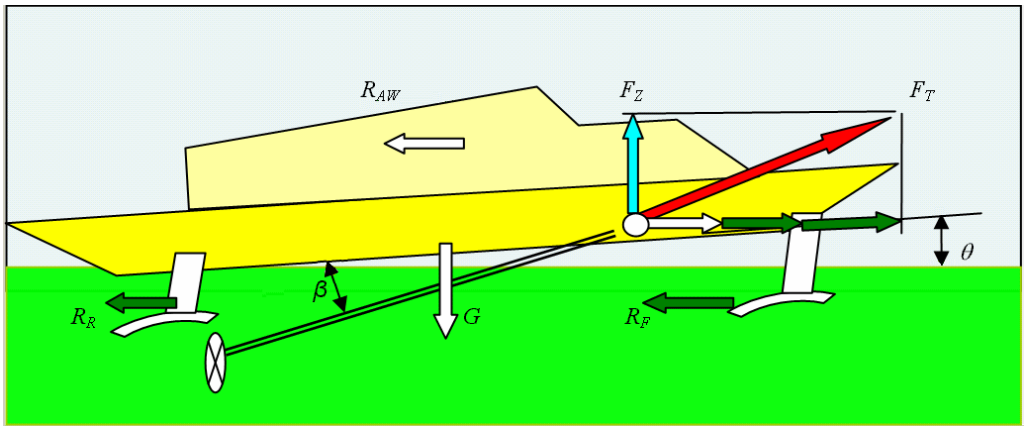

Fig. 1. Forces acting on a hydrofoil vessel; R_R, R_F – resistance of rear and front foil, R_{AW} – air resistance, F_T – towing force, F_Z – vertical component of towing force, β – angle between shaft and base line, θ – trim angle, G – gravity force, R_{TM} – total resistance, where $R_{TM} = R_R + R_F + R_{AW}$

The vertical force F_Z generated by the sloping shaft line and by the dynamic trim angle is introduced in the used proportional force simulator:

$$Z(t) - F_Z < \varepsilon, \tag{1}$$

$$Z(t) = R_{TM}(t) \times \text{tg}\,(\beta + \theta(t)), \tag{2}$$

where:

$Z(t)$ – dynamically measured vertical force,

ε – minimized value.

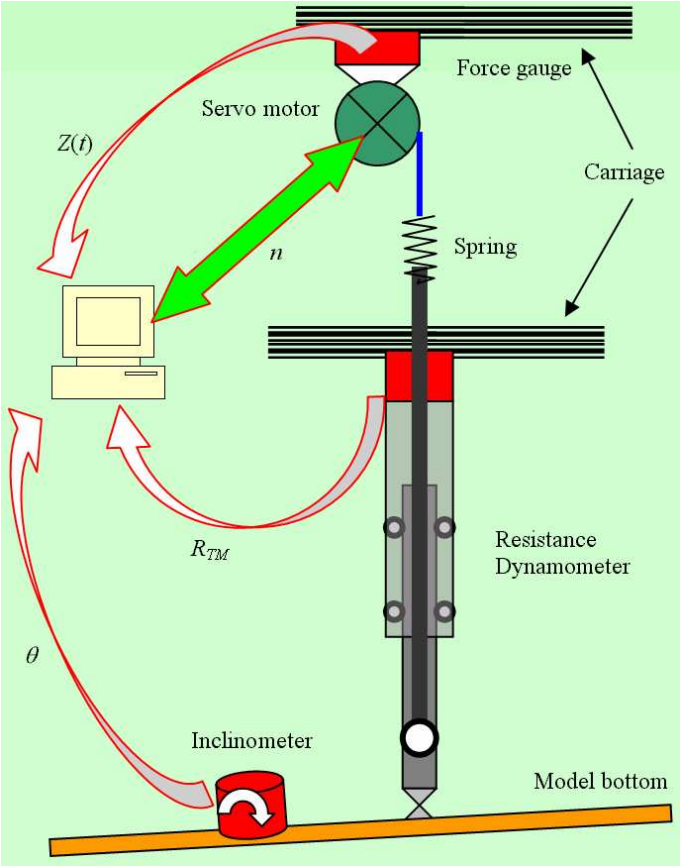

Fig. 2. The scheme of the measurement system with vertical force simulator; n – servo motor revolutions

According to the additional tests on a rough sea the simulator was completed with the differential term. The constants of the proportional-differential (PD) simulation system were selected on a experimental way. In the hydrofoil vessel dynamic occurrence this approach was sufficient for suitable tracking precision during model accelerating with transient movements. Application of an elastic component in the simulation system has allowed an omission of the integrating element in the control algorithm. This was necessary to separate the influence of the towing carriage vibrations. In the simulating system a stepper motor was used.

2.2. Extrapolation to full scale

In general, the result extrapolation method from the model to full scale is based on the same rules as for the conventional ships, i.e. test results received in the form of the total model resistance R_{TM} measured at the model moving with subsequent constant speeds V_M were transformed to the ship scale on the base of an assumption that this resistance is represented by viscous and by residuary (wave making and wave breaking) resistance.

$$C_{TM} = C_{FM} + C_{RM} + C_{AW}, \tag{3}$$

where:

C_{TM} – total resistance coefficient,
C_{FM} – frictional resistance coefficient,
C_{RM} – residuary resistance coefficient,
C_{AW} – air resistance coefficient.

But in the case of hydrofoil vessels some modifications in the standard method are made.

For all of calculations in the case of hydrofoil vessels the volume Froude number instead of standard Froude number is used:

$$F_{n\nabla} = \frac{V}{\sqrt{g\nabla^{1/3}}}, \tag{4}$$

where:

V – ship speed [m/s],
∇ – volume displacement [m^3],
g – gravity acceleration [m/s^2].

For the calculation of equivalent flat plate frictional resistance coefficient the Prandtl-Schlichting formula is used:

$$C_{FO} = \frac{0.455}{(\log R_n)^{2.58}}, \tag{5}$$

where:

R_n is the Reynolds number.

The hydrofoil vessel frictional resistance coefficient is based on the algebraic sum of the frictional resistance of hull, foils and foil struts, according to the following formula:

$$C_F = H_K[C_{FO} + \Delta C_F] + H_{pn}\sum C_{Fpn} + H_{wsp}\sum C_{Fwsp}, \tag{6}$$

where:

C_{Fpn}, C_{Fwsp} – frictional resistance coefficients of foils and struts, calculated using the Prandtl-Schlichting formula,

ΔC_F – roughness allowance,

H_K, H_{pn}, H_{wsp} – coefficients dependent on the hull, foils, struts wetted surface area.

3. Experiment data

For the experiments a wooden, four meters long hydrofoil vessel with fully submerged, low immersed foils was taken.

3.1. Hydrofoil vessel model

Table 1. Hydrofoils data (m, m^2, m^3)

	ship	model
Length between perpendiculars	32.80	3.976
Length on waterline	33.32	4.039
Breadth moulded	6.60	0.800
Breadth on waterline	6.28	0.761
Draught: fore	1.12	0.136
Draught: aft	1.12	0.136
Displacement volume	64890	0.115
Wetted surface	160.25	2.354
Block coefficient	0.277	
Midship section coefficient	0.524	
Prismatic coefficient	0.529	
Waterplane coefficient	0.688	

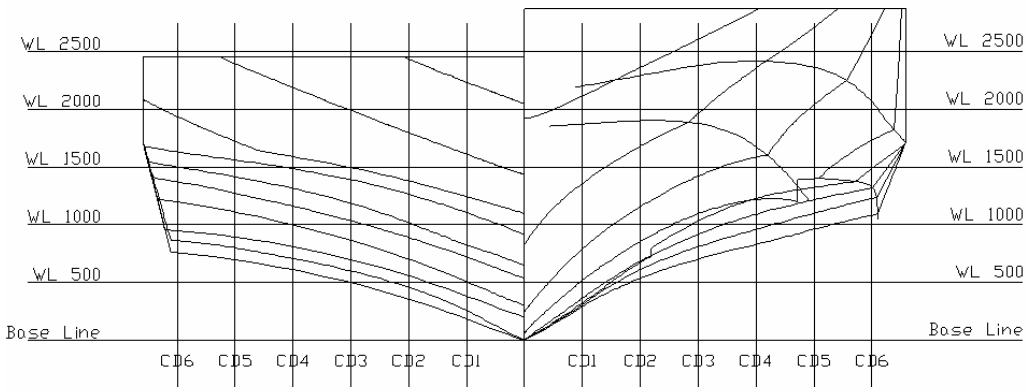

Fig. 3. Hydrofoil vessel hull body lines

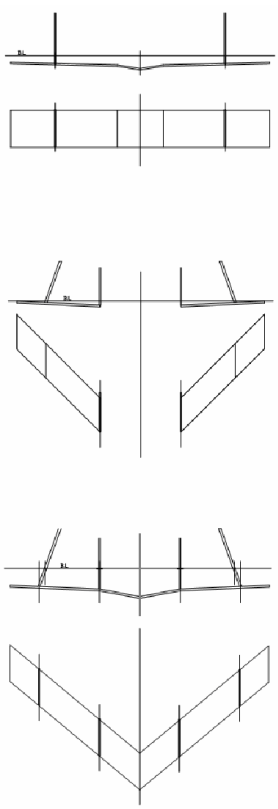

Fig. 4. Geometry of foils; downwards: rear foil, stabilizing front foils and front foil

3.2. Experiment plan

The tests were carried out for constant initial displacement, for three values of static trim and three combinations of foil angle of attack, according to the following conditions:

Table 2. Hydrofoil model conditions for resistance tests (°)

Trim	Geometric angle of attack of front foil	Geometric angle of attack of rear foil
1.0	+1.0	0.0
0.3	+1.0	0.0
1.5	+1.0	0.0
1.5	+1.0	−0.5
1.0	+1.0	−0.5
0.3	+1.0	−0.5
0.3	+1.5	−0.5
1.0	+1.5	−0.5
1.5	+1.5	−0.5

3.3. Test results

A part of the test results is shortly presented in a form of a table and on figures with standard non-dimensional resistance coefficients. The trim angle is also presented.

Table 3. Results of hydrofoil model resistance tests

V (kn)	V_M (m/s)	R_{TM} (N)	$10^3\, C_{TM}$	T_F (m)	T_A (m)	L_{WL} (m)
5.6	1.00	13.63	7.505	0.082	0.178	4.033
7.3	1.31	24.11	7.818	0.082	0.180	4.035
8.9	1.60	36.73	7.978	0.078	0.183	4.031
10.6	1.90	52.79	8.329	0.064	0.187	4.001
12.3	2.20	73.76	8.945	0.042	0.194	3.931
14.0	2.50	95.72	9.525	0.012	0.200	3.773
15.7	2.81	110.10	9.270	−0.011	0.195	3.549
17.3	3.10	119.46	8.719	−0.029	0.192	3.307
19.0	3.40	125.56	8.367	−0.047	0.184	3.059
20.7	3.71	116.55	7.736	−0.048	0.162	2.939
22.3	4.00	112.46	8.491	−0.057	0.144	2.729
23.8	4.27	104.34	8.327	−0.054	0.120	2.559
25.7	4.60	87.75	7.676	−0.049	0.087	2.201
27.4	4.91	80.25	7.498	−0.071	0.069	1.231
29.1	5.20	77.76	7.107	−0.076	0.041	0.359
30.7	5.50	76.12	6.417	−0.076	0.022	0.000
32.5	5.82	76.18	5.873	−0.079	0.007	0.000
34.1	6.10	77.39	5.534	−0.085	−0.002	0.000
36.2	6.49	82.02	5.337	−0.089	−0.009	0.000
37.9	6.79	85.69	5.203	−0.088	−0.008	0.000
40.0	7.16	98.33	5.531	−0.090	−0.011	0.000

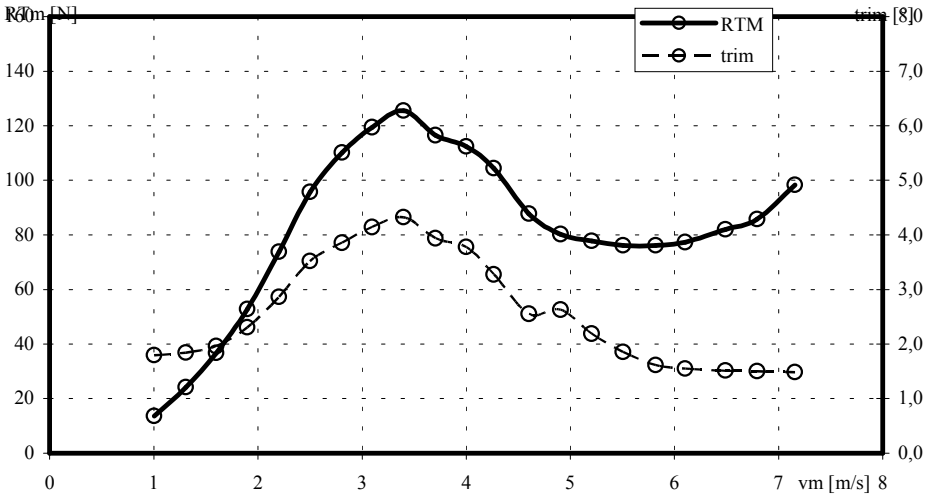

Fig. 5. Model resistance and trim angles for 1.0° front, 0.0° rear foil angles of attack and 1.5° initial trim

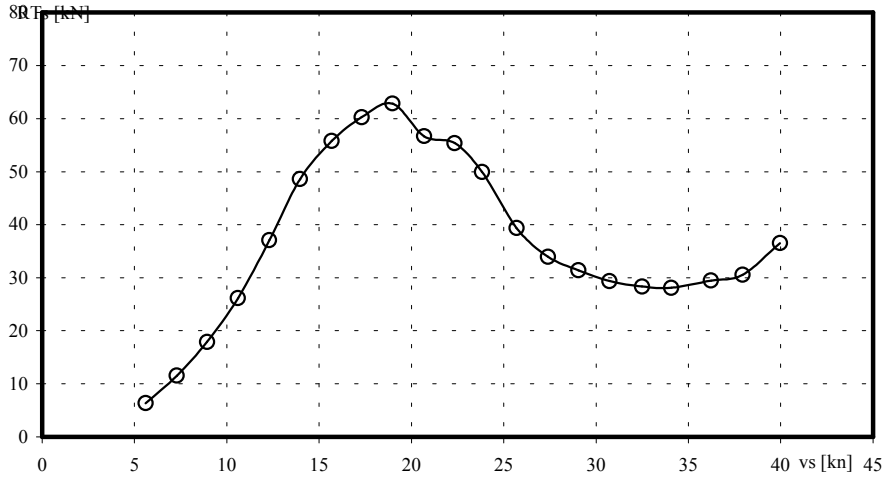

Fig. 6. Resistance of hydrofoil vessel model extrapolated to full scale

4. Methodology and result analysis, comments

The use of vertical force simulator in resistance experiments has allowed the determination of influence of the force generated by the inclined shaft and propeller on the dynamic trim values and on the resistance. The correct operation of the system in the resistance tests and in the dynamic experiments on the rough sea shows that on this basis a full simulation system of trimming moments could be introduced to the hydrofoil vessels model tests, what will enable the full quantification of the acceleration problem of hydrofoils in the transient phase.

The extrapolation method seems to be a rational method for full scale resistance prediction, but a validation with full scale experiments is necessary.

During the research project a comprehensive method for hydrofoil model tests and result extrapolation was developed, what may be a good impulse for further experiments and projects.

References

[1] Reichel M.: *Model tests of Vietnamese hydrofoil*, RH-2006/T-089E Technical Report, Ship Design and Research Centre, Gdańsk, 2006.

Badania modelowe wodolotów w Centrum Techniki Okrętowej S. A.

Artykuł przedstawia badania modelowe oporu wodolotów przeprowadzone w Centrum Techniki Okrętowej S.A. Badania zostały przeprowadzone na dużym basenie holowniczym

Ośrodka Hydromechaniki Okrętu. Eksperymentowi poddany został czterometrowy, wykonany z drewna, model wodolotu, wyposażony w dwa płaty nośne oraz stabilizujący płat dziobowy. Pomiary oporu przeprowadzone zostały dla kombinacji trzech wstępnych kątów przegłębienia i dwóch kątów natarcia płatów nośnych. Artykuł zasadniczo przedstawia badania modelowe w aspekcie metodologicznym. Przedstawiono nowo wdrożoną metodykę badań, umożliwiającą optymalizację kąta nachylenia linii wałów napędowych, związaną z symulacją składowej pionowej siły naporu. Krótko, przedstawiono także wyniki pomiarów w postaci standardowych, bezwymiarowych współczynników oporu w funkcji liczby Froude'a.

ARCHIVES OF CIVIL AND MECHANICAL ENGINEERING

Vol. VII 2007 No. 3

Aircraft ditching: a free surface / free motion problem

H. STRECKWALL
Hamburg Ship Model Basin (HSVA), D-22305, Hamburg, Germany

O. LINDENAU
Technical University Hamburg-Harburg (TUHH), D-21073 Hamburg, Germany

L. BENSCH
Airbus Deutschland GmbH, D-21129, Hamburg, Germany

Within a national research project on aircraft dynamic loads and resultant structural response the task was given to investigate aircraft emergency landings on water, generally called "ditching". The work was initiated and funded by Airbus Industries. As controlled experiments for such events are costly and difficult to extrapolate to full-scale, the study at HSVA was completely based on computer simulations. The commercial RANS solver "Comet" was used to determine the path of the aircraft fuselage from initial conditions in air given at $t = 0$. After being released in air, the aircraft fuselage was free to react on the forces and moments developing at the free surface. In order to simplify the approach the hydrodynamic forces were derived in all details by the RANS simulation while the aerodynamic forces and moments were approximated. Simultaneously, the simulations were performed at the TUHH using the program "Ditch", based on an extension of the "momentum method" developed by von Karman and Wagner. The results are presented in this paper for generic fuselage shapes called *A*-, *D*- and *J*-Body in terms of motion histories and section forces.

Keywords: *aircraft ditching, fuselage, 6 degrees of freedom, free surface*

1. Introduction

In aviation, planned ditching is a controlled emergency landing of an aircraft on water. Hence, during ditching the pilot keeps some control over the airplane and is able to perform a landing close to instructions given in the flight manual. Regulations require that the manufacturer of an aircraft has to prove the survivability of the ditching for the passengers and crew and a safe post ditching egress.

When the aircraft structure gets into contact with the dense medium water, high impact loads and resulting accelerations occur along the different structural aircraft components like the fuselage, wings, tails, engines, etc. The high loads possibly lead to damages of the local and global aircraft structure and together with the violent accelerations present a substantial risk of severe injuries for passengers and crew. Thus the task in ditching investigation is to determine the loads and motions acting on the aircraft during water impact. Full-scale experiments on aircraft ditching are too risky and prohibitive expensive. It remains to investigate the problem either experimentally in model scale or to develop and apply numerical approaches that deliver equivalent data.

Söding [1] developed the computer program “Ditch” for this task. The method calculates the hydrodynamic forces acting on a section grid of the aircraft main components (e.g. fuselage, wings, tails and engines). The force calculation is based on an extension of von Karman’s [2] and Wagner’s [3] “momentum method” accounting for ventilation and cavitation effects with the help of empirical factors. This approach, based on a combination of an analytical method and empirical factors derived from test data or evaluation of other numerical methods is termed as “hybrid method”. Aerodynamic forces, engine thrust and drag forces of minor aircraft components (e.g. landing gear and landing gear bays) are modeled as well. The forces acting on the aircraft are integrated and introduced into motion equations for 3 degrees of freedom in the vertical symmetry plane of the aircraft.

A related approach was derived by Shigunov [4] considering a Wagner type pressure distribution along the sections. Summaries on the approaches and applications are presented by Shigunov [5] and Bensch [6]. A merged version of the two methods additionally considering fuselage and wings as elastic finite-element beam models was developed by Lindenau [7]. Here the treatment of the equations of motion follows the added mass approach given by Söding [8].

“Ditch” is a fast method, i.e. the simulations run in the order of real-time on a normal PC, and has been validated by a number of seaplane and ditching experiments. Söding [9–10] also used a simplified version of the ditching simulation program to calculate the motion of planing boats in waves.

Extending the scope of the hybrid approach, recently developed CFD methods capture the dynamic behavior of the free surface. In view of this additional capacity a sequence of simple fuselage shapes was analyzed using the RANS solver “Comet” to:

- establish a general experience on RANS simulations of a combined free surface / free motion problem.
- support the enhancement of “Ditch” with respect to the hydrodynamic force modeling, i.e. especially regarding the empirical models and factors for ventilation and cavitation effects.

The RANSE solver “Comet” provides a free surface model based on the volume-of-fluid approach discretised with the HRIC scheme [11]. To predict the path of the fuselage we made use of a recent “Comet” module with the acronym “6DoF” which adopts the developments of Xing-Kaeding [12]. “6DoF” stands for “6 Degrees of Freedom” and allows to simulate free, i.e. unguided, motions.

There are alternative approaches to simulate a free motion at a free surface. The Smooth Particle Hydrodynamics (SPH, [13–14]) has advantages for the coupling of fluid forces to a structure model. On the other hand the SPH-method seems to fail to predict suction forces, which are the driver of the pitch motion during the impact, where the forward velocity is still considerable high.

To compare the different computational methods, the NACA report TN2929 [15] gives a well documented basis at which experimental ditching results of generic fuselage shapes are presented. From this report, we selected the shapes called *A*-, *D*- and

J-Body to compare simulations with test results. In the ditching tests the fuselages were equipped with identical high-wing and *T*-shaped tail configurations. The complete aircraft models were landed in a water tank at speeds in air of 30, 40, 50 and 60 feet per second. A high-speed motion picture camera served to trace the motion. The motion-picture records were analyzed to obtain time histories of forward speed, pitch attitude and center of gravity height above water for the model.

2. Computational set-up for viscous "Comet" analysis

2.1. Simplifications

The following simplifications are made to focus the complex simulation to major effects, rather than trying to be too complex. A rigorous numerical approach to aircraft ditching should solely need the final configuration in air (e.g. mass, moments of inertia, axial speed in air, descending speed in air, flap settings and pitch attitude) and then simulate the subsequent motion. When using "Comet" we introduced a simplification on the aerodynamic side. In the viscous analysis we accounted solely for the fuselage geometry and replaced the main wing and the horizontal tails by velocity and pitch dependant external forces and moments, determined by the same module as used in "Ditch". This helped to compare the results in view of the hydrodynamic acting.

2.2. 6DoF implementation

One may divide the loads acting on and around the CG of the fuselage into [12]:

- force due to gravity,
- external forces/moments (here representing the aerodynamic response),
- reaction force ($-m\ a$) on directional acceleration and reaction moment on angular acceleration $\dot{\omega}$ and
- surface forces from pressure and shear force integration.

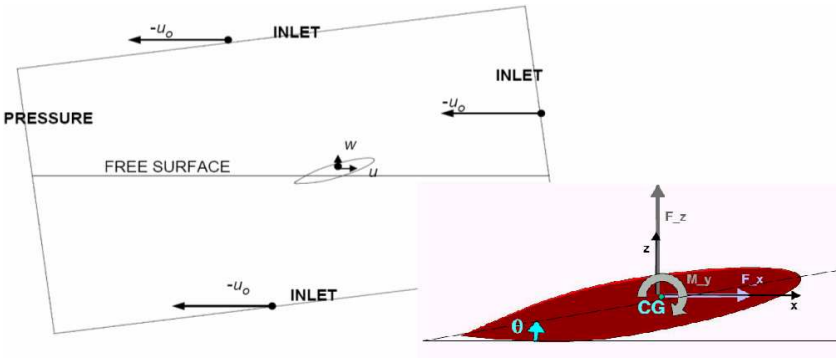

Fig. 1. Boundary conditions, velocity components, forces, moments and coordinate system (right picture also refers to *A*-Body shape)

The sum of gravity, external and surface forces must compensate the reaction force ($-m\ a$) as the sum of external and surface moments has to compensate the reaction moment. Accordingly, it is the task of the solver to provide a suitable acceleration (a) for the center of gravity motion and a suitable angular acceleration $\dot{\omega}$ for rotations around the principle axis at any state of the transient simulation. An acceleration of a body is simulated by time stepping motions of the body contour. To realize a motion step we displaced the whole cell system, implying a call of the "Comet" pre-processor after every time step.

2.3. Coordinates and boundary conditions

In our simulations the global coordinate system x, y, z of "Comet" does not represent an earth fixed system. It is moving with the initial axial velocity u_o of the body. Accordingly, "Comets" global system sees the flow coming with $-u_o$ through the Inlet (Figure 1). In our approach the axial component of the grid always reads $u = 0$ at the start and $u = -u_o$ when the fuselage has come to rest. The vertical velocity (w) is positive upwards. At the start the grid usually shows a non-zero initial $w = -w_o$. The y-axis points to port side. Positive angles for the pitch attitude (θ) are defined as shown in Figure 1. The acceleration due to gravity points into the negative z-direction. The boundaries show mainly the "Inlet"-type except for the downstream end where the "Pressure"-type was applied.

2.4. Geometry and grids

The *A*-, *D*- and *J*-Body models show a length of 1.22 m. They are not associated to a full-scale fuselage so there is no model scale given. The *A*-Body is a complete body of revolution. A side view of the *A*-Body is given in Figure 1.

The *D*-Body (Figure 2, left) shows the same outline as the *A*-Body when looking from aside. From above the *D*-Body reveals a nearly rectangular tail contour, which has a significant effect on the ditching behavior.

The *J*-Body (Figure 2, right) is more slender than the *A*- or *D*-Body and shows a third tail alternative. Looking from aside the tail of the *J*-Body is swept upward. Looking from above the *J*-Body appears as a body of revolution.

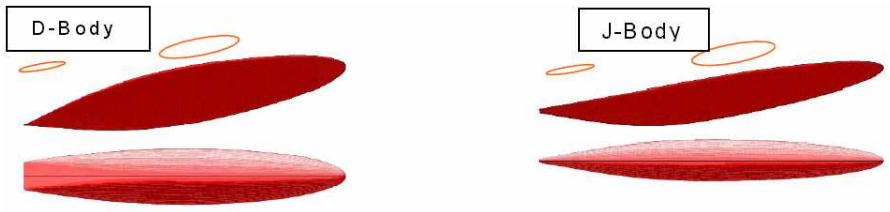

Fig. 2. *D*-Body and *J*-Body from aside and from above (location of main wing and horizontal tails is indicated (but these surfaces are not included in the grid)

The grid for the *A*-Body looks as given in Figure 3 when cut in the center plane. In case of the *A*- and *D*-Body we used 592 000 cells for one fuselage half. For the *J*-Body we utilized 390 000 cells.

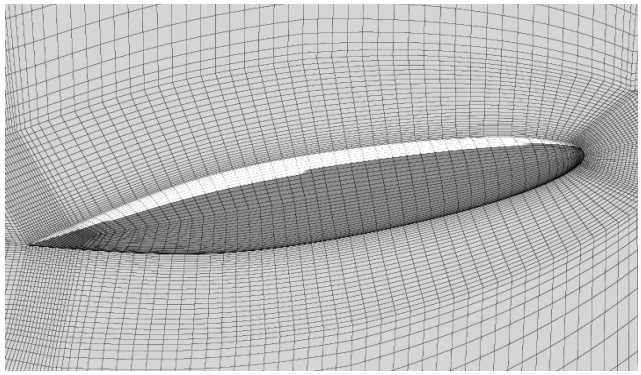

Fig. 3. Grid for the *A*-Body (surface and volume resolution)

2.5. Simulated cases

For all 3 geometries we simulated initial axial speeds of u_o = 9.14 m/s (30 feet/s) and u_o = 15.23 m/s (50 feet/s). Using Froude scaling and assuming a large passenger aircraft the 9.14 m/s model speed would correlate with the order of a typical approach velocity in case of ditching. The initial pitch was 10° as reported from the test and we assumed an initial vertical velocity component of w_o = 0.2 m/s for all cases. The same module as used for Ditch provided externally the forces of main wing and tails. The module requires the actual speed and pitch to determine the forces and moments. The actual angle of attack is related to a lift coefficient, which we defined to be:

$$C_l = L/(\frac{1}{2}\rho \cdot v^2),$$

where:

v is the actual velocity magnitude,

L is the actual lift in air of density ρ.

Figure 4 gives the assumed relation between C_l and the actual pitch θ. The C_l is the fix point which holds for the initial pitch (the sample linked to Figure 4 assumes 8°) reflects the weight of the aircraft. The slope reflects the aspect ratio while the lift limit is based on an analysis of the wing configuration and Reynolds number at impact. For the latter value ($C_{l,\max}$) we assumed

Case u_o = 9.14 m/s, $C_{l,\max}$ = 2.0,

Case u_o = 15.23 m/s, $C_{l,\max}$ = 1.15.

Since the wing configuration was identical this holds for *A*-, *D*- and *J*-Body.

2.6. Solver settings

The settings for the RANS approach are characterized by a small constant time step with Δt = 0.0003 s, by a large number of outer iterations within each time step (20) and by the fact that the momentum scheme was based on upwind differencing (UD). The latter setting was necessary to increase the robustness of the simulation. It was confirmed by test calculations on other slender bodies, which were subject to guided motions, that the surface forces did not change significantly when changing from UD to central differences (CD).

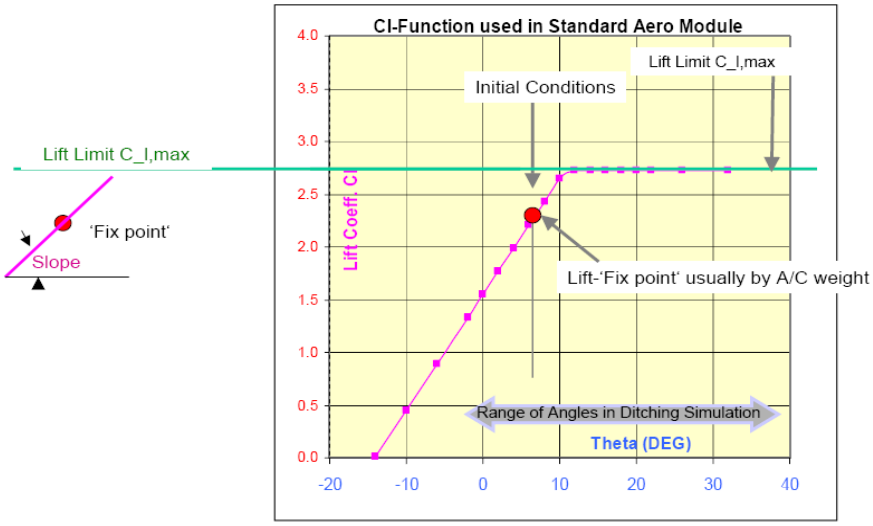

Fig. 4. The actual lift coefficient C_l for the main wings was read from a graph which shows the elements: a) lift fix point (related to the initial pitch θ and deduced from the aircraft weight), b) lift curve slope (deduced from the aspect ratio Λ) and c) upper lift limit reflecting the wing configuration and Reynolds number at impact

3. Simulation set-up for "Ditch" simulations

Unlike "Comet", "Ditch" uses a discretisation of 150 cross-sections for the *A*-, *D*- and *J*-Body fuselages. Each cross-section in turn is given as polygon line. To determine the hydrodynamic forces, a method based on the extension of the von Karman "momentum method" was selected. The aerodynamic model used for the "Comet" calculations is the same as implemented in "Ditch".

Regarding the vertical velocity in the "Ditch" simulations, values closer to the actual test data were individually selected for each test case. However, apart from small differences at the beginning of the resulting time histories this parameter appeared to be of minor importance for the overall behavior of the models. The next section presents the comparison of the "Ditch", "Comet" and test results.

4. Results of simulations compared to ditching test

Below are given the results in terms of instant pictures of the ditching sequence taken form the "Comet" simulations. The diagrams give the forward velocity with respect to the initial velocity u/u_o, the pitch attitude θ, and the center of gravity (CG) height above water with respect to the fuselage length plotted against the elapsed time for the ditching test as well as the "Comet" and "Ditch" simulations. Additionally, the pressure distribution for one representative time-step is given as a "footprint". Hereby, the pressure coefficient is based on the stagnation pressure calculated from the initial velocity u_o and the density of water. Besides, the mirrored half of the picture shows the water/air volume fraction. Below the "footprint" the free-surface deformation is given.

Figure 5 shows the first phase of a ditching simulation for the *A*-Body. The fuselage touches the water first at $t = 0.06$ s. The *A*-Body pitches heavily at about $t = 0.3$ s and is already close to be at rest at 0.72 s. The comparison of simulated forward velocity, pitch and CG-height above water with the test is given in Figure 6. Both simulations show a similar realistic behavior with respect to the forward velocity by gradually decelerating after the water impact. The strong deceleration given in the test data appears to be not correct. While the maximum pitch is over-predicted by the "Comet" simulation, it is underestimated by "Ditch". Both simulations are close to the test data for the height of the center of gravity above water. It can be deduced form both, the test data and the computational results, that the characteristics of the *A*-Body at initially $u_o = 9.14$ m/s are strong fluctuations in pitch and week fluctuations in the CG-height. Figure 7 shows the pressure distribution and the water/air volume fraction together with the free-surface deformation at $t = 0.18$ s. The pressure distribution shows a pronounced region of high pressures in the front area of the submerged part and negative pressures with respect to the ambient pressure in the convex curved part at the rear.

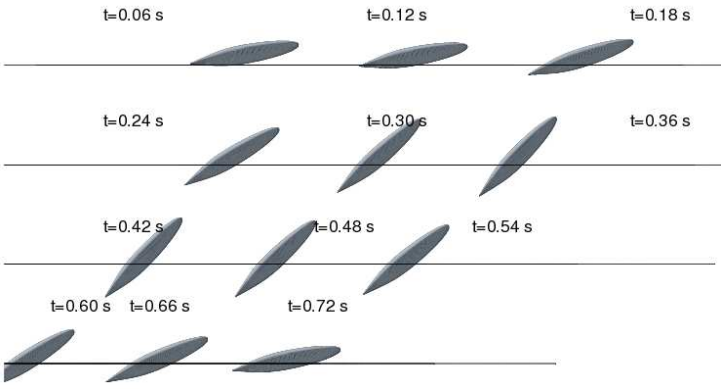

Fig. 5. Ditching of *A*-Body at 9.14 m/s – position of model with respect to calm water surface resolved every 0.06 s for $t = 0.06$–0.72 s in "Comet" simulation

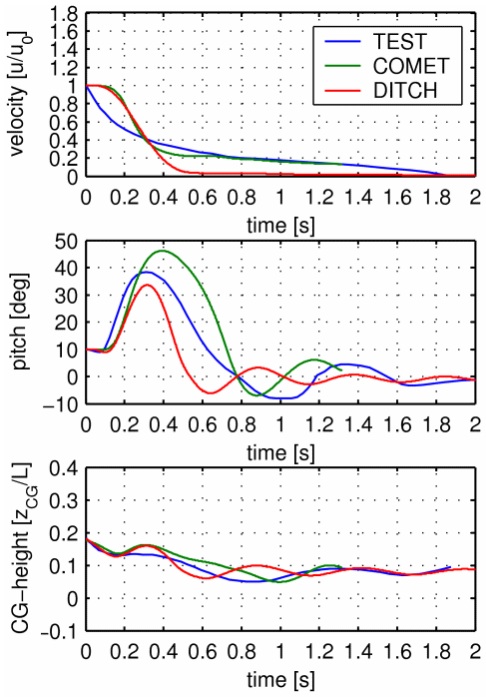

Fig. 6. Ditching of *A*-Body at 9.14 m/s – forward velocity (top), pitch (middle) and height of center of gravity above water (bottom) for "Comet" and "Ditch" simulations compared with test

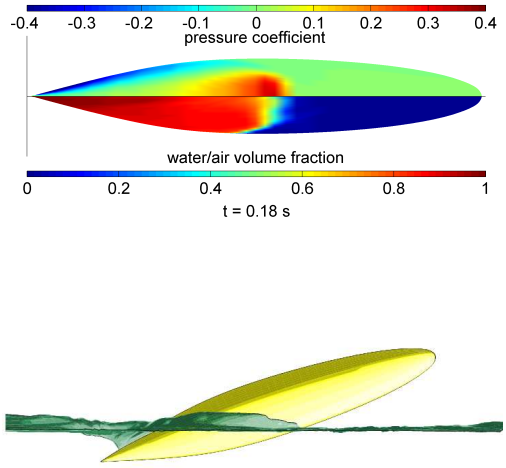

Fig. 7. Ditching of *A*-Body at 9.14 m/s – footprint of pressure coefficient and water/air volume fraction (top) and free-surface deformation (bottom) for "Comet" simulation at time t = 0.18 s

Figure 8 gives the ditching sequence for the *D*-Body when released at 9.14 m/s. For the comparison with the ditching test we refer to Figure 9. The simulations predict the general ditching behavior of the *D*-Body quite well, although the pitch up tendency is under estimated by the "Ditch" simulation. At 9.14 m/s the *D*-Body shows weak fluctuations in pitch as well as for the CG-height above water line. This characteristic is obvious form both, the test and the simulations. Compared to the *A*-Body the deceleration and the downstream disturbance of the free water surface is significantly weaker for the *D*-Body (compare free surface at t = 0.18 s in Figure 7 and Figure 10).

When released at 15.23 m/s the simulations for the *D*-Body give a ditching sequence as displayed in Figure 11. Looking at Figure 12 to compare the experimental finding for pitch and CG-height with the computed results one recognizes that the pitch up tendency is well covered and the CG-height is strongly overestimated in the "Comet" simulation. In the "Ditch" simulation maximum pitch height and CG-height are showing a time-shift. In both computations the *D*-Body emerges completely again, which is also slightly apparent in the test data. One may conclude that the aerodynamic model is responsible for this deviation. It is plausible for a higher initial speed that the ditching sequence becomes more sensitive to errors in the modeling of the

aerodynamic forces. Especially the modeling of aerodynamic lift and drag beyond stall, which is of particular importance in these model tests, is marked for further development.

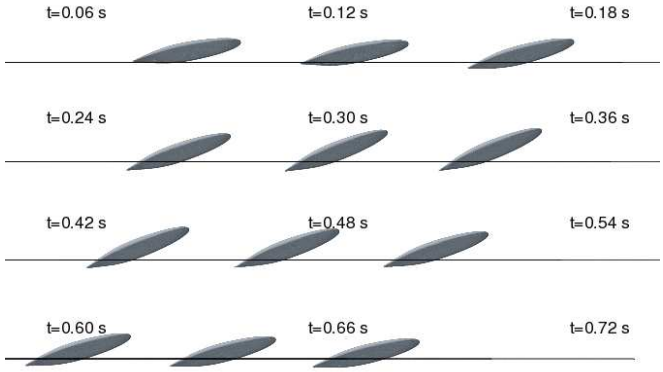

Fig. 8. Ditching of *D*-Body at 9.14 m/s – position of model with respect to calm water surface resolved every 0.06 s for t = 0.06–0.72 s in "Comet" simulation

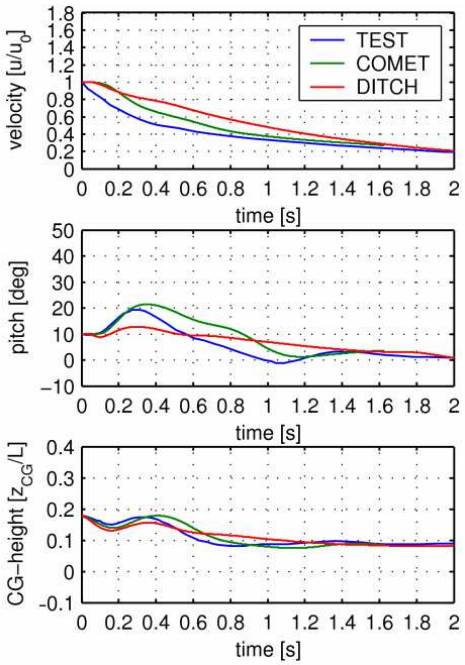

Fig. 9. Ditching of *D*-Body at 9.14 m/s – forward velocity (top), pitch (middle) and height of center of gravity above water (bottom) for "Comet" and "Ditch" simulations compared with test

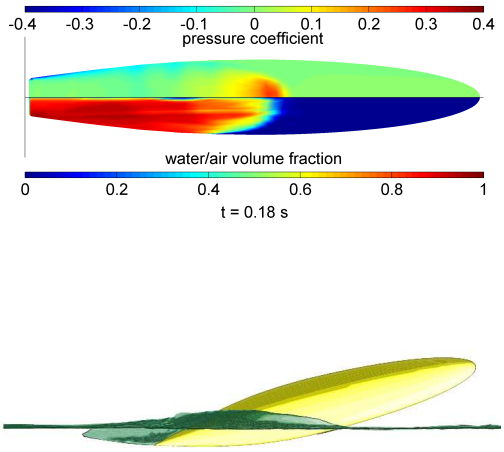

Fig. 10. Ditching of *D*-Body at 9.14 m/s – footprint of pressure coefficient and water/air volume fraction (top) and free-surface deformation (bottom) for "Comet" simulation at time t = 0.18 s

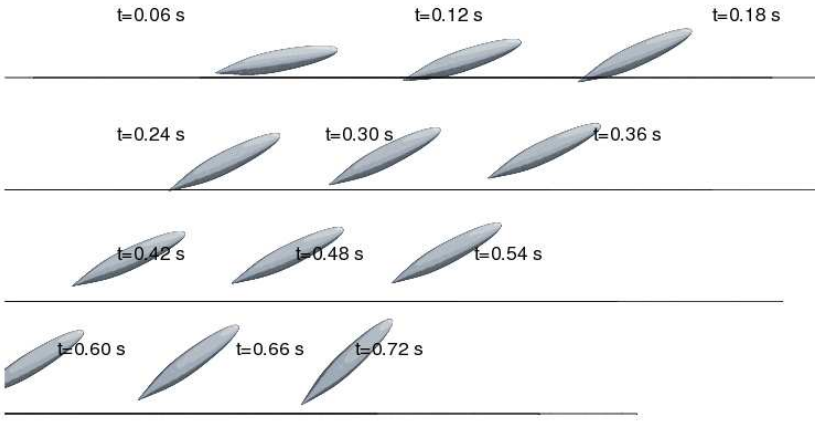

Fig. 11. Ditching of *D*-Body at 15.23 m/s – position of model with respect to calm water surface resolved every 0.06 s for t = 0.06–0.72 s in "Comet" simulation

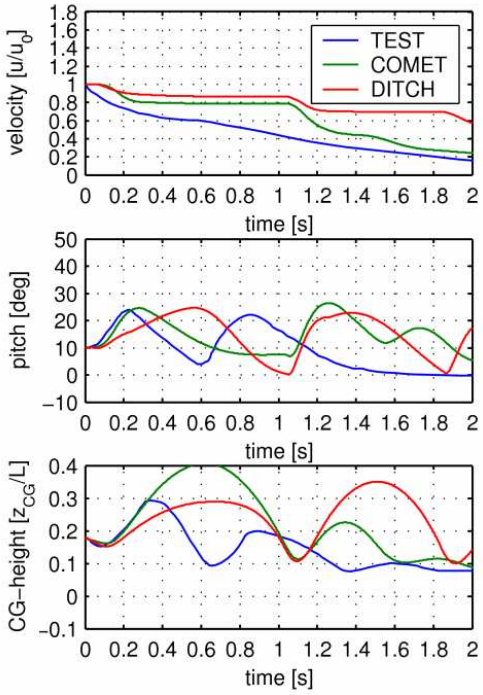

Fig. 12. Ditching of *D*-Body at 15.23 m/s – forward velocity (top), pitch (middle) and height of center of gravity above water (bottom) for "Comet" and "Ditch" simulations compared with test

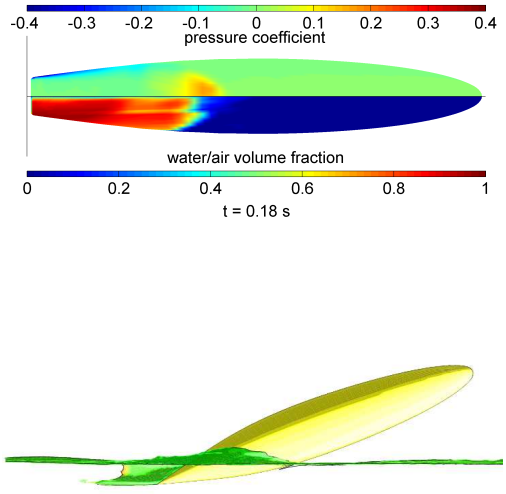

Fig. 13. Ditching of *D*-Body at 15.23 m/s – footprint of pressure coefficient and water/air volume fraction (top) and free-surface deformation (bottom) for "Comet" simulation at time t = 0.18 s

While we obtained good results for the *A*- and *D*-Body at low speed (9.14 m/s) the experimental findings for the "low speed" *J*-Body differed from the simulations applying "Comet" as can be taken from Figure 14. The "footprint" of the *J*-Body at t = 0.18 s and the free surface deformation are given in Figure 15.

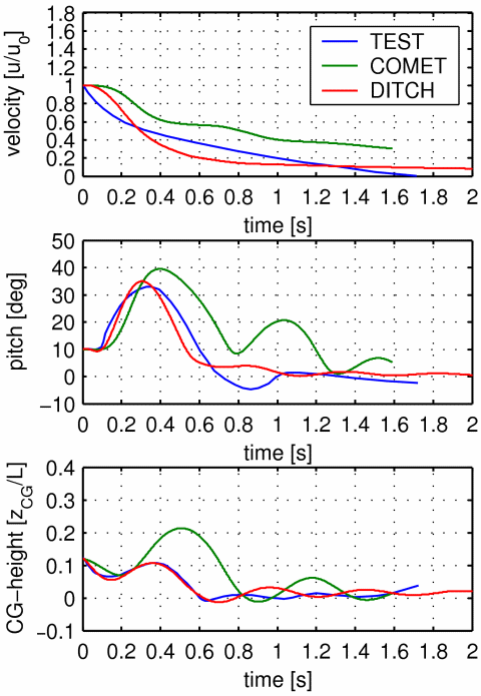

Fig. 14. Ditching of *J*-Body at 9.14 m/s – forward velocity (top), pitch (middle) and height of center of gravity above water (bottom) for "Comet" and "Ditch" simulations compared with test

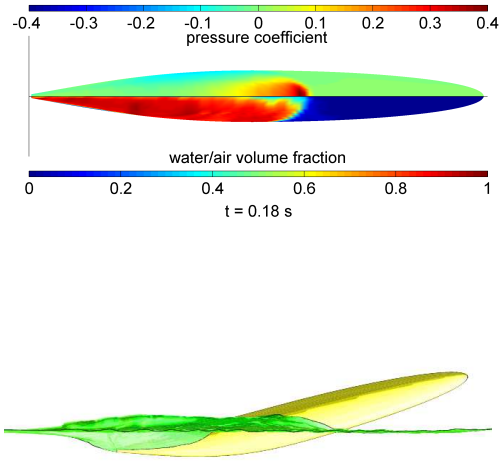

Fig. 15. Ditching of *J*-Body at 9.14 m/s – footprint of pressure coefficient and water/air volume fraction (top) and free-surface deformation (bottom) for "Comet" simulation at time t = 0.18 s

At the higher speed (15.23 m/s) the "Comet" computations for the *J*-Body led to similar results as obtained for the "high speed" *D*-Body. Solely the *A*-Body behavior could be reproduced for 15.23 m/s applying "Comet".

Regarding pitch attitude and CG-height above water, the "Ditch" simulations are close to the test data also at the higher speed, while again the realistically simulated deceleration differs from the test data. However, one should keep in mind that the test results are derived in 1953, when measurement techniques were not as precise as today.

5. Comparison of “Comet” and “Ditch” – simulations

The comparison presented above shows the quality of the modeling of integral forces and pitch moment for the two simulation methods. Both methods determine motions, which can be compared to the test data. Unfortunately, no local loads in terms of section forces or pressure data are generally given in published ditching test data. Thus, only the two simulation methods can provide such data, which allows a comparison in view of local loads. In order to exclude differences in the aerodynamic modeling, the free-flight motion simulated with “Comet” is taken as input for additional guided simulations with “Ditch”, allowing a detailed comparison of hydrodynamic forces over the total simulation time.

Section forces are the step between integral global forces and pressure distribution and suit for comparing simulation results on a lower level. Hereby, the forces are made non-dimensional by the stagnation pressure based on the initial velocity applied to an area of fuselage diameter times section slice length. Figure 16 and Figure 17 give the vertical section forces in this form for the longitudinal section position of the fuselage (0 = nose and 1 = tail) at the time t = 0.12 s. For the approach speed of 9.14 m/s (30 fps) the section forces are depicted for the *A*-Body (Figure 16) and *J*-Body (Figure 17). Both force distributions show pronounced upwards acting forces near the longitudinal center of gravity position and downward forces acting towards the rear. Whereas the upwards forces basically lead to deceleration of the sinking of the aircraft model, the downwards acting forces with their lever arm to the center of gravity introduce the pitch up motion seen in Figure 6 (*A*-Body) and Figure 14 (*J*-Body). The maximum section forces simulated by “Ditch” are higher than those calculated with “Comet”, while the integral of the upwards forces is again very similar. Up to now “Ditch” is lacking a ”bow-wave”-model spreading the forces in the front part of the submerged

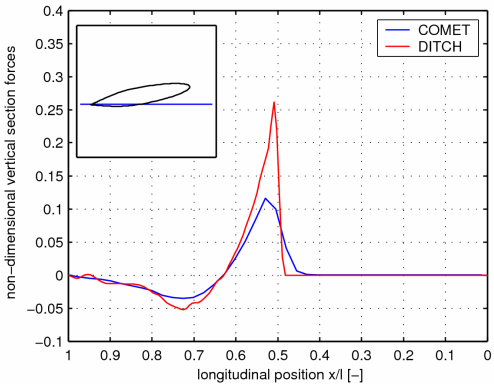

Fig. 16. Ditching of *A*-Body at 9.14 m/s – vertical section forces along fuselage for “Comet” and guided “Ditch” simulations at t = 0.12 s

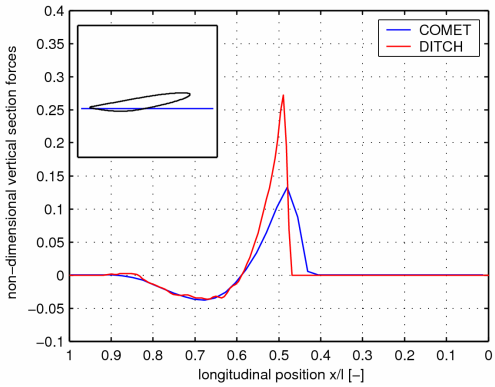

Fig. 17. Ditching of *J*-Body at 9.14 m/s – vertical section forces along fuselage for “Comet” and guided “Ditch” simulations at t = 0.12 s

area over a larger area. In the "Comet" simulations the section forces are expected to increase with a finer grid in this area likely going along with a reduction in the amount of air simulated in this spray zone (see water/air distribution in Figure 7 and Figure 15).

6. Conclusion

The free-flight ditching motions of three generic aircraft models impacting a water surface were simulated applying the RANS method "Comet" and the hybrid method "Ditch" and were compared to test data. Additionally, the section forces for the two numerical methods are compared for a time-step shortly after water impact.

Increased confidence in taking these ditching test data as validation basis was gained, but the theoretical results also marked the deficiencies of the test with respect to the forward motion. When comparing to the test results, the measurement technology at the time of the ditching tests and the partly uncertain boundary conditions have to be bared in mind. Overall reasonable good correlation for both simulation methods could be shown.

Three phase flow simulations of water, air and vapor including cavitation (relevant for full-scale ditching analysis) were also performed but are not presented here. Thus the scope of this first published application of a RANS method to aircraft ditching was actually broader. Comparing "Comet" and "Ditch" section forces and pressure results is ongoing work, introducing the free-flight "Comet" motion as guided motion into the "Ditch" simulation.

Acknowledgement

The work on Aircraft Ditching was sponsored by Airbus Germany and by the Federal Dept. of Industry in the German Aeronautical Research Program LuFo III.

References

[1] Söding H.: *Berechnung der Flugzeugbewegung beim Notwassern*, Report Nr. 602, Dept. of Fluid Dynamics and Ship Theory TU Hamburg-Harburg, Hamburg, 1999.

[2] Von Karman T.: *The impact on seaplane floats during landing*, Technical Note 321, National Advisory Committee for Aeronautics (NACA), Washington, 1929.

[3] Wagner H.: *Über Stoß und Gleitvorgänge an der Oberfläche von Flüssigkeiten*, Zeitschrift für Angew. Mathematik und Mechanik 12/4, Berlin, 1932, pp. 193–215.

[4] Shigunov V.: *Berechnung der Flugzeugbewegung beim Notwasssern*, Report Nr. 608, Dept. of Fluid Dynamics and Ship Theory of the Technical University Hamburg-Harburg, Hamburg, 2001.

[5] Shigunov V., Söding H., Zhou Y.: *Numerical simulation of emergency landing of aircraft on a plane water surface*, 2nd International EuroConference on High-Performance Marine Vehicles (HIPER'01), Hamburg, 2001, pp. 419–430.

[6] Lindenau O.: *Advances in simulation of ditching of airplanes*, 4th International Conference on High-Performance Marine Vehicles (HIPER'04), 2004, pp. 152–161.

[7] Söding H.: *How to integrate free motions of solids in fluids*, 4th Numerical Towing Tank Symposium, Hamburg, 2001.
[8] Bensch L., Shigunov V., Söding H.: *Computational method to simulate planned ditching of a transport airplane*, 2nd MIT Conference on Computational Fluid and Solid Mechanics, Boston, 2003, pp. 1251–1254.
[9] Söding H.: *Planing boats in waves*, 5th Numerical Towing Tank Symposium, Pornichet, France, 2002.
[10] Azcueta R., Caponetto M., Söding H.: *Planning boats in waves*, 15th International Conference on hydrodynamics in ship design, safety and operation (HYDRONAV 2003), 2003, pp. 257–268.
[11] Muzaferija S., Peric M., Sames P., Schellin T.: *A Two-Fluid Navier-Stokes solver to simulate water entry*, 22nd Symp. Naval Hydrodynamics, 1998, pp. 638–650.
[12] Xing-Kaeding Y.: *Unified approach to ship seakeeping and maneuvering by a RANSE method*, Doctor thesis, TU Hamburg-Harburg, Hamburg, 2004.
[13] Pentecôte N., Kohlgrüber D.: *Full-scale simulation of aircraft impacting on water*, Intern. Crashworthiness Conference (ICRASH 2004), San Francisco, 2004.
[14] Climent H., Benitez L., Rueda F., Toso Pentecôte N.: *Aircraft ditching numerical simulation*, 25th Intern. Congr. Aeronaut. Sciences (ICAS 2006), Hamburg, 2006.
[15] McBride E.E., Fisher L.J.: *Experimental investigation of the effect of rear-fuselage shape on ditching behavior*, Technical Note 2929, National Advisory Committee for Aeronautics (NACA), Washington, 1953.

Przymusowe wodowanie samolotu: zagadnienie ze swobodną powierzchnią i ruchem z wieloma stopniami swobody

W ramach krajowego projektu badawczego dotyczącego dynamicznych obciążeń samolotu i reakcji konstrukcji na obciążenia, jednym z zadań było zbadanie przymusowego wodowania samolotu, manewru określanego terminem “ditching” w języku angielskim. Projekt był zapoczątkowany i finansowany przez Airbus Industries. Ponieważ całkowicie kontrolowane doświadczalne badania modelowe takiego manewru są kosztowne i występują trudności z ekstrapolacją wyników do skali samolotu, w HSVA zostały przeprowadzone badania oparte całkowicie na symulacjach komputerowych. Do wyznaczania toru ruchu kadłuba samolotu, począwszy od położenia początkowego w powietrzu w chwili $t = 0$, zastosowany został komercyjny program komputerowy rozwiązujący uśrednione równania Naviera–Stokesa “Comet”. Od chwili początkowej kadłub miał pełną swobodę ruchu w wyniku reakcji na siły i momenty działające w pobliżu swobodnej powierzchni wody. W celu uproszczenia zagadnienia siły hydrodynamiczne były obliczane dokładnie na drodze rozwiązania równań uśrednionych równań N-S, podczas gdy siły i momenty aerodynamiczne były aproksymowane. Równocześnie symulacje były wykonywane w TUHH przy użyciu programu “Ditch” opracowanego w oparciu o rozszerzoną “metodę pędu” von Karmana i Webera. W referacie zostały przedstawione wyniki dla konwencjonalnych kształtów kadłuba oznaczonych jako *A*-, *D*- i *J*-Body, w postaci trajektorii ruchu i sił działających na przekroje.

ARCHIVES OF CIVIL AND MECHANICAL ENGINEERING

Vol. VII 2007 No. 3

Mutual hydrodynamic interaction between the operating propeller and the rudder

J. A. SZANTYR
Gdańsk University of Technology, ul. Narutowicza 11/12, 80-958 Gdańsk

The paper presents a description of the algorithm and computer program developed for numerical analysis of the hydrodynamic interaction between operating propeller and ship rudder. The program is based on unsteady lifting surface model representing the propeller and on boundary element model representing the rudder. The program accepts arbitrary geometry of both the rudder and the propeller as the input data. Interaction with the ship hull is taken into account in the form of given non-uniform velocity field of the ship wake. The mutual hydrodynamic interaction is taken into account by simultaneous solution of the unsteady kinematic boundary condition on both objects. The results of calculation include time-dependent pressure distribution on the propeller and on the rudder together with fluctuating hydrodynamic forces on both objects. Apart from that the program is capable of detecting and describing the dynamic development of different forms of the cavitation phenomena on the propeller and on the rudder. The paper includes the results of calculation of the hydrodynamic characteristics and cavitation phenomena of different propeller-rudder configurations. These results are compared with experimental data wherever available. This comparison confirms the effectiveness of the described computation method as the tool for design and analysis of the propeller-rudder configurations.

Keywords: *ship hydrodynamics, propulsor, rudder, cavitation*

1. Introduction

The existence of strong and complicated mutual hydrodynamic interaction between operating propeller and ship rudder has been well known for many years. In contemporary propeller-rudder configurations (cf. for example Figure 1), these effects are becoming more visible due to the specific geometry and to increased power of the propeller. This problem has attracted substantial research attention, for example in [1, 2]. The most characteristic aspects of this interaction may described as follows:

- the propeller markedly changes the kinematics of flow around the rudder, introducing the complicated three-dimensional unsteady field of its own induced velocity. This leads to generation of non-zero angles of attack on the rudder even at nominal zero rudder deflection. These angles have opposite signs above and below the propeller axis. In general propeller accelerates the flow over the rudder, thus leading to an increased risk of cavitation on the rudder and to increased values of the hydrodynamic forces (which is an advantage from the point of view of manoeuvrability). Hydrodynamic forces generated on the rudder due to propeller operation are unsteady, thus leading to fatigue effects on the rudder. The basic period of unsteadiness of these forces is related to the blade passage frequency;

- the non-uniform inflow to the propeller resulting from the ship wake amplifies the unsteadiness of the hydrodynamic forces generated on the rudder due to the propeller interaction;
- propeller interaction leads to the asymmetric hydrodynamic characteristics of the rudder, i.e. absolute mean values of forces generated at the same deflection angle to port and starboard are essentially different. Identical values of these forces may be expected only in case of the rudder symmetrical with respect to propeller axis and located behind the propeller operating in the uniform inflow field;
- in most configurations rudder influences the flow around propeller blades. This influence depends on the current mutual location of the propeller blade and the rudder – i.e. it is the function of blade angular position and the rudder deflection angle. In general this influence leads to an increase of the angle of attack at propeller blades and to increased values of the hydrodynamic forces on the blades;
- rudder interaction may visibly influence some forms of cavitation generated on the propeller. Especially susceptible to this effect is the cavitating tip vortex shed from the propeller blades.

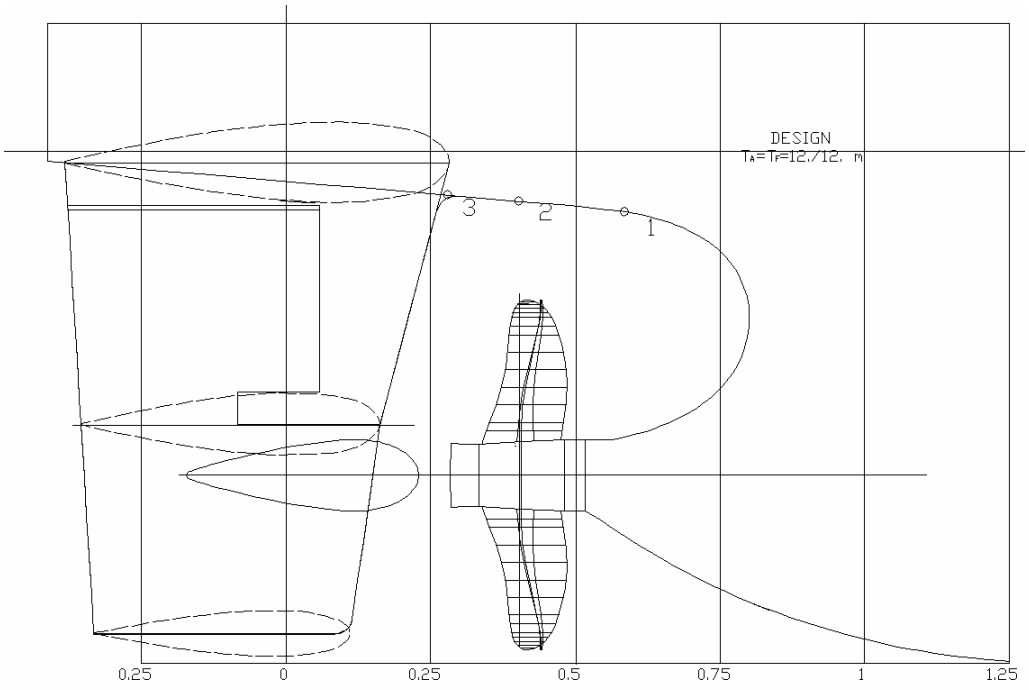

Fig. 1. Example of the propeller-rudder configuration

The above described propeller-rudder interaction effects seriously influence ship operation both from the propulsive and maneuvering point of view. Consequently,

they should receive an adequate attention at the design stage of most ships. For this purpose the designers require suitable computational methods which may be used for the hydrodynamic analysis of the propeller – rudder system. In this paper such a method is proposed. This method is an extension of the unsteady propeller analysis method which has been in practical use for many years [3]. The extended method requires the following input data:

- description of propeller geometry and operating parameters,
- description of the rudder geometry and location,
- description of the inflow velocity field to the propeller.

The results of computations include:

- unsteady pressure distribution on the propeller and on the rudder,
- mean and time-dependent values of the hydrodynamic forces on the propeller and on the rudder,
- description of the unsteady cavitation phenomena on the propeller and on the rudder,
- pressure pulses induced by the cavitating propeller – rudder in the selected points of space.

In the subsequent sections of the paper the most important features of the algorithm of the method are briefly discussed and selected results of calculations are presented and compared with experimental data where possible.

2. Computational model

Taking the method described in [3] as the reference, two main areas of extension and modification may be defined in the algorithm, namely: hydrodynamic interaction between the rotating propeller and the stationary rudder, and influence of the rudder on the propeller cavitation phenomena. The details of the algorithm concerning these two areas are presented below.

2.1. Hydrodynamic interaction between propeller and rudder

The essence of the mutual hydrodynamic interaction between propeller and rudder lies in the velocity induced by one of the objects on the other. These velocities should be included in the kinematic boundary condition, which must be solved simultaneously on both objects for each of the consecutively analysed blade positions. The kinematic boundary condition for ideal fluid flows states that the normal component of the resultant relative velocity at the boundary surface should be equal zero. When this is applied to a number of control points selected on the boundary surfaces of propeller and rudder, the system of linear algebraic equations for the unknown intensities of vortices modeling the flow is obtained. This system is shown schematically in Figure 2.

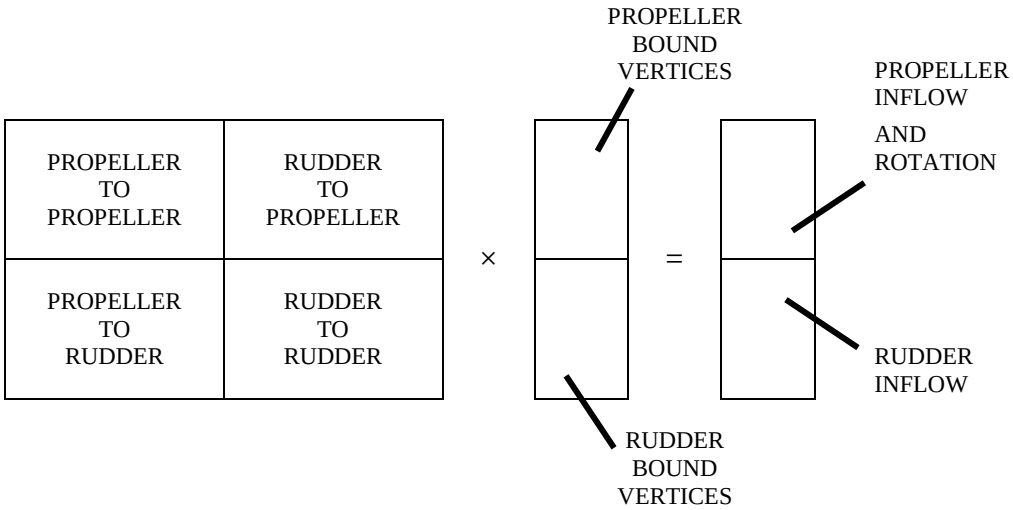

Fig. 2. Scheme of the kinematic boundary condition on the propeller-rudder

The main difference between inflow velocities for propeller and rudder lies in incorporation of the rotation effect in the propeller section of the right hand side matrix. Apart from that the propeller section of the right hand side includes the local values of the non-uniform velocity field of the ship wake, while the rudder section of this matrix is based on the average inflow velocity calculated for the ship plane of symmetry. It should be pointed out that due to the changing mutual location of propeller blades and the rudder the interaction parts of the main matrix must be re-calculated in every analysed propeller blade position. Solution of the above system of equations leads to determination of the hydrodynamic loading on the propeller and on the rudder. This loading reflects mutual interaction in the current geometrical configuration at the given angular position of the propeller.

When the hydrodynamic loading on the propeller and rudder, represented by the intensity of individual bound vortex elements, is known for any blade position, the current pressure distribution may be calculated according to the following formula for the non-dimensional pressure coefficient:

$$C_p = \frac{p - p_\infty}{1/2 \rho V_{\text{ref}}^2} = 1 - \left(\frac{V_{\text{loc}}}{V_{\text{ref}}} \right)^2 , \tag{1}$$

where:

p is the pressure at propeller (or rudder) surface,

p_∞ is the pressure far away from the propeller and rudder

and where in the case of the propeller there is $V_{ref} = V_{inf} + V_{rot}$ and $V_{loc} = V_{ref} + V_{pip} + V_{rip} + V_{pg}$ and in the case of the rudder there is $V_{ref} = V_{inf}$ and $V_{ref} = V_{ref} + V_{pir} + V_{rir} + V_{rg}$,

where:

V_{inf} is the inflow velocity resulting from the non-uniform hull wake field,
V_{rot} is the velocity resulting from propeller rotation,
V_{pip} is the velocity induced on the propeller by the propeller,
V_{rip} is the velocity induced on the propeller by the rudder,
V_{pg} is the local bound vortex intensity on the propeller,
V_{pir} is the velocity induced on the rudder by the propeller,
V_{rir} is the velocity induced on the rudder by the rudder,
V_{rg} is the local bound vortex on the rudder.

The calculated pressure distribution on the propeller and rudder is empirically corrected for the viscosity effects and further employed for computation of the resultant hydrodynamic force and moment components on both objects. Furthermore, this pressure distribution is the basis for cavitation prediction. The method for this prediction described in [3] is retained, except one specific cavitation form which is presented below in detail.

2.2. Specific cavitation phenomena in the propeller-rudder configuration

As the mutual propeller – rudder interaction influences and changes pressure field on both the propeller and the rudder, it must also modify all forms of cavitation present on the propeller blades and on the rudder. However, there is one specific form of cavitation which is particularly susceptible to this influence, namely the propeller cavitating tip vortex.

Cavitation tunnel experiments with propeller – rudder configurations show that the interaction between them leads to a very dynamic behaviour of the sections of the cavitating kernel of the propeller tip vortex in the vicinity of the rudder leading edge. An example of this is shown in Figure 3. It may be seen that the tip vortex cavitating kernel leaving the blade tip has a variable diameter, following the changes in propeller loading resulting form the ship wake structure. Particularly thick section of the vortex corresponds to the high blade loading in the upper wake peak region. Then as the cavitating kernel approaches the rudder leading edge, it changes its shape and diameter in the pressure field generated by the rudder under influence of the propeller. Later the thick section of the vortex enters the high pressure area in front of the rudder leading edge stagnation point, where it undergoes compression. Then the sections of the vortex slide downstream along the rudder into the area of low pressure, where they again increase their diameter and simultaneously they disintegrate into a cloud of bubbles. The details of this process may look differently at different rudder deflection angles, but the basic phases look always the same, even at zero deflection. This process

may take place even when there is no sheet cavitation on the rudder. The dynamic variation of volume of the tip vortex cavitating kernel due to the presence of the rudder leads to generation of additional strong pressure pulses in the surrounding space and it may cause erosion damage on the rudder.

Fig. 3. Cavitating propeller tip vortex distorted by the rudder

Simultaneous measurements of pressure pulses on the ship hull model with and without rudder show a considerable increase of pressure harmonic amplitudes with rudder present – cf. Table 1. All three pressure pick-ups are located along the ship symmetry plane, with point no. 1 located in front of the propeller, point no. 2 directly above propeller and point no. 3 at the rudder leading edge (cf. Figure 1). The table includes amplitudes of the first harmonic of the blade frequency A1 and second harmonic A2, both re-calculated to full scale. As there was no cavitation on the rudder at zero deflection angle and no visible change in cavitation on the propeller blades due to rudder presence, this increase may be attributed to the above described dynamic interaction of the cavitating propeller tip vortex with the rudder. A marked increase in the higher order harmonic amplitudes points to the complicated character of this interaction.

Table 1. Pressure pulses induced by cavitation in the propeller-rudder configuration

Pickup no.	With rudder		No rudder	
	*A*1 [kPa]	*A*2 [kPa]	*A*1 [kPa]	*A*2 [kPa]
1	0.976	0.773	0.730	0.569
2	2.630	2.960	1.963	2.310
3	2.731	3.036	1.560	2.071

In order to model the above described interaction effects numerically, an extended tip vortex model developed from [3] and [4] is proposed, based on the following assumptions:

- the velocity and pressure fields induced by the vortex is calculated using the traditional simple Rankine vortex model,
- the diameter of the Rankine vortex kernel is related to the boundary layer thickness in the tip region of the blade,
- the cavitating vortex kernel of the tip vortex is divided into small sections, each of which is modelled by a circular cylinder,
- dynamics of each section is modelled by the equation analogous to the Rayleigh-Plesset equation, solved numerically in the time/space using Runge-Kutta method,
- the contents of the cavitating tip vortex are assumed to be only vapour, firstly because realistic data on gas content are not available in most cases and secondly because vaporization is much faster than diffusion and vapour dominates inside the kernel,
- the pressure field driving the cavitating kernel dynamics results from the combined propeller and rudder effects,
- the primary purpose of the model is to describe the first cycle of compression /rebound of the cavitating tip vortex sections, disregarding subsequent disintegration into bubble and cloud cavitation.

Then the dynamics of each section of the cavitating vortex kernel is calculated using the equation developed for the cylindrical geometry along the same lines as Rayleigh – Plesset equation. In this case the flow is treated as two-dimensional and purely vaporous content of the kernel is assumed, what leads to the following equation:

$$-\frac{d^2R}{dt^2}R\ln R-\left(\frac{dR}{dt}\right)^2\left(\ln R+\frac{1}{2}\right)+\frac{\sigma}{\rho R}+\frac{2\mu\, dR/dt}{\rho R}=\frac{\Delta p(t)}{\rho}, \tag{2}$$

where:

R is the cylinder radius,

t is time,

ρ is the water density,

σ is the water surface tension,

μ is the dynamic viscosity coefficient,

Δp is the pressure difference across the vortex kernel wall, including propeller and rudder effects.

Figure 4 shows the results of calculation based on Equation (2) referring to the four sections of the cavitating tip vortex kernel. The selected sections approach the rudder leading edge in such a way that two of them slide along one side of the rudder, while the other two slide on the other side (as indicated on the sketch in Figure 4). The

curves in the diagram show the variation of the volume of each section as it moves along the rudder. It may be seen in the diagram, that sections 1 and 2, which slide along the pressure side, undergo only compression i.e. reduction of volume. At the same time the sections 3 and 4, sliding along the suction side, undergo a limited compression, then expansion and compression again. Points marked on the curves indicate the time of passing by the rudder leading edge. This calculation example was performed in model scale, using time step ΔT = 700 [μs].

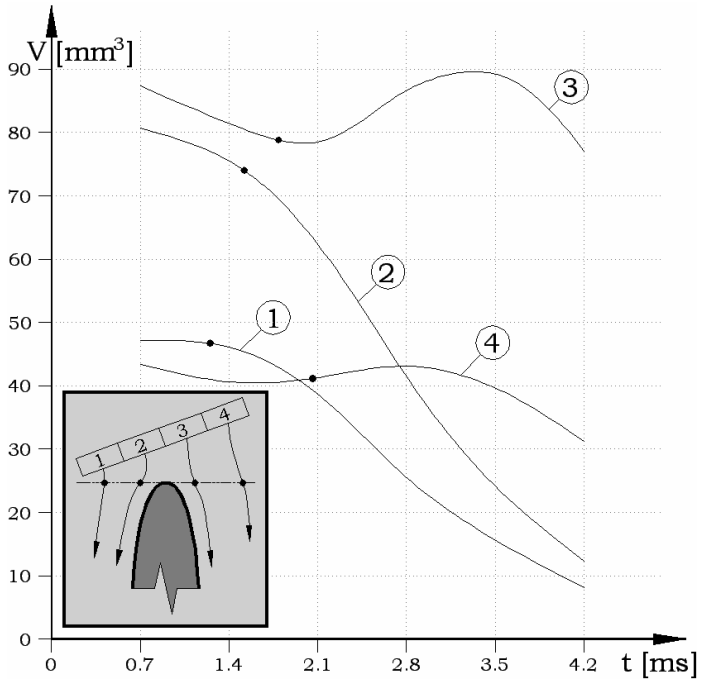

Fig. 4 Calculated dynamics of the cavitating tip vortex kernel passing by the rudder

When the values of R and dR/dt are determined for each ΔT, the effect of the cavitating tip vortex dynamics on the pulsating pressure field generated by the entire propeller – rudder system may be calculated. This is done following the approach already incorporated in the propeller analysis method [4]. In this approach each cavitating tip vortex section is modelled by a point source, described by its mean value Q, constant within each ΔT and reflecting the quasi-steady displacement effect and by dQ/dt, reflecting the vortex dynamics. Both these values are employed in calculation of pressure pulses according to the linearized form of the Cauchy-Lagrange equation:

$$P_H = \frac{\rho}{4\pi}\left(V_S \sum_i \frac{Q_i x_i}{r_i^3} + \sum_i \frac{Q_i}{r_i^2}\frac{dr_i}{dt} - \sum_i \frac{1}{r_i}\frac{dQ_i}{dt} \right), \tag{3}$$

where:

P_H is the pulsating pressure,

V_S is the ship velocity,

r is the distance from source to the calculation point,

x is the component of r in direction of ship velocity.

The sources in the above equation are calculated in the following way:

$$Q_i = \pi\left(R_i^2 - R_{i-1}^2\right)\sqrt{V_S^2 + (\pi Dn)^2}\,, \tag{4}$$

$$\frac{dQ_i}{dt} = \pi\left[\left(\frac{dR_i}{dt}\right)^2 - \left(\frac{dR_{i-1}}{dt}\right)^2\right]\sqrt{V_S^2 + (\pi Dn)^2}\,, \tag{5}$$

where:

D is the propeller diameter

n is the propeller number of revolutions per second

The more detailed description of the above presented theoretical model of tip vortex cavitation may be found in [5].

3. Examples of calculations

The new computational method was extensively tested on a number of examples. The tests were concentrated on two aspects: prediction of the hydrodynamic forces on the rudder and prediction of the pressure pulses generated by the propeller – rudder system.

3.1. Calculation of the hydrodynamic characteristics

Only a few complete examples of measurement of the hydrodynamic forces on the rudder may be found in the literature. One of them is published in [6]. This example is based on standard B4 Wageningen propeller model tested with a symmetrical spade rudder in configuration shown in Figure 5. The results of comparative calculations performed by the above described method are shown in Figure 6 together with the experimental data for the hull drift angle equal to 7.5 [deg] and for three values of the propeller advance coefficient J.

The method described in this paper can perform calculations for several types of rudders, namely: spade rudder, horn rudder, Schilling rudder and rudder incorporating a bulb. The experimental results for these rudders are not available yet, but nevertheless the results of calculations are presented below. The main characteristics of the propeller P1 used in calculations are given in Table 3. Three rudders have been used in calculations: spade rudder, horn rudder and Schilling rudder. Their trapezoidal outlines are given in Table 2.

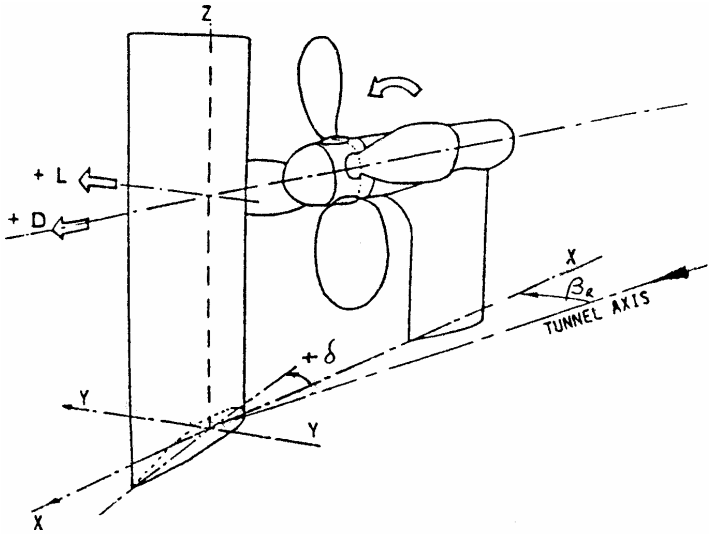

Fig. 5. Propeller-rudder configuration in model experiments [6]

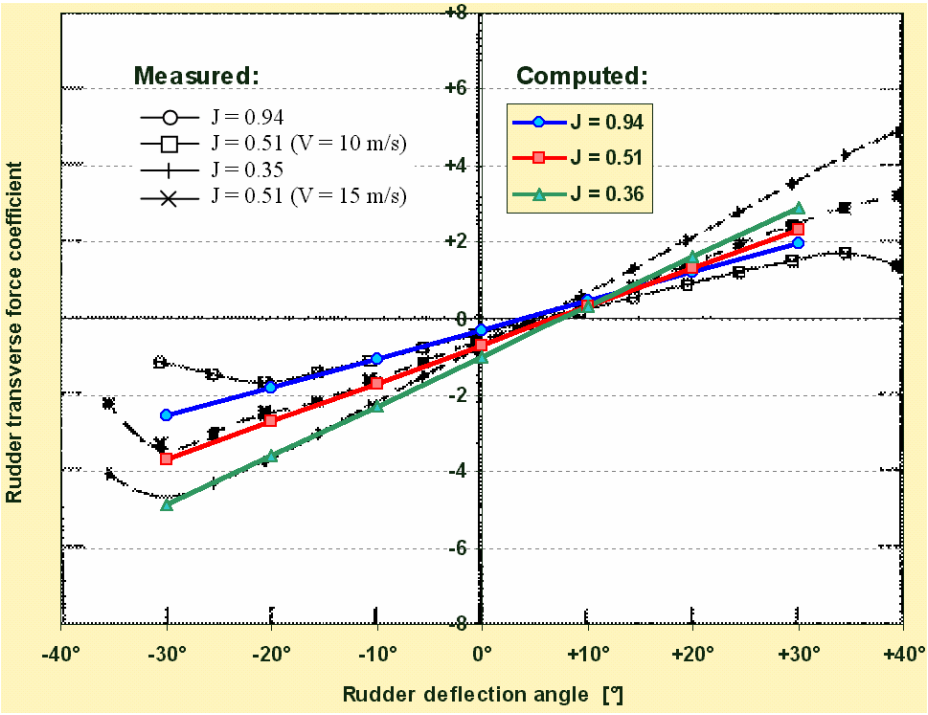

Fig. 6. Comparison of the calculated and measured transverse force coefficient on the rudder (measured results from [6])

Table 2. Outline of the rudders

Type of rudder	Spade and horn rudders		Schilling rudder	
Height [m]	Total chord [m]	Chord forward [m]	Total chord [m]	Chord forward [m]
–3.4500	3.8000	1.3000	4.2000	1.1200
–1.6100	4.3200	1.6000	4.4800	1.4000
0.2300	4.8400	1.9000	4.7600	1.6800
2.0700	5.3600	2.2000	5.0400	1.9600
3.9100	5.8800	2.5000	5.3200	2.2400
5.7500	6.4000	2.8000	5.6000	2.5200

Table 3. Main characteristics of the propeller P1

Propeller diameter			D = 8.200 [m]	
Number of blades			Z = 5	
Number of revolutions			RPM = 99.0	
Ship velocity			V = 20.5 [knots]	
r/R	Chord [m]	P/D [-]	Skew [m]	Camber [m]
0.25	2.2875	0.9694	–0.096	0.0979
0.4	2.5913	1.0167	–0.316	0.0834
0.5	2.7779	1.0402	–0.387	0.0715
0.6	2.9325	1.0539	–0.337	0.0632
0.7	3.0323	1.0547	–0.153	0.0578
0.8	3.0416	1.0352	0.152	0.0516
0.9	2.8226	0.9859	0.569	0.0417
0.95	2.3355	0.9494	0.834	0.0321
1.0	0.0	0.9090	1.156	0.0

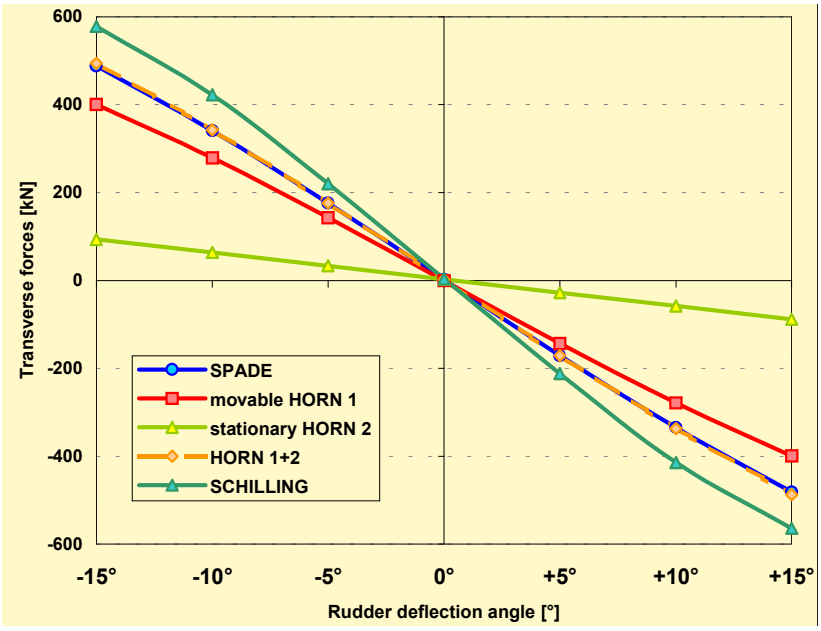

Fig. 7. Calculated transverse forces on the spade, horn and Schilling rudders

The results of calculation of the transverse force on the three rudder types are plotted in Figure 7. It may be noted that in the case of the horn rudder the method calculates forces separately on the moving and on the fixed part of the rudder.

3.2. Calculation of the cavitating tip vortex and resulting pressure pulses

The calculation of the pressure pulses generated by the propeller and rudder with special attention to the effect of the cavitating tip vortex were performed for the configuration shown in Figure 1 using the propeller P1 and the spade rudder defined at zero deflection. Table 4 shows the results of calculation with and without the rudder. It may be noticed that inclusion of the rudder effect on the cavitating tip vortex shed from propeller blades brings the results of calculations in closer agreement with the results of the measurements.

Table 4. Calculated and measured pressure pulses induced by the propeller–rudder configuration

Pickup No.	Mesured with rudder	Calculated without rudder	Calculated with rudder
1	0.976	1.480	1.563
2	2.630	1.880	2.470
3	2.731	1.890	2.658

4. Conclusion

The paper describes an extension of the existing numerical method enabling the detailed analysis of the mutual hydrodynamic interaction between the operating propeller and the rudder. The assessment of the results of calculations presented above leads to the following conclusion:

- the method presented in this paper enables effective prediction of the hydrodynamic forces and cavitation phenomena on the interacting propeller and rudder,
- despite the inevitable simplifications of the theoretical model the accuracy of the method is sufficient for its application as the practical design tool,
- the method may be used for design of propellers, rudders and as an auxiliary tool in the analysis of manoeuvring characteristics of ships,
- a new model of the propeller cavitating tip vortex interaction with the rudder, enabling more accurate prediction of the pressure pulses induced by the propeller and rudder, is the important feature of the above presented method.

References

[1] Da-Qing Li: *A Non-linear Method for the Propeller-Rudder Interaction with the Slipstream Deformation Taken into Account*, Comput. Methods Applied Mech. Eng., No. 130, 1996, pp. 115–132.

[2] Hang Le Thuy: *A Lifting Surface Method for the Analysis of Propeller-Rudder Interaction*, Ph. D. Thesis, Gdańsk University of Technology, 2002.
[3] Szantyr J. A.: *Analytical Prediction of Propeller Cavitation*, The Naval Architect July–August, 1991.
[4] Szantyr J. A.: *A Method for Analysis of Cavitating Marine Propellers in Non-uniform Flow*, Intern. Shipbuilding Progress, Vol. 41, No. 427, 1994.
[5] Szantyr J. A.: *A Computational Model of the Propeller Cavitating Tip Vortex Interacting with the Rudder*, Proc. 6th Intern. Symp. on Cavitation CAV'06, Wageningen, The Netherlands, September, 2006.
[6] Molland A. F., Turnock S. R.: *The Effect of Hull on the Manoeuvring Performance of Rudders*, Proc. RINA Conf. On Ship Motions and Manoeuvrability, London, February, 1996.

Wzajemne oddziaływanie hydrodynamiczne pomiędzy pracującą śrubą i sterem

Referat przedstawia opis algorytmu i programu komputerowego do analizy numerycznej oddziaływania hydrodynamicznego pomiędzy pracującą śrubą a sterem. Program jest oparty na niestacjonarnej powierzchni nośnej reprezentującej śrubę i na metodzie elementów brzegowych do reprezentacji steru. Danymi wejściowymi są dowolna geometria śruby i dowolna geometria steru. Oddziaływanie kadłuba statku jest brane pod uwagę w postaci niejednorodnego pola prędkości strumienia nadążającego. Wzajemne oddziaływanie hydrodynamiczne jest uwzględniane poprzez jednoczesne rozwiązanie niestacjonarnego kinematycznego warunku brzegowego na sterze i na śrubie. Wyniki obliczeń obejmują zmienne w czasie rozkłady ciśnienia na śrubie i na sterze wraz z wynikającymi z nich siłami hydrodynamicznymi. Ponadto program może wykrywać i opisywać różne formy dynamicznie zmiennych zjawisk kawitacyjnych występujących na sterze i na śrubie oraz wyznaczać ich hydrodynamiczne skutki. Referat zawiera wyniki obliczeń charakterystyk hydrodynamicznych i zjawisk kawitacyjnych różnych konfiguracji ster-śruba. Wyniki obliczeń zostały porównane z dostępnymi rezultatami badań eksperymentalnych. Porównanie to potwierdza skuteczność przedstawionej metody obliczeniowej jako narzędzia do projektowania i analizy konfiguracji śruba-ster.

Information for Authors

Send to: *Archives of Civil and Mechanical Engineering*
Polish Academy of Sciences, Wrocław Branch
Podwale 75, 50-449 Wrocław, Poland

Archives of Civil and Mechanical Engineering (ACME) publishes both theoretical and experimental papers which explore or exploit new ideas and techniques in the following areas: structural engineering (structures, machines and mechanical systems), mechanics of materials (elasticity, plasticity, rheology, fatigue, fracture mechanics), materials science (metals, composites, ceramics, plastics, wood, concrete, etc., their structures and properties, methods of evaluation), manufacturing engineering (process design, simulation, diagnostics, maintenance, durability, reliability). In addition to research papers, the Editorial Board welcome: state-of-the-art reviews of specialized topics, letters to the Editor for quick publication, brief work-in-progress reports, brief accounts of completed doctoral thesis (one page is maximum), and bibliographical note on habilitation theses (maximum 250 words). All papers are subject to a referee procedure, except for letters, work-in-progress reports and doctoral and habilitation theses, which are briefly reviewed by the Editorial Board.

The papers submitted have to be unpublished works and should not be considered for publication elsewhere.

The Editorial Board would be grateful for all comments on the idea of the journal.

Submit three copies, each complete with abstract, tables, and figures.
Detailed information about the Journal on web:
http://www.pan.wroc.pl
www.ib.pwr.wroc.pl/wydzial/czasopismoACME.html
http://www.wmech.pwr.wroc.pl

Price 15 zł
(0% VAT)

Subscription orders should be addressed to:

Oficyna Wydawnicza Politechniki Wrocławskiej
Wybrzeże Wyspiańskiego 27
50-370 Wrocław